A water-Cherenkov muon veto for the nEXO neutrinoless double beta decay experiment

Soud Al Kharusi

Department of Physics

McGill University, Montréal

January 8, 2024

This thesis is presented in partial fulfilment of the requirements for the degree of

Doctor of Philosophy in Physics

Abstract

The nEXO neutrinoless double beta decay experiment aims to detect a hypothetical decay mode in the isotope xenon-136. A positive observation of this decay mode would serve as direct evidence for lepton number violation and confirm the Majorana nature of neutrinos, representing a breakthrough in physics beyond the Standard Model. Such an observation could also offer new pathways for understanding the mass generation mechanism of fermions, and potentially provide insights into the matter-antimatter asymmetry problem. To increase the likelihood of observing neutrinoless double beta decay, nEXO requires stringent measures for background mitigation, such as placing the experiment deep underground to shield it from cosmic rays. Despite these measures, the residual cosmic muon flux remains a concern.

This thesis presents an evaluation of the cosmogenic background rate in nEXO as well as the impact of these backgrounds on the experiment's sensitivity to neutrinoless double beta decay. It introduces the initial design for an anti-coincident water-Cherenkov muon veto aimed at mitigating these cosmogenic backgrounds. Additionally, the low background environment of nEXO enables the search for other rare interactions at the MeV scale, including those from astrophysical sources. As such, a preliminary evaluation of nEXO's sensitivity to neutrinos originating from nearby galactic core-collapse supernovae is provided.

Abrégé

L'expérience nEXO, axée sur la double désintégration bêta sans neutrino, vise à identifier un mode de désintégration hypothétique dans l'isotope xénon-136. Une observation positive de ce mode de désintégration fournirait une preuve directe de la violation du nombre de leptons et révélerait la nature de Majorana des neutrinos, constituant ainsi une avancée dans la physique au-delà du modèle standard. L'observation de neutrinos de Majorana ouvrirait de nouvelles voies pour comprendre l'origine de la masse des fermions et pourrait peut-être résoudre le mystère de l'asymétrie matière-antimatière. Pour avoir une chance d'observer la double désintégration bêta sans neutrino, nEXO devra respecter des exigences strictes en matière de réduction du bruit de fond, y compris en plaçant l'expérience dans un environnement souterrain profond pour se protéger des rayons cosmiques. Néanmoins, le flux résiduel de muons cosmiques doit être pris en compte.

Cette thèse présente une évaluation du taux de bruit de fond cosmogénique dans nEXO, son impact sur la sensibilité de nEXO à la désintégration double bêta sans neutrino, et la conception initiale d'un veto muon Cherenkov à eau anti-coincident, atténuant les bruits de fond cosmogéniques de nEXO. En outre, l'environnement à faible bruit de fond de nEXO offre la possibilité de rechercher d'autres interactions rares à l'échelle du MeV, y compris celles provenant de sources astrophysiques. Une évaluation de la sensibilité de nEXO aux neutrinos provenant de supernovae à effondrement de noyau galactique proche est donc fournie.

Acknowledgements

Statement of Contribution

This research could not have been possible without the collaboration of many people, the majority of whom are in some way connected to the nEXO experiment. Here, I list the major contributions of myself, and my collaborators, to this thesis. All work is my own unless explicitly stated otherwise here, or in the body of the text.

Chapter 1 presents a theoretical overview of the symmetry structure of the Standard Model of particle physics. The chapter focuses on building intuition and developing an understanding of the accepted mass generation mechanism of fermions (the Higgs mechanism) and electroweak symmetry breaking from my perspective as a graduate student in experimental particle astrophysics.

Chapter 2 provides an overview of our current understanding of neutrino physics with some historical context. The chapter also connects the notion of neutrino masses to the cosmological problem of matter-antimatter asymmetry. A survey of current experimental programs studying neutrinos is presented, and the motivation for neutrinoless double beta decay searches is outlined.

Chapter 3 introduces the nEXO experiment, highlighting the operational principles of its time projection chamber (TPC), and multi-parameter profile-likelihood analysis methods. Novel figures presenting simulated 10 year datasets of nEXO are shown, and the distinguishing features of nEXO compared to alternative experimental searches for neutrinoless double beta decay are emphasized. The new nEXO plots were generated by me, but are the result of work with Sander Breur, Ralph DeVoe, Ako Jamil, Brian Lenardo and David Moore (nEXO data representation team).

Chapter 4 focuses on cosmogenic background estimates for nEXO, and develops mitigation strategies against them. This work builds on the prior FLUKA studies from Joshua Albert and Jacob Zettlemoyer. Under the guidance of Lisa Kaufman and Raymond Tsang, the Geant4 cosmogenics simulation was developed. The mitigation strategies presented were developed by me, with the TPC tag building on the EXO-200 ^{137}Xe veto algorithm by Caio Licciardi and Kevin Murray. The work presented on different underground locations was performed by the nEXO site selection team, of which I am also a member, who contributed to nEXO's Assessment of Alternatives study for the U.S. Department of Energy: Samuele Sangiorgio, Richard Saldanha, Scott Schwartz, Brian Lenardo and Seth Thibado. The bootstrapping of nEXO exclusion limits was built from Brian Lenardo's code for the background scaling studies in the 2021 nEXO sensitivity paper. The toy MC referenced in this chapter was one developed originally by myself, and later (independently) by Richard Saldanha following the same algorithm for cross-checking. The primary cosmogenics datasets on which the conclusions are drawn were generated by me, except for the light-only reconstruction of energy spectra from $^{136}\mathrm{Xe}(n,\gamma)^{137}\mathrm{Xe}$

(and other) de-excitation cascades. Those were generated by Scott Schwartz using EXO-200 Geant4 event generators with macro files I provided. The correlation plots of different activations were generated by Samuele Sangiorgio, from the same Geant4 Shielding dataset. The halflife exclusion limits resulting from the combination of ^{137}Xe scaling and deadtime losses were calculated by me, and are not the same as those found in NEXO-SIM-029 / LLNL-TR-849598.

Chapter 5 assesses the muon tag efficiency of the nEXO outer detector. Here, the muon generation algorithms developed by the author in the previous chapter are used to produce Cherenkov light on simulated PMTs in Geant4. The analysis methods and algorithms developed are my own, with the exception of the PMT quantum efficiency code which is built from Remington Hill's code. Ako Jamil was the first user of Chroma in nEXO and provided a lot of insight into the feasibility of adding the muon physics into Chroma. Emma Klemets ported the Cherenkov physics code I wrote in Python for a project on parallelized ray tracing with Numba into the Chroma framework. Regan Ross then ported my muon generation code from Geant4 into Chroma and FLUKA. Liam Retty was responsible for all CAD file geometries, and imported the STL files according to specifications from Daya Bay and Hamamatsu. Samin Majidi set up the final PMT configuration in Chroma, based off the light map study I provided. The muon tagging analysis for Chroma datasets was coded by Liam Retty under my supervision. Much of the work in this chapter was discussed during outer detector simulation calls led by myself, with valuable insights from Thomas Brunner, Erica Caden, Caio Licciardi, Allen Odian, and Ubi Wichowski.

Chapter 6 presents the first evaluation of the supernova neutrino interaction channels in nEXO, both in the outer detector and the TPC. This chapter is the result of my discussions with various attendees of the first SNEWS 2.0 meeting in 2019.

Chapter 7 provides a summary of the main findings of the thesis, along with potential avenues for further development.

All figures in this thesis are my own, aside from those stated otherwise in the caption.

Words of Gratitude

I cannot thank my supervisors enough: Thomas and Daryl, you have given me such an enriching experience as a graduate student. Thank you for always guiding me, and providing ample opportunity for development and for rest. I hope to one day also be an "experienced user" of expensive lab equipment, inspire others to dream big, and focus on what is important. I would also like to thank Jonathan Sievers, whose presence at my initial supervisory committee meeting led me down a long rabbit hole that resulted in a much deeper understanding of the connection between neutrinos and cosmology.

Thank you to the many academics I have interacted with over the years. In particular, the postdocs (at the time) Thomas McElroy, Raymond Tsang, Chris Chambers, and Brian Lenardo: you have each taught me valuable lessons in labwork, analysis, and life in academia. A special thanks to David G. for sharing his expertise in C++ and ROOT. I am so grateful for your time, and especially impressed by your patience. To Ako and the BνL/MEGA groups, thank you for sharing in my frustrations, and sharing yours — it has been a blast going through them with you. I would also like to express my gratitude to the late Prof. Alex Flournoy. His online physics lectures have been both a joy and a blessing to watch.

To my friends and family in Oman and elsewhere, thank you for your support. I have been gone too long, and I do not know where I am going nor when I will be back. To my mother, I am so grateful to have you and for your patience in my absence during these last few years. To my sisters Naila, Lubie, and Scherri: thank you for understanding (or pretending to) and always welcoming me to your homes when I needed it. To Harrison, thanks for keeping me in check with the page count.

To Alexandra, Aleks, and Janay thank you for taking me in like a stray. To Brendon, Nico, Chris and Robert, thank you for bearing with me in our apartment, and throwing it on the Split. To the Cinque à Set volleyball team, thanks for keeping me active by the net, and to Eric and the Empty Nesters for keeping me expressive on stage.

Thank you to my office mates: Rodrigo, Simon, Ben, and Adam for fighting the good fight during the desk wars, and to my former teachers (and now friends) for their inspiration and continuous support, Jacqueline Darby, Damien d'Souza, and Chris Hassan. Thank you to all my friends, for all the *good* times we have had over the last few years: Alex W., Alice, Doug, Richie, Tom, Nick C., Maclean, Megan, Hannah, Aidan, Nick V., Bobby, Andrew, Mairead, Christian, Thanh, Nathan, Gary, Connor, Laura, Julia and MG.

To my father, Mohammed Samir Al Kharusi

and to my nephew, Hilton Samir Olivella

Contents

List of Figures

List of Tables

List of Acronyms

BSM	beyond the Standard Model of particle physics.
CνB	cosmic neutrino background.
CCSN	core collapse supernova.
CDF	cumulative density function.
CEνNS	coherent elastic neutrino-nucleus scattering.
CKM	Cabibo-Kobayashi-Maskawa matrix.
CMB	cosmic microwave background.
DNN	deep neural network.
EOI	energy of interest.
EWSB	electroweak symmetry breaking.
FPGA	field-programmable gate array.
FV	fiducial volume.
GPU	graphical processing unit.
HFE	hydrofluoroether-7200 heat transfer fluid from 3M / Novec.
IBD	inverse beta decay.
LNV	lepton number violation.
LXe	liquid xenon.
MC	Monte Carlo.

NME nuclear matrix element.

OC outer cryostat vessel.

OD outer detector.

PDF probability density function.

PMNS Pontecorvo-Maki-Nakagawa-Sakata matrix.

PMT photomultiplier tube.

QE quantum efficiency.

QFT quantum field theory.

RAM random access memory.

ROI region of interest.

SiPM silicon photomultiplier.

SM Standard Model of particle physics.

SPE single photo-electron.

TPC time projection chamber.

VEV vaccuum expectation value.

Chapter 1

Introduction

The focus of this thesis is to develop a specialized radiation detector that is designed to explore the nature of the neutrino, a fundamental particle of the Standard Model (SM). In particular, we are designing a nuclear decay experiment called nEXO to answer the question: "is the neutrino a Majorana fermion?", i.e., a spin-$\frac{1}{2}$ particle that is its own antiparticle. If found to be true, the neutrino must derive some component of its mass from a mechanism other than the Higgs mechanism, which is conventionally ascribed to all other fermions in the SM, such as electrons, and quarks. Some of these alternative mass generation mechanisms for neutrinos will also play a role in answering an open question in fundamental physics and cosmology: the matter-antimatter asymmetry problem. To investigate these topics, the nEXO experiment will search for neutrinoless double beta decays ($0\nu\beta\beta$) of the isotope ^{136}Xe — a hypothesized nuclear decay mode. We now know that the halflife of this decay, if it exists, must be longer than our best estimate for the current age of the Universe. Therefore, any $0\nu\beta\beta$ observation would be an extremely rare occurrence.

All natural materials on Earth are slightly radioactive and, when searching for potentially rare decay modes such as $0\nu\beta\beta$, one has to go to great lengths to avoid

unnecessary levels of radioactivity in our detectors that wash-out the searched for signal. For this reason, nEXO must be situated in a deep underground cavern, where kilometers of rock overburden shield the detector from cosmic rays: charged particles that rain down on us from the upper atmosphere. Still, residual cosmic rays (namely, muons) punch through to the underground cavern, releasing neutrons from neighbouring nuclei along their tracks. These neutrons can be captured by nuclei inside the nEXO detector, making them temporarily radioactive. Collectively, these newly activated nuclei in the detector are referred to as cosmogenic backgrounds.

To mitigate the effect of cosmogenic backgrounds on the $0\nu\beta\beta$ search, a large water tank surrounds nEXO. Highly energetic charged particles, such as the muons that make it so deep underground, produce Cherenkov light as they traverse the water tank. Detecting the Cherenkov light bursts from the traversing muons allows us to reject cosmogenic backgrounds, as they will be correlated with the time of the muons passage.

This thesis is outlined as follows: the rest of this chapter will overview the Standard Model of particle physics with an emphasis on building intuition for, as opposed to providing a rigorous derivation of, the core concepts that underpin our understanding of fermion mass generation.

Chapter 2 will give a historical review of neutrino physics, and describe how the discovery of their masses does not easily fit into the context of the SM in an obvious way. Chapter 3 will introduce the nEXO experiment, and describe its operational principles and analysis techniques. Chapter 4 addresses the effect of cosmogenic backgrounds, and evaluates the impact they will have on nEXO's sensitivity to $0\nu\beta\beta$. Chapter 5 will go over

the optical simulations of Cherenkov light in the water tank, leading to the design of the nEXO outer detector (OD). Finally, the radiopure liquid xenon environment of nEXO and its large instrumented water tank, allows the experimental set up to be used as a supernova neutrino observatory. The sensitivity of nEXO to galactic supernova neutrinos is evaluated in Chapter 6.

1.1 Fundamental particles and their interactions

The basic components of matter in our Universe appear in the form of particles, which can be interpreted as excitations, or fluctuations, in their respective quantum fields. The identifying features and unique characteristics of each particle consist of a defined mass, spin, and several charges. These features play a role in their propagation through space, and interactions with other particles. If we restrict ourselves to a discussion of particles considered to be fundamental — i.e., those not made up of additional components and lacking any internal structure — then it has been shown that all matter particles are fermionic (carrying quantum spin-$\frac{1}{2}$) and all force-carrying particles are bosonic (possessing integer spin). The combination of all known fundamental particles and their interactions makes up what is called the Standard Model of Particle Physics (SM), and its development is widely heralded as one of the world's greatest scientific achievements due to its incredible accuracy in describing nature using only 12 particles of matter (fermions), and 12 force-mediating bosons.[1] A summary of these known particles is shown in Figure 1.1.

[1]Successes of the SM include the prediction of massive $W^{\pm}$ and Z^0 bosons, the observation of a Higgs boson, the predicted magnetic moment of the electron, and the prediction of the additional quarks (strange, bottom, and top) prior to their discovery.

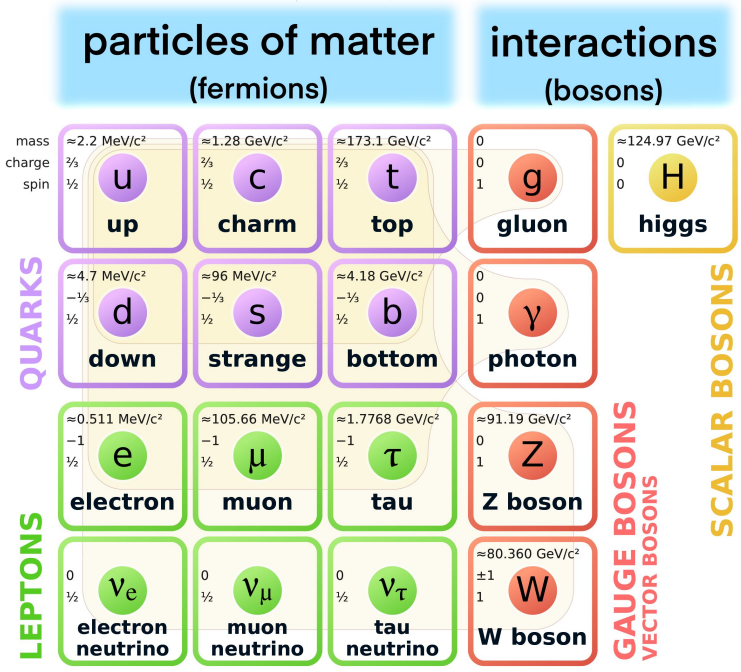

Figure 1.1: Particles in the Standard Model. Those with measured masses are provided from [1], but neutrino mass limits are omitted. Figure adapted from Wikimedia under the Creative Commons license [2].

1.2 The role of symmetry in modern physics

In the early 20th century, Emmy Noether published a manuscript which proved that for every continuous, differentiable symmetry of the action of a physical system there must be an associated conservation law [3, 4]. The theorems outlined in her 1918 paper, commonly referred to as Noether's theorems, have had profound consequences in our understanding of modern theories of fundamental physics including Einstein's general relativity and the development of the SM. The proceeding sections of this introductory chapter will attempt to provide an intuition connecting Noether's theorems to the mathematical framework of the SM.[2]

[2] Additional background on Noether's theorems and their relation to gauge theories and Lie groups can be found in Appendix A.

1.3 The symmetry structure of the Standard Model

The symmetry group corresponding to the high energy representation of the SM is

$$SU(3) \times SU(2)_L \times U(1)_Y, \tag{1.1}$$

defining the set of transformations that can be applied to the SM Lagrangian while leaving observable physics unchanged. The first term, $SU(3)$, is the Lie group associated with the strong force, and the latter two terms together are associated with the electroweak force.

In particular, $SU(3)$ is the group of special unitary matrices of rank 3; a group of traceless 3×3 matrices which leave the length of a 3-vector unchanged i.e., the determinants of these matrices are real and are equal to 1. The basis of the 3-vectors on which these $SU(3)$ matrices act are the colour basis of the strong force. In this framework, the 3-vectors being discussed are called $SU(3)$ flavour triplets. The group $SU(3)$ has 8 generators in total, corresponding to one for each colour charge of the strong force (red, blue, green) as well as their anti-colour counterparts (anti-red, anti-blue, anti-green) and their linear combinations subtracting one (due to the tracelessness of $SU(3)$ matrices allowing only antisymmetric combinations of colour charges). This totals 8 generators, which are identified as 8 gluons, the strong force mediating particles of the SM.

Our focus in this chapter however is on the slightly more complex electroweak terms of the SM symmetry group,

$$SU(2)_L \times U(1)_Y. \tag{1.2}$$

These two terms can be interpreted as follows: electroweak interactions must act on $SU(2)$ doublets (2-vectors). The subscript, L, caveats that electroweak interactions only act on left-handed states; this fact will be uncovered in Section 1.4, but for now note that it is associated with the parity-violating nature of the weak force. One of the "charges" of the electroweak group is called weak isospin, and it is associated with $SU(2)$. Weak isospin behaves analogously to quantum mechanical spin in terms of how it is added, subtracted, and acted on. There are 3 generators of $SU(2)$, which come as a result of the 2×2 traceless nature of $SU(2)$, analogously to the strong force. The three generators of the $SU(2)$ group are identified as 3 (massless) vector bosons denoted $\mathrm{W}_{1,2,3}$.

The second half of the electroweak group, $U(1)_Y$, denotes the set of complex-valued numbers with absolute value 1, i.e., multiplication of numbers that correspond to rotations in the complex plane — a phase change. The associated conserved charge of the $U(1)_Y$ group is called weak hypercharge, and it is denoted as Y. The $U(1)_Y$ group has one generator: the massless vector boson commonly denoted as B.[3]

Each left- or right-handed state of a particle is assigned a weak hypercharge, and a weak isospin. Similar to the way in which $\pm$ charges in electromagnetism determine how (and if) an object would interact with an electromagnetic field, weak hypercharges and isospins determine how a particle interacts with the weak force.

[3]Notice that this is a direct analogy to electromagnetism, which is invariant under transformations of the U(1) group and has a massless vector boson associated with it: the photon. See Appendix A for more details.

1.4 Parity violation, handedness, and chirality

The electroweak symmetry group (Equation 1.2) explicitly shows that there is a dependence of the electroweak interactions on the handedness of particles. In this section, we define what we mean by handedness, and how handedness can be manifested physically in subatomic interactions.

A common description of handedness utilizes the projection of spin onto the momentum of a particle. The sign of the dot product $h = \mathbf{s} \cdot \mathbf{p}$ is known as helicity and is illustrated in Figure 1.2. Here, the 3-momentum $\mathbf{p}$ is a true vector: when taking all of its components and negating them, $\mathbf{x} \to -\mathbf{x}$, i.e., performing a reflection in a mirror — a parity transformation, the actual direction of the momentum changes: $\mathbf{p} \to -\mathbf{p}$. Spin however has units of angular momentum, the cross product of a displacement with a momentum, $\mathbf{r} \times \mathbf{p}$. Upon a parity transformation, $\mathbf{x} \to -\mathbf{x}$, both vectors gain a negative sign which cancel out with each other. Hence, spin, whether thought of as quantum mechanical spin or as classical angular momentum, is a pseudovector (also called an axial vector) whose sign does not change under a parity transformation.

Helicity can be used to define a handedness in the world. If one can measure the helicity of outgoing particles in physical interactions, one can measure the handedness of the responsible force. This is precisely what was done by Dr. Wu's team in 1956 via β-decays of ^{60}Co [5]. β-decays are a weak interaction process, and outgoing electrons in these decays were measured to be left-handed, having their spins and momenta pointing in opposite directions. This was the first indication that the weak force is indeed a parity violating force, as predicted by Lee and Yang the prior year [6].

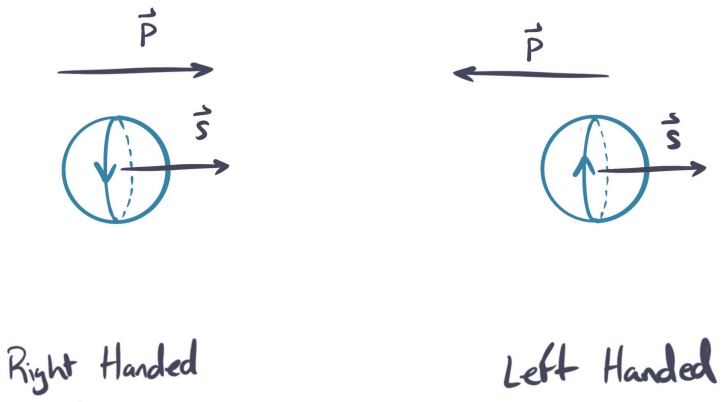

Figure 1.2: Helicity is defined as the dot product of the spin and momentum vectors of a particle in motion. A particle's helicity changes sign under parity, and is dependent on our frame of reference. I.e., a Lorentz boost may take us to a reference frame in which the particle appears to move in the opposite direction relative to its motion in the original reference frame. In this scenario, there is an additional negative sign in the momentum vector, but not the spin vector, of the particle when evaluated in the new frame. This additional negative sign changes the value of the particle's helicity.

On a more fundamental level, the handedness of the particles in a quantum field theory (QFT) is defined by the way in which the fields change under particular transformations of the Poincaré group: translations in spacetime, rotations in 3-space, and Lorentz boosts. In particular representations of these fields (e.g., Dirac spinor representations), one can define projection operators that remove either the left- or right-handed components [7]. This notion of handedness is called chirality, and the subscripted L in Equation 1.2 actually denotes the fact that the weak force acts on left-chiral fields only.

This distinction of chirality versus helicity in defining handedness becomes important for massive particles, since helicity is not relativistically invariant: there exists frames of

reference one can boost to where the sign of the momentum of the particle will reverse without the reversal of its spin, therefore changing the value of a particles helicity. In contrast, chirality is a Lorentz invariant quantity, but is not necessarily a constant of motion (we will return to this when discussing the masses of fermions). Only in the limit where particle energies are much greater than their masses do the values of helicity and chirality coincide. This ultrarelativistic limit is the context in which every neutrino that we have observed has been measured, and this fact will enter in the discussion of neutrino masses in Chapter 2.

1.5 Electroweak symmetry breaking

Electroweak symmetry breaking (EWSB) is a cornerstone in the development of the SM [8–11]. At high energies, the electromagnetic and weak interactions are unified under a single framework [12–14], the electroweak force, which carries the symmetry structure of Equation 1.2. The electroweak force is mediated by four massless vector bosons $W_{1,2,3}$ and B, the generators of the electroweak symmetry group (outlined in Section 1.3). These massless bosons would give rise to infinitely long range interactions, similar to the electromagnetic force, and would therefore couple more strongly to particles compared to the massive vector bosons $W^{\pm}$ and Z^0 we observe in particle accelerators today. EWSB allows us to correspond the massless $W_{1,2,3}$ and B bosons with the massive vector bosons of the SM that limit the effective range of the weak force and, by the Higgs mechanism (or BEH mechanism), will also allow for a mass generation mechanism for fermions [12, 15]. We will focus here on why fermions in the SM start off as massless, and how the Higgs mechanism resolves this issue.

1.5.1 Massless fermions

In natural units ($\hbar = c = 1$),[4] mass terms for fermions in the SM Lagrangian must have units of the field they are representing squared, i.e.,

$$\mathcal{L}_{mass} \sim k\psi\overline{\psi}, \tag{1.3}$$

where k is a constant that is associated with a particle's mass, and the particle itself described as an excitation of its field, ψ, and the Dirac adjoint of this field is $\overline{\psi}$. This intuitively makes sense: if we require that a particle and its antiparticle both have the same mass, as is experimentally observed, then you would expect ψ and its adjoint $\overline{\psi}$ to be connected to the same mass term. This mass term will appear in the potential term of the Lagrangian, as it represents an energy density that is present even in the absence of motion. Moreover, it also must not arise directly from interactions with other particles, i.e., the term must be present in the vacuum, when the particle is merely existing.

Our problem arises because all known particles of matter (fermions in the SM) have been experimentally observed to interact via the weak force. Thus, the terms associated to the fermion fields in the Lagrangian must be broken up into left- and right-chiral components, since the weak force is parity violating (Section 1.4). If the Lagrangian is to obey the electroweak symmetry of Equation 1.2, all terms written in the Lagrangian must be weak hypercharge neutral (otherwise they will not be gauge invariant under $U(1)_Y$ transformations). The combination of these two facts forces all fermion fields to be

[4] Natural units will be used throughout this thesis. Hence, masses will be written without a factor of $1/c^2$, and momenta without a factor of $1/c$.

massless because:

1. both left- and right-chiral particle and antiparticle pairs must have the same mass (coupled in the same mass term);

2. combinations of left- and right-chiral terms are not weak hypercharge neutral, since only the left-chiral fields interact via the weak force, and they carry a different magnitude of weak hypercharge than the right-chiral component.

In other words

$$\mathcal{L}_{mass} \nsim k(\psi_L\overline{\psi_R} + \psi_R\overline{\psi_L}), \tag{1.4}$$

where k is a constant mass term. It is not allowed in the SM because the terms $\psi_L\overline{\psi_R}$ and $\psi_R\overline{\psi_L}$ are each charged differently under $SU(2)_L$ and $U(1)_Y$, and cannot be invariant under the transformations of electroweak symmetry group $SU(2)_L \times U(1)_Y$ [16].

1.5.2 The Higgs mechanism

The Higgs (BEH) mechanism famously provides a pathway to mass generation in the fermion sector of the SM and assigns masses for the weak force's gauge bosons [12, 15]. Here we will sketch the mechanism, but refer the reader to the review article [17] for a more in depth treatment.

In the early 1960s, Anderson considered the possibility of spontaneously broken symmetries as a basis for the generation of an effective mass for the photon, thereby explaining the expulsion of magnetic fields from a superconductor in the Meissner effect [18]. Meanwhile, Goldstone was investigating the behaviour of scalar fields [19] in a

Lagrangian that possesses certain continuous symmetries. Goldstone recognized that in a system whose symmetry is spontaneously broken there will be massless spin-0 particles that will result (these are now known as Goldstone bosons or Goldstone modes, and they correspond to additional degrees of freedom resulting from symmetry breaking). Higgs then made the connection that one can add two complex scalar fields, ϕ_1 and ϕ_2, to the electroweak Lagrangian and allow for interactions with massless vector bosons ($W_{1,2,3}$ and B) in a gauge-invariant way. The additional complex scalar fields can possess the continuous symmetry as per Goldstone's description, thereby allowing for additional spin-0 massless bosons after spontaneous symmetry breaking [11]. The additional Goldstone modes are absorbed by the massless electroweak bosons, $W_{1,2,3}$ and B, and the particularities of the mixing and gauge-fixing of the bosons gives rise to massive $W^{\pm}$ and Z^0 mediators of the weak force, and the massless photon of electromagnetism as per Salam's description of electroweak unification [13]. Only the one real component of ϕ_1 remains (the Higgs field), the other 3 degrees of freedom from ϕ_1 and ϕ_2 (one real, and two complex) are absorbed into longitudinal polarizations of the vector bosons, giving them mass terms.

Illustrating this further, Higgs postulated the existence of an additional $SU(2)$ doublet field in the SM, now referred to as the Higgs doublet, that permeates all of spacetime. These additional complex fields ϕ_1 and ϕ_2 are usually represented as a column vector, similarly to the flavour doublets of the lepton and quark sectors

$$\begin{pmatrix} \phi_1 \\ \phi_2 \end{pmatrix}, \begin{pmatrix} e \\ \nu_e \end{pmatrix} \begin{pmatrix} \mu \\ \nu_\mu \end{pmatrix} \begin{pmatrix} \tau \\ \nu_\tau \end{pmatrix}, \begin{pmatrix} u \\ d \end{pmatrix} \begin{pmatrix} s \\ c \end{pmatrix} \begin{pmatrix} t \\ b \end{pmatrix}. \tag{1.5}$$

The Higgs doublet field starts off in a high energy configuration early in the Universe. As the Universe expands and cools, the field configuration quickly relaxes to a local minimum. The simplest potential of the Higgs field in the SM Lagrangian is taken as

$$V(\Phi) = \mu|\Phi|^2 + \lambda|\Phi|^4, \tag{1.6}$$

where μ and λ are constants that control the shape of the potential (shown in Figure 1.3), and $\Phi = \phi_1 + \phi_2$. Notice that the μ parameter is a Higgs self-coupling term, the Higgs mass!

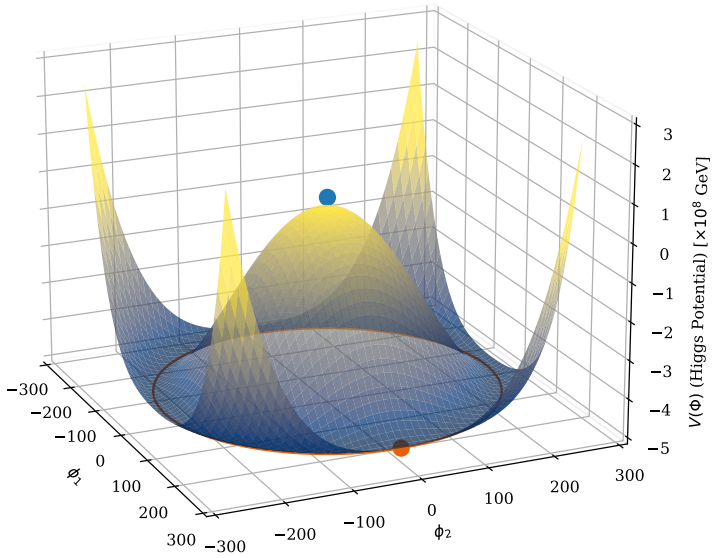

Figure 1.3: Higgs potential in the SM Lagrangian as a function of magnitude of the scalar fields of ϕ_1 and ϕ_2. Once symmetry in the ϕ_1-ϕ_2 plane is broken, i.e., going from the blue dot to the orange dot, there is an additional degree of freedom (the orange circle) representing the Goldstone mode. The process of the field configuration settling into the orange circle is referred to as EWSB.

After the EWSB process, the Higgs potential relaxes taking

$$\begin{pmatrix} \phi_1 \\ \\ \phi_2 \end{pmatrix} \rightarrow \begin{pmatrix} v + \delta\phi \\ \\ 0 \end{pmatrix} \tag{1.7}$$

for a particular choice of gauge (setting $|\phi_2| = 0$). The radial offset from the zero potential configuration ($\phi_1, \phi_2 = (0, 0)$) is called the vacuum expectation value (VEV) of the Higgs field, v, i.e., the radius of the orange circle in Figure 1.3 is $\frac{v}{\sqrt{2}}$ and its size is determined by the masses of the vector bosons, $W^{\pm}$ and Z^0 through their couplings to the Higgs field. The $\delta\phi$ term is a fluctuation in the Higgs field which manifests physically as the Higgs boson particle. By measuring the mass of the Higgs particle, and the masses of the vector bosons $W^{\pm}$ and Z^0, we can extract all the parameters that determine the shape of the potential in Figure 1.3.

The lower energy representation of the symmetry groups of the SM after EWSB now become

$$SU(3) \times SU(2)_L \times U(1)_Y \rightarrow SU(3) \times U(1)_{EM} \tag{1.8}$$

where the electroweak symmetry group is lost and gives rise to the new $U(1)$ gauge symmetry of electromagnetism.[5]

[5]Electric charge is a particular combination of weak hypercharge and weak isospin that is determined by the sizes of the couplings of the Higgs to the massive vector bosons, and the Weinberg mixing angle [14].

1.5.3 Dirac masses of fermions

After EWSB the Higgs field acquires a nonzero VEV, which means that particles will continuously feel the presence of the Higgs field and interact with it. We can write terms in the SM Lagrangian such as

$$\mathcal{L}_{SM} \sim Y_C H(\psi_L \overline{\psi_R} + \psi_R \overline{\psi_L}), \tag{1.9}$$

where Y_C is a Yukawa coupling constant, H is the Higgs doublet from Equation 1.7, and ψ represents fermion doublet fields. These new terms can be written as weak hypercharge neutral since the Higgs field was constructed in a way to preserve the gauge invariance of the SM.

After the EWSB process, Equation 1.9 can now be expanded to

$$\mathcal{L}_{SM} \sim Y_C v(\psi_L \overline{\psi_R} + \psi_R \overline{\psi_L}) + Y_C \delta\phi(\psi_L \overline{\psi_R} + \psi_R \overline{\psi_L}), \tag{1.10}$$

where the first term has a field-squared multiplied by $Y_C v$, a constant which can be identified as a mass term. The second term $Y_C \delta\phi$ is an interaction term of the fermion field ψ with the Higgs boson, typically denoted h, a fluctuation in the Higgs field. This mechanism of mass generation for fermions is the standard mechanism through which spin-$\frac{1}{2}$ particles (represented as Dirac spinors ψ) generate their mass in the SM and is hereafter referred to as the Dirac mass generation mechanism. Each particle's mass is determined by the strength of its Yukawa coupling to the Higgs field. The masses of all SM fermions are shown in Figure 1.4.

In this way, Higgs *et al.* were able to unify the electromagnetic and weak forces, supply masses to the weak vector bosons making the weak force short ranged, and supply a mass generation mechanism of fermion fields, which contain a right- and left-chiral component. The resulting theory has a symmetry group that is spontaneously broken in the lower energy state, but still reflects connections to the underlying high energy theory through patterns in the SM (number of gauge bosons of the weak force, the $U(1)$ symmetry of the electromagnetism, and existence of doublets of particles even though the $SU(2)_L$ group is broken). For a review of modern experimental tests of the Higgs boson properties see [20, 21].

Chapter 2 will overview the history of neutrinos and survey how experiments in the 20th century showed that all neutrinos have been observed to be left handed, and all antineutrinos right handed. These experimental results pose a challenge in the context of the SM: one must accept that neutrinos are massless due to the absence of oppositely handed counterparts to couple to them in the Dirac mass generation mechanism, or alternatively posit the existence of sterile (anti)neutrinos which do not interact via the weak force (due to having the wrong handedness) but participate in the conventional mass generation mechanism for fermions regardless. These sterile neutrinos are additional degrees of freedom that must be added to our model, and we will not be able to probe them directly through SM interactions. If these sterile right-handed neutrinos do indeed exist, then another mystery arises: why would the neutrino masses be so much smaller than their charged lepton counterparts as exhibited in Figure 1.4?

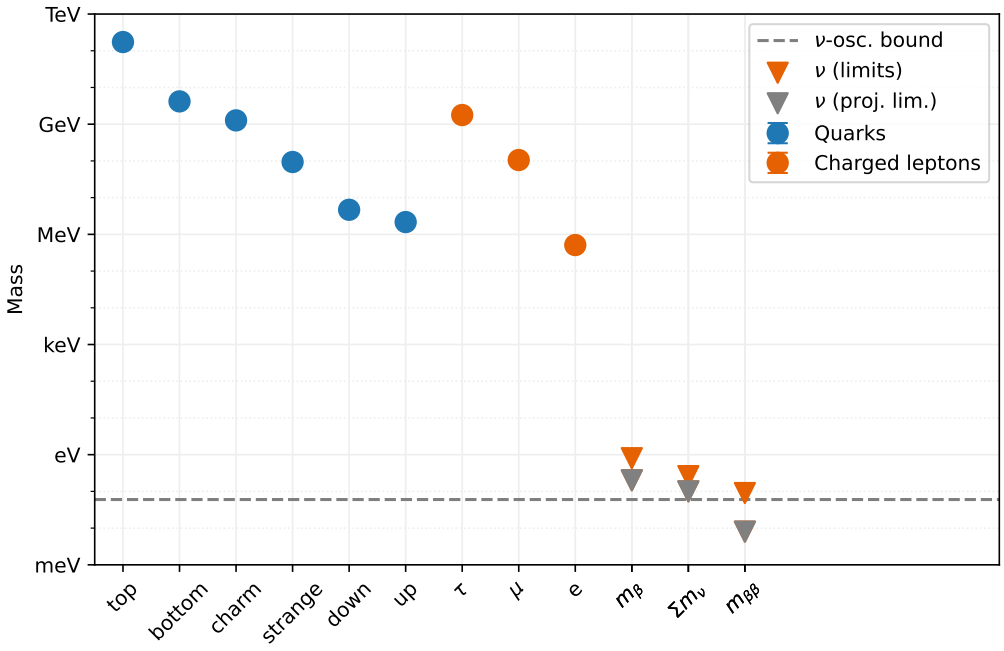

Figure 1.4: Masses of fermions in the SM. In the case of neutrinos, upper limits (and projected limits) are given instead, for each of the standard mass measurements that are made for neutrinos: $\sum m_\nu$ from cosmology [22, 23], $m_{\beta\beta}$ from neutrinoless double beta decay searches [24, 25], and m_β from direct kinematic measurements [26]. The dashed line represents the minimum possible neutrino mass, obtained by summing the square-roots of the mass-squared differences that are measured in neutrino oscillation experiments (outlined in Chapter 2). The large discrepancy between the masses of charged fermions and neutrinos is the subject of this thesis.

Chapter 2

Neutrino Physics

Neutrinos are fundamental particles originally postulated by Pauli in 1930 to explain the continuous energy spectra of measured electrons in β-decays [27]. The idea was simple: there must be a light, electrically neutral particle that is sharing energy with the electron. If this hypothetical particle exists, the total decay energy present in the nucleus (the mass difference of the initial and final states) is not being deposited into a detector, as detectors can only measure the energy deposited by charged particles and their ionization processes in the detection medium. In this case, only the energy of the outgoing charged electron is measured and the energy carried away by the neutrino is missing, leaving the electron spectrum continuous as opposed to discrete and equal to the available decay energy in the nucleus.[1]

This chapter introduces the current consensus on what neutrinos are, how they behave in the world within the framework of the SM, and active research areas on neutrinos after the discovery of neutrino masses.

[1] Although the nucleus itself does receive a kick from the decay process as well, the kinematics of a nuclear β-decay work out such that almost all of the available decay energy would go into the outgoing electron and neutrino.

2.1 Historical account of neutrinos

The Cowan and Reines experiment [28] discovered the existence of neutrinos by measuring the electron anti-neutrino ($\bar{\nu}_e$) flux coming from a nearby nuclear reactor. Cowan and Reines measured the inverse-beta decay (IBD) process:

$$\bar{\nu}_e + p \rightarrow n + e^+. \tag{2.1}$$

They achieved this by having 100 L volumes of water sandwiched between tanks of liquid scintillator and performing a coincidence measurement. In the IBD process, protons (p) capture $\bar{\nu}_e$ and convert to neutrons (n) while emitting positrons (e^+). These positrons would quickly annihilate with nearby electrons producing two coincident 511 keV γ-rays to be detected in the liquid scintillator via photomultiplier tubes (PMTs). The outgoing neutron (n) would capture on a cadmium nucleus; e.g., ^{108}Cd, which was dissolved in the water as a salt and has a large thermal neutron capture cross section compared to hydrogen. The newly created ^{109}Cd would then relax to its ground state by emission of several γ-rays with energies totalling a few MeV. These neutron capture γ-rays were then also detected in the liquid scintillator in delayed coincidence with the 511 keV pair of γ-rays from positron annihilation. Measurements of the IBD process, and the use of large volumes of water for neutrino detection, became a core technique in subsequent studies of neutrinos that is still in use today. This delayed coincidence neutrino detection technique is explored in the context of supernova neutrino detection in Chapter 6.

2.1.1 The solar neutrino problem

The Homestake neutrino experiment (1970–1994) [29] played a pivotal role in shaping the field of neutrino research in the late 20th century. The experiment was designed to measure the neutrino flux coming from the Sun by looking for electron neutrino interactions on chlorine-37 nuclei: $\nu_e + {}^{37}\mathrm{Cl} \rightarrow {}^{37}\mathrm{Ar}^{+} + e^{-}$. If the Sun were indeed powered by nuclear fusion at its core (an indirectly tested hypothesis in the early 20th century), a large flux of neutrinos was predicted to continuously pass through the Earth. The expected rate at which neutrinos would reach the Earth was calculated by John Bahcall [30]. Simultaneously, Ray Davis devised an experiment to be performed underground in the Homestake gold mine (shielding the experiment from cosmic rays). The experiment periodically bubbled helium gas through dry cleaning fluid that contained the target nucleus, ^{37}Cl. By measuring the decay of the collected radioactive ^{37}Ar as a function of time relative to stable argon, Davis was able to deduce the number of neutrino interactions that had taken place in the fluid.

Results of the Homestake experiment were perplexing, as the measured neutrino flux was consistently $\sim \frac{1}{3}$ the value calculated by Bahcall. This discrepancy, dubbed the solar neutrino problem, was then observed across several other neutrino experiments including Kamiokande and SNO [31] exacerbating the issue. There were, however, theoreticians who already had explored some solutions to this problem. In particular, Bruno Pontecorvo had suspected that although the Sun was a source of electron neutrinos, the flux of neutrinos arriving at the Earth was modified; the electron neutrinos were changing into other neutrino flavours, e.g., $\nu_e \rightarrow \nu_\mu$ where ν_μ could not take part in the chlorine-37 reactions described above [32, 33].

2.1.2 Discovery of neutrino oscillations

Experimental measurements made throughout the 20th century, trying to extract the neutrino mass directly through endpoint measurements of nuclear β-decay energies, suggested that neutrinos were in fact massless [34–38]. As the decades went by, and the SM was developed, there was also theoretical motivation to expect neutrinos to be massless: right (left)-handed (anti-)neutrinos have never been experimentally observed [39]. Thus, there would be no available counterpart to the left-chiral neutrino field in the SM to be glued to their right-chiral counterparts as per the standard Dirac mass generation mechanism outlined in Section 1.5.3.[2] It was not until after the Homestake experiment, and subsequent solar neutrino observations, that proved that neutrinos were in fact massive particles due to their ability to oscillate between flavour states.

Similarly to the Cowan and Reines experiment, the Kamiokande detector also utilized water as a medium through which to detect neutrinos. In this case, Kamiokande employed a 3 kilotonne water tank beneath the Kamioka mountains in Japan [40]. This water tank was instrumented with 1000 20-inch PMTs that were submerged in the water and distributed throughout the tank's surfaces. The PMTs detected the Cherenkov light of scattered electrons from neutrino interactions. By counting the Cherenkov flashes, and measuring the direction of travel of these Cherenkov events at particular energies, the Kamiokande experiment also observed a deficit in solar neutrino flux compared to theoretical predictions [41].

[2] Although helicity and chirality are being used interchangeably here, the bases converge in the ultrarelativistic limit ($E \gg m$), and this is the regime in which neutrinos exist naturally at everyday energy scales. This is not the case for all other fermions of the SM.

In 1998, the upgraded Super-Kamiokande detector published the first results indicating that neutrinos do in fact change flavour as they propagate through space. This was shown by measuring the ratio of electron-like to muon-like events in their detector in the 0.1 to 10 GeV range [42]. The upgraded detector had a much higher PMT density and fiducial mass of water. The new detector was able to distinguish Cherenkov rings of muon-like Cherenkov rings (sharp and defined), and electron-like rings (blurred, due to the much less massive electron scattering as it travels in the tank). The neutrino source in this measurement was not the Sun, but atmospheric neutrinos: neutrinos emitted due to cosmic ray interactions with nuclei in the upper atmosphere, which produces neutrinos at energies much higher than solar neutrinos.

Concurrent with the Super-Kamiokande experiment, the Subury Neutrino Observatory (SNO) experiment was operating 2 km underground in Ontario, Canada. The SNO experiment [43] was designed specifically to address the solar neutrino problem by enabling neutrino interaction channels that were flavour-blind, i.e., sensitive to all neutrino flavours from the Sun. This was done by replacing the ultrapure H_2O with deuterated (heavy) water instead, D_2O. The replacement enabled an additional neutral current interaction, involving the Z^0 boson, to occur:

$$\nu_x + d \rightarrow p + n + \nu_x, \tag{2.2}$$

where d is a deuteron and ν_x is any flavour of neutrino ($x = e, \mu, \tau$). The solar flux measured through the neutral current channels (by detection of neutron capture de-excitation γ-rays) could then be compared to those from charged current interactions (detected via electron

Cherenkov light) which are only sensitive to the electron neutrino component of the solar flux:

$$\nu_e + d \rightarrow p + p + e^-. \tag{2.3}$$

Comparison of the fluxes measured by neutral and charged current reactions revealed that the missing neutrinos in the Homestake results can be attributed to neutrinos of other flavours which are still present, but passing through the Homestake experiment undetected. After accounting for this oscillation into other flavours, the total expected neutrino flux as calculated by Bahcall was validated, solving the decades-long solar neutrino problem [44].

In the context of the SM, neutrinos are spin-$\frac{1}{2}$ particles that are electrically neutral, and manifest as SU(2) flavour doublets, one alongside each of the charged leptons: the electron, muon and tau particles. Neutrinos are only able to interact via the weak force, and so far only the left(right)-chiral (anti-)neutrinos have been detected. The discovery of neutrino oscillations proved that they are massive (this fact is demonstrated in Appendix B.1), but the origin of their mass remains unknown and is subject to ongoing research.

2.2 Neutrino mass: physics beyond the SM

The discovery of solar neutrino flavour oscillations provided strong evidence for massive neutrinos — the combined effect of vacuum oscillations (which require massive neutrinos), as well as matter-induced oscillations (the Mikheyev–Smirnov–Wolfenstein effect [45, 46]) accounts fully for the measured solar neutrino deficit. However, neutrino masses are a significant challenge to the SM, which does not naturally accommodate massive neutrinos.

One must choose to add additional degrees of freedom to the SM for the Dirac mass generation mechanism to apply. At least two additional right-handed inert (sterile) counterparts [47] must be added to the active, observed, left-handed neutrinos in order to agree with current neutrino oscillation measurements. This drive to understand the origin of neutrino masses has motivated several experimental investigations alongside various theoretical extensions to the SM. Some of these extensions to the SM are proposed to account for neutrino masses, and also contribute solutions to puzzles in other areas of physics and cosmology; e.g., the seesaw mechanism in the context of leptogensis, and the matter-antimatter asymmetry problem (Section 2.3.1).

2.2.1 Physics of neutrino oscillations

The probability to detect a neutrino in the electron versus μ or τ states varies as both a function of energy and distance travelled from the neutrino source. This is what is referred to as neutrino oscillations. As neutrinos propagate through the vacuum, there is no possibility for this effect to occur unless there is a non-zero mass-squared splitting between neutrino eigenstates (a derivation of this is provided in Appendix B.1); the oscillation probability disappears as $\Delta m^2 \to 0$. For neutrino oscillation to occur between all three neutrino flavours (e, μ, τ) as is now observed, there must be at least two mass-squared splittings, and that at most one neutrino mass state is massless. This is because production (and detection) of neutrinos can only occur through the weak interaction, which produces neutrinos in pure, definite, flavour eigenstates that are a coherent superposition of mass states.

The Pontecorvo-Maki-Nakagawa-Sakata (PMNS) matrix shown here, is a unitary matrix relating the neutrino mass (ν_i, where $i = 1, 2, 3$) and flavour (ν_α, where $\alpha = e, \mu, \tau$) eigenstates:

$$\begin{pmatrix} \nu_e \\ \nu_\mu \\ \nu_\tau \end{pmatrix} = \begin{pmatrix} U_{e1} & U_{e2} & U_{e3} \\ U_{\mu 1} & U_{\mu 2} & U_{\mu 3} \\ U_{\tau 1} & U_{\tau 2} & U_{\tau 3} \end{pmatrix} \begin{pmatrix} \nu_1 \\ \nu_2 \\ \nu_3 \end{pmatrix}. \tag{2.4}$$

This matrix can be expressed conveniently in terms of mixing angles between the neutrino mass states ν_i, a CP-violating phase δ, and two Majorana phases α_1 and α_2:

$$\begin{pmatrix} c_{12}c_{13} & s_{12}c_{13} & s_{13}e^{-i\delta} \\ -s_{12}c_{23} - c_{12}s_{23}s_{13}e^{i\delta} & c_{12}c_{23} - s_{12}s_{23}s_{13}e^{i\delta} & s_{23}c_{13} \\ s_{12}s_{23} - c_{12}c_{23}s_{13}e^{i\delta} & -c_{12}s_{23} - s_{12}c_{23}s_{13}e^{i\delta} & c_{23}c_{13} \end{pmatrix} \begin{pmatrix} e^{i\alpha_1/2} & 0 & 0 \\ 0 & e^{i\alpha_2/2} & 0 \\ 0 & 0 & 1 \end{pmatrix}, \tag{2.5}$$

where $s_{ij} \equiv \sin(\theta_{ij})$, and $c_{ij} \equiv \cos(\theta_{ij})$.

The mixing angles can be determined by making precision measurements of neutrino oscillation probabilities across a wide range of energies and distances, and the CP-violating phase δ (later written δ_{CP}) can be obtained by observing how the neutrino and anti-neutrinos oscillate compared to each other (see Section 2.4.1 for more details). However, oscillation experiments cannot provide information on the Majorana phases α_1 and α_2, which are only present if neutrinos are their own antiparticles, nor can they provide information on how heavy the lightest neutrino mass state is, i.e., the absolute neutrino mass scale. For a review on the PMNS paradigm and experimental measurements of the mixing parameters see [48].

2.2.2 Majorana mass

Due to the parity violating nature of the weak force (explained in Section 1.4), we have only ever measured (anti-)neutrinos helicity as being (right) left handed. Nevertheless, we observe massive neutrinos. Thus, there must be a way for extensions of the SM to account for their mass. The standard Dirac mass generation mechanism in Section 1.5.3 cannot account for neutrino masses unless we choose to tune the Yukawa coupling term for neutrinos to be at least 6 orders of magnitude smaller than the electron — a fine-tuning problem. Even worse, we will have to accept that there are at least two additional non-interacting right-handed neutrino fields to add to our model.

A potential alternative solution comes from the peculiar physicist Ettore Majorana.[3] In 1937, Majorana proposed an alternative relativistic formula for fermions to the Dirac Equation which would be applicable to particles that are their own charge conjugate [50]:

$$i\gamma^{\mu}\partial_{\mu}\psi_{L} - m\psi_{R}^{c} = 0, \tag{2.6}$$

This was not done specifically to address neutrinos, but the formalism was quickly applied after the discovery of their oscillations.

For Majorana fermions, the mass term can be written as a coupling between charge-conjugates of fields which have the same chirality. These can then enter the Lagrangian (for

[3] At the age of 31, Majorana purchased a boat ticket from Palermo to Naples and subsequently vanished without a trace. Reports indicate that he withdrew all the money from his bank account prior to the journey and sent cryptic messages to his colleagues. These actions have given rise to a plethora of theories regarding his disappearance [49].

neutrinos) as:

$$\mathcal{L}_{\text{Majorana}} = \frac{1}{2} M \overline{\nu_R^c} \nu_R + \text{h.c.}. \tag{2.7}$$

In the full Lagrangian (including the right-left couplings for Dirac masses) we now have:

$$\mathcal{L}_{\text{mass}} = \frac{1}{2} \begin{pmatrix} \bar{\nu}_L^c & \bar{\nu}_R \end{pmatrix} \begin{pmatrix} M_L & m_D \\ m_D & M_R \end{pmatrix} \begin{pmatrix} \nu_L \\ \nu_R^c \end{pmatrix} + h.c., \tag{2.8}$$

where the superscript ^{c} denotes a charge conjugate, and $h.c.$ denotes Hermitian conjugate terms.[4]

The BSM Majorana mass terms, M_L and M_R, are not associated with the Higgs field and therefore have no association to the energy scale of the VEV — they can be made arbitrarily large. The Majorana terms couple left-left and right-right terms of the neutrino fields. The third mass term, m_D, is the Dirac mass term that couples the left- and right-handed neutrino fields together, as per the standard Dirac mass generation mechanism described in Section 1.5.3. We will see in the next section how these Majorana mass terms can play a role in suppressing the mass of the physical neutrino today.

2.2.3 The seesaw mechanism

This section outlines the most basic of seesaw mechanisms, the Type-I seesaw, but others do exist [51–53]. All seesaw mechanisms have in common the core concept of a heavy mass scale suppressing the active neutrino's mass scale, as will be illustrated here.

In the Type-I seesaw mechanism, three possible mass terms exist for neutrinos at various

[4]The mass matrix in Equation 2.9 is really a single neutrino representation and not the full 3 neutrino form.

energy scales, M_L, M_R and m_D described in the previous section and laid out in Equation 2.8. In the context of the seesaw mechanism described here, the dimensionless Yukawa coupling constant Y_c need not be made arbitrarily small for neutrinos, but can remain order ~ 1 relative to the size of the Yukawa coupling terms for the other fermions. Thus, the Dirac mass of neutrinos remains tied to the scale of the Higgs VEV as $m_D \sim Y_c v$.

Recall that due to the $SU(2)_L$ symmetry of the electroweak group, the form of the Lagrangian must be symmetric for interchanges between the charged left-chiral leptons and left-chiral neutrinos, i.e., $\nu_{eL} \leftrightarrow e_L$, etc... Therefore, the coupling of left-left terms here is forbidden since the coupling of two left handed electrons, which are electrically charged, breaks $U(1)_{\text{EM}}$ gauge invariance. Hence, we set $M_L = 0$.[5] Now, the mass matrix can be written as:

$$\mathcal{M}_{\text{mass}} \sim \begin{pmatrix} M_L & m_D \\ m_D & M_R \end{pmatrix} \rightarrow \begin{pmatrix} 0 & m_D \\ m_D & M_R \end{pmatrix}. \tag{2.9}$$

If $m_D \ll M_R$, then the two eigenvalues are:

$$m_1 \approx \frac{m_D^2}{M_R} \text{ and } m_2 \approx M_R, \tag{2.10}$$

which are the physical mass eigenstates of the neutrino that are observable. The first mass, m_1, is much smaller than the Higgs VEV and therefore smaller than the masses of other fermions. The second mass, m_2, can be made arbitrarily large and is associated with heavy right handed Majorana neutrinos that are sterile (inert) to SM forces.

[5] M_R Majorana mass terms from $\nu_R \nu_R$ are allowed since ν_R is uncharged under the electroweak group $SU(2)_L \times U(1)_Y$ and does not interact with the weak force. The equivalent $e_R e_R$ term is not present due to electric charge conservation, and there is no symmetry between ν_R and e_R requiring $e_R e_R$ terms to exist.

2.2.4 The Weinberg operator

One way to connect the notion of Majorana neutrinos and the seesaw mechanism is through the Weinberg operator [54, 55]. The operator can be added to the SM Lagrangian as:

$$\mathcal{L}_{\text{Weinberg}} \sim \frac{Y_c v^2}{\Lambda} \bar{L} H H^\dagger L, \tag{2.11}$$

which connects two SM left-handed lepton doublets L, with two Higgs doublets H. The operator explicitly violates lepton number conservation, and provides Majorana mass terms for neutrinos after EWSB via, e.g., the seesaw mechanism with the Yukawa coupling (Y_c) and the Higgs VEV (v). It is the only dimension-5 operator available if we consider only the known SM particles and respect the symmetries of the SM [56]; in the context of an effective field theory expansion this is a unique next-leading order term. The Λ here is a natural cutoff scale for the theory: if $\Lambda \gg v$, then this new operator will transform as a singlet under the SM symmetry group and will not be involved with SM interactions [57]. This fact can be used to set the energy scale for new physics [58], provided Y_c is not $\ll$1.

Taking v to be 246 GeV, $Y_c \sim 1$, and the current scale of neutrino mass limits to be 0.1 eV, we obtain $\Lambda \sim 10^{14}$ GeV assuming Y_c remains naturally of order 1.[6] This enormous energy scale is ten orders of magnitude above the center of mass energy of the LHC. Hence, new physics associated with heavy Majorana neutrinos (if you choose to associate Λ with M_R) is not expected to appear at colliders in our lifetime.[7]

[6] This calculation is analogous to Fermi's contact theory of beta decay, which is valid up to the mass scale of the mediating particles (the $W^\pm$ bosons).

[7] This does not mean that new physics *will appear at* 10^{14} GeV, only that it *must* appear above this energy to be consistent with the SM today.

2.3 Role of neutrinos in cosmology and astrophysics

Neutrinos are estimated to be the second most abundant particle in the Universe after photons. They are produced in a wide variety of astrophysical processes and are currently expected to range in energy from the sub-meV (relic neutrinos from the big bang) all the way to PeV neutrinos detected in the IceCube experiment [59], spanning over 18 orders of magnitude. Neutrinos have been detected coming from both galactic [60] and extragalactic sources [61], but the largest continuous flux of (currently detectable) neutrinos that arrive at Earth overwhelmingly comes from the Sun.

Neutrinos also play a significant role in the very early Universe. From the smearing out of small structure formation [62], to making modifications to the dynamics of big bang nucleosynthesis and affecting the abundance ratios of the lightest nuclei [63]. This section provides a review of neutrino emission in stellar processes as they pertain to the context of this thesis, and associates the presence of neutrinos in the very early Universe with open cosmological problems today.

2.3.1 Leptogenesis & matter-antimatter asymmetry

The matter-antimatter asymmetry problem is a fundamental puzzle in modern physics. The laws of the SM treat matter and antimatter on equal footing, provided there is a parity change: substituting left-handed matter with right-handed antimatter everywhere in the Universe should leave physics unchanged. Why is it then, that we live in a world with such a stark imbalance of matter and antimatter?

The Sakharov conditions provide a framework for dynamically breaking the matter-antimatter symmetry [64]. The conditions state that, in the early Universe:

1. there must be baryon number non-conservation,

2. there must be violation of C and CP symmetries,

3. there must have been a departure from thermal equilibrium.

We will address each of the three conditions separately in the context of neutrinos.

First, both baryon and lepton number (B and L, respectively) are accidental conservation laws in the SM: there is no global symmetry group that gives rise to the conserved baryon or lepton numbers in particle interactions.[8] Moreover, a natural consequence of the non-trivial vacuum structure of the electroweak gauge theory (i.e., the gauge fields mixing with the Higgs field) is the existence of sphaleron processes [65, 66]: saddle points connecting different vacua, where the numbers of quarks and leptons are different on either side [67]. The non-conservation of baryon number can therefore be attributed to sphaleron processes which naturally arise in the gauge theory of the SM, but that have not been observed thus far due to the extreme energy densities required for such processes to occur; e.g., temperatures above the electroweak scale ∼100's GeV, but concentrated in such a small space that current colliders will be unable to produce such events [68], even though these processes are likely to have occurred frequently in the early Universe [69]. Models utilizing the sphaleron process as a way to supply a net baryon asymmetry through a net lepton asymmetry in the early Universe are collectively referred to as models of leptogenesis [70], for a review see [71, 72].

[8] As opposed to the conservation of electric charge in electromagnetism due to U(1) gauge invariance.

Second, the SM neutrinos already exhibit CP violation due to the chiral nature of weak interactions; only left-(right-)handed (anti-)neutrinos have been observed to interact with the weak force satisfying the second Sakharov condition. Further, hypothetical massive right-handed Majorana neutrinos do not carry a lepton number (specifically, a left-handed lepton number) and inherently supply a lepton asymmetry when they decay; they generate an imbalance in the left-right symmetry of fermions, depending on their oscillation rates into their left-handed counterparts. After the Universe has cooled below a temperature of M_R, only decays (and not production) of heavy neutrinos are possible. Since only left-handed leptons can participate in SM sphaleron processes, the left-right asymmetry is translated into a baryon asymmetry.

The third condition, the non-equilibrium state of the Universe, is satisfied by the expansion of the Universe after inflation: interactions that occur slower than the Hubble expansion rate cannot equilibriate [72]. Depending on the strengths of the Yukawa coupling Y_c, embedded in the Dirac mass term (m_D) of Equation 2.8 (the connecting term between left- and right-handed neutrinos), relative to the expansion rate of the Universe, we can generate the required lepton asymmetry. In this way, small neutrino masses as a result of the seesaw mechanism (Section 2.2.3) are involved in a potential solution to the matter-antimatter asymmetry problem [73].

The Weinberg operator (Section 2.2.4) therefore connects Majorana neutrino masses, the seesaw mechanism, and the matter-antimatter problem in an elegant manner, being agnostic to new physics at much higher energy scales.

2.3.2 Neutrinos in stellar processes

Neutrinos are emitted during various nuclear fusion processes. The most common of those being the proton-proton (pp) chain, whereby an electron anti-neutrino ($\lesssim 400$ keV) is emitted upon the β-decay of one of the protons after being fused together to form a deuteron [30]. This is not the only reaction however; once a star gets to a certain age, fusion of two helium nuclei cannot occur directly. Instead, catalytic fusion reactions mediated by nuclei of carbon, nitrogen, and oxygen, emit neutrinos of slightly higher energy than those from the pp chain (called CNO neutrinos), and the emitted neutrinos are only of the electron flavour type. It is the CNO neutrinos that were measured by Homestake, Kamiokande and the SNO experiment that lead to the solar neutrino problem and its resolution (Section 2.1.1).

Neutrinos are also expected to play a significant role in the deaths of the most massive stars. At the end of a star's life, once the fusion of iron and nickle nuclei (the most tightly bound nuclei) has begun, there is a significant drop in the outgoing radiation pressure from the stellar core balancing against inward gravitational pressure of the massive star. The disruption of hydrostatic equilibrium triggers a core collapse supernova (CCSN), a gravitational collapse leading to the demise of the star. Without a neutrino-driven explosion mechanism, it is difficult to explain how stars explode in Type-II supernovae, where hydrogen is detected in their spectra [74].

2.3.3 Supernovae and multimessenger astronomy

After decades of solar neutrino observations (Section 2.1.1), SN1987A marked a true inflection point in the era of multimessenger astronomy (MMA). A CCSN in our satellite

galaxy, the Large Magellanic Cloud, located 50 kiloparsecs away, was detected by conventional optical telescopes and subsequently in multi-wavelength observation campaigns [75]. It has become one of the most studied astrophysical events of our lifetime. The neutrinos associated with SN1987A were detected hours before supernova shock breakout, across multiple water Cherenkov detectors worldwide. The handful of neutrinos ($\sim$12) that were detected provided limits on the mass of the neutrinos [76], temperature of the stellar core [77], overall energy emission from a CCSN, and confirmed our canonical understanding of neutrino-driven explosion mechanisms.

Today, there have been numerous multimessenger observations of astrophysical events. In 2017, the IceCube observatory detected high-energy neutrino emissions from the blazar TXS 0506+056. This observation coincided with an increase in high-energy gamma-ray emissions, with both the neutrinos and gamma rays carrying energies upward of hundreds of GeV. A retrospective study provided evidence for high-energy neutrino emission coinciding with the locations of blazars across the universe, providing indirect evidence that quasars can accelerate hadrons to extremely high energies. Consequently, they are potential candidates for solving the mystery behind cosmic ray acceleration [78]. Later the same year, the neutron star merger GW170817 marked the first astrophysical event to be observed simultaneously with both gravitational and electromagnetic messengers [79]. The event provided novel measurements on nucleosynthesis of heavy elements [80], tests of general relativity [81], the Hubble constant [82], and a limit on the number of extra spacetime dimensions [83].

Multimessenger astronomy (MMA) is now a field that is bursting with development. The 'holy grail' of MMA detection would be the simultaneous detection of gravitational,

electromagnetic, and neutrino signals from the same astrophysical object. CCSN are prime candidates for this 3-component emission, as a non-spherical collapse models will produce gravitational wave (GW) emission due to the presence of nonzero quadrupole moments [84]. Unfortunately, these non-spherical collapse models are not well constrained, and therefore difficult to detect via LIGO's standard matched-filtering technique. Instead they use LIGO's coherent waveburst pipeline [85]. Furthermore, the GW emission would be much weaker in strength compared to compact binary inspirals, limiting the detectable range of these events to within a few kiloparsecs (kpc). Electron-type neutrino detection however, will provide a ∼millisecond timestamp at the moment of core collapse due to rapid deleptonization. This timestamp can greatly limit the search window for the CCSN in the global GW antenna network [86]. Moreover, any triangulation or pointing extracted from neutrinos may uncover a reduced search region in the antenna patterns of GW observatories, thus enhancing sensitivities. This is even more vital for the case of electromagnetic signals that may be obscured by dust, e.g., searching for a potential CCSN event through the galactic plane of the Milky Way. A more comprehensive overview of global CCSN neutrino detection efforts, set against the backdrop of the nEXO experiment, is presented in Chapter 6.

2.4 Experimental probes of neutrino properties

Today, there are several active areas of research pertaining to understanding the physics of neutrinos. These are broadly classified as: neutrino oscillation measurements, direct mass measurements, cosmological probes to constrain neutrino properties, and searches for exotic nuclear decay modes such as neutrinoless double beta decay. This section aims to provide a summary of modern experiments with a focus on their interplay with nEXO's double beta decay program.

2.4.1 Neutrino oscillation measurements

Neutrinos are known to be massive due to their ability to oscillate between flavour eigenstates (Section 2.2.1). Over the last three decades, experiments characterized the disappearance or appearance of particular neutrino flavour types across a broad range of energy scales and baselines (distances between the detector and the neutrino source). At the lowest energies ($\sim$ MeV) and longest baselines we have solar neutrinos: these experiments provided evidence for the large mixing angles of the PMNS matrix [87], and a measurement of one of the neutrino mass-squared splittings, $\delta m^2_{sol} \approx 7.5 \times 10^{-5}$ eV^2. The Super-Kamiokande water-Cherenkov detector [42] contributed to measurements of the atmospheric mass splitting $\Delta m^2_{atm} \approx 2.5 \times 10^{-3}$eV^2 measured with neutrino energies above $\sim$100 MeV. Both these classes of experiments utilized a relatively fixed baseline (the sun or the upper atmosphere), but measured neutrinos coming from natural sources which produced them across a broad energy range. Values for the mass splittings are from the Particle Data Group [1].

The next class of experiments utilized man made sources, such as accelerators or

nuclear reactors to perform precision measurements of the mixing angles of the PMNS matrix (Equation 2.4) and mass splittings. The Double Chooz, Daya Bay, and RENO experiments [88–90], measured the non-zero value of θ_{13} by electron antineutrino disappearance measurements from nearby nuclear reactors. Meanwhile, the Super-Kamiokande detector was exposed to neutrino beams at various baselines, comprising the K2K and T2K measurements [91, 92], which constrained the values of θ_{12} and θ_{23}. In the United States, the NuMI neutrino beam has been utilized by several experiments making complementary measurements to those of Super-Kamiokande, using not water as a detection medium but a variety of organic scintillator targets [93, 94], as well as liquid argon targets [95]. Together, these experiments have constrained the unitary nature of the PMNS matrix, and revealed its radically different structure than that of the equivalent mixing matrix in the quark sector, the CKM matrix [96].

The next phase of neutrino oscillation experiments are now under construction to determine the CP violating phase (δ_{CP}) of the PMNS matrix. This is done by measuring the way neutrinos and anti-neutrinos oscillate as they propagate through matter, and undergo the Mikheyev-Smirnov-Wolfenstein (MSW) effect [46]. Long baseline experiments such as DUNE [97] utilizing large liquid argon time projection chambers and Hyper-Kamiokande [98] (a large water Cherenkov successor to Super-Kamiokande), aim to extract this information using precision measurements of the neutrino fluxes and energies at various baselines, by employing detectors both near and far from the neutrino source. In contrast, JUNO [99] is an organic scintillator experiment that, at a medium baseline from nuclear reactor sources, aims to measure elements of the PMNS matrix to unprecedented

precision. These near-future experiments are expected to determine the ordering of the neutrino mass eigenstates: ν_1, ν_2, ν_3, and extract the value of δ_{CP}. Recall however, that oscillation measurements cannot provide any information about the absolute neutrino mass scale (only mass-squared splittings), nor can they extract information on the Majorana nature of neutrinos (the Majorana phases do not enter in oscillation formulae).[9]

2.4.2 Direct neutrino mass measurements

A model-independent method to measure the absolute neutrino mass scale is via β-decay measurements. By searching for shifts in the endpoint energies of the outgoing electron's spectrum in β-decays, one can infer the mass of the invisible outgoing neutrino via a Fermi-Kurie plot. Thus far, only upper limits have been obtained on the neutrino mass this way, they are denoted m_β. Most notably, these experiments have been by measuring the β-decays of tritium to obtain limits on m_β. Currently, the KATRIN experiment is underway with the latest result for m_β being limited to $<$0.8 eV at the 90% C.L., and a planned ultimate sensitivity goal of 0.2 eV [26].

Next generation experiments aim to use novel techniques such as electron capture spectroscopy of ^{163}Ho (HOLMES [100] and ECHo [101]) or measuring the cyclotron radiation of electrons in tritium β-decay (Project 8 [102]). These next-generation experiments are now establishing scalable technologies to push their sensitivities well below the 1 eV level. In the case of Project 8, the goal is a sensitivity to the electron neutrino mass at the $\sim$ 40 meV level.

[9] For an understanding of how neutrino oscillations depend on their mass see Appendix B.1.

2.4.3 Cosmological probes

Neutrinos play a significant role in the early Universe due to their number density being second only to photons of the cosmic microwave background (CMB). They have significant contributions to the overall energy density of the Universe today, and due to their non-zero masses, they are contributing at least an order of magnitude more to the overall energy density of the Universe than the CMB. Understanding the physics of neutrinos is therefore key to a thorough understanding of the history of the Universe, and measurements of cosmological parameters constrain neutrino parameters within the confines of the cosmological model.

In short, the low interaction cross sections of neutrinos as well as their small masses mean that once the expansion rate of the Universe exceeded the weak interaction rates of neutrinos, they decoupled from the primordial plasma. This happened at a temperature of about 1 MeV, much earlier than the decoupling of CMB photons.[10] The decoupling of neutrinos affects the matter-radiation inequality, which results in shifts in the peak heights of the CMB power spectrum [103–105]. More dramatically, the free-streaming of neutrinos through the Universe after decoupling will smear out small-scale structure formation at early times, i.e., the formation of galaxies. This is because relativistic neutrinos will not be trapped in the gravitational potential wells of cold dark matter clusters, due to their lack of interactions with the surrounding environment, in the standard ΛCDM model (this argument does not hold for alternative models such as those in [106]).

[10] This means that relic cosmic neutrino background is a measurement of the Universe older than the CMB. Moreover, this cosmic neutrino background (CνB) is a unique source of non-relativistic neutrinos today due to their redshift.

By precisely measuring the structure scales in the early Universe, we obtain a measurement of the overall energy density of neutrinos. This is coupled to the summed neutrino mass $\sum m_\nu$ (really, the sum of masses of relativistic species in the early Universe), and the number of effective relativistic degrees of freedom $N_{\rm eff}$ [107]. Currently, $N_{\rm eff}$ is in 1σ agreement with the number of light neutral leptons N_ℓ (neutrinos) that couple to the Z^0 boson as measured by LEP and SLC collider data, i.e., $N_{\rm eff} \approx N_\ell \approx 3$ [1, 22]. The sum of neutrino masses can then be obtained via measurements of the matter distribution through large galaxy surveys (SDSS [108], BOSS [109], DES [110]) or low density gas distributions via Ly-α forest measurements [111]. These measurements, in conjunction with those of the dark matter distribution measured via gravitational lensing, strongly constrain $\sum m_\nu$ in the ΛCDM model, but provide little information on the neutrino mass ordering. Currently, the upper bounds on $\sum m_\nu$ are <120 meV level at 95% C.L. [22].[11] This result primarily comes from the combination of the CMB anisotropies and polarization measurements from the Planck satellite, with baryon acoustic oscillation measurements from all-sky surveys.

Results from future sky surveys like eBOSS [112], DESI [113], and LSST [114] (now the Vera C. Rubin Observatory), along with next-generation CMB experiments (CMB-S4 [23]), will have interesting interplays with terrestrial oscillation measurements: if the combined mass splittings δm^2_{sol} and Δm^2_{atm} are considered at face value, then these experiments will not provide an upper limit, but actually measure the value of $\sum m_\nu$ with an uncertainty of in the tens-of-meV range. This will place strong constraints on the neutrino mass ordering, and reduce the available parameter space for neutrinoless double beta decay.

[11] Notably, the exact level of this upper limit changes drastically depending on which datasets are included in the statistical inference. However, all published limits today lie below the ∼500 meV level.

2.4.4 Searching for neutrinoless double beta decay

Neutrinoless double beta decay ($0\nu\beta\beta$) is a rare nuclear decay mode that, if observed, would prove the Majorana nature of the neutrino. Regular double beta decay ($2\nu\beta\beta$) was first considered by Maria Goeppert-Mayer [115]. In $2\nu\beta\beta$, there is a simultaneous conversion of two neutrons inside of an atomic nucleus X, into two protons with the emission of two electrons and two electron anti-neutrinos.[12] This process is written as:

$$ {}^{A}_{Z}X \rightarrow {}^{A}_{Z+2}X + 2e^{-} + 2\bar{\nu}_{e}, \tag{2.12} $$

which conserves total lepton, and lepton-flavour numbers, and is an allowed process in the SM (e^{-} and $\bar{\nu}_{e}$ carry opposite lepton, and lepton flavour numbers). Even in 1935, Goeppert-Mayer's original calculations predicted that these decays would have half-lives exceeding 10^{17} years, making the observation of $2\nu\beta\beta$ only possible in isotopes that are energetically unable to decay via regular single $\beta^{\pm}$-decays, or electron captures (see Figure 2.1). It is in these isotopes that a second-order weak interaction process (e.g., $\beta\beta$-decays) becomes observable.

The $2\nu\beta\beta$ process has been observed in several isotopes [117–122], all with half-lives significantly longer than the current age of the Universe ($\sim 1.4\times10^{10}$ years); for a review of this decay process, see [123]. The measured energy spectra of these decays are continuous and similar to those of single β-decay, where the outgoing electron's energy is the measurable quantity, but the neutrino energy is unmeasured (see Figure 2.2).

In analogy to regular β-decay, the kinematics of this nuclear reaction forces the vast

[12] Technically this is the $\beta^{-}\beta^{-}$ decay process, an analogous $\beta^{+}\beta^{+}$-decay, and double electron captures, are possible where protons are converted to neutrons instead.

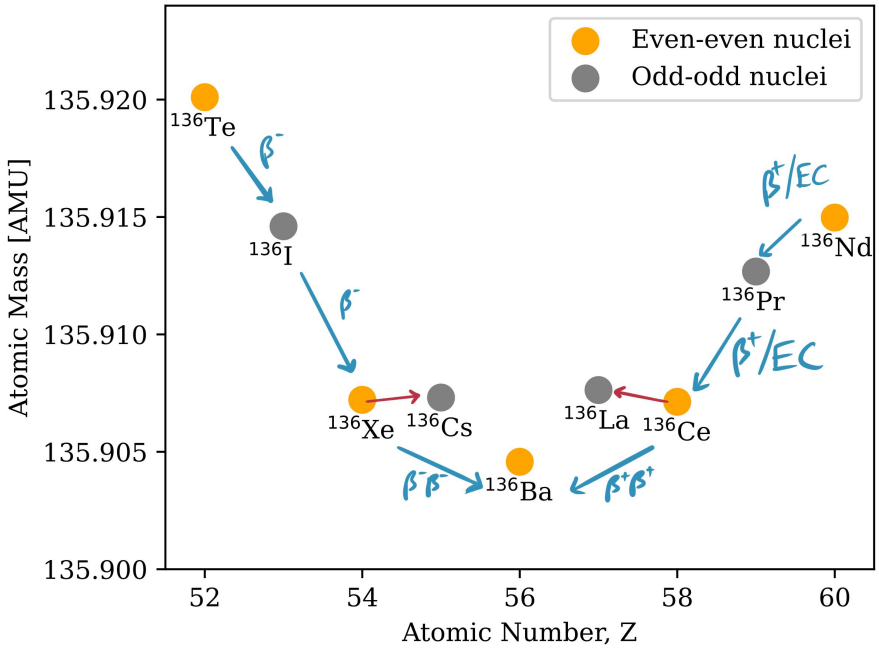

Figure 2.1: Isobar diagram showing the masses of nuclei at A=136. It is energetically impossible for ^{136}Xe to undergo single β-decay due to the larger mass of the neighbouring nucleus ^{136}Cs, whereas double beta decay to ^{136}Ba is possible. Data retrieved from [116].

majority of the decay energy to go into the relatively light outgoing products $e, \bar{\nu}_e$, as opposed to the recoil of the nucleus. Hence, for the lepton number violating (LNV) neutrinoless decay mode:

$$ {}^{A}_{Z}X \rightarrow {}^{A}_{Z+2}X + 2e^{-}, \tag{2.13} $$

a key signature would be a peak in the measured summed electron energy spectrum at the endpoint (Q-value) of a regular $2\nu\beta\beta$ spectrum.

Any observation of $0\nu\beta\beta$ would be evidence of physics beyond the SM based off the fact that $0\nu\beta\beta$ is a LNV process. There is, however, an even richer space to explore concerning neutrino properties: the half-lives of $0\nu\beta\beta$ decays in any isotope can be connected to the Majorana nature of neutrinos, and values of the PMNS matrix. Furthermore, the Schechter-

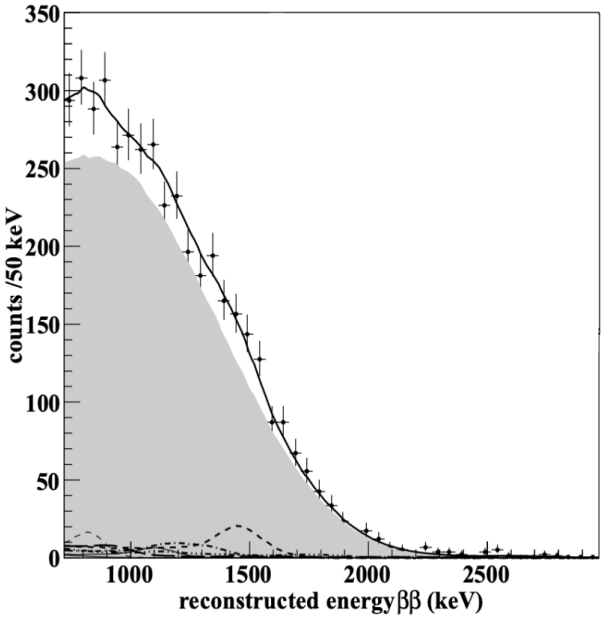

Figure 2.2: EXO-200 $2\nu\beta\beta$ summed electron energy spectrum (shaded in grey). The absence of a peak at the endpoint of the $2\nu\beta\beta$ indicates a non-observation of $0\nu\beta\beta$. Figure adapted from [121].

Valle theorem [124], commonly referred to as the black box theorem, states that for $0\nu\beta\beta$ to occur in any isotope there must be a contribution to the Majorana mass terms of the neutrino.

There are a variety of theoretical models that may enable $0\nu\beta\beta$ decay modes, but the simplest of all is the light Majorana neutrino exchange mechanism [125] shown in Figure 2.3. In the light Majorana exchange mechanism, the annihilation of two anti-neutrinos corresponds to a measurable mass, the effective Majorana mass of the electron neutrino:

$$< m_{\beta\beta} >= |\sum_{i=1}^{3} U_{ei}^2 \nu_i|, \tag{2.14}$$

where U_{ei} are the elements in the first row of the PMNS matrix (Equation 2.4), and ν_i are the neutrino mass eigenstates.

Values of $<m_{\beta\beta}>$ (henceforth denoted $m_{\beta\beta}$) can be extracted from halflife measurements

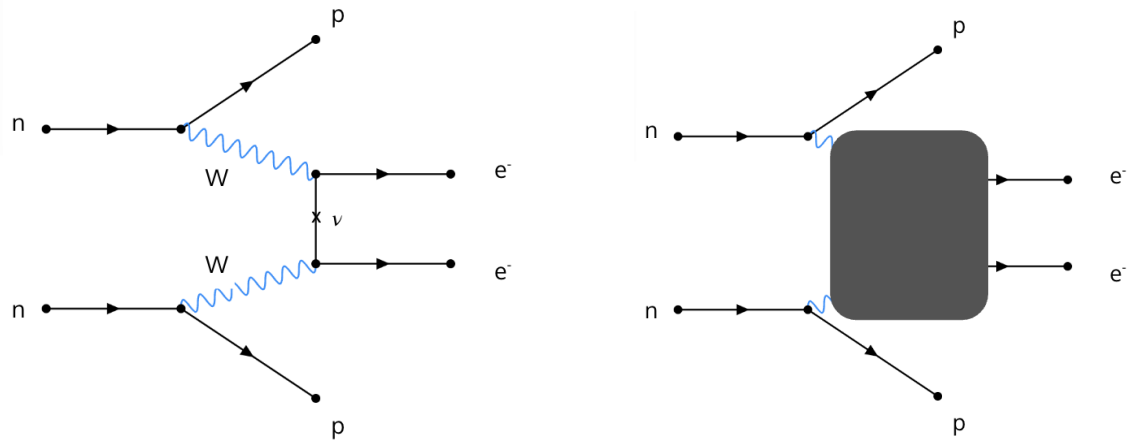

Figure 2.3: Feynman diagrams of $0\nu\beta\beta$; the left figure shows the interaction occurring at the nucleon level under the light Majorana neutrino exchange mechanism (the annihilation of two $\bar{\nu}_e$). The right figure shows the same interaction with a black box overlayed indicating that any process that occurs inside of it still results in the lepton number violating production of two electrons, and contributes to a Majorana mass term for neutrinos as per [124].

of $0\nu\beta\beta$ decays under the paradigm of light Majorana neutrino exchange via:

$$(T^{0\nu}_{1/2})^{-1} = \frac{m^2_{\beta\beta}}{m^2_e} G^{0\nu} g^4_A |M^{0\nu}|^2, \tag{2.15}$$

where $T^{0\nu}_{1/2}$ is the $0\nu\beta\beta$ half life, m_e is the electron mass, $G^{0\nu}$ a phase space factor (accounting for available atomic phase space for the decay), g_A the axial-vector coupling constant (determines the coupling between quarks and $W^{\pm}$), and $M^{0\nu}$ the nuclear matrix element (NME), which accounts for the ways in which the nucleus can transition between its initial and final states.

Experiments searching for $0\nu\beta\beta$ select elements with a relatively high natural abundance of the $\beta\beta$ candidate isotope, mitigating the need for excessive isotopic enrichment. Furthermore, $Q_{\beta\beta}$ of the selected isotope should be above the majority of

natural radioactive γ-lines, so that the penetrating γ-rays cannot scatter electrons to energies at $Q_{\beta\beta}$ and mimic the $0\nu\beta\beta$ signal. Of particular concern are the γ-lines from primordial decay chains of ^{238}U and ^{232}Th, which are present in trace amounts in all detector materials and contribute to backgrounds. Finally, experiments should have a good energy resolution, and have the ability to discriminate between energy deposits from different kinds of ionizing radiation, i.e., distinguish between α, β, and γ radiation. Given these criteria, no single isotope stands out as the optimal choice for a $0\nu\beta\beta$ experiment. Thus, experimental programs are tailored to use various isotopes, optimizing the aforementioned features according to the specific advantages of each element. For a comprehensive review of $0\nu\beta\beta$ see [126, 127].

The main experimental efforts today aim to utilize tonne-scale targets in the isotopes: ^{76}Ge [128, 129], ^{100}Mo [130], ^{130}Te [131, 132], and ^{136}Xe [24, 25]. However, there is also the ambitious multi-isotope NEMO program [133–136] which searches across a broad range of isotopes (^{100}Mo, ^{82}Se, ^{150}Nd, ^{96}Zr, ^{130}Te, ^{116}Cd, and ^{48}Ca), but with smaller masses of target material ($\sim$10-100 kg, or as low as $\sim$10 g in the case of ^{48}Ca). This thesis focuses on background reductions for the nEXO experiment, which searches for $0\nu\beta\beta$ in ^{136}Xe using a liquid xenon time projection chamber. The next chapter will overview the experimental details and analysis procedure of nEXO, but for now we will consider its ultimate sensitivity in the context of global neutrino physics investigations.

2.5 nEXO in the global context of neutrino physics

The proposed nEXO experiment would be sensitive to $0\nu\beta\beta$ half-lives in ^{136}Xe up to 1.35×10^{28} years at 90% confidence level (C.L.) after 10 years of live time [25], a testament to the ability of nEXO to measure extremely rare interactions at the MeV-scale in its liquid xenon time projection chamber.[13] This halflife sensitivity can be translated into a limit on the effective Majorana mass of the electron neutrino by Equation 2.15. However, the choice of nuclear matrix element (NME) significantly impacts the value of $m_{\beta\beta}$ obtained. Theoretically calculated NME values encode the number of ways the nucleus can transition between the initial and final states (see [137] for a review). Most theoretical groups do not provide uncertainties on these calculations, as it is difficult to account for systematics of including or disregarding various multi-body nuclear forces in solving the difficult quantum many-body problem. If we take the maximum and minimum NME values published for ^{136}Xe, then we can plot nEXO's exclusion bands on the upper limit of $m_{\beta\beta}$ as shown in Figure 2.4. Note, however, that recently there have been advances in ab-initio (first-principles) calculations of the NME values [138]. These computational methods utilize a chiral effective field theory approach of quantum chromodynamics and electroweak theory [139], as opposed to phenomenological nuclear calculations that require normalization against experimental data.

A fruitful $0\nu\beta\beta$ program to search for the hypothesized LNV decay is therefore one that incorporates many different candidate isotopes and experimental strategies, e.g., ^{76}Ge, ^{130}Te, and ^{136}Xe as there is no expectation that the $0\nu\beta\beta$ half-lives will coincide across isotopes, and

[13] The procedure outlining how this number is calculated is outlined in the next chapter (Section 3.4).

the physics parameter of interest ($m_{\beta\beta}$) is not strongly constrained theoretically as referenced in the previous paragraph.

We are at the cusp of a transformative era in neutrino physics. If cosmological measurements are correct and without too large of a systematic offset, then in the next decades CMB-S4 will provide a measurement of $\sum m_\nu$, which will determine the neutrino mass ordering in a complementary way to next-generation neutrino oscillation measurements. If $\sum m_\nu$ is not measured, then either the standard cosmological models are wrong, or our understanding of neutrino mixing from oscillation measurements is flawed.

The connection between $0\nu\beta\beta$ half-lives and $m_{\beta\beta}$ provides for an interesting interplay between cosmological measurements, terrestrial oscillation, and direct mass measurements with $0\nu\beta\beta$ searches. Because the values of the PMNS matrix are already acquired through neutrino oscillations, one can vary these parameters within their central values and uncertainties, and sample the available parameter space assuming complete ignorance of the unknown Majorana phases as shown in Figure 2.4

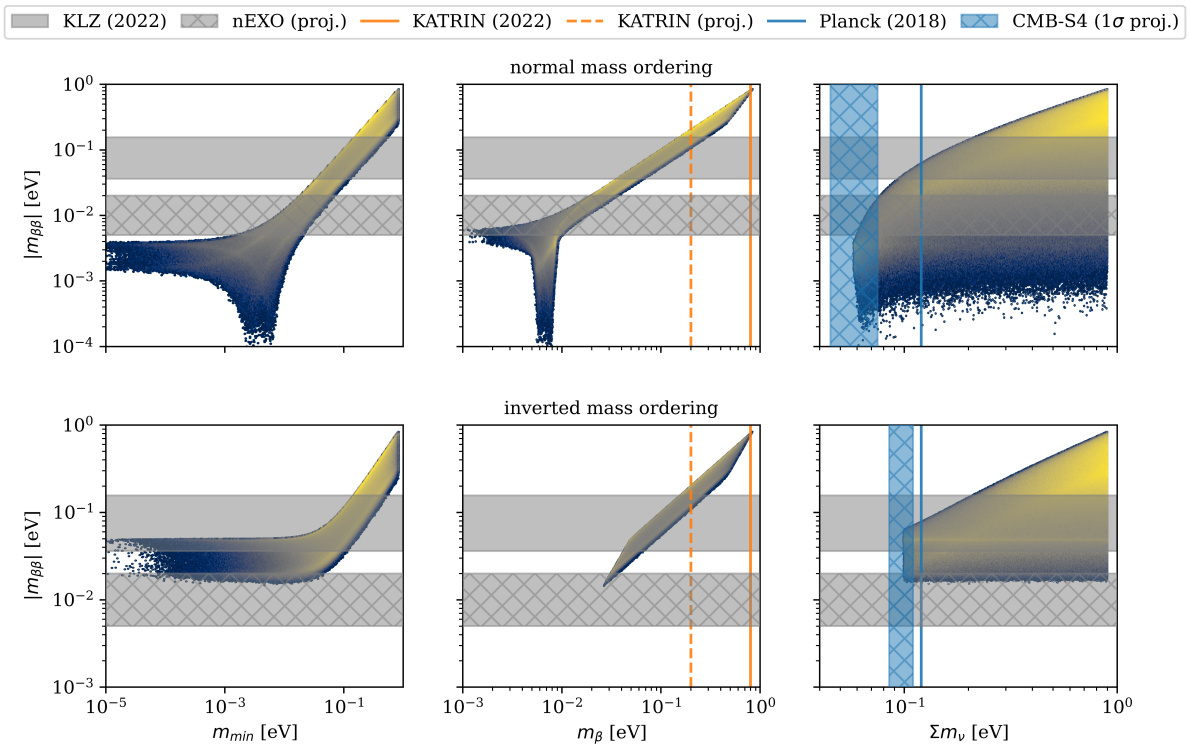

Figure 2.4: Available parameter space for $m_{\beta\beta}$ based on Gaussian error assumptions for neutrino oscillation measurements, a uniform prior on $\sum m_\nu$ up to 0.9 eV, and no prior knowledge of Majorana phases in the PMNS matrix. The nEXO band illustrates the upper limit on $m_{\beta\beta}$ for various NME values. The parameter space was constrained above a minimum $\sum m_\nu$, calculated as the square root of the mass-squared splittings from neutrino oscillation experiments, for both normal and inverted mass orderings. Neutrino mixing data retrieved from the Particle Data Group [1].

Chapter 3

The nEXO Experiment

The nEXO experiment is a proposed next-generation neutrinoless double beta decay ($0\nu\beta\beta$) experiment. Its predecessor, the Enriched Xenon Observatory (EXO-200), was a time projection chamber (TPC) experiment filled with ∼200 kg of liquid xenon (LXe), enriched to 80.6% in the target isotope, ^{136}Xe. EXO-200 discovered the $2\nu\beta\beta$ decay mode in ^{136}Xe [121] and set world-leading limits on its $0\nu\beta\beta$ halflife [140], only recently surpassed by the KamLAND-Zen [24].

Building on EXO-200's achievements, nEXO will utilize a multi-tonne enriched LXe TPC with advanced photodetector and charge-readout technologies, as well as modern analysis techniques. Further improvements from EXO-200 include constructing the nEXO TPC out of ultra-radiopure electroformed copper, therefore reducing background contributions from pervasive ^{238}U and ^{232}Th decay chains. nEXO will also need to be operated deep underground to achieve its sensitivity goals to $0\nu\beta\beta$. The rock overburden will shield the experiment from the cosmic rays incident at the Earth's surface, and subdue cosmogenic backgrounds (surveyed in Chapter 4). Finally, the experiment will employ a 1.4 kilotonne water tank to act as a radiation shield and water-Cherenkov muon veto (described in Chapter 5).

3.1 Liquid xenon as a radiation detector

Liquid xenon is an excellent medium for radiation detection [141] due to several key features, many of which are especially applicable to $0\nu\beta\beta$ searches. Its low excitation threshold (W-factor)[1] of 11.5±0.5 eV [143] means that events can be observed at or below energies of 1 keV [145], and in the case of MeV-scale interactions such as $0\nu\beta\beta$ there are $\mathcal{O}(10^5)$ charges that are liberated which can be detected.

The LXe environment is transparent to its own scintillation light of 175 nm, which is vacuum ultraviolet but within the range of direct detection; i.e., the light can be detected without the use of wavelength shifters that may smear pulse timing and degrade imaging capabilities. The scintillation light is also produced rapidly, with rise and decay times totalling ∼10's of nanoseconds. Thus, LXe can be used in high event rate environments [146].

Another significant feature of LXe is that the charge and light signals have anti-correlated fluctuations [147]. The charges liberated in LXe upon energy deposition can either recombine with xenon ions, forming excited dimers which release scintillation light, or they can be drifted in the presence of an electric field toward an anode. This enables the optimization of energy resolution based on expected charge and light collection efficiencies, and provides an event discrimination handle based off the charge-to-light signal ratio; e.g., separating α from β/γ events.

The dense medium of LXe provides twoadvantages to $0\nu\beta\beta$ searches: the first being that

[1] There have been several measurements and redefinitions of the W-factors for LXe in the last few decades. A nominal 13.7 eV [142] has been widely used since 2002, but values closer to 11.5 eV have been recently reported [143, 144].

its density of 3.1 gcm^{-3} at the triple point of 161 K [148], in combination with its high atomic number, results in a large γ-ray interaction cross section and short attenuation length. This means that LXe is inherently a self-shielding medium against external backgrounds, and is likely to capture the full energy deposited from a single γ-ray after multiple Compton scatters, increasing the likelihood of correct event identification. Its density also allows for the compactification of the detector compared to gas-phase technologies, increasing the number of $0\nu\beta\beta$ candidate nuclei per unit of instrumented volume.

The inert nature of xenon as a noble element, alongside its usage in liquid or gas phase at cold, but not cryogenic, temperatures means that it can easily be scrubbed for impurities, and will remain chemically stable for long periods of time. It can also be purified continuously while the experiment is running which removes any contaminants leaching into the xenon from detector components, except other noble gases. In-situ purifiability allows for maximization of transparency to scintillation light, and of charge-cloud drift lengths due to the removal of VUV-absorbing compounds (H_2O) and elecronegative impurities (O_2) which can capture liberated ionization electrons.

All of the listed advantages are inherent to xenon's chemical properties and its general applicability as a radiation detector. But, in the context of $0\nu\beta\beta$ searches, xenon offers a unique capability: the isotopic ratios of the $0\nu\beta\beta$ candidate (e.g., ^{136}Xe) can be easily modified relative to other isotopes without changing the detection principle or replacing detector components. This allows for a control measurement using the same detector in the case of a positive $0\nu\beta\beta$ observation, by substituting the enriched xenon with natural or depleted xenon.

3.2 nEXO's time projection chamber

nEXO's TPC plays an essential role in the $0\nu\beta\beta$ search. Located at the heart of the experiment, the TPC consists of a 1.3 m diameter right-cylinder filled with 4.8 tonnes of LXe enriched to 90% in the target isotope ^{136}Xe. The cylindrical barrel wall is lined with inward-facing silicon photo-multipliers (SiPMs): pixelated, radiopure, VUV light sensors capable of single-photon counting with nanosecond-scale timing resolution; for suitable nEXO candidates, see [149, 150]. The SiPMs are used to detect the prompt scintillation light signal from energy deposits in the TPC, and provide rough localization capability on their own due to solid angle effects of isotropic light sources (individual energy deposits) near and far from the SiPM array on the cylindrical wall.

Of the 4.8 tonnes of LXe, a 3.3 tonne fiducial volume is situated inside a copper field cage maintaining an electric field strength of 400 V/cm [151]. Energy deposits within the fiducial volume create both prompt scintillation light to be detected on SiPMs and anti-correlated charge signals. Liberated charges are drifted through the electric field toward a segmented anode, providing an x-y projection of the energy deposits in the TPC. The 2D projection of charge clouds on the anode allow for β- and γ- event discrimination: γ-rays tend to scatter multiple times in the TPC, showing up as multi-sited deposits on the x-y plane, and as multiple temporal deposits if distributed along the z-axis; β-like events, due to the short range of MeV-scale β-particles in the dense LXe environment, appear as single-site events a few millimeters in radius. Combining the prompt scintillation signal with the delayed charge signals provides a 3-dimensional reconstruction of events in the TPC, allowing for precise event localization at the cubic-cm scale, see Figure 3.1.

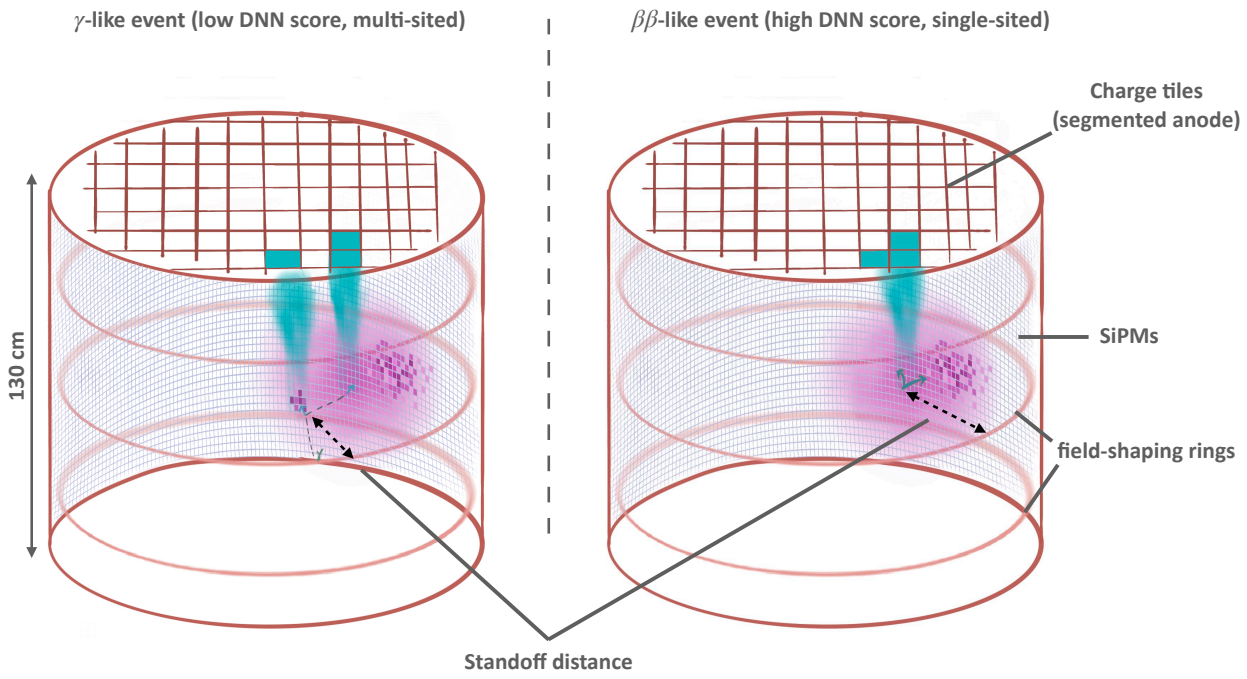

Figure 3.1: Left: a γ-like event ionizes the LXe in multiple deposits with macroscopic distances between them. Right: a double beta decay event (green arrows) ionizes the LXe environment along the β-particle tracks in a single cluster. In either case, newly formed Xe^+ can produce dimers of Xe_2^+, which when neutralized will emit 175 nm isotropic scintillation light shown in pink ($\sim$10 ns timescale). This light is detected on the SiPMs lining the TPC barrel. Meanwhile, liberated electrons (shown in turquoise) from the ionization tracks are drifted towards the segmented anode in a uniform electric field shaped by copper rings ($\sim$ mm/μs in a 400 V/cm electric field). Their detection on the anode provides a 2D projected reconstruction of the decay vertex, smeared by the diffusion of charges during the drift time. Combining the timing of the light signal and the delayed time of the charge signal enables the full 3D event reconstruction. Clustering on the charge tiles allows a deep neural network (DNN) to provide topological separation between β-like and γ-like events.

3.3 nEXO's multi-parameter analysis strategy

To optimize the signal extraction and background discrimination capability of nEXO, a multiparameter analysis approach is used. For each event in the TPC, 3 high-level analysis variables are extracted: energy, position, and topology. Here, topology refers to the output of a deep neural network where an output value of 1 is assigned to $\beta\beta$-like event, and a 0 is assigned to γ-like events, see [152] for details. Position refers to standoff distance, i.e., the distance to the nearest detector component. In standoff space, energy deposits due to γ-ray interactions are exponentially attenuated as we approach the center of the TPC volume due to the LXe self-shielding effects mentioned earlier (see Figure 3.2). The energy of the event is then the final handle. The TPC is designed to reach sub-percent energy resolution at the signal energy, $Q_{\beta\beta}$= 2.458 MeV, by measuring recombined charge and light signals.

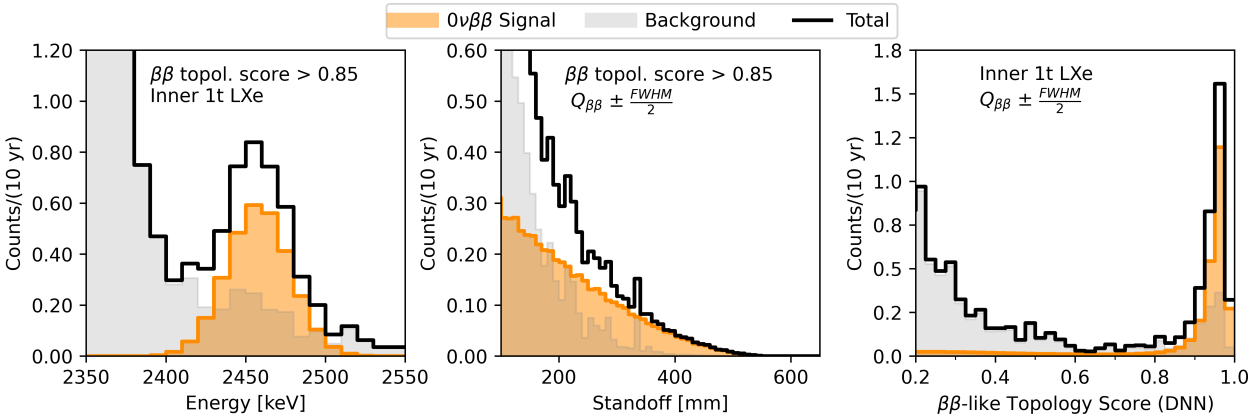

Figure 3.2: Each event in nEXO produces 3 analysis variables and contributes a 3-dimensional histogram. Shown here are the 1D projections of the full 3D probability density function onto each axis, for a livetime of 10 years and an energy resolution of 0.7%. The $0\nu\beta\beta$ signal amplitude here corresponds to $T^{0\nu}_{1/2} = 7.4\times10^{27}$ years, the 3σ discovery potential of nEXO.

Measuring the energy, standoff, and topology distributions of all events throughout the full TPC volume provides not only a high signal extraction efficiency, but also a precise, measured, characterization of backgrounds allowing for a sensitivity that is robust against background fluctuations and enables an improved sensitivity to $0\nu\beta\beta$ relative to a cut-and-count analysis in the energy window around $Q_{\beta\beta}$ alone [153]. Moreover, an anomalous signal in nEXO would have to match the expected signal probability density function (PDF) in all 3 analysis variables. For example, for γ-rays in the deepest locations of the LXe volume to mimic a $0\nu\beta\beta$ signal, there will have to be a corresponding background component that will fall off exponentially in standoff parameter space according to the attenuation length for that particular γ-ray energy. The nEXO analysis strategy exploits this effect, and constrains the activities of all γ-ray backgrounds based on this correlated drop-off (see Figure 3.3).

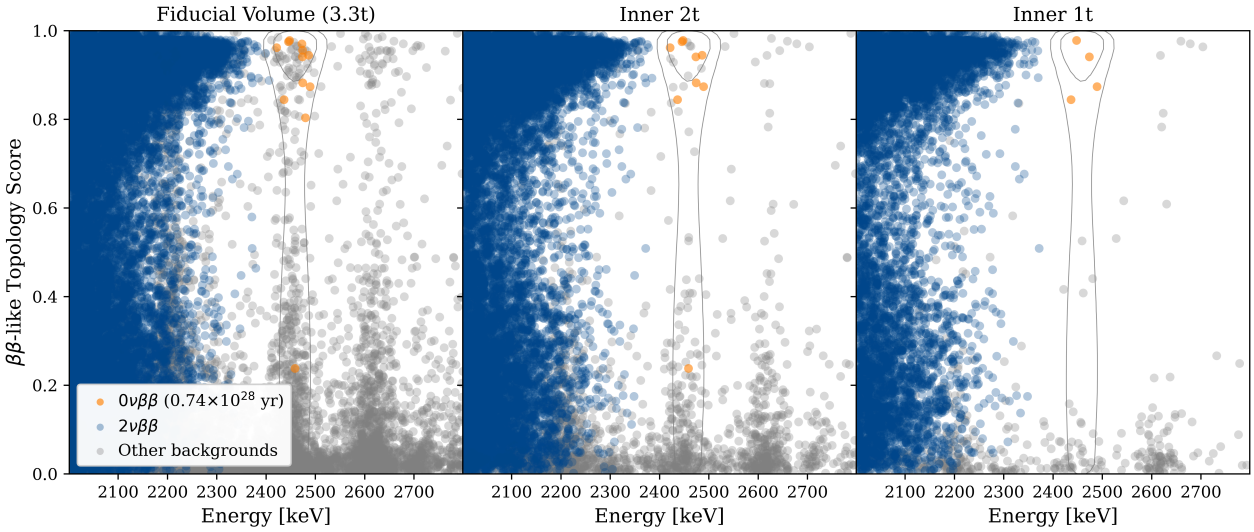

Figure 3.3: Example toy dataset from nEXO after 10 years of livetime shown in the combined energy and topology space, for 3 slices of mass fiducialization. The grey contours designate the 1σ and 2σ containment of the $0\nu\beta\beta$ signal. As can be seen here, the proximity of ^{214}B and ^{208}Tl γ-lines (2448 and 2617 keV, respectively) to the signal region falls off exponentially as a function of depth in the xenon (smaller mass fiducializations).

3.4 Sensitivity to $0\nu\beta\beta$ and effective Majorana mass

nEXO's sensitivity is calculated by performing many hypothesis tests on toy Monte Carlo (MC) datasets that are based on measured radioactivity levels of detector materials. Specifically, every detector material is screened for its radiopurity prior to installation in nEXO; measuring the activities of various decay chains using several techniques including γ-spectroscopy with high purity germanium counters, neutron activation analysis, α-counting, and others [151]. These data are uploaded into a centralized database [154]. A detailed nEXO model is built in Geant4, a radiation and particle tracking MC software package [155]. The software models particle transport through the nEXO geometry and the location of energy depositions. Scintillation and ionization processes in liquid xenon are modelled with NEST [156], and together with Geant4, a high-statistics simulation is then obtained for the specific decays in the background component being investigated, e.g., copper in the TPC, providing a 3-dimensional PDF of that component's contributions in the correlated energy, standoff, and topology spaces. This process is repeated for all detector materials and components.

The measured background rate of each detector component is then scaled to its designed mass and/or surface area in nEXO, which sets the scaling factor of each of the 3D PDFs. A Poisson fluctuation is applied to each background component's mean event rate, and a corresponding number of random samples are drawn from for each background component, including each event's correlation in the three analysis variables. After iterating through all detector materials, we obtain a single realization of the background contributions in nEXO after 10 years of livetime, as shown in Figure 3.3. Once a suitable number of realizations is

obtained, usually $\mathcal{O}(10^5)$ toy data sets, a distribution is constructed of the exclusion limits calculated from non-observation of $0\nu\beta\beta$ in each of the toy datasets, the median of these exclusion limits (at 90% C.L.) is then quoted as nEXO's sensitivity to the $0\nu\beta\beta$ halflife. An analogous calculation is performed as a function of signal strength ($0\nu\beta\beta$ event rate), also allowing for Poisson fluctuations in the signal event rate based off a given halflife of $0\nu\beta\beta$. A distribution of $0\nu\beta\beta$ half lives giving a 3σ signal is obtained, the median of which is quoted as nEXO's discovery potential (this is what is used to set the signal strength in Figures 3.2 and 3.3). Table 3.1 summarizes the latest published median sensitivity and median discovery potential of nEXO [25], along with the corresponding limits on $m_{\beta\beta}$ for various NME values.[2]

	Exclusion sensitivity (90% C.L.)	Discovery potential (3σ)
Halflife, $T^{0\nu}_{1/2}$	1.35×10^{28} yr	7.4×10^{27} yr
Majorana mass, $m_{\beta\beta}$	4.7–20.3 meV	6.4–27.5 meV

Table 3.1: Summary of nEXO median sensitivity and median discovery potential. The range in $m_{\beta\beta}$ is a result of the various NMEs in the literature. For details, see [25].

The sensitivity evaluation strategy as explained above glossesover complicating factors associated with background contributions from in-situ cosmogenic backgrounds. This class of backgrounds depends on where the experiment is located (amount of shielding, overburden), and whether or not mitigation strategies will be put in place. Furthermore, cosmogenic backgrounds are known to have long-tailed non-Poissonian distributions of radioactivity, and so Poisson-sampling of the mean activation rate is no longer valid. Addressing the aforementioned complications, and building mitigation strategies minimizing the impact of cosmogenic backgrounds in nEXO is the focus of the following two chapters of this thesis.

[2]The sensitivity data is also presented in the previous chapter (Figure 2.4) alongside available parameter space, and limits from current and future $\sum m_\nu$ and m_β.

3.5 $0\nu\beta\beta$ searches in Xe beyond nEXO

There are a number of reasons LXe TPCs are a promising technological strategy for future $0\nu\beta\beta$ searches. First, TPCs have a long-standing history in the field of particle physics, particularly in the context of liquid noble calorimeters. The extensive experience and successful implementation of liquid noble TPCs in various detector environments affirm their reliability and longevity as a technology. As such, the utilization of liquid noble TPCs, including LXe TPCs, in the investigation of double beta decay processes is poised to persist and be continuously improved upon in the search for these rare events.

Liquid noble TPC volumes (and therefore masses) grow as the cube-root of their characteristic lengths. In the case of LXe, going from 5 tonnes to 50 tonnes only requires an increase of the characteristic size by $10^{1/3}$ giving $\sim$ 3.5 m for the size-scale of such a TPC.[3] With experiments like DUNE coming online in the next decades [97], we are demonstrating that we know how to build TPCs of similar sizes to those required for LXe TPCs beyond nEXO. The larger size of TPCs will further exploit the self-shielding effects of LXe, which causes LXe TPC searches for $0\nu\beta\beta$ to approach the background-free regime due to their homogeneity, as opposed to segmented cryogenic detector technologies which will likely plateau in their background count per unit mass (i.e., their background index) as their target mass grows due to proximity of surfaces to sensitive detector regions. This is the scenario in which there is no discovery, and additional motivation to search for $0\nu\beta\beta$ is provided.

[3] Naively, this would amount to a factor of $\sim$10 improvement in sensitivity to $0\nu\beta\beta$ halflife due to the increased exposure to the target nucleus, for the same experimental run time. However, the self-shielding effects of LXe means that the increased mass in a monolithic volume will also have reduced backgrounds in the sensitive region of the detector. This is partly why nEXO can attain a $\sim 100\times$ higher sensitivity compared to EXO-200, with only a $\sim 25\times$ increase in mass of ^{136}Xe.

In the case of $0\nu\beta\beta$ discovery, the current research and development of gaseous xenon (GXe) technologies in high pressure TPCs is important [157]. These GXe TPCs will have the ability to reconstruct angular and energy correlations of the emitted electrons in $0\nu\beta\beta$ events, allowing for the deciphering of the decay mechanisms. Hence, if $0\nu\beta\beta$ is discovered in an LXe TPC, where discovery potential per unit volume is maximized, design constraints can be immediately set on the GXe TPCs, and $0\nu\beta\beta$ decay mechanisms can be readily explored. In contrast, the progression of technologies used for $0\nu\beta\beta$ searches in other isotopes (e.g., cryogenic crystals) to detectors capable of investigating decay mechanisms within those same isotopes remains uncertain.

Another advantage of liquid or gaseous TPCs is the potential for extraction and identification of the daughter isotopes in-situ [158–162]. In the case of $0\nu\beta\beta$ searches in ^{136}Xe, the extraction and identification of ^{136}Ba ions will remove all backgrounds, except those arising from $2\nu\beta\beta$ decays, providing a secondary confirmation strategy as opposed to a natural or depleted xenon control run years after the experiment has been run. Furthermore, the ability to identify background production mechanisms, e.g., those from irreducible solar neutrino backgrounds such as $\nu_e + ^{136}\text{Xe} \rightarrow ^{137}\text{Cs}$ (which can later decay to the daughter isotope ^{136}Ba), via mass spectrometry of daughter ions from signal candidate events adds to the robustness of a $0\nu\beta\beta$ discovery.

In summary, nEXO is a world-leading proposed $0\nu\beta\beta$ experiment. It is designed to probe the full inverted mass ordering parameter space, as well as a significant fraction of the normal ordering parameter space, under the paradigm of light Majorana neutrino exchange (see Figure 2.4). The experiment will lead the developments of LXe-based TPCs for $0\nu\beta\beta$ searches

in ^{136}Xe, a scalable and robust technology with the potential to push $m_{\beta\beta}$ sensitivity below the 10 meV level. Development of these LXe TPC technologies and solving associated engineering and manufacturing problems will allow for its increased use in all realms of radiation detection, including medical [163, 164] and fundamental physics research.

In the following chapter we will address the effects of cosmogenic backgrounds on nEXO's sensitivity to $0\nu\beta\beta$. Quantifying the effect of these backgrounds will be relevant to any future low background LXe TPC experiment and, as for nEXO, cosmogenic background mitigation strategies will need to be developed.

Chapter 4

Cosmogenic Backgrounds to nEXO

True backgrounds to nEXO's $0\nu\beta\beta$ search are those which are produced homogenously in the TPC volume, depositing energies around the $Q_{\beta\beta}$ energy window, in $\beta\beta$-like interactions with single-site event topologies. Thus, unwanted signals are predominantly due to backgrounds that cannot be filtered out of noble liquids (e.g., radon impurities), or coming from point-like interactions that leave no preceding ionization tracks, e.g., from β-delayed decays after neutron activation or neutrino interactions. The latter are driven by cosmogenic backgrounds: backgrounds produced as a result of high energy cosmogenic muon interactions, and interactions of secondary particles in muon showers, with material inside or surrounding the nEXO detectors.

This chapter provides an overview of cosmogenic backgrounds to nEXO, estimates of expected background rates, explains their out-sized role in the evaluation of nEXO's sensitivity to $0\nu\beta\beta$, and assesses possible mitigation strategies for the various underground sites in consideration.

4.1 Defining the nEXO region of interest

Before we begin a discussion of backgrounds in nEXO, it is helpful to define a metric to measure the effect of various backgrounds on the $0\nu\beta\beta$ search. nEXO's multiparameter search for $0\nu\beta\beta$ (outlined in Section 3.4) makes it difficult to compare the effects of different backgrounds, or detector configurations, without a full sensitivity evaluation for each background component contribution, and potential detector configuration. Still, we can define a proxy metric to reduce the complexity of such studies. We define this proxy based off the contribution of a given background component to the signal region.

Given nEXO's designed energy resolution of 0.7% at $Q_{\beta\beta}$ of ^{136}Xe, the energy window of interest (EOI) is defined as E = [2417.5, 2498.4] keV. It is more helpful, however, to define a 3-dimensional cut for use as a figure of merit: events with deposits in the EOI, appearing with single-site topology, and within the inner 2 tonnes of the LXe TPC volume are considered events in the region of interest (ROI).[1] Throughout the rest of this thesis, the nEXO cuts for the ROI are defined as: an energy deposit within the EOI, producing a deep neural network (DNN) event topology discriminator score >0.85 (where, in DNN space, the $0\nu\beta\beta$ signal dominates over background for the inner 2 tonnes of LXe), and a reconstructed standoff distance >104 mm (corresponding to a 2 tonne fiducial volume); refer to Figures 3.2 and 3.3 for a visualization.

[1] The inner 2 tonne boundary is where the single-site signal/background ratio in the EOI is approximately equal to 1.

4.2 Homogenous backgrounds in the TPC

We will start by surveying the homogenously distributed backgrounds in the LXe to highlight why certain cosmogenic backgrounds are particularly concerning to the $0\nu\beta\beta$ search. The dominant uniformly distributed background in nEXO results from radon outgassing into the xenon from detector components. Radon, being a noble element, is difficult to filter out in conventional xenon recirculation systems. Thus, daughter isotopes in the decay chain of ^{222}Rn are viable background candidates if their half-lives are long enough to allow significant diffusion into the TPC. In particular, the daughter isotope ^{214}Bi has a small probability to β-decay into an excited state of ^{214}Po and release a 2447 keV photon, directly producing events in the ROI via photoelectric absorption of the γ-ray. Fortunately, the daughter isotope ^{214}Po, decays via α-emission to ^{210}Pb within 200 μs. The α-particle is easily identified in the nEXO TPC due to its high charge/light ratio, resulting from the density of the ionization tracks of α's relative to β/γ events. This 200 μs Bi-Po coincidence is used to efficiently remove the majority of ^{222}Rn backgrounds in nEXO, the dominant of the homogenously distributed backgrounds. See [165] for optimization strategies and more on the Bi-Po coincidence tag.

Another uniformly distributed background in nEXO is due to neutrino interactions from the Sun. Although, the low interaction cross sections are expected to provide only a small $\sim$2% contribution the total background in the ROI [25]. Hence, it is subdominant to radon emanating from copper components which contributes $\sim$50% to the ROI. Finally, the $2\nu\beta\beta$ rate in ^{136}Xe is itself a background to the $0\nu\beta\beta$ search due to the TPC's finite energy resolution. However, nEXO's high energy resolution effectively removes the $2\nu\beta\beta$ background, which currently contributes 0.8% to the total background budget [25].

4.3 The ^{137}Xe background

Cosmogenic backgrounds are produced continuously and in-situ, even in a deep underground laboratory. The main background concern to nEXO in this category results from ^{137}Xe, as expected from EXO-200 results [166] and demonstrated in [167]. This background is of particular concern because it is produced as a result of neutron activation of ^{136}Xe, and is inherently distributed uniformly in the LXe; ^{136}Xe has low neutron interaction cross sections (thermal neutron capture cross section of 0.26 ± 0.02 barn [168]), and so self-shielding of LXe is not applicable to neutron radiation for TPCs at the scale of nEXO. Neutron activation in nEXO, both from radiogenic neutrons entering the TPC and cosmogenic neutrons, has been shown to be homogenous throughout the detector. The primary source of neutrons is expected to come from spallation products of the residual flux of high-energy cosmogenic muons in an underground laboratory. These neutrons will have a relatively broad energy spectrum and can penetrate, thermalize, and capture throughout all detector components. Newly created ^{137}Xe atoms produced this way can diffuse and circulate throughout the LXe volume until they decay via β-emission with a Q-value that eclipses $Q_{\beta\beta}$, potentially depositing events in the ROI (see Figure 4.1).

The multi-step neutron activation to β-decay process is:

$$n + {}^{136}\mathrm{Xe} \rightarrow {}^{137}\mathrm{Xe}^{*}, \tag{4.1}$$

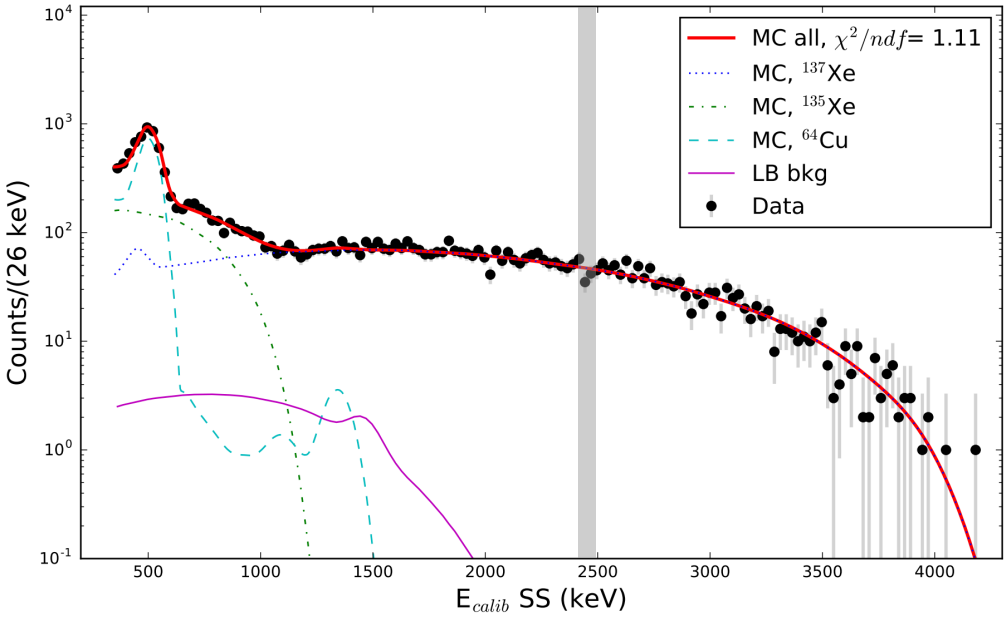

Figure 4.1: EXO-200 measured calibration spectra including β-decays of ^{137}Xe as a result of neutron activation of ^{136}Xe in the TPC with an AmBe neutron source. Notice the broad energy spectrum of ^{137}Xe β-decays overlapping the single site (SS) EOI, indicated by the vertical grey bar around $Q_{\beta\beta}$= 2458 keV. Figure adapted from [169].

which promptly de-excites to its ground state:

$$^{137}\text{Xe}^{*} \rightarrow ^{137}\text{Xe} + \gamma' s \ (\sum E_{\gamma} = 4.025 \text{ MeV}), \tag{4.2}$$

and then β-decays with $T_{1/2} = 3.81 \pm 0.15$ minutes (228±9 seconds) [143]:

$$^{137}\text{Xe} \rightarrow ^{137}\text{Cs} + e^{-} + \bar{\nu}_e \ (Q_{\beta} = 4.17 \text{ MeV}). \tag{4.3}$$

The several-minute halflife of ^{137}Xe, coupled with the relatively high xenon flow rates in the nEXO TPC of 1-30 mm/s (position dependent) [170], means that the β-decays of ^{137}Xe are unlikely to be correlated with a triangulated position of the de-excitation γ-rays emitted

previously when the ^{137}Xe was created (Equation 4.2). I.e., the distance an atom can travel in a single halflife of ^{137}Xe can be larger than the size scale of the nEXO TPC. Thus, a TPC-wide veto upon detection of the γ-cascade signal ($\sum E_\gamma = 4.025$ MeV) will need to be developed, the details of which will be outlined in Section 4.7.4.

Cosmogenics as the primary source of neutrons in the LXe

The primary source of neutrons in the TPC is expected to result from cosmogenic-related interactions. Other sources of neutrons to nEXO will be those resulting from (α, n) interactions in the cryofluid (HFE) surrounding the TPC. These (α, n) interactions occur when high energy α-particles overcome the Coulomb barriers of low-Z nuclei (e.g., the carbon in organic materials) and are captured by them. These α-particles result from the decay chains of ^{238}U/^{222}Rn such as:

$$\alpha + {}^{13}C \rightarrow {}^{16}\mathrm{O} + n + \gamma, \tag{4.4}$$

where the resulting neutron is fast, carrying several MeV of energy. Thus, it can thermalize and capture on ^{136}Xe if it enters the LXe volume.

This source of neutrons can be mitigated by handling the HFE and building the TPC in a low-radon environment, which mitigates surface contamination with α-emitting isotopes from mine air. The expected ^{137}Xe rate from cosmogenics can then set engineering constraints on the quality of the radon-reduced air environment required during detector assembly.

4.4 Cosmogenics simulations with Geant4

The primary simulation software framework for nEXO, `nexo-offline` is based on Geant4 [155], and deployed with SNiPER [171], a C++/Python wrapper for Geant4 code bases. A detailed nEXO geometry has been developed in `nexo-offline`, including the liquid xenon volume, SiPM detectors, copper TPC, field cage, cathode, segmented anode, HFE, carbon fiber cryostat vessels, as well as a stainless steel tank filled with water, situated in a large underground cavern of norite rock modelled after the cryopit at SNOLAB [172] — nEXO's preferred host site. The geometry can be seen in Figure 4.2.

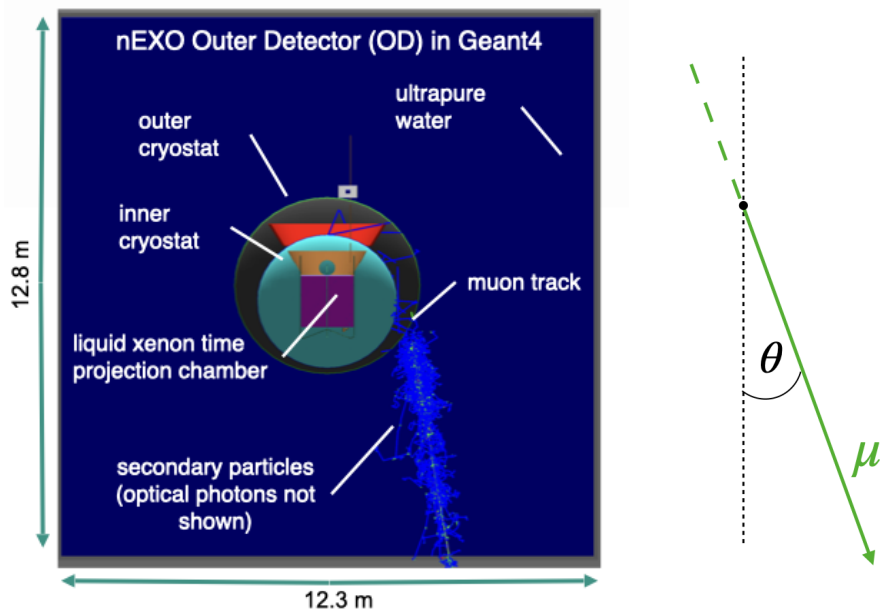

Figure 4.2: Left: nEXO Outer Detector in Geant4 shown with an example muon track and associated electromagnetic shower. Right: Schematic definition of zenith angle for muons (angle from the vertical), denoted θ.

Although the physics of hadronic interactions has been built into `nexo-offline`, additional muon-nuclear interactions needed to be included. Hence, two of the standard physics lists built into Geant4v10.5 were used for the cosmogenics studies: `Shielding` and

QGSP_BERT_HP. Both of these physics lists contain updated neutron cross sections, relevant hadronic and electromagnetic interaction cross sections, and allow for high-precision neutron transport down to thermal energies. In particular, the Shielding reference list is recommended as a basis for cosmogenics studies.[2]

4.4.1 Underground muon parameterizations

In order to precisely characterize the cosmogenic backgrounds being driven by the underground muon flux, a detailed model for that muon flux needed to be generated; the muon flux models used throughout these cosmogenics studies are outlined in this section.[3]

Due to the large rock overburden of ∼2 km, muons incident on nEXO at SNOLAB would have correlated energy and angular distributions. This is because muons that are coming down away from zenith (closer to the horizon), travel a greater distance through the rock, losing additional energy to radiative and ionization processes before reaching the underground site under consideration. This additional 'slant depth' causes the flux of muons coming in further from zenith to have an attenuated flux, but a higher average energy.

At SNOLAB, experiments typically employ the so-called Mei & Hime muon flux parameterization [175] for a depth of 6.01 km water-equivalent (km w.e.), which is then normalized to the measured muon flux from SNO [176]. The Mei & Hime angular spectrum[4] is adopted from [179], which proposes a depth-intensity relation for muons at

[2]Preliminary FLUKA [173, 174] results from nEXO colleagues (Regan Ross) show consistency in the mean ^{137}Xe rate produced in FLUKA and Geant4v10.5, corroborating the findings from EXO-200 [166].

[3]The framework outlined here is written in nEXOPrimaryGeneratorAction.cc of nexo-offline under the function Generate_CosmicMuon().

[4]Preliminary studies using the alternative 'Miyake' muon angular distribution for large overburden [177] produced no significant difference to the activation rates in nEXO at SNOLAB, although it did provide a slightly widened angular distribution . There is ongoing work on muon flux parameterizations to improve these models and account for seasonal variations in the muon flux. See [178] for an example.

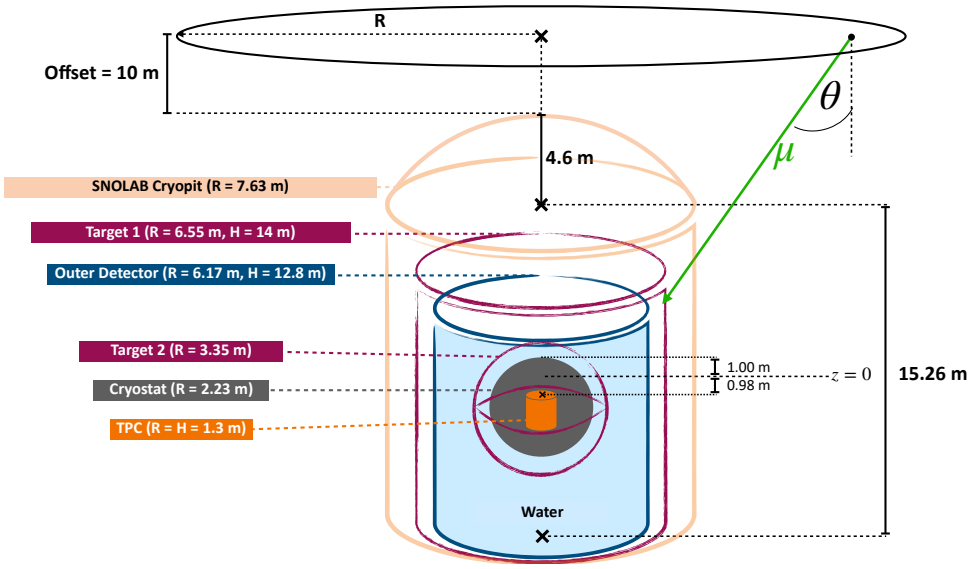

Figure 4.3: Muon targeting scheme for Monte Carlo sampling. Muons are sampled uniformly on the generation disc with radius R. The height is selected such that the minimum travel distance for muons is 10 meters through the rock (doubling the height did not produce changes in the activation rates). The radius of the generation disc is tuned so that the muons entering the target volumes (purple) achieve an angular coverage of 99%, i.e., the angular distribution of simulated muons matches that from [175] for any muon entering the specified target.

between slant depths (h) 1–10 km:

$$I(h) = I_1 e^{-h/\lambda_1} + I_2 e^{-h/\lambda_2}, \tag{4.5}$$

which is then fitted to experimental data at various underground locations for the values of $I_{1,2}$ and $\lambda_{1,2}$, and presented in [175].

The Mei & Hime energy distribution is the same as that from Gaisser *et al.* [180, 181]:

$$\frac{dN}{dE} = Ae^{-bh(\gamma-1)}(E + \varepsilon(1 - e^{-bh}))^{-\gamma}, \tag{4.6}$$

valid for the large slant depths in consideration throughout this thesis. The parameters $b = 0.4$ km w.e., $\varepsilon = 693$ GeV, $\gamma = 3.77$, control the shape of the spectrum. $h = h_0/\cos\theta$ km w.e. is the slant depth parameterized by the muon's incident zenith angle θ, and h_0 is the vertical depth in km water-equivalent. E is the muon energy in GeV, and A is a normalization constant.

Using standard acceptance-rejection sampling methods, zenith angles (θ) are obtained from the Mei & Hime distribution in Equation 4.5. For each sampled θ, the Gaisser energy distribution (Equation 4.6) is then used to sample an energy, given the calculated slant depth of a muon at SNOLAB coming in at a given angle θ. The resulting energy-angle relation can then be seen in Figure 4.4, which has a 99% angular coverage for zenith $\theta < 1.05$ rad (60.1 deg) and a mean muon energy of 362 GeV, consistent with the measured mean muon energy at SNOLAB of 363.0 $\pm$ 1.2 GeV [182].

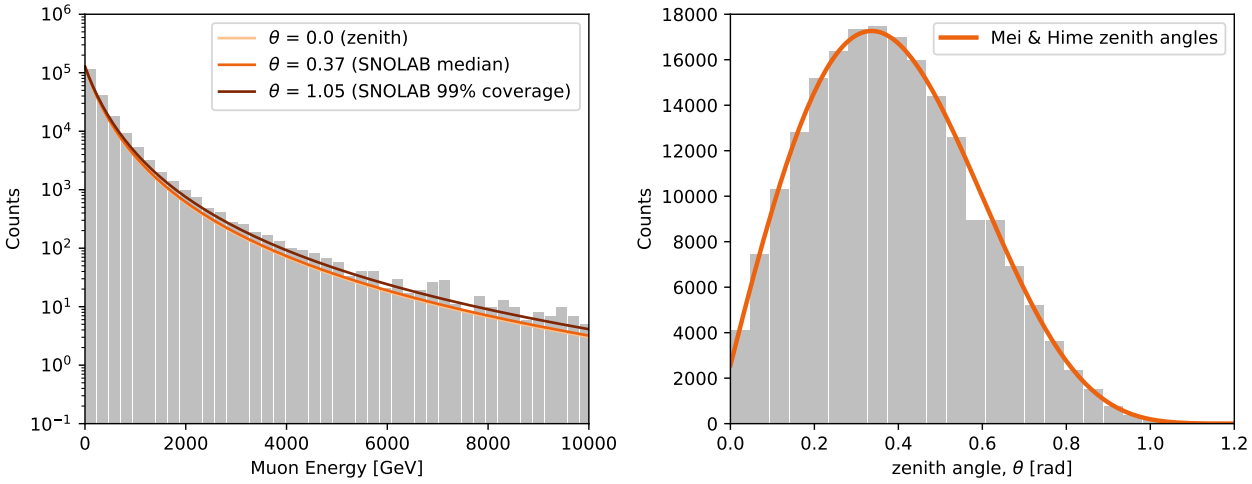

Figure 4.4: Energy and angular distributions of sampled SNOLAB muons according to the sampling methods outlined in the text with a mean energy of 362 GeV. Notice that at sites as deep as SNOLAB, the variation in the sampled energy histograms is weakly coupled to the muon angle (and therefore its slant depth), this is not true for shallower sites.

4.4.2 Muon generation & targeting in Geant4

To generate the muons, the procedure outlined in [166] is used. First, a randomly selected position is chosen from a generation disc placed 10 meters into the norite rock, above the cryopit. This allows for sufficient track length in the rock for spallation and muon shower interactions to occur.[5] Then, a zenith angle θ is selected according to the Mei & Hime distribution (Equation 4.5),[6] and an energy, $E_\mu \in$[1 GeV, 25 TeV], is assigned based off the Gaisser distribution (Equation 4.6). A uniform azimuthal angle $\phi \in [0, 2\pi]$ is then sampled. The flat overburden above SNOLAB does not attenuate muons as a function of ϕ, as opposed to a mountainous overburden so a uniform sampling is appropriate.

At this stage, one could propagate the muons after assigning them an appropriate electric charge. However, doing so would propagate muons both towards and away from the LXe volume — the volume in which we would like to study cosmogenic activation. Propagating the muons in this way would therefore be a waste of computational resources, as we expect there to be a dependence on the distance of the muon track from the TPC on cosmogenic activation rates due to the relativistic velocities of all particles involved (this effect becomes apparent later, and is addressed in Section 4.4.5). In order to save computational resources and develop an efficient simulation, the relativistic muons are approximated to travel in a straight line trajectory. Intersection points are then analytically calculated for some target volume using θ and ϕ angles as inputs for muon momenta. If there is no intersection with

[5] Doubling the height of the generation disc did not change the cosmogenic activation rates calculated later, but did slow the simulation down. This is because there were many more muons rejected from propagation due to the smaller solid angle of the target as viewed from the generation disc.

[6] Note, directly applying Equation 4.5 is inappropriate, as the flux would need to be adjusted for generation on a flat disc as opposed to a hemisphere; hence, an additional factor of $cos(\theta)$ is applied to account for this solid angle correction.

the target volume, then the muon's position on the generation disc, muon's momentum in θ and ϕ, and muon's energy are all resampled in succession. If there is an analytical intersection point with the target volume, then a muon charge is selected based off the ratio $\mu^+/\mu^- = 1.25$ (see [183] for an interpretation of this value) and the muon is propagated from the generation disc through the selected target volume (see Figure 4.3).

4.4.3 Muon flux calculations

We need to know the true flux of muons through the target volumes in order to translate activation rates in the Geant4 cosmogenics simulations into an estimate of the yearly activation rate. In the case of a spherical geometry, the flux is simply what is quoted in the literature as the total muon flux multiplied by the cross sectional area of the sphere, πr^2. However, in the case of non-spherical geometries (e.g., nEXO's water tank and TPC) the calculation is more involved. We require the effective viewing area, A_{eff}, of the target as a function of the differential angular muon flux. In the case of an upright cylinder and a uniform azimuthal muon distribution, such as nEXO at SNOLAB,[7] the cylindrical symmetry of our problem reduces the calculation's complexity.

Definition of Target 1 and Target 2

There are two target volumes used throughout the rest of this thesis. The first is a target cylinder centered on the TPC with dimensions of H=14 m and R=6.55 m, larger than the water tank by 1.2 m in height and 40 cm in radius, hereby called Target 1. The second

[7]The flat overburden above SNOLAB results in a uniform distribution of muons in the ϕ direction. At underground sites situated beneath a mountain, this is not the case.

target, Target 2, is a sphere centered on the TPC of radius 3.35 m (1.5× the radius of the outer cryostat), enclosing the cryostat vessel shown in Figure 4.3.

Analytic calculations of muon flux through the target volumes

Beginning at zenith, the muon flux simply sees the top of the cylinder, a disc of radius R with area πR^2. As we deviate from zenith, the muon flux now penetrates the cylindrical wall as well, which has height H and rectangular cross sectional area $2RH$. The further we deviate from zenith, the smaller the disc's area is, and the larger the viewed area of the wall. The area of the cylindrical wall grows as $\sin(\theta)$ and the disc shrinks as $\cos(\theta)$. Hence the formula for the effective viewed area of the muon flux through a cylinder as a function of zenith angle, assuming flat overburden, is:

$$A_{eff}(\theta) = \pi R^2 \cos(\theta) + 2RH \sin(\theta), \tag{4.7}$$

for $\theta \in [0, \frac{\pi}{2}]$. Thus, the angular flux distribution in Equation 4.5 can be normalized to the measured total underground muon flux at the various sites in consideration, and convolved with Equation 4.7 for an arbitrary cylinder size.

4.4.4 Cosmogenic activation rates

The preliminary iteration of MC simulations consisted of muons passing through Target 1 (the purple cylinder in Figure 4.3). In this iteration, both the `QGSP_BERT_HP` and `Shielding` default physics lists in Geant4v10.5 were used. A total of 2.5×10^6 muons were simulated through the water tank for each physics list. The corresponding effective livetime for these

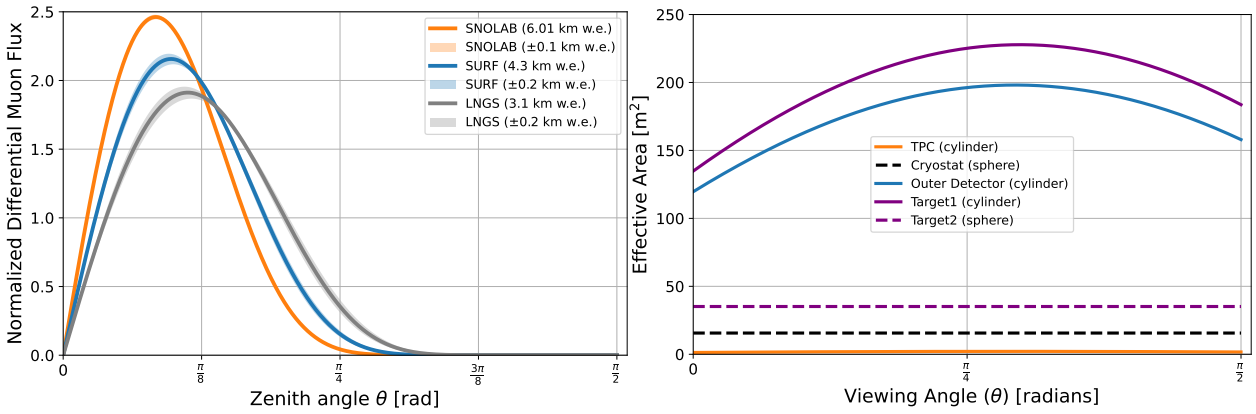

Figure 4.5: Left: Normalized Mei and Hime parameterizations [175] of (zenith) angular spectrum muon flux for the three different sites being considered for nEXO. Right: effective area as a function of zenith for different nEXO detector components and targets for the muons. The product of the effective area and the corresponding differential angular flux, normalized by the measured total muon flux at each site [184–186], gives the total muon flux through the volumes in Table 4.1.

MC runs were 149.5±0.6 years of underground exposure at SNOLAB (translated using results from Table 4.1).

The first MC at SNOLAB produced a total of 2749 ^{137}Xe atoms over all the muons. Taking this at face value, we obtain a mean ^{137}Xe activation rate of 18.39±0.35 per year, assigning a Poisson uncertainty. However, there is a subtlety here: the muons produce ^{137}Xe in shower events which have high neutron multiplicity, making it doubtful that the spread in the distribution is truly Poissonian.[8] When investigating the multiplicity distribution of ^{137}Xe, i.e., the number of ^{137}Xe produced per muon passage, we found that its mean deviated from 1 quite significantly (see Figure 4.6). Hence, a truer representation of the underlying distribution of ^{137}Xe production rates can be obtained by bootstrapping

[8] A Poisson process requires that each event is independent from every other event. However, in the case of cosmogenic activation there is a strong correlation between activation events due to the large number of neutrons produced in a single muon shower, resulting in a non-Poissonian distribution for the statistics of cosmogenic activation.

	TPC	Cryostat	Target 2	Water Tank	Target 1
SNOLAB	0.5028 ± 0.0021	4.468 ± 0.019	10.05 ± 0.043	45.79 ±0.19	52.1 ± 0.22
SURF	8.275 ± 0.26	71.68 ± 2.3	161.3 ± 5.2	754.5 ± 24	859.2 ± 28
LNGS	54.41 ± 0.16	460.3 ± 1.3	1036 ± 3	4967 ± 15	5661 ± 17
LNGS†	58.96 ± 0.17	460.3 ± 1.3	1036 ± 3	5411 ± 16	6197 ± 18

Table 4.1: Analytic calculations of muon flux through various volumes (see Figure 4.5) in units of muons/day according to the Mei & Hime angular distribution, normalized to the total muon flux measured at each of the sites SNOLAB, Sanford Underground Research Facility (SURF), and Laboratori Nazionali del Gran Sasso (LNGS). † denotes the alternative use of the measured angular spectrum from the Borexino experiment instead of the Mei & Hime parameterized angular flux.

the cosmogenics results. I.e., sampling many batches of muons (with replacement) equivalent to one year of underground exposure, and summing the total ^{137}Xe produced in this trial and then repeating the process to build a distribution. In the case of simulations through Target 1, this amounts to 19,000 muons from the full 150-year cosmogenics datasets. Each individual year's worth of muons would result in a total ^{137}Xe activation level that increments a corresponding bin in Figure 4.7.

Bootstrapping

The bootstrapping statistical method is a resampling technique that is used to estimate the properties of a sampled distribution, such as its mean and spread, without an apriori guess of what the underlying (true) distribution is. It works by repeatedly generating bootstrap samples (sub-populations) of the larger dataset, with continuous replacement of samples. By doing so, the bootstrapped samples now provide a distribution of means and their variance, while capturing the variability of the underlying dataset. As more bootstrap sample means and variance are generated, they will approach the true mean and variance by the central

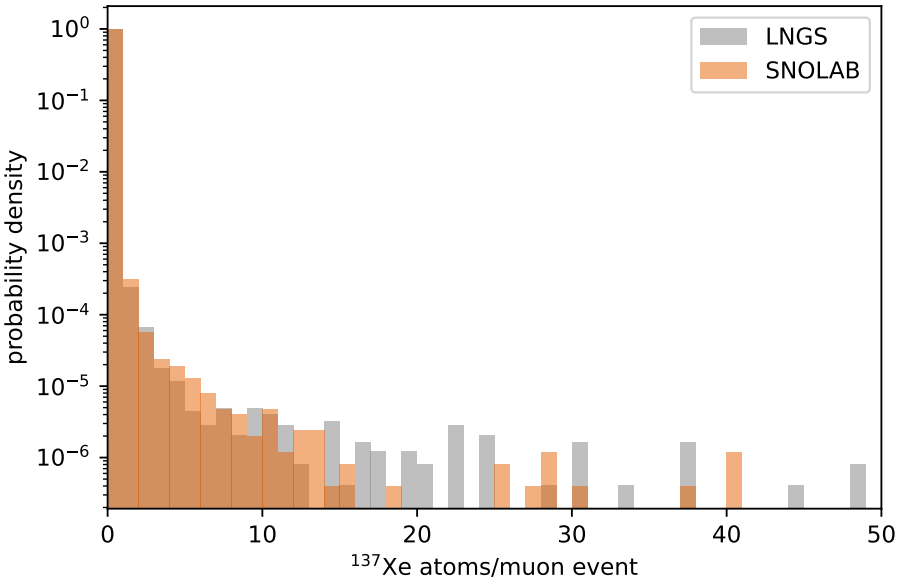

Figure 4.6: Multiplicity distribution of cosmogenically activated ^{137}Xe. The mean activation multiplicity of ^{137}Xe was found to be 2.36±0.14 at SNOLAB, and 2.27±0.02 at LNGS. The LNGS dataset used the muon flux (both energy and angle) parameterization from Mei and Hime for 3.1 km w.e. overburden. Only ∼0.1 % of all simulated muons resulted in at least one activation product.

limit theorem.

The bootstrap samples are then used to build a distribution of the cosmogenic activation rates. Backgrounds that are produced at a rate greater than 1% the ^{137}Xe rate, and have delayed β-decays ($T_{1/2}$ >100 ms) with Q-values or gamma lines above $Q_{\beta\beta}$ are shown alongside ^{137}Xe in Figure 4.8. Note however that ^{64,66}Cu is produced on detector components at the edge of the TPC and are not homogenously distributed throughout the LXe volume. Therefore, they have a much smaller impact than ^{137}Xe on nEXO's overall $0\nu\beta\beta$ sensitivity.

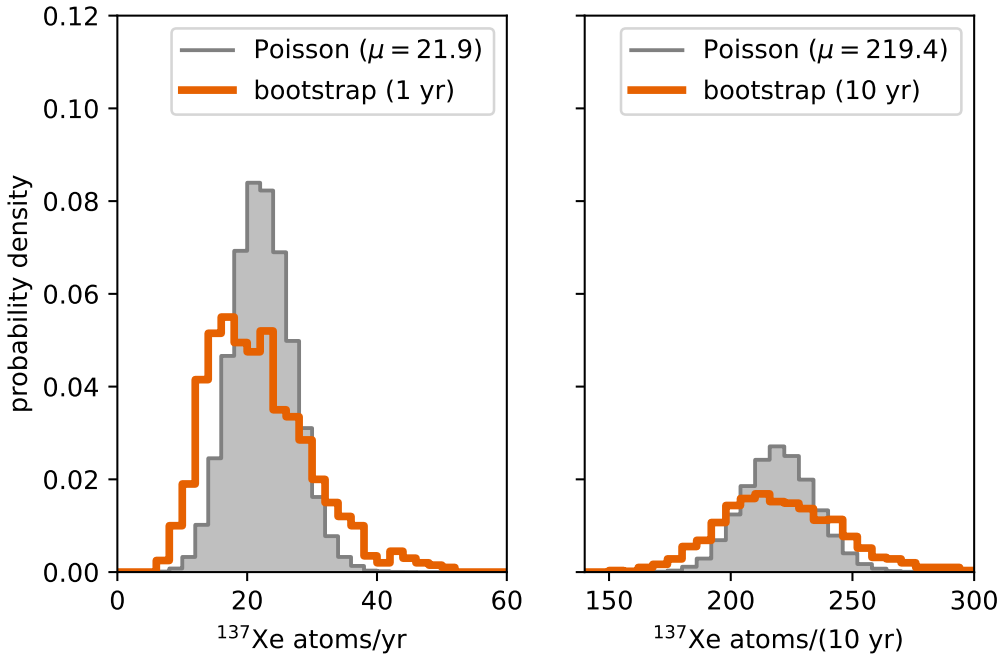

Figure 4.7: Bootstrapped cosmogenic activation rates of ^{137}Xe shown with a reference Poisson distribution of the same mean as the full dataset. The updated nEXO sensitivity code now employs the bootstrapped distributions for sampling a ^{137}Xe background level in the generation of each toy dataset used in the sensitivity calculations. This change more accurately represents the year-to-year variation in the ^{137}Xe background rate compared to a Poisson distribution.

4.4.5 Muon impact parameter

Upon closer study of the muons that produced ^{137}Xe, a few notable muon properties stand out. The first being that muons which produce either secondary or tertiary cosmogenic neutrons have on average a harder energy spectrum compared to those which did not. This implies that deeper sites (which have a higher average muon energy) would produce backgrounds with a higher multiplicity. This effect may be present in the averages of multiplicity distributions shown in Figure 4.6, but seems to be marginal relative to the differences in muon flux between the shallowest and deepest sites in consideration ($\sim$100$\times$

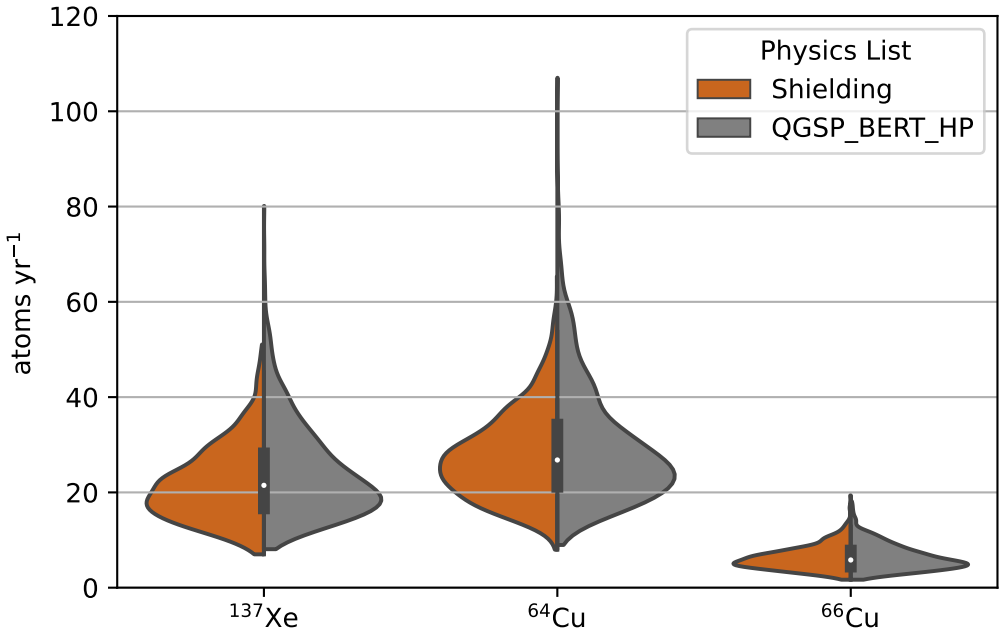

Figure 4.8: Bootstrapped distributions (1000× 1 year trials) of yearly activation rates in nEXO for two standard Geant4v10.5 physics lists. Resulting distributions are coming from a simulation of 2.5×10^6 muons for each physics list ($\sim$ 150 years SNOLAB exposure), with a total xenon mass of 4810 kg, and 537 kg of copper. The white dot denotes the mean activation rate for each isotope from 1000 trials. A boxplot is provided at the center of the violin plots showing the interquartile range and full spread (whiskers) of the underlying distributions. Note that the statistical variation in activation is much larger than the uncertainty in thermal neutron capture cross sections, which in these isotopes are known to better than the 10% level [168]. Hence, the uncertainties are not considered here.

difference between LNGS and SNOLAB). Next, the perpendicular distance of produced secondaries from the muon track demonstrates a steep exponential drop off with a characteristic size scale smaller than the water tank dimensions (see Figure 4.9). So, it was expected that the distance of the muon track to the LXe volume should be investigated, as this might allow for streamlining of optimizations of the muon veto in the next chapter of this thesis.

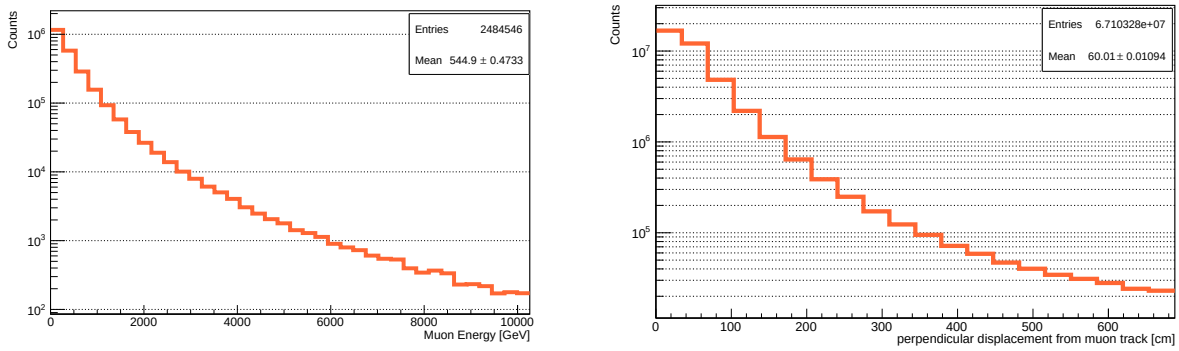

Figure 4.9: Left: energy spectrum of muons in the 150-year shielding dataset which produced secondary particles above 50 keV in the cryostat or TPC, or neutrons of any energy. Notably, these muons have an average energy 183 GeV above the mean muon energy at SNOLAB (362 GeV). Right: perpendicular distance of generated positions of all secondary particles from the muon track in the same dataset, showing a characteristic displacement of ∼1 m as expected from the traverse length scales associated with hadronic showers at these energies.

The perpendicular distance of the muon track to the center of the LXe volume is defined as the muon impact parameter, b. Distributions of b were constructed for events with and without ^{137}Xe production in the TPC (see Figure 4.10) revealing a clear effect of muon impact parameter on background production, which has also been noted by other experiments at SNOLAB [182].

Lateral and longitudinal spread of cosmogenic muon showers has been explored in Super-Kamiokande [187–189]. The main findings, summarized in [190], are that:

1. Almost all spallation backgrounds are associated with muon showers, and are a result of secondary particles from these showers and not the muons directly.

2. Muon showers are rare, and so their occurrence and localization can be used to define background rejection algorithms.

3. Almost all isotope-producing showers (e.g., those leading to neutron captures) are produced in hadronic showers.

We notice that the characteristic perpendicular distance from a muon track, for all secondary particles, in the 150-year SNOLAB dataset for the shielding physics list is $\sim$ 1 m; consistent with the expected transverse spread of hadronic showers for muons at energies of 100's of GeV as demonstrated in [187].

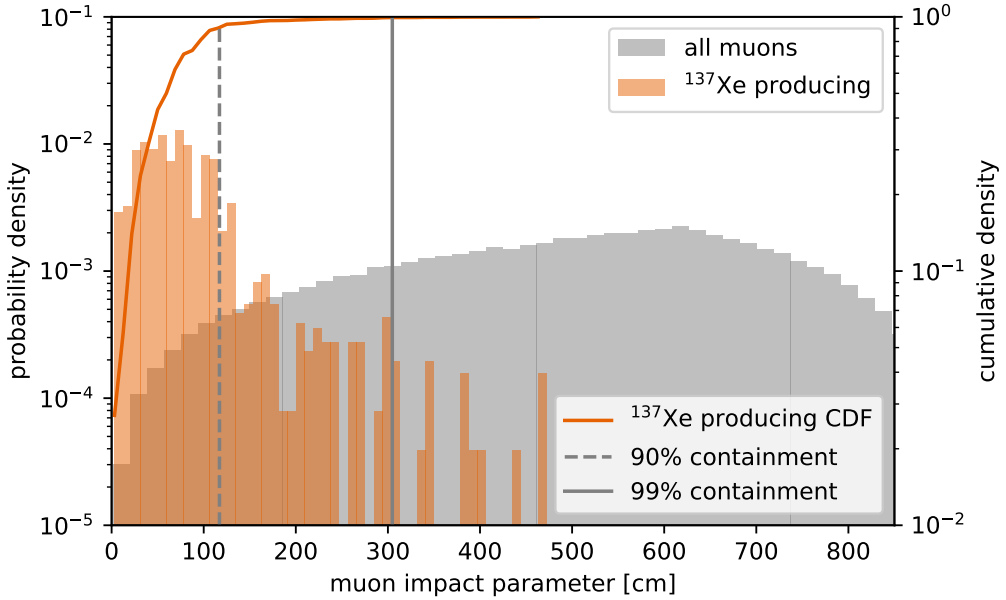

Figure 4.10: Muon impact parameter distributions from the Shielding dataset. The 99% containment for the background-producing muons, as shown by the cumulative density function (CDF) in the figure, occurs at an impact parameter of $\sim$3 m. The grey distribution is the impact parameter distribution of all simulated muons passing through the water tank, whether or not they produce energy deposits in the TPC.

4.5 Cosmogenic background mitigation strategies

In this section, we will overview the different mitigation strategies against cosmogenic backgrounds, assess their various impacts on background reduction, and discuss their relative advantages and limitations. Section 4.9 translates the reduced background contributions into $0\nu\beta\beta$ sensitivities.

4.5.1 Prompt and delayed cosmogenic backgrounds

There are two main categories of cosmogenic backgrounds pertinent to these studies: prompt and delayed backgrounds. Prompt backgrounds produce events in the ROI <1 second after the passage of a muon. In the case of EXO-200, these prompt backgrounds can be seen in the muon veto-tagged dataset of [166] shown in Figure 4.11, appearing $\lesssim$3 μs after a muon passes the TPC. Provided the muon tagging efficiency is sufficiently high, these can be removed almost entirely by vetoing the TPC data stream (in post-analysis) for as long as $\sim$10 ms per muon without much consequence, i.e., amounting to negligible losses in sensitivity due to the reduced livetime (quantified later in Section 4.7.1).

The second category, delayed backgrounds, are the result of neutron activation. Here, the muon passes and produces neutrons that thermalize (100's μs) and then capture on nuclei inside the TPC. The activated isotopes then decay predominantly by β-emission, with half-lives upwards of a minute. Some of these activated isotopes can be produced homogenously in the LXe. In this category, ^{137}Xe is the dominant contributor, with all other delayed backgrounds contributing <1% compared to the ^{137}Xe in the ROI. Hence, ^{137}Xe will be used as a proxy for all other cosmogenic backgrounds throughout the rest of this chapter.

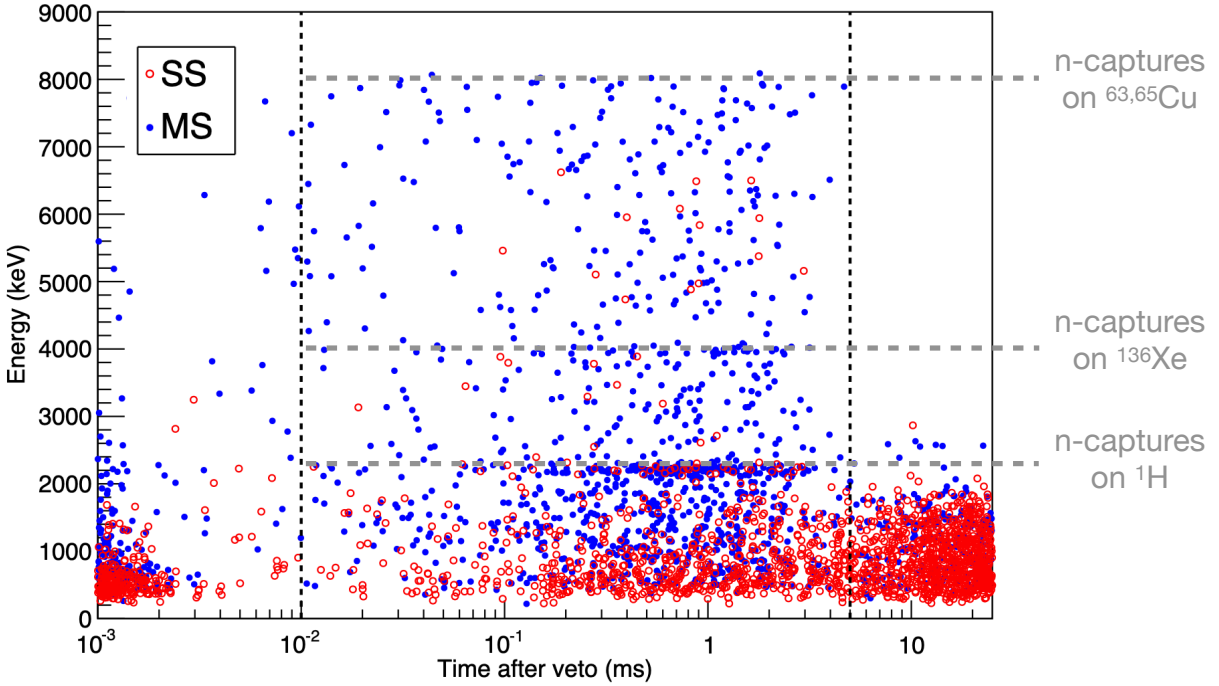

Figure 4.11: EXO-200 muon veto-tagged data showing the timescales of energy deposits in the LXe TPC after a muon veto trigger. Notice the prominent multi-site (MS) events resulting from from neutron capture on hydrogen (2.2 MeV γ-line), ^{136}Xe (4.025 MeV γ-cascade), and the 8 MeV summed γ-energy from neutron capture on copper isotopes. Figure adapted from [166].

4.5.2 Overview of mitigation strategies

Solutions to mitigate cosmogenic backgrounds leaching into the $0\nu\beta\beta$ dataset include:

1. shield against or attenuate the cosmogenic muon and/or neutron flux;

2. add neutron poisons, i.e., isotopes with large neutron-capture cross sections, to particular detector components to preferentially capture neutrons on the added isotopes;

3. tag the muons as they pass nearby the TPC;

4. tag the activation products inside the TPC as they are created.

nEXO will employ some combination of these strategies, as they each have certain limitations that will be quantified in this chapter. The first two solutions are considered passive solutions: their implementation does not affect the overall live time of the experiment, and requires no additional analysis for their evaluation, aside from incorporating the reduced background rate. The active category encompasses the latter 2 methods, and involves the tagging of events and subsequent vetoing of the datastream. The veto length must be chosen carefully, as livetime losses will reduce nEXO's sensitivity to $0\nu\beta\beta$. At some point, the reduction in sensitivity due to livetime loss will outweigh the gain from reduced backgrounds. This veto length can be optimized in data analysis, assuming all events of interest are recorded.

4.6 Passive cosmogenic background mitigation

4.6.1 Shielding against muons and cosmogenic neutrons

The SNOLAB cryopit is nEXO's preferred host site. SNOLAB is the deepest underground clean laboratory barring Jinping mine in China [191] which is 700 m deeper in meters water-equivalent [192], but the mountainous overburden at Jinping yields a total muon flux that is nearly identical to that at SNOLAB [193]. There are no suitable deeper locations as of date. The underground muons at these depths have mean energies in the 100's of GeV and so there is no reasonable possibility to further shield directly against muons to attenuate their flux.

The XENON1T dark matter experiment (located at LNGS, 3.1 km w.e.) has shown that additional water thickness surrounding a xenon TPC can provide some shielding

against muon-induced (cosmogenic) neutrons. However, this effect is not too significant, only reducing the total incident cosmogenic neutron flux by a factor of 10 for every ∼2 additional meters of water shielding [194], and this effect has not been examined as a function of neutron energy. nEXO's water tank dimensions, 12.3 m diameter and 12.8 m height, are nearly at the maximum allowable size given the space available in the SNOLAB cryopit cavern. Hence, there is no feasible option to increase the water shielding enough to make a significant difference in shielding against cosmogenic neutrons. Preliminary studies of the minimal (10 meter radius, 11 m height) versus maximal (12.34 meter diameter, 13.3 m height) water shield dimensions, within the constraints of the cryostat vessel size and the SNOLAB cryopit cavern size, have shown that there is no significant change in the ^{137}Xe rates given an identical exposure to muon fluxes through Target 1 (results of these studies are presented in Appendix C). This result is consistent with the hadronic shower argument outlined in Section 4.4.5: muon-induced neutrons are responsible for activation in the TPC, and these neutrons are produced within a characteristic distance scale of ∼1 m for the muon track. Therefore, additional shielding multiple meters away from the TPC will have a negligible effect.

4.6.2 Neutron poisons

The second passive method is to mitigate the (delayed) cosmogenic backgrounds by preferentially capturing cosmogenic neutrons on isotopes which do not contribute to backgrounds. These additive isotopes can be placed in the LXe itself, or the surrounding materials (water, HFE). Inspired by the NEXT collaborations experimentation with ^{3}He

added in their GXe TPCs to mitigate ^{137}Xe production [195], we considered modifying the isotopic ratio of xenon in the nEXO TPC, as well as adding additional dopants to the heat transfer fluid in the cryostat. An additional 50 kg of ^{124}Xe in the TPC reduces the ^{137}Xe activation rate by a factor of two. Adding boron salts into the HFE at 1% mass concentration provides a similar effect (results presented in Appendix D).

Although the initial results are promising, a feasibility study in terms of cost and chemical stability has not been performed and so these modified isotopic considerations are outside the scope of nEXO's baseline design, but will likely be worth pursuing if TPC-wide vetos are necessary for ∼100 t LXe TPCs in the future. Moreover, we will see in the coming sections that, for LXe TPC with masses in the few tonne range such as nEXO, there are more suitable active mitigation strategies that do not increase engineering risk.

4.7 Active cosmogenic background mitigation

Active mitigation strategies involve the tagging of muons as they pass through the underground cavern, or activation products as they are created within the LXe volume. In both cases, the general idea is to tag an event of interest (muon passage or neutron activation), and veto the subsequent data stream for a period of time. Livetime will be lost in each case, i.e., there will be a reduced exposure to the $0\nu\beta\beta$ candidate isotope (^{136}Xe) which will degrade the sensitivity of the experiment.

In nEXO, the main contributing background motivating these vetos is the ^{137}Xe background (Section 4.3). First, we will examine how nEXO's sensitivity scales with reductions in livetime, and how it scales with reductions in ^{137}Xe rates. Once these scaling

relations are understood, and there is a clear method to optimize veto lengths, we will examine the possibility for a muon veto system and highlight its required features. Finally, we will develop a ^{137}Xe TPC tag, whereby each ^{136}Xe$(n, \gamma)^{137}$Xe event can be identified, and a veto window can be applied.

4.7.1 Sensitivity scaling with livetime

nEXO's overall sensitivity grows quickly within the first couple of years of livetime, but then tapers off as the experiment enters the background-limited regime. In this regime, the sensitivity growth gains a component that scales as:

$$\mathcal{S} \propto \sqrt{Mt}, \tag{4.8}$$

where M is the mass of the target isotope, ^{136}Xe , and t is the livetime of the experiment (see Appendix B.2 for a derivation of the $\sqrt{Mt}$ scaling). The product Mt is referred to as exposure, and commonly expressed in units of tonne-years. We will consider the late-time sensitivity scaling of nEXO sensitivity to livetime, at an exposure of several tonne-years, see Figure 4.12.

We can calculate the expected livetime loss (deadtime) for a given veto length t_v, by the expression:

$$\mathcal{T}_{\text{lost}} = \varphi \times t_v, \tag{4.9}$$

where φ is the expected number of veto windows that are opened during 10 years of runtime, calculated separately for muon tags (Section 4.7.3) and for TPC tags of

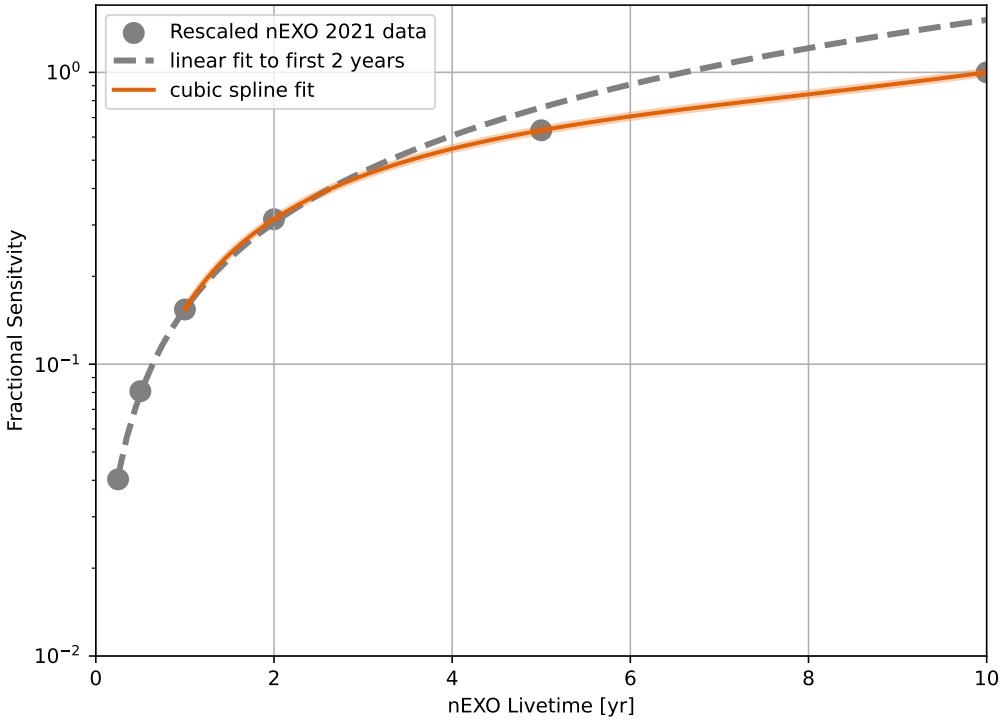

Figure 4.12: nEXO sensitivity as it grows with livetime (exposure). The first 2 years are background-free (i.e., statistical fluctuations of the low background are not contributing significantly), but as the experiment runs longer it obtains a $\sqrt{Mt}$ component. The cubic spline fit for large exposures is what is used in the following analyses. Data is originally published in [25], but the y-axis has been rescaled such that 1.0 in the figure is equivalent to a median halflife exclusion limit of 1.35 $\times 10^{28}$ years (90% C.L.).

^{136}Xe$(n, \gamma)^{137}$Xe processes (Section 4.7.4).

Now, for a fixed experimental runtime (i.e., time the detector is operating, and not necessarily taking low-background data) of 10 years, the sensitivity of nEXO will be reduced in the presence of a veto by a factor:

$$\mathcal{S}_{rv}(t_v) = \frac{\mathcal{S}_r}{\mathcal{S}_{\text{baseline}}}. \tag{4.10}$$

Here, $\mathcal{S}_r$ is the *reduced* sensitivity of nEXO due to livetime losses for a given veto length

t_v, and $\mathcal{S}_{\text{baseline}}$ is the baseline nEXO sensitivity, i.e., the case where $t_v \to 0$ and all the ^{137}Xe remains in the low-background dataset. This reduction in sensitivity is governed by the late time scaling in Figure 4.12. Note that the expression in Equation 4.10 does not account for the *gain* in sensitivity resulting from reduced background as t_v grows (and ^{137}Xe atoms decay before resuming low-background data taking); this sensitivity gain is evaluated in the next section.

4.7.2 nEXO sensitivity scaling with ^{137}Xe

We focus here on ^{137}Xe because it is the dominant (delayed) cosmogenic background, but this technique is applicable to any long-lived background with halflife $T_{1/2}$ that is cosmogenically activated during muon passage.

nEXO's sensitivity analysis strategy (outlined in Section 3.4) is calculated by performing fits on thousands of toy datasets in all three analysis variable (energy, standoff, and topology). Each toy dataset produces a 90% C.L. exclusion limit on the $0\nu\beta\beta$ signal rate. The signal counts are translated into a halflife sensitivity by:

$$\mathcal{S} = \frac{MeN_A}{A}\frac{\varepsilon \ln(2)}{s}t, \tag{4.11}$$

where $M = 3.281 \times 10^6$ is the fiducial mass of LXe in grams, $e = 0.9$ the enrichment fraction of ^{136}Xe, N_A is Avogadro's constant and $A = 135.8$ the average atomic mass of the LXe, t the livetime in years, $\varepsilon = 0.96$ the signal efficiency, and s the number of signal counts.

In Figure 4.13, we present the 90% C.L. limits on the signal rate for different normalization factors of the ^{137}Xe PDF in the background model. The median of each

signal count distribution is then converted into a halflife exclusion limit (presented in [25]). However, the nominal error on the median exclusion sensitivity has not been determined before. In this analysis, we bootstrap each distribution of the 90% C.L. limits on signal rate, to obtain a distribution of calculated median sensitivities using 50% of the toy datasets per trial, and a total of 20,000 trials. The resulting Gaussians (right side of Figure 4.13) can then be used to provide a nominal error on the median exclusion limit on the signal counts. Associated errors are obtained by calculating the halflife sensitivities for the mean $\pm 1\sigma$ of the resulting Gaussians of median exclusion sensitivities. These results are presented in Figure 4.14. Note that there will be additional systematic effects that will broaden the error bands on the presented curve of sensitivity scaling with ^{137}Xe. A proper evaluation of, e.g., the error on the signal efficiency, will be determined with calibration data. Until such calibration data is obtained, we cannot provide a precise assessment of these systematics. However, the shape of the sensitivity scaling curve captures the impact of reduced ^{137}Xe backgrounds. The shape and offset of this curve is not expected to change with the inclusion of additional systematic uncertainties at greater than the few-percent level.

The latest nEXO sensitivity study [25] provides a plot showing how nEXO's sensitivity will scale as a function of the ^{137}Xe background rate in the dataset.[9] We can use this data (Figure 4.14) to interpolate and extract what the improvement factor with a veto will be, which we denote $\mathcal{S}_{iv}$, to what nEXO's sensitivity would be for a fixed 10 year livetime, given

[9]The curve relies on Wilks' approximation [196], which streamlines the sensitivity analysis, especially for larger backgrounds, by avoiding the need to recalculate the critical likelihood ratio test statistic for each toy dataset to obtain a 90% C.L. estimate. While this may overestimate sensitivity at very low ^{137}Xe rates, the curve's shape should still asymptotically approach a limit above the 1.35 $\times 10^{28}$ year bound resulting from the full calculation which does not assume that Wilks' approximation holds. See [153, 197] for more details.

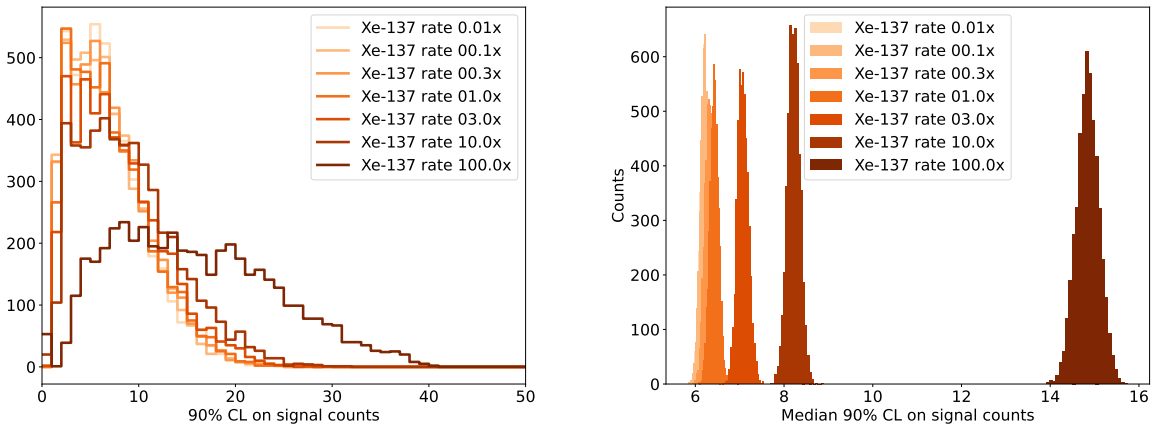

Figure 4.13: Left: 90% C.L. excluded signal count distributions as a function of ^{137}Xe rate scaling, each from 5000 toy datasets. Right: Bootstrapped medians of exclusion limits on the signal counts at 90% C.L., resulting from sampling the left distributions. The mean and 1σ of the Gaussians is then used to obtain a spread on the calculated median halflife exclusion limits, which is typically what is quoted as nEXO's sensitivity to $0\nu\beta\beta$.

some amount of ^{137}Xe in the dataset.

Setting a particular veto length (t_v), allows one to calculate the number of remaining ^{137}Xe atoms in the low-background dataset based on the ^{137}Xe halflife. Thus, a scale factor for the ^{137}Xe background (S_X) relative to baseline for any given t_v is determined. By knowing the trigger efficiency for the veto window, the frequency of correctly opening a veto window, and the frequency of false positives (accidental vetos) one can calculate the total livetime lost for a given t_v. By taking the product:

$$\mathcal{S}_{iv} \times \mathcal{S}_{rv} = \mathcal{S}_v(t_v), \tag{4.12}$$

we obtain nEXO's sensitivity relative to the baseline, $\mathcal{S}_v$, after 10 years of runtime assuming some veto scheme with fixed veto window length. The methods outlined in this section and

the previous one set the stage for how the nEXO muon veto system and ^{137}Xe TPC tag are evaluated.

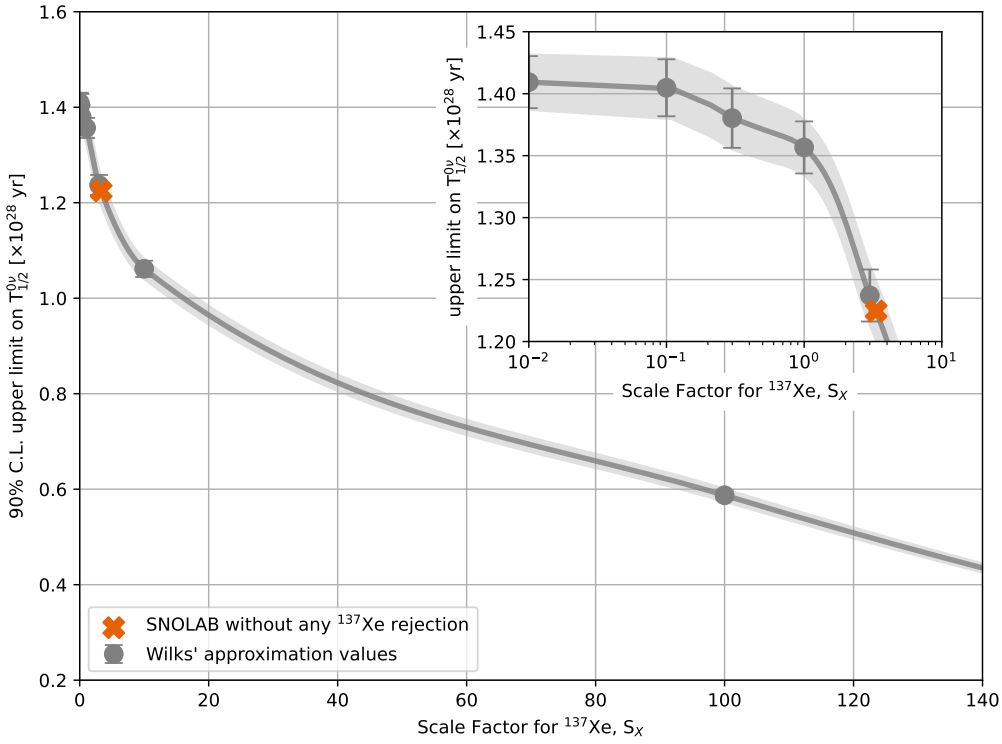

Figure 4.14: nEXO sensitivity scaling with ^{137}Xe rate, shown with cubic spline interpolation. The orange cross shows nEXO's sensitivity at SNOLAB given the background model in [25], without any ^{137}Xe control mechanisms. The inlay log-scales the x-axis for the smallest ^{137}Xe rates, showing a plateau once ^{137}Xe no longer contributes to the background model of nEXO. The error bars are taken as the standard deviation of the corresponding Gaussian, resulting from the bootstrap samples of 90% C.L. limits (Figure 4.13), translated into a halflife sensitivity by Equation 4.11.

4.7.3 Motivation for nEXO's muon veto system

Muon tagging is the standard way in which low-background experiments handle cosmogenic backgrounds. A tag is triggered when a muon passes the experiment, depositing energy in a veto detector. These veto detectors are typically measuring the Cherenkov radiation of muons as they pass through water, scintillation light as it passes through a stack of plastic scintillator blocks, or scintillation light produced in a noble liquid detector. Precise timing of these muons allows for an anti-coincidence rejection window to be started, such that muon-induced interactions can be removed from the low-background dataset. This anti-coincidence window is called a muon veto.

In the case of nEXO, the muon veto time window (τ_{mv}) is expected to be of order $\lesssim$100 ms per muon, which accounts for neutron thermalization time, γ-ray de-excitation cascades, and the majority of subsequent β-decays — all of which are prompt cosmogenic backgrounds.[10] This short veto time τ_{mv} removes the vast majority of cosmogenic backgrounds from the dataset, provided the muon tagging efficiency is sufficiently high.

Recall however that ^{137}Xe has a long halflife of 3.82 minutes, rendering it a homogenous background in the LXe and only loosely correlated to the timestamps of passing muons. Thus, the obvious question to ask is: can the muon veto window, τ_{mv}, be extended to several half-lives of ^{137}Xe, or will the deadtime accrued negate the sensitivity gain resulting from reduced backgrounds? We can answer this question using the information on deadtime and ^{137}Xe scaling relations with nEXO sensitivity (Sections 4.7.1 and 4.7.2).

[10] γ-ray cascades are electromagnetic interactions that have extremely short half-lives of 100's of ns. Typical neutron thermalization times in hydrogenated materials (water, HFE) are 100's of μs, and neutron capture times in LXe have a mean of $\sim$620 μs.

To determine what ^{137}Xe scaling factor (S_X) to use, which will be as a function of τ_{mv}, we first assume an optimal tagging efficiency of 100% for the muon veto.[11] Then, the scaling factor S_X is simply:

$$S_X = \frac{N'}{N} = \frac{1}{2}^{\frac{\tau_{mv}}{T_{1/2}}}, \tag{4.13}$$

where N' is the leftover ^{137}Xe after a veto of length τ_{mv}, and N is the number of ^{137}Xe atoms produced by the muon.

Now, given the muon fluxes through the water tank in Table 4.1, we can estimate the deadtime induced by a muon veto length τ_{mv}. For the ideal case of 100% muon tagging efficiency in the Outer Detector with negligible accidental triggers, we have a trigger rate $\varphi = 46$ muons/day at SNOLAB. Using this trigger rate, we can now estimate the total deadtime after 10 years of operation at SNOLAB to be: $46 \times 365 \times 10 \times \tau_{mv}$, which we can subtract from 10 years to estimate the total loss in exposure for each value of τ_{mv}. Hence, we can obtain the sensitivity loss factor, $\mathcal{S}_{rv}$, as a function of τ_{mv} by reading off the curve in Figure 4.12.

Next, we calculate S_X as a function of τ_{mv} up to 10 half-lives of ^{137}Xe. Then, we extract the sensitivity improvement factor $\mathcal{S}_{iv}$, by interpolating the data in the sensitivity vs ^{137}Xe scaling curve (Figure 4.14). Taking the product of the two curves ($\mathcal{S}_{rv} \times \mathcal{S}_{iv}$) yields nEXO's relative change in sensitivity as a function of τ_{mv}.

We can repeat the above process for the case of perfect muon tracking capabilities in the water tank. In this scenario, we are using the fact that $> 97\%$ of all ^{137}Xe is produced by muons passing within the cryostat volume, which has a radius of 2.23 m (Figure 4.10). Now,

[11] Muon tagging efficiencies for water Cherenkov muon vetos above 99% has been demonstrated in other experiments [194, 198].

reading the flux through the cryostat from Table 4.1, we see that instead of 46 we are now interested in $\varphi = 4.46$ muons/day at SNOLAB. Repeating the same process for this reduced trigger rate, we obtain the dashed curves in Figure 4.15. Repeating this process for the muon fluxes at the shallower sites, we can examine how much the sensitivity will change given the idealized muon trigger conditions, if a longer veto window of length τ_{mv} was opened every time a muon passes as opposed to setting $\tau_{mv} \lesssim 100$ ms.

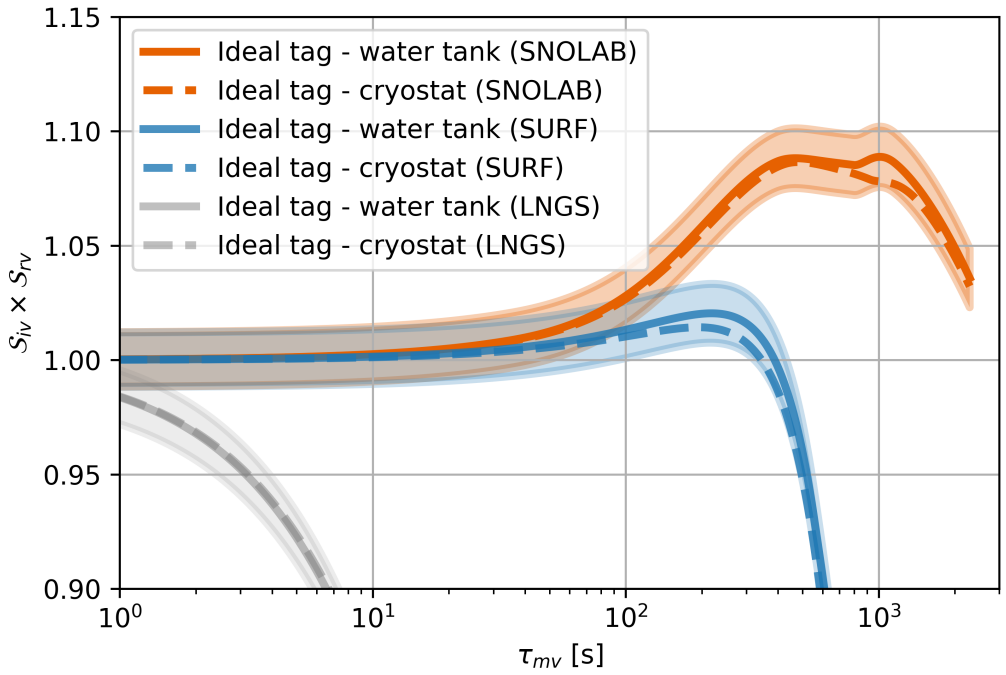

Figure 4.15: Relative sensitivity change for 100% efficient muon tag in the Outer Detector due to balancing of livetime losses and ^{137}Xe rate in nEXO at the different sites under consideration. The shaded region represented the 1σ containment of the median sensitivity improvement factor. Notice that in the case of LNGS, triggering a longer veto window for every muon always results in a loss of sensitivity due to the much higher muon flux. For the deeper sites (SURF and SNOLAB), the improvement is $< 10\%$.

4.7.4 A ^{137}Xe TPC veto

There may be sources of neutrons aside from those that are cosmogenic which activate ^{136}Xe (see Section 4.3). Hence, we require a method to tag and reject ^{137}Xe from the $0\nu\beta\beta$ dataset using the TPC only, regardless of the origin of the neutron that captured on ^{136}Xe.

The basic working principle of the ^{137}Xe rejection algorithm is to tag the ^{136}Xe$(n, \gamma)^{137}$Xe process via the de-excitation γ-rays emitted from nuclear relaxation after neutron capture, and veto the subsequent datastream from the $0\nu\beta\beta$ dataset for several half-lives of ^{137}Xe (τ_{xv}). EXO-200 had a similar veto scheme, and ultimately achieved a rejection efficiency against ^{137}Xe of 21±5% [199]. The previously modelled de-excitation γ-cascade spectra used in EXO-200 analysis [200] will be used in this analysis to estimate a rejection efficiency for nEXO. EXO-200 data will then be used in conjunction with nEXO cosmogenics MC data to obtain deadtime estimates, allowing for a translation of the reduced background contribution and reduced livetime from the implementation of this new veto into a nEXO sensitivity estimate.

To begin our investigation, let us first consider the signatures of ^{136}Xe$(n, \gamma)^{137}$Xe, which will be multi-sited events with summed energies of 4.025 MeV. Recall that due to the long halflife of ^{137}Xe relative to the high LXe flow rates in the TPC, the location of the subsequent ^{137}Xe β-decay is not expected to be correlated with the location of the ^{136}Xe$(n, \gamma)^{137}$Xe event (Section 4.3). Hence, a positive γ-cascade tag will have to trigger a TPC-wide veto for several half-lives of ^{137}Xe; which is why we need to quantify not only the tag efficiency of $\sum E_\gamma = 4.025$ MeV, but also the false tag rate as it will result in additional deadtime, and

therefore a reduced exposure to potential $0\nu\beta\beta$ decays and a reduction in sensitivity.

Event rates and pileup

Cosmogenic muons are highly relativistic, and produce electromagnetic and hadronic showers in a halo around their tracks. Every charged particle in these shower halos can produce prompt energy deposits in the TPC, either via bremsstrahlung γ-rays, or direct transit through the TPC and ionization of the LXe. nEXO is not optimized for operation in a high event-rate environment such as this one, where there are many long ionization tracks throughout the whole TPC. The drift time of charge clouds to the anode can be as long as 700 μs, which is on a similar timescale to the neutron thermalization and capture time of 100's of μs in LXe. This will result in pile-up in the charge readout and will require a complex charge-light matching algorithm (yet to be developed) in order to utilize the charge/light anti-correlation features of nEXO's TPC, i.e., improved energy resolution and position reconstruction.

The nEXO SiPM readout ($\sim$1 μs, as estimated by the digitization rate of 2 MS/s [151]) and LXe light production ($\lesssim$100 ns) timescales are fast compared to neutron capture timescales, rendering it unlikely that multiple neutron capture events will happen in the same acquisition window in the light readout. So, instead of disentangling the mixed charge-light signals in the TPC, the approach we opt for is to use the TPC as a light-only liquid xenon calorimeter, which degrades the position reconstruction and energy resolution in exchange for reduced pile-up rates.

This light-only calorimetric approach has the secondary advantage of measuring energy

deposits in the LXe that are outside the field cage. An effective neutron capture tag requires accounting for all γ-rays resulting from a multi-γ de-excitation cascade. Deposits outside the field cage completely evade detection on the anode, producing a degraded energy spectrum due to the escaped energy of γ-rays that leave the field cage. This degraded spectrum may be more difficult to tag, as we lose the unique $\sum \mathrm{E}_\gamma = 4.025$ MeV identifying feature.

Simulating the ^{136}Xe(n, γ)^{137}Xe process

The γ-cascade spectrum of ^{136}Xe(n, γ)^{137}Xe processes was modelled in [200] and utilized in EXO-200 analyses, it was simulated in nEXO using the standard nEXO physics list [153]. A number of γ-rays are propagated simultaneously from a single point in the LXe volume (corresponding to the location of ^{136}Xe activation), with their energies and multiplicities corresponding to single ^{137}Xe de-excitation event.[12] These gamma rays would then propagate in the LXe, depositing energy throughout the LXe volume via pair production, Compton scattering, and photoelectric absorption processes.

A large dataset of 10^8 neutron capture events on ^{136}Xe was simulated uniformly in the LXe, both internal and external to the field-cage volume. Standard nEXO reconstruction scripts were then used to translate the true MC energy deposits from Geant4 into realistic, reconstructed, light-only energy measurements. A similar process is repeated for several other isotopes, in particular for the neutron captures: ^{63,65}Cu(n, γ)^{64,66}Cu in the TPC, field rings, and cathode, as well as ^{19}F(n, γ)^{20}F and ^{1}H(n, γ)^{2}H in the HFE cryofluid. The de-excitation capture cascade spectra for each isotope utilized the same model used in EXO-200

[12] This is encoded in the `RandomGammas` model of `Generate_nCapXe136()` of `nEXOPrimaryGeneratorAction.cc`.

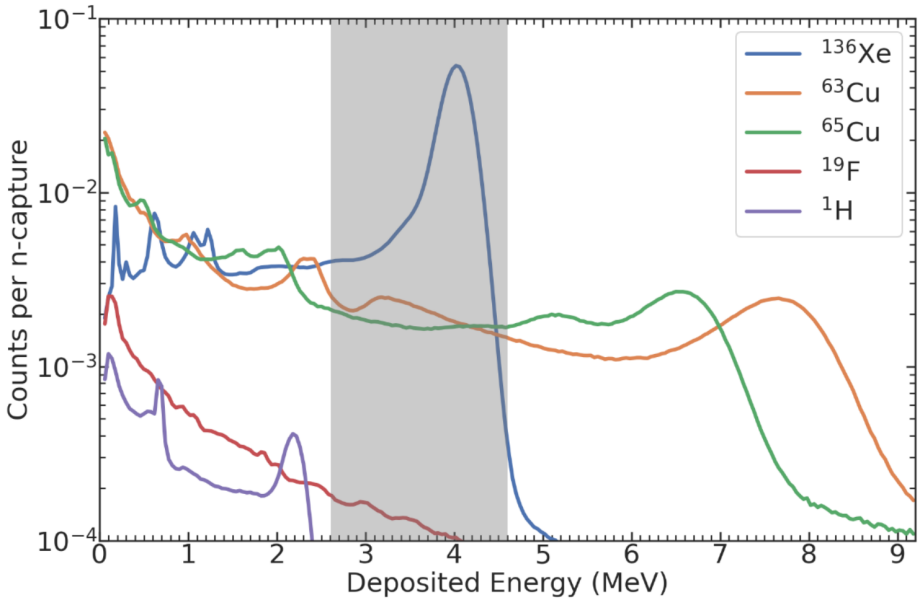

Figure 4.16: De-excitation γ-spectra of nuclei after neutron capture as measured by the TPC after smearing by light-only reconstruction algorithms of nEXO. The grey shaded region represents the selection window for tagging ^{136}Xe activation events in the TPC using a light-only analysis. Figure adapted from [201].

analyses [166]. A total of 10^8 capture events were simulated for all isotopes, except copper, for which 10^7 captures were simulated for each of the two isotopes. The light-only reconstructed energy spectra for these neutron-capture de-excitations are shown in Figure 4.16.

Overall rejection efficiency and handling ^{137}Xe multiplicity

Because cosmogenic ^{137}Xe is produced with a mean multiplicity greater than 1, we are actually more likely to tag $^{136}\mathrm{Xe}(n,\gamma)^{137}\mathrm{Xe}$ events than one would expect from simple efficiency measurement of 4.025 MeV deposits. This combinatoric advantage allows us to remove multiple potential ^{137}Xe background deposits with a single veto window.

To account for this effect, we first decide on what energy deposit should constitute a $^{136}\mathrm{Xe}(n,\gamma)^{137}\mathrm{Xe}$ tag. Lowering the threshold to 2.6 MeV (above the smeared capture line

of neutrons on hydrogen of 2.2 MeV, and at the upper edge of the primordial ^{238}U/^{232}Th gamma spectra) and the upper bound fixed 4.6 MeV (the smeared upper bound of the ^{136}Xe$(n,\gamma)^{137}$Xe de-excitation γ-cascade) we obtain a conservative detection efficiency of 70% per neutron capture, with a 9% chance to trigger off of the copper isotopes (see grey shaded region in Figure 4.16).

The tag efficiency ϵ against cosmogenic ^{136}Xe$(n,\gamma)^{137}$Xe processes is then:

$$\epsilon = 1 - (1-p)^N, \tag{4.14}$$

where $p = 70\%$ is the probability to tag a single ^{136}Xe$(n,\gamma)^{137}$Xe event, and $N = 2.36 \pm 0.14$ is the average multiplicity of ^{136}Xe$(n,\gamma)^{137}$Xe; i.e., the number of neutrons capturing on ^{136}Xe from a single muon passage, if any neutrons capture on ^{136}Xe at all (the full distribution of multiplicities was shown in Figure 4.6). Thus, for the [2.6, 4.6] MeV energy window per ^{136}Xe$(n,\gamma)^{137}$Xe de-excitation γ-cascade we calculate an overall tag efficiency of cosmogenic ^{136}Xe$(n,\gamma)^{137}$Xe to be $93.7^{+1.0}_{-1.1}$ % due to the effect of cosmogenic ^{137}Xe multiplicity.[13] The overall expected cosmogenic rejection efficiency (i.e., ability to remove ^{137}Xe from the low-background dataset) is then:

$$R_{\text{Xe-137}} = \epsilon(1 - \frac{1}{2}^{\frac{\tau_{xv}}{T_{1/2}}}), \tag{4.15}$$

where τ_{xv} is the time for which the datastream will be vetoed, $T_{1/2} = 3.81 \pm 0.15$ minutes is the halflife of ^{137}Xe, and $\epsilon = 93.7^{+1.0}_{-1.1}$ % is the tag efficiency ^{136}Xe$(n,\gamma)^{137}$Xe events as calculated in Equation 4.14. For the purposes of this thesis, τ_{xv} is fixed at 25 minutes and

[13] In the case of radiogenic neutron capture, which will likely arrive with a multiplicity of 1, the rejection efficiency is simply 68%, with negligible accidental coincidences, for a trigger window of [3, 4.6] MeV — where the lower bound is now above all primordial gamma lines in the ^{238}U and ^{232}Th series.

corresponds to 6.5 halflives of ^{137}Xe.

False neutron-capture tags and correlations with other isotopes

To obtain a handle on the rate at which other isotopes trigger the TPC veto and add deadtime without removing ^{137}Xe, a toy MC was developed that utilized the cosmogenic multiplicity information of ^{137}Xe alongside its correlations with other isotopes that deposit significant γ-energy in the LXe upon neutron activation. We limit ourselves to a discussion for a ^{136}Xe$(n, \gamma)^{137}$Xe TPC tag window of [2.6, 4.6] MeV, the most conservative scenario.[14]

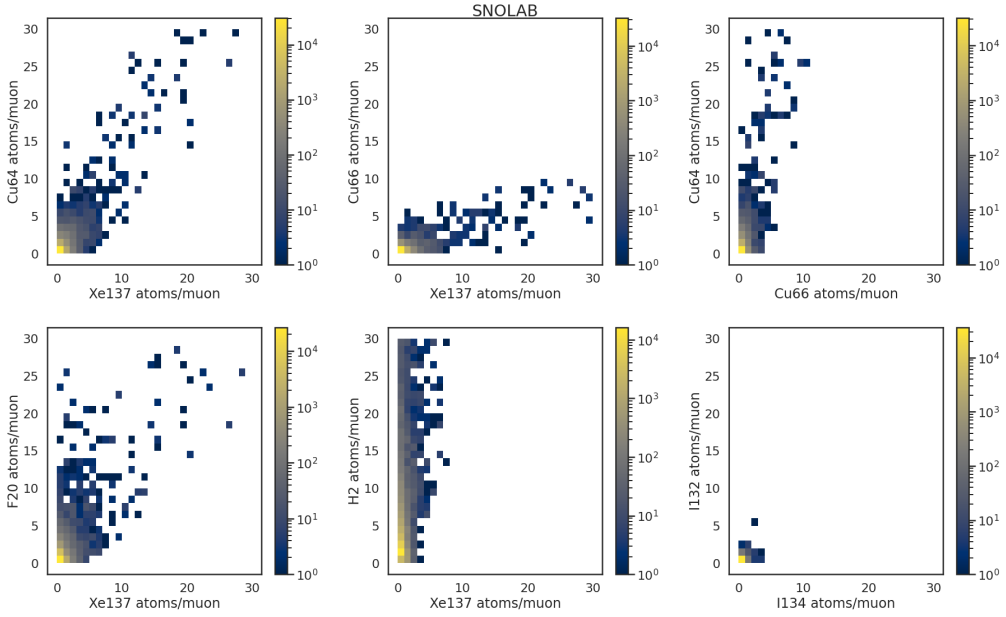

Figure 4.17: Activation correlations at SNOLAB. Each entry in these 2D histograms come from a single muon event. Notice that ^{137}Xe production is loosely correlated with neutron activation of copper isotopes in the TPC. Analogous histograms for alternative underground sites can be found in [202].

The toy MC first samples from the ^{137}Xe multiplicity distribution (previously shown in

[14]The activation events and their correlations cannot be simulated directly from a muon simulation to obtain a deadtime estimate, as the probability to create ^{137}Xe (dominant) per muon through the water tank is $(4.28 \pm 0.08) \times 10^{-4}$.

Figure 4.6), giving the number of ^{137}Xe created in this event. Then, it samples from the correlation plots shown in Figure 4.17, to obtain the total number of neutron activations for every other isotope that may be produced in conjunction with ^{137}Xe.

Treating each activation process (i.e., the (n, γ) de-excitations for any isotope) as an independent trial,[15] we then calculate the probability of triggering a veto window of length τ_{xv}. If a veto window is opened, one unit of $\tau_{xv} = 25$ minutes is added to a counter, and the amount of ^{137}Xe left is calculated by throwing a random number $r \in [0, 1]$ for every ^{137}Xe produced. If $r > R_X$ (the rejection efficiency of Equation 4.15), the atom is considered to have not been rejected and remains counted in a final 10 year dataset. This process is repeated until the number of activation events simulated corresponds to 10 years of nEXO operation (runtime).

The additional deadtime due to false coincidences (in the absence of ^{137}Xe activation) is estimated from the efficiency of ^{63,65}Cu activation to trigger a veto window of length τ_{xv} for a light-only energy [2.6, 4.6] MeV, which is ∼9%. This deadtime is obtained from the correlation plots, for ^{137}Xe and the ^{63,65}Cu isotopes, where the number of ^{137}Xe atoms is zero (first column of the upper left and upper middle panel of Figure 4.17). Knowing the muon flux in 10 years at SNOLAB passing through the water tank, we translate the activation rates and their correlations to an additional deadtime, which is added to the running sum of τ_{xv}.

This whole process is repeated for 10,000 trials where each trial is considered a 10 year runtime experiment of nEXO, producing a mean number of ^{137}Xe atoms before and after a

[15] Recall, in the light-only calorimetric approach we treat each neutron capture as an independent trial and can neglect pileup due to the light readout time being much faster than the neutron capture times.

the light-only veto window of $\tau_{xv} = 25$ minutes is applied. A summary of results is presented in Table 4.2.

	Mean ^{137}Xe activation [atoms/yr]	Mean untagged ^{137}Xe (70% tag eff. / ^{136}Xe activation)	Mean deadtime [days/(10 years)]
SNOLAB	18	2.2	1.3
SURF	265	31	-
LNGS	1700	199	120

Table 4.2: ^{137}Xe activation rates before and after TPC tag for the three sites in consideration. SURF did not have a deadtime estimate calculate directly because a toy MC for SURF was not performed. The presented results for SURF are the SNOLAB results rescaled by the ratio of the respective muon fluxes of both sites (~ 16).

4.8 An overview of spallation backgrounds

Spallation backgrounds include those which are produced in particle interactions other than muon-induced neutron capture. These backgrounds include those that come from the removal of nucleons and α particles from xenon (producing iodine and tellurium isotopes), and charge exchange reactions such as p+^{136}Xe $\rightarrow$ ^{136}Cs+n. These backgrounds do not necessarily produce signals that have been well modelled in the context of the nEXO TPC, and may contribute additional backgrounds in the signal region and therefore their production rates must be quantified.

From the nEXO assessment of alternatives site selection study [201, 202], the total (unvetoed) rate of the sum of all spallation backgrounds in the single site nEXO ROI (i.e., events with low DNN discriminator values which are β-like), scaled from the KamLAND cosmogenics results published in [203], is $\sim$25% the rate of single site ROI events from

^{137}Xe after implementation of the TPC veto (Table 4.2). This is due to the fact that the majority of spallation backgrounds are positron emitters, which have a low single-/multi-site fraction in the nEXO TPC (the SS/MS fractions in the EXO-200 TPC for positrons in the 1–3 MeV range is $\lesssim$1.4%). Thus, we can use the scaling curve for nEXO's sensitivity as a function of ^{137}Xe (Figure 4.13) as a proxy to quantify the effect of any unaccounted for spallation backgrounds. Since the spallation backgrounds are produced at a rate of 25% of the remaining ^{137}Xe rate, we can increase the ^{137}Xe rate in the dataset by a factor of 1.25 to evaluate the impact this would have on nEXO's sensitivity. At SNOLAB, the $0\nu\beta\beta$ sensitivity of nEXO is $1.37(2)\times10^{28}$ yr after implementation of the TPC tag. Increasing the ^{137}Xe background level by 25% produces a sensitivity consistent with this value. Hence, the two sensitivities for SNOLAB are consistent whether or not we include the additional spallation backgrounds after the TPC veto is implemented. This is not true for the other sites under evaluation, where varying the ^{137}Xe background factors of 1.25 produces a measurable change in sensitivity due to the much higher ^{137}Xe contribution to the overall background of nEXO at that site, even after implementation of the TPC veto.

A complete list of all cosmogenically produced isotopes in nEXO is provided in [167]. Those that are produced at a rate greater than 1% the ^{137}Xe rate and can potentially produce backgrounds in nEXO were included in the toy MC correlation analyses (Figure 4.17) during the nEXO assessment of alternatives site selection study.[16]

[16]The rescaling of KamLAND results was done by Brian Lenardo, and the estimate of the SS/MS fraction of positrons by Seth Thibado.

4.9 Impact of cosmogenic backgrounds on the $0\nu\beta\beta$ sensitivity of nEXO

Ultimately, nEXO's sensitivity to $0\nu\beta\beta$ depends on its exposure to $0\nu\beta\beta$ decays, as well as the number of background events in the ROI. Throughout this chapter, we have been focusing on the cosmogenic ^{137}Xe background component, the dominant muon-induced background of concern. We will address now the impact of the primary tool against ^{137}Xe that we have in our arsenal, the ^{136}Xe$(n, \gamma)^{137}$Xe TPC tag, on the overall sensitivity of the experiment.

For each toy MC trial, a given level of ^{137}Xe remains in the dataset after 10 years with the TPC tag applied. Moreover, there is a given amount of deadtime accumulated. The minimum deadtime (deadtime from positive ^{136}Xe$(n, \gamma)^{137}$Xe tags only) has a marginal effect at all sites, as the deadtime estimates are $< 3.3\%$ after 10 years of runtime even at the shallowest site with the highest muon flux, LNGS. The additional deadtime accumulated due to accidental coincidences with other studied isotopes, e.g., neutron activation of copper, is $<6\%$ across all sites. Given the scaling relations of nEXO sensitivity to ^{137}Xe background level (outlined in Section 4.7.2) we can estimate what the sensitivity will be after applying the light-only TPC tag. Results are presented in Figure 4.18.

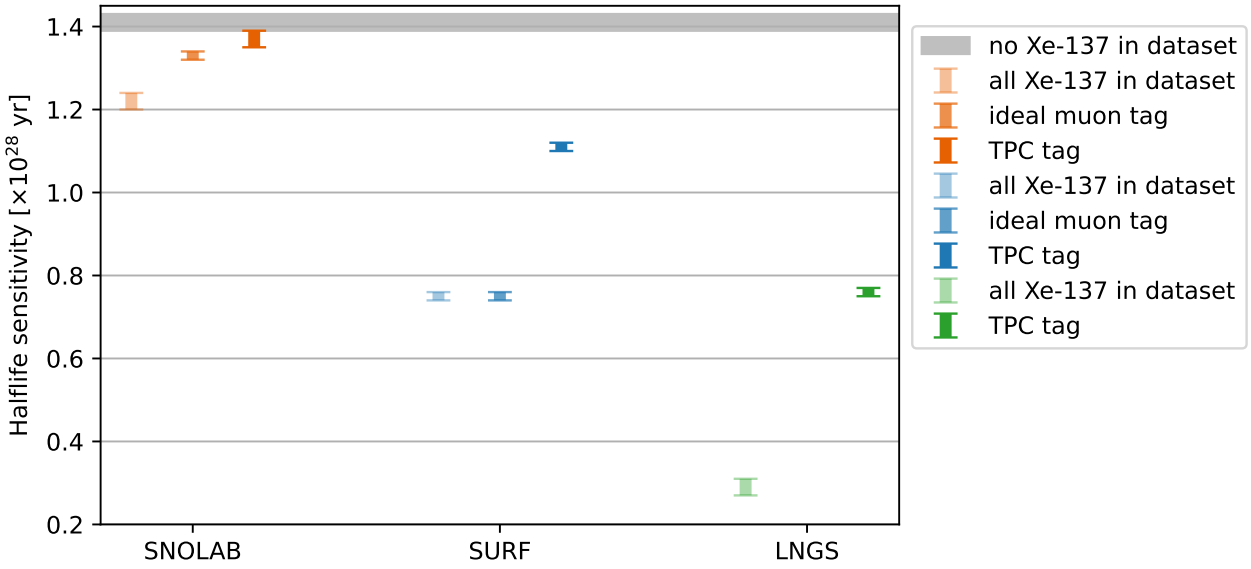

Figure 4.18: nEXO sensitivity at different underground locations. TPC tag refers to the results of the Toy MC outlined in the text for 70% tag efficiency per ^{136}Xe$(n, \gamma)^{137}$Xe event. The ideal muon tag is the optimum improvement for each site from the Outer Detector trigger alone (Figure 4.15).

4.10 Summary

We have demonstrated that nEXO will have a rejection efficiency of 88% against cosmogenic ^{137}Xe for all three sites in consideration (Table 4.2), and that the method of tagging activation events in the TPC is superior to vetoing for long periods of time after the passage of every muon through the Outer Detector. This is because the probability for a hadronic shower to occur near the TPC is sufficiently low at $\lesssim$0.1% compared to all muons passing the water tank. To obtain these estimates, we developed a toy MC to sample the underlying distributions coming from raw Geant4 MC simulations, capturing the variability in ^{137}Xe activation multiplicity from muon shower events. We have accounted for the deadtime accrued from the proposed light-only ^{136}Xe(n, γ)^{137}Xe tag in the TPC, and that of false-coincidences from other spallation backgrounds. Sensitivity estimates were then obtained by combining studies on livetime and ^{137}Xe scaling of the low-background dataset. Bootstrapping the underlying exclusion limits of signal counts from the Asimov datasets in the ^{137}Xe scaling and livetime studies were used to provide a 1σ bound on the median excluded halflife of $0\nu\beta\beta$. This showed that for SNOLAB, any further improvements to the ^{137}Xe rejection will make the experiment consistent with a version of nEXO without any ^{137}Xe in the dataset (Figure 4.18). For nEXO to exceed the 10^{28} yr halflife exclusion limit goal at LNGS, the use of additional passive mitigation strategies will likely be required. These strategies include changing the isotope ratios in the TPC, or doping the heat transfer fluid with neutron poison.

4.11 Discussion and future work

During these studies, the activation processes (e.g., ^{136}Xe(n, γ)^{137}Xe) and the production rates of isotopes were studied in separate simulations. This is because the ability to use NEST (correctly producing scintillation and charge quanta in the LXe) and the Shielding physics list is currently not compatible in `nexo-offline`. Furthermore, if there is a way to override the default γ-cascade models in Geant4 to those measurements of EXO-200 then a more realistic understanding of the high-rate environment in the TPC after a muon shower event can be obtained, and more directly compared to data to constrain the correlations and cross sections of various spallation processes on xenon nuclei.

Utilizing characteristic γ-lines (or summed γ-cascade energies) could be used to reduce all spallation backgrounds independently, as opposed to applying a blanket 25 min veto following a muon passage through the TPC. Here, we have only searched specifically for ^{137}Xe activation with its summed 4.025 MeV γ-cascade energy deposited in the LXe. But, there is a persistent 600 keV γ-line associated with the ^{136}Xe(n, γ)^{137}Xe cascade. This γ-line can be searched for in the charge readout of nEXO as a 600 keV cluster of some characteristic radius. This cluster will then identify a ^{137}Xe activation event with high probability, provided the cluster is isolated and that other spallations do not also produce this identifying feature. Similar methods can be used to identify other spallation products in nEXO, and in larger future LXe experiments. The veto window corresponding to each of these identifying γ-lines can then be tuned and optimized independently of one another.

In future $0\nu\beta\beta$ searches employing 10–100 t of LXe the results of these studies should be considered. For example, a 50 tonne LXe TPC will be larger in size by a factor $10^{1/3} \approx 2.15$

compared to nEXO, having a characteristic length scale of almost 3 meters. This is now larger than the length scales associated with hadronic showers for mean muon energies at the deepest underground laboratories, and the homogenous distribution of ^{137}Xe activation throughout the detector may need to be reinvestigated. Furthermore, the long halflife of ^{137}Xe coupled with the large fluid velocity in the nEXO TPC meant that the ^{137}Xe veto needed to be TPC-wide (as opposed to producing temporary fiducial cuts) which resulted in lost livetime. This will not be significant for nEXO at SNOLAB, but a future $0\nu\beta\beta$ detector may have to address this problem more carefully since a larger TPC diameter would mean muons from further away from the LXe center can produce spallation backgrounds of concern.

Although not presented in this thesis, ongoing FLUKA simulations by nEXO collaborators show that mean activation rates of ^{137}Xe at SNOLAB match those from the Geant4 `Shielding` dataset. However, the spread in yearly activation rates determined with FLUKA is larger, which may improve the rejection efficiency estimate from these studies if the additional spread can be attributed to higher ^{137}Xe activation multiplicity, and lower per-muon production rates of ^{137}Xe. Impact parameter distributions from both Geant4 and FLUKA are so far consistent with each other. Results from the KamLAND spallation study [203] suggest that FLUKA cross sections for spallation interactions around A=136 may be higher than reality by 10–20 %. Once nEXO is online, a similar study to that from KamLAND can confirm this and cross-check against Geant4 Shielding cross sections. Another note is that the charge ratio of muons (Section 4.4.2) in both the FLUKA and Geant4 studies from nEXO is left constant at 1.25, but this can have some energy dependence [183], and additional μ^- at the shallower sites can produce more

captures; as muons that are negatively charged can capture on atomic nuclei and produce additional neutrons. However, for them to be capture on nuclei they must first come to rest, which is more likely at the shallower sites such as LNGS where the average muon energy is lower and the overall muon flux is higher.

Finally, the precise optimizing of the prompt veto window and the TPC tag window has not been done for nEXO as it is unlikely to make a significant difference to the sensitivity at SNOLAB based of the ^{137}Xe scaling curve. This may be revisited once a nEXO muon veto-tagged dataset is obtained.

Chapter 5

Development of a Water-Cherenkov Muon Veto for nEXO

This chapter outlines the objectives of the nEXO Outer Detector (OD): a large water radiation shield and Cherenkov detector. Here we will develop simulations of cosmogenic muons passing through the OD, and assess the muon detection efficiency for various photomultiplier tube (PMT) configurations and trigger conditions. Throughout this chapter, nEXO will be considered to be located in the cryopit at SNOLAB. This allows us to use the findings of Chapter 4 to guide these studies, and develop the muon veto system.

5.1 Objectives of the nEXO Outer Detector

The nEXO OD serves two purposes: to shield the inner TPC vessel against external radiation backgrounds and to tag muons passing near the TPC with high efficiency. The latter enables the vetoing of prompt cosmogenic backgrounds, and allows for coincidence tagging of $^{137}\mathrm{Xe}(n,\gamma)^{137}\mathrm{Xe}$ events in the TPC triggering a longer veto (Section 4.7.4),

which improves ^{137}Xe background rejection while minimizing deadtime losses. We begin by addressing the first objective, radiogenic shielding.

5.1.1 Radiogenic background shielding

The nEXO OD must be designed such that backgrounds in the ROI (defined in Section 4.1) coming from the OD instrumentation (water tank, cabling, PMTs, and the water itself) and backgrounds from the external environment (rock, concrete, and experimental hardware in the cavern) are both considered negligible; i.e., account for <0.01% of the total background. There are two kinds of external radiation we must be wary of due to their penetrating power through water at ∼MeV energies (typical energies of natural nuclear interactions): neutron and gamma radiation.

In the case of neutron radiation, radiogenic neutrons come from spontaneous fission and (α, n) interactions in the rock, concrete and shotcrete. At SNOLAB, about half the neutrons are thermal with a flux 4000 neutrons/m^2/day entering from the surfaces of the cavern, and the other half of the neutrons have energies that are epithermal extending up to 10 MeV. Water thicknesses larger than a few meters will shield against all of these neutrons, as the hydrogen in water is an excellent neutron moderator.

For shielding against γ-radiation, the dominant contributing γ-lines affecting the $0\nu\beta\beta$ search are those emitted in the decays of ^{214}Bi and ^{208}Tl, with the latter being dominant. The γ-rays of ^{208}Tl (2.617 MeV) will enter the water tank at SNOLAB at a rate of about 500 kHz in total based off their surface flux density on the cryopit walls (Appendix C.1.1). These two primordial γ-lines also happen to be at the upper end of the

primordial gamma energy spectrum and, in the case of ^{208}Tl, the line intensity is strong enough such that when it Compton scatters electrons that are above Cherenkov-threshold velocity in water, a non-negligible amount of visible light will be produced. This will limit the trigger conditions of the OD system, as the DAQ trigger conditions and thresholds will need to be tuned to minimize non-muon triggers to avoid saturation. The minimum required size of the OD to sufficiently shield against the ^{214}Bi and ^{208}Tl γ-lines coming in from the cryopit walls is a height of 11 m, and a radius of 5 m, which is also sufficiently large to shield against all other potential γ-background sources outside the cryostats, e.g., the PMTs, cabling etc... More details on the shielding constraints of the OD size can be found in Appendix C, and the nEXO internal reports [204–207].

5.1.2 Muon tagging & cosmogenic background rejection

nEXO will inherit ∼600 Hamamatsu R5912 PMTs from the Daya Bay neutrino experiment to be used to detect the Cherenkov radiation of muons passing through the water.[1] Some fraction of the 600 PMTs that meet the operational standards for nEXO will be installed on the water tank surfaces. We plan to read out these PMTs using CAEN VX2740 digitizers [210], providing 8 ns time binning, appropriate for the R5912 rise times of $\sim$ 5 ns. These PMTs will be inward facing, and distributed throughout the OD surfaces inside the water.

The main purpose of the muon veto system will be to tag muons of interest (those with low impact parameter) at high efficiency. A muon veto of τ_{mv} =10 ms can be applied to the low background dataset of nEXO, enabling the rejection of all prompt cosmogenic backgrounds.

[1] The Daya Bay PMTs are described and modelled in [208]. Reference [209] provides a model-independent way to estimate the s.p.e. energy resolution of PMTs if needed in future work.

The secondary purpose of the muon veto system is to allow for coincidence searches of a muon tag in the OD with a ^{136}Xe$(n,\gamma)^{137}$Xe tag in the TPC, a [2.6, 4.6] MeV light-only tag (Section 4.7.4). This coincidence between the muon veto and the TPC is required to lower the threshold of the ^{136}Xe$(n,\gamma)^{137}$Xe tag below 3 MeV (radiogenic gamma lines and $2\nu\beta\beta$ decays of ^{136}Xe continuously produce signals in the TPC <3 MeV). Searching for signals below 3 MeV is necessary for more elaborate rejection algorithms against ^{137}Xe and other cosmogenic backgrounds. Thus, these coincidences of muon tags in the OD and light-only measurements in the TPC will initiate a longer veto window of $\tau_{xv} = 25$ minutes, 6.5 half lives of ^{137}Xe, maximizing ^{137}Xe rejection and minimizing deadtime losses.

5.2 Design criteria for the muon veto system

We can determine the required tagging efficiency of the OD by examining how nEXO's sensitivity to $0\nu\beta\beta$ varies as a function of the allowed ^{137}Xe background (calculated previously in Section 4.7.2). After implementing the TPC tag, nEXO at SNOLAB is already very close ($\sim 1.4\sigma$) to the ^{137}Xe-free regime (shown in Figure 4.18), and other cosmogenic backgrounds contribute negligible amounts to the background relative to ^{137}Xe (Section 4.8). Hence, we set a benchmark requirement of a muon tagging efficiency of >95% for muons that tend to produce cosmogenic backgrounds.

The distance of closest approach of a muon to the center of the TPC, referred to as muon impact parameter, was found to be correlated to the frequency of ^{137}Xe production. Muons passing within 3.35 meters of the LXe have a tendency to produce ^{137}Xe at a much higher rate, accounting for over 99% of cosmogenic ^{137}Xe production (shown in Figure 4.10). This

3.35 m distance scale is consistent with the transverse scale of hadronic showers from muons with energies in the 100's of GeV [187]. Since all spallation-based backgrounds (prompt and delayed) are produced in hadronic showers, we optimize the OD to tag muons with impact parameters <3.35 m away from the LXe volume. Thus, we refine our benchmark: the nEXO OD should achieve a muon tagging efficiency of >95% for muons with impact parameters <3.35 m, roughly 1 m radially outward from the cryostat-water interface.

There is an expected PMT failure rate of 2% per year.[2] During nEXO's 10–12 year operation, this amounts to a total of $(0.98)^{10} \approx 80\%$ of PMTs that are expected to still be operating normally at the end of the experiment. Thus, a buffer of 30% more PMTs will be installed over what is required to achieve satisfactory muon tagging capabilities.

The maximum OD size due to engineering constraints is limited by the size of the SNOLAB cryopit, subtracting about 1.5 m radially for maintenance and construction access. The minimum size is set primarily by the passive shielding against ^{208}Tl γ-rays coming in from the rock surrounding the water tank (Appendix C.1.1, references [204–206]). As currently designed, the OD is 12.8 m in height, including a 30 cm nitrogen buffer gas region to prevent radioactive mine air from entering the water. The diameter of the OD is 12.3 m. The tank will be constructed from stainless steel, and filled with 1.4 kilotonnes of ultra-pure water.

[2] From internal communication with Daya Bay scientists.

5.3 Geant4 simulations of the muon veto

The R5912 PMTs were modelled in Geant4 as hemispheres with an 8" radius made up of borosilicate glass layer, and a thin photocathode surface. The photocathode surface was backed by a thin opaque layer of aluminium as to not allow photons entering the back of the glass to register as a hit. The PMTs were distributed uniformly in area over the surfaces of the OD. This was done by taking the total area of the water tank surfaces and dividing it into three components: ceiling, cylindrical wall, and floor. The number of PMTs on each component was distributed based on the ratios between the surface areas of the three components. Once the number of PMTs was decided, the approximate linear grid-spacing between them was taken as the square root of the PMT-to-surface-area fraction for each surface component, i.e., the wall, ceiling or floor. The simulations were initially done assuming a 500 PMT maximum, so to make the equal-spacing algorithm work with an integer number of PMTs, a total of 472 PMTs were algorithmically placed in the baseline 'uniform' configuration. These PMTs provide a photocoverage area of 0.44 % for every 100 PMTs installed, as calculated based off surface areas of the 8" PMTs and the tank surfaces only. This baseline arrangement of PMTs is shown in Figure 5.1.

Simulation details and optical properties

The water's refractive indices were set to those from [211], scattering lengths from [212], and absorption lengths were taken from [213]. Although, the latter two numbers are not expected to impact the performance of the muon veto significantly for any reasonable water

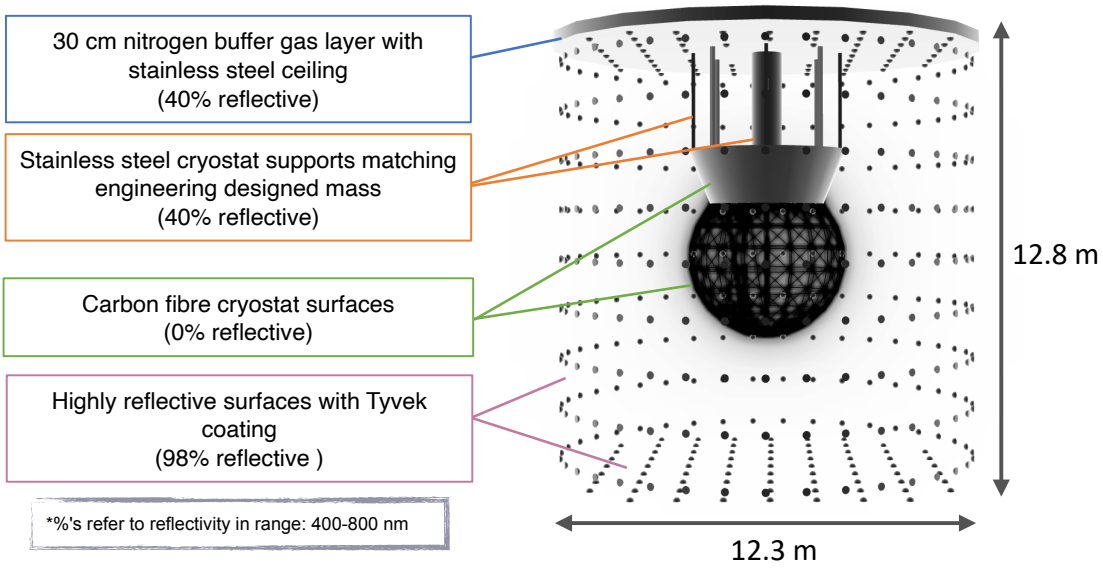

Figure 5.1: Outer detector geometry in Geant4 with 472 8" hemispherical PMTs.

quality.[3] The quantum efficiency of the PMTs was obtained via private communication with Daya Bay scientists and cross checked with that from the R5912 datasheet [215].

The baseline design employs a reflective coating on all the outer surfaces of the OD in direct contact with the water (cylindrical wall, floor). This is presumed to be similar to [194, 198] (i.e., a reflectivity of ∼99% in the optical) for the purposes of these simulations. Applying such a foil increases the effective photocoverage of the PMTs due to reduced light losses from reflections. These surfaces of the OD were assigned a reflectivity of either 40, 80 or 98% in the optical range where the PMTs are sensitive and their quantum efficiencies defined [230, 800] nm, depending on the study being performed. However, wavelength shifting properties, such as those observed in XENON1T [194] were not applied to the reflective

[3] In water-Cherenkov detectors, such as Super-K, typical scattering and absorption lengths are upwards of ∼100 m [214], much larger than the dimensions of nEXO's OD.

foil in this simulation. Any unaccounted for wavelength shifting will benefit nEXO's muon tag efficiency, as it will shift the near-UV portion of the Cherenkov spectrum toward the peak of the quantum efficiency curve for R5912 PMTs. The R5912 PMT QE and Cherenkov spectrum of muons is shown in Figure 5.2.

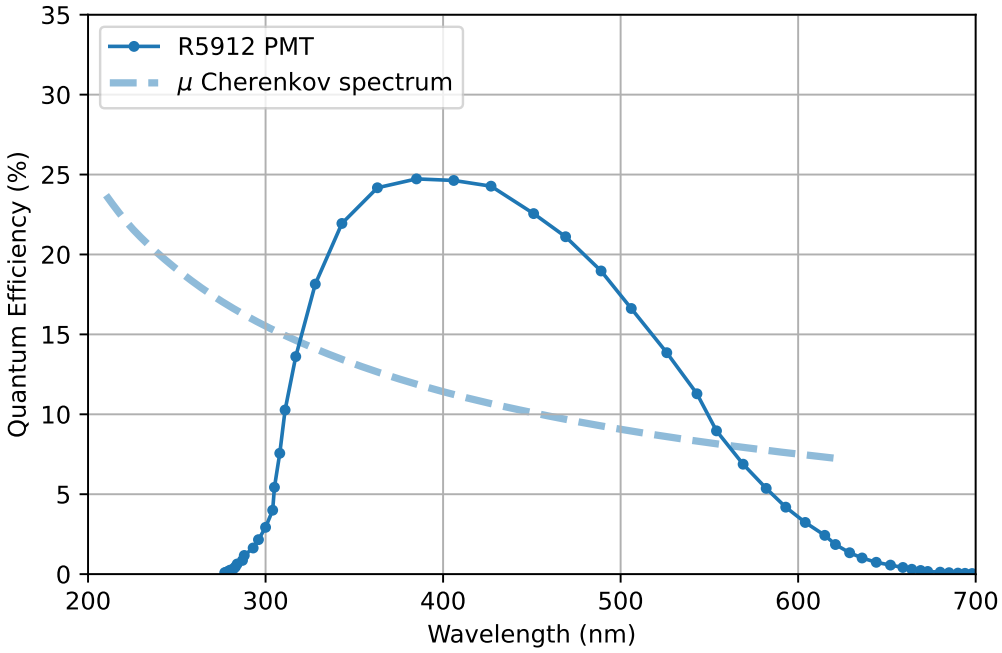

Figure 5.2: Hamamatsu R5912 quantum efficiency as used in the simulations, with a dashed line representing the Cherenkov emission spectrum of 362 GeV muons.

In the spirit of being conservative, the carbon fibre cryostat vessel was set to 0% reflective at all wavelengths, as opposed to 0–30% depending on the surface finish of the carbon fibre being used, which is still undetermined. The stainless steel support structure to mount PMTs to the water tank wall, and those components exposed to the buffer nitrogen gas layer near the ceiling of the OD was set to a constant 40% reflectivity for bare stainless steel. All optical properties were only set for the wavelength range with definite quantum efficiencies for the R5912 PMTs defined in the previous paragraph.

For performance considerations, everything inside the outer cryostat vessel (LXe, TPC,

HFE...) was removed from the Geant4 geometry model for the muon tagging simulations. The standard Geant4v10.5 Shielding physics list was used, but with optical properties that were manually turned on to allow for production and propagation of Cherenkov photons both from the muon itself, and associated charged secondary particles.

5.4 Analysis of Geant4 simulations

A total of 25,000 muons, corresponding to ∼1.5 year of underground exposure at SNOLAB, were simulated through the target volume for each dataset. In this case, the water tank itself (12.3 m diameter, 12.8 m height), based on the muon generation procedure outlined earlier in Section 4.4.2 was used as the target volume. Each simulated dataset has the same 472 PMT configuration, but with different reflectivity settings of the OD cylindrical wall and floor, corresponding to different estimates of the surface coverage of the reflective foil; i.e., 40% reflective steel would be a conservative worst-case scenario of bare stainless steel in the OD meeting the minimum requirements for nEXO, 80% corresponds to the 99% reflective foil applied to ∼80% of the surface area, and 98% corresponding to near-total coverage of the OD wall and floor with a reflective coating.

The Cherenkov light from simulated muons, and associated secondary particles from electromagnetic and hadronic shower events, are propagated through the water until they are absorbed. Any photons incident on a PMT's photocathode (embedded inside a borosilicate glass hemisphere) is absorbed with 100% efficiency.[4]

[4]This absorption process can be found in `Simulation/DetSim/nEXOSim/src/nEXOAnalysis.cc`. This file also includes kill statements for particles below Cherenkov-threshold in the water to preemptively end their tracks and speed up the simulation.

5.4.1 Conversion of photon hits to waveforms

After the base Geant4 simulation is completed, a SNiPER C++ algorithm (`ODPMTAlg`) converts the recorded photon hits into detected hits in waveforms and reduces the overall size of the raw data files by a factor of 20–30. The processed data files contain each event's muon impact parameter, generated energy, zenith angle, total track length through the water, total light yield, and photon timestamps on each PMT's photocathode binned at 8 ns intervals.

To go from the raw photon hit information on the photocathodes to semi-realistic waveforms, we use the PMTs quantum efficiency as measured by Daya Bay (shown previously in Figure 5.2). For each photon of a given wavelength absorbed on a photocathode, a random number is generated in the interval [0, 1]. Only if the generated number falls below the value of the R5912 quantum efficiency at that wavelength is the photon registered as a hit, and added to a corresponding bin of width 8 ns associated to that PMT.[5] At this stage, no electronics noise or temporal response of the PMTs are included other than the digitization rate.[6] Moreover, dark noise contributions to the waveforms are negligible as will be evidenced shortly.

A profile (averaged) quantum efficiency-corrected waveform is extracted for all the PMTs, see Figure 5.3. It is clear from the figure that, given the 8 ns time binning expected from the VX2740 digitizers, looking for single photoelectron (s.p.e) coincidences over a $\sim$ 240 ns coincidence windows between PMTs is an appropriate starting point to develop a muon tag.

[5] This process can be found in the `Analysis/ODPMTAlg/src/ODPMTAlg.cxx` file.

[6] Rise times of R5912 PMTs are faster than the sampling rate of the VX2740 digitizers, and since we are not interested in Cherenkov ring-reconstruction, the timing to not important below the $\sim$100 ns level, as the prompt cosmogenics veto in the TPC will be 10 ms long.

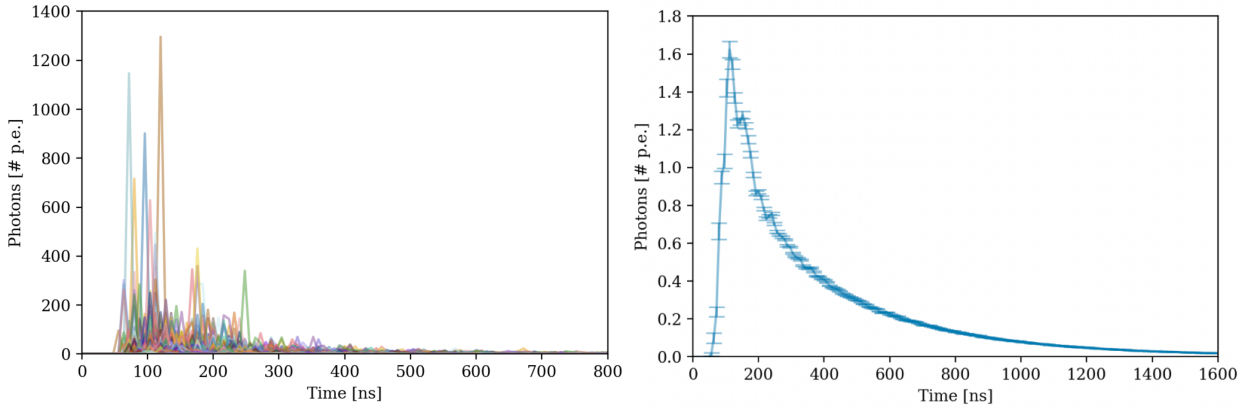

Figure 5.3: Left: Waveforms detected by PMTs from a subset of 179 muons passing through the water tank. Right: averaged waveform of 2000 muons (∼1 month at SNOLAB), showing characteristic timescale of ∼200 ns where the profile waveform is above the 0.5 p.e. level.

5.4.2 PMT arrangement

To trial-and-error many different PMT arrangements would be cumbersome, computationally expensive, and storage requirements steep. Instead, we reprocess the 472 PMT waveforms coming out of `ODPMTAlg` many times over, for different reflectivity settings on the OD surfaces. Analysis scripts are then used to decide which of the 472 waveforms to include in a given muon tag efficiency measurement, for a given PMT arrangement, defined as a subset of the 472 PMT uniform configuration.[7] By undergoing this process of turning off waveforms repeatedly, with randomly-sampled waveforms from each event, we build distributions of muon tag efficiencies as a function of number of PMTs for arbitrary PMT arrangements. A sample of 100 different PMT configurations were processed for every

[7]This is valid because the summed surface area of all 472 PMTs in the simulation relative to the stainless steel surface area is very low at ∼ 2.1%. Thus, when turning off certain PMTs but leaving them in the simulation, we are not changing the overall reflectivity of the entire system significantly relative to the configuration with fewer PMTs, but are still effectively changing the PMT placements.

PMT number tested.[8]

5.4.3 Coincidence levels

Ultimately what limits the muon tagging efficiency of any PMT configuration is the maximum tolerable trigger rate of the DAQ system. We cannot saturate the DAQ and hence allow for untagged muons. The trigger level of each PMT is expected to be set at the single photoelectron level (s.p.e.) as indicated in Figure 5.3. An expected tolerable trigger rate is conservatively set to 1 kHz, which is defined by the maximum data throughput of the 16 bit VX2740 digitizers (1 Gbps), for the 8 ns timing and waveforms of length 2.4 μs. A trigger rate above 3 kHz will saturate the DAQ if full-waveform data is recorded for 2.4 μs on all 64-channels of the digitizer.

The false coincidence rate due to dark counts of the R5912 PMTs, measured to be $\lesssim 3$ kHz [216], is expected to be a negligible contribution to the overall trigger rate for a 240 ns coincidence window required for a 3–7 PMT coincidence. However, the ambient Cherenkov light inside the tank due to ^{208}Tl 2.617 MeV γ-rays (and others) scattering electrons above Cherenkov-threshold in the water (260 keV) will be of concern, as they enter the tank at a rate of about 500 kHz. Thus, a total of 10^7 2.6 MeV γ-rays were simulated emanating from the stainless steel walls. Of these, only 0.5% of gammas produced a trigger meeting the 5-fold PMT coincidence level, i.e., produced single p.e. pulses on 5 different PMTs anywhere in the OD within a 240 ns window. None of the gammas passed the 7-fold coincidence level trigger condition. The 5-fold PMT coincidence is therefore sufficient in keeping the data rate

[8] The processing of data coming out of `ODPMTAlg` is in a standalone C++ script called `pmt_toy_mc/MuonTag.cpp`, which can be found in a GitHub repository dedicated to these studies (Appendix E).

low for the long 2.4 μs waveforms. Should the trigger rate still be too high then reducing the length of the recorded waveform is possible, as waveforms as short as 1.2 μs still envelop the vast majority of the light pulse from muons (see Figure 5.3). Moreover, the VX2740 has the ability to compress data using an onboard FPGA and only output integrated waveform charge, peak pulse time, and other higher-level analysis variables which can further loosen the trigger conditions while allowing for a manageable data rate.

The VX2740 also has the additional capability to group PMTs together. This can be used to set a requirement at the FPGA level such that, e.g., 3 of the 5 PMTs must all be on the floor (since SNOLAB muons are downward going with a tight polar angular distribution due to the large overburden), which can lower coincidence levels while keeping the trigger purity of muons high, and still saving full waveforms. Hence, even though the ambient ^{208}Tl γ-rays (and other ambient radiogenic processes) can produce some events in the OD with 5-fold coincidence, there are various strategies to mitigate their impact on the performance of the muon veto.

Finally, given the track length difference of muons of interest passing with impact parameters below 3.35 m (>8 m tracks) and the expected track lengths of electrons with energies at the MeV-scale in water (∼cm), there will be little confusion in event identification of muons of concern and radiogenic background events based off the total light yield measured across all PMTs. The total light yield is a quantity that is proportional to track length (above Cherenkov velocity) for particles of the same magnitude in electric charge, e.g., $e^{\pm}$ and $\mu^{\pm}$. Thus, there is a difference in total light yield of at least an order of magnitude between the two classes of events. This difference in light

yield should be observable given sufficient light collection efficiency, which can be verified in simulations once the final design specifications for the OD are decided.

5.4.4 Determining the required of number of PMTs

To obtain an estimate of the number of required PMTs, N_{PMTs}, we analyzed the 25,000 muon datasets as follows:

1. Keeping the ratio of PMTs on the wall, floor, and ceiling the same, a subset of N_{PMTs} waveforms was selected (binned to 8 ns).

2. A vector of ones (called the `kernel`) with length (240 ns / 8 ns) was convolved with each of the binned waveforms.

3. The result of the convolutions of each binned waveform with the `kernel` was converted to boolean vectors with a 1 assigned if the bin was above s.p.e. level, and a 0 otherwise.

4. The resulting boolean vector for each PMT was appended as a row of a matrix called the `triggerMatrix`.

5. A sum along each column of the trigger matrix was performed, yielding a vector `columnSums` which tells us for any given 240 ns window the maximum s.p.e. coincidence level between PMTs.

6. The `columnSums` vector was scanned over and a muon would be considered tagged if any bin in the vector is above the required coincidence level between PMTs.

7. Steps 2–5 are repeated for every muon in the dataset resulting in one measurement of the muon tag efficiency.

8. Steps 1–6 are then repeated 100 times, providing 100 different random configurations of N_{PMTs} that are approximately uniformly distributed in the OD.

The tagging efficiency of muons as a function of coincidence level is shown in Figure 5.4. It is clear that at nominal PMT numbers (∼80) we will have achieved our goal of a tagging efficiency >95% with a 5-fold PMT coincidence to not trigger on most of the gamma background, allowing us to save waveform-level data for potentially more elaborate analyses in the future. However, given the expected failure rates of PMTs after 10 years of operation, assuming a 2% failure rate from Daya Bay, a nominal number of 125 of PMTs was chosen as the baseline. Assuming some spare channels will be required, and channels will need to be reserved for calibration systems, these 125 PMTs will be distributed on three VX2740 digitizer boards to allow for any of the complex trigger mapping capabilities described in the previous paragraphs.

5.5 Chroma simulations of the muon veto

Chroma is an open-source GPU-accelerated ray tracing software that computes photon paths on CUDA-enabled devices [217, 218]. In the context of nEXO, Chroma was originally used to develop a light transport efficiency map in the TPC of events in the LXe as opposed to propagating them directly to the SiPMs in Geant4. It was developed further by the nEXO OD simulations group to propagate photons of multiple wavelengths, produce muon tracks

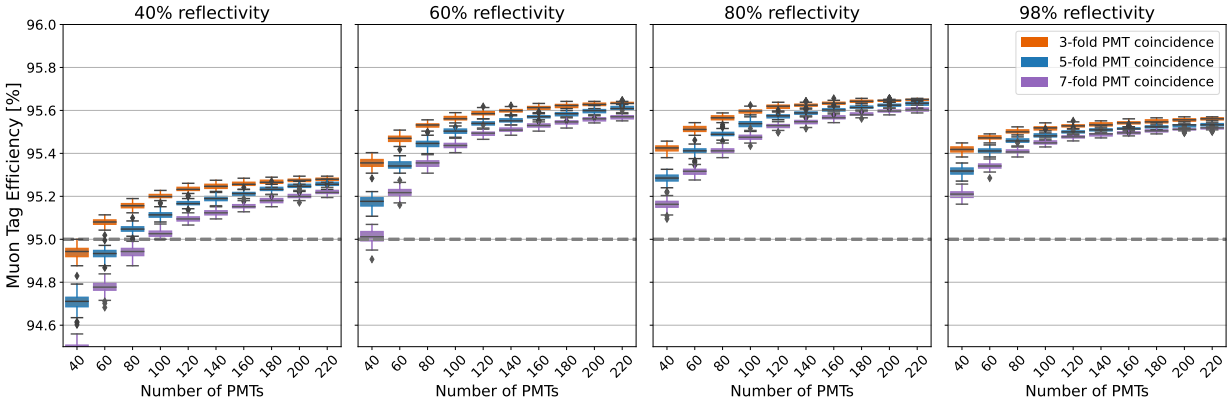

Figure 5.4: Muon tag efficiency as a function of PMT number for various coincidence levels between PMTs at 1 p.e threshold within a 240 ns window. These box plots demonstrate the variation in the tag efficiency for 100 different PMT configurations constrained to be uniformly distributed across the wall, floor and ceiling of the OD. I.e., each box plot individually represents a distribution of tagging efficiencies for of 100 different randomly sampled PMT configurations. The dashed grey line represents to 95% tagging efficiency goal. Each panel shows the data for 40%, 60%, 80% and 98% reflective cylindrical wall and floor in the OD for the specified PMT numbers. The cryostat and ceiling were set to be fully absorbing and 40% reflective at all wavelengths, respectively. These results are for muons with impact parameters <325 cm from the LXe center.

according to cosmogenic muon fluxes, and produce Cherenkov light patterns of muons at SNOLAB in the OD. The CAD models of the Daya Bay PMTs (Figure 5.5a), and of the current OD design can be directly imported into the simulation geometry as `.stl` files, as opposed to making approximations to the geometries in Geant4. The GPU-acceleration then provides a factor of $\sim$ 50 speedup compared to the equivalent CPU-simulations in Geant4 studies, with the caveat that Geant4 also spends additional computational time for producing muon shower events, and propagates the Cherenkov light of secondary particles.

5.5.1 Simulating muons in Chroma

Cherenkov cones and light yields are derived from the Frank-Tamm formula [219]:

$$\frac{d^2E}{dx\,d\omega} = \frac{q^2}{4\pi}\mu(\omega)\omega\left(1 - \frac{c^2}{v^2n^2(\omega)}\right), \tag{5.1}$$

which is valid for particles with velocities: $\beta = \frac{v}{c} > \frac{1}{n(\omega)}$ where v is the velocity of the particle, and c is the speed of light in vacuum. Here $\mu(\omega)$ and $n(\omega)$ are the frequency-dependent permeability and index of refraction of the traversed medium, respectively, and q is the electric charge of the particle. The emitted photon angle corresponds to the index of refraction of the medium (water in the case of the OD) via $\cos\theta = \frac{1}{n\beta}$. The values of n are identical in Chroma and in Geant4.

Muons are approximated to travel in straight lines, and their energies and zenith angles are sampled according to the procedures outlined in Section 4.4.2. Given the intersection points of the muon with the OD, a track length (L_μ) is calculated. Integrating Equation 5.1 from $x = 0$ to $x = L_\mu$ gives the total number of photons that will be emitted, N_γ, in the wavelength region of interest, which is currently set to (290, 600) nm in Chroma. Specifically, this is taken as

$$N_\gamma = 2\pi\alpha(\frac{1}{\lambda_{min}} - \frac{1}{\lambda_{max}})(1 - \frac{1}{\beta^2n^2}), \tag{5.2}$$

the form given in [220] with α being the fine structure constant. This approximation for singly charged particles at constant velocity yields $N_\gamma = 33$ photons/mm, which is what is set in Chroma for determining the number of photons to be emitted by a given muon track.[9]

[9]Note that in the Geant4 studies [λ_{min}, λ_{max}] = [230, 800] nm which yields 58 photons/mm.

Then, N_γ random positions along the track are selected as the origin points of photons, with wavelengths sampled from the Cherenkov spectrum from Equation 5.1 for $\beta = 1$. The start time of photons, t_0, is set by the distance, d, of the photon origin from the start of the muon track divided by the speed of light: $t_0 = d/c$. A subset of Cherenkov photons from an example muon track is shown in Figure 5.5b.

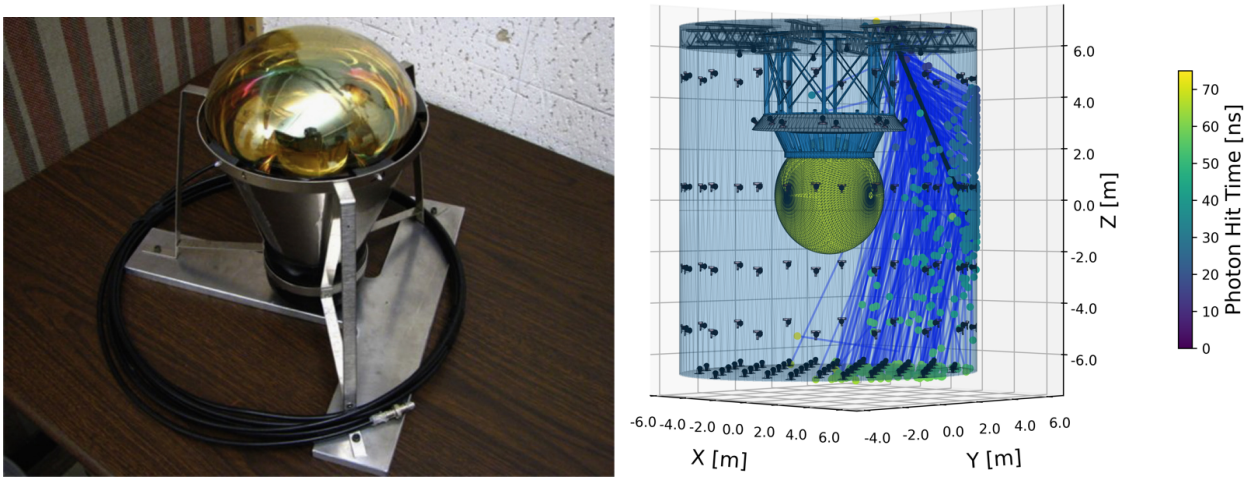

(a) PMT assembly from Daya Bay.

(b) Example muon track in Chroma.

Figure 5.5: Left: PMT assembly from Daya Bay showing the PMT, its "Tee" base and magnetic shielding. Image adopted from [221]. Right: example muon track with Cherenkov light cone in Chroma for one of the test configurations. PMTs in Chroma are modelled after the Daya Bay assembly shown on the right.

5.5.2 Chroma photon yields compared to Geant4

We investigated the light map (photon hit patterns) as well as light yield resulting from our Chroma simulation and Geant4 simulations outlined in Section 5.3. The light map resulting from 1 year's worth of muons at SNOLAB simulated in Chroma is shown in Figure 5.6. About half the photons are incident on the cylindrical tank wall, and about

half of these photons are incident on the lower third of the tank. The OD floor receives ∼40% of the total incident light. Hence, the final PMT distribution investigated in this thesis, presented in the next section, has a downward bias for the distribution of PMTs. The vertical distribution of PMTs follows the approximate distribution in the percentages of incident light yield on the surfaces.

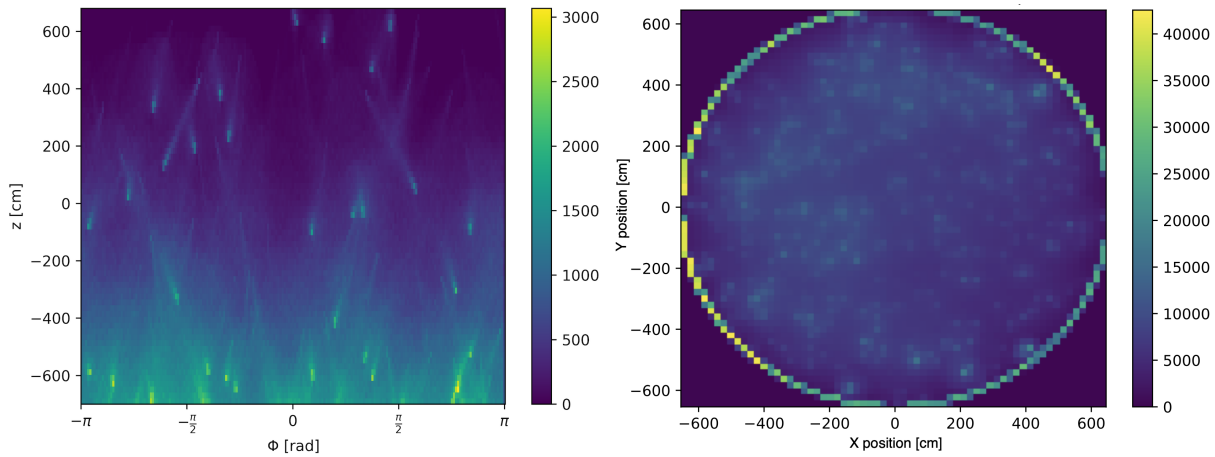

Figure 5.6: Left: hit pattern of photons on cylindrical wall (no cryostat) for one year of muons. Right: hit pattern of photons projected onto the x-y plane for the same dataset.

The light yields from Geant4 are generally higher than those from Chroma due to the additional Cherenkov light of secondary particles, which can be seen in Figure 5.7. Hence, the Chroma results are to be thought of as a lower estimate on the muon tag efficiency for a particular PMT and structural configuration of the OD.

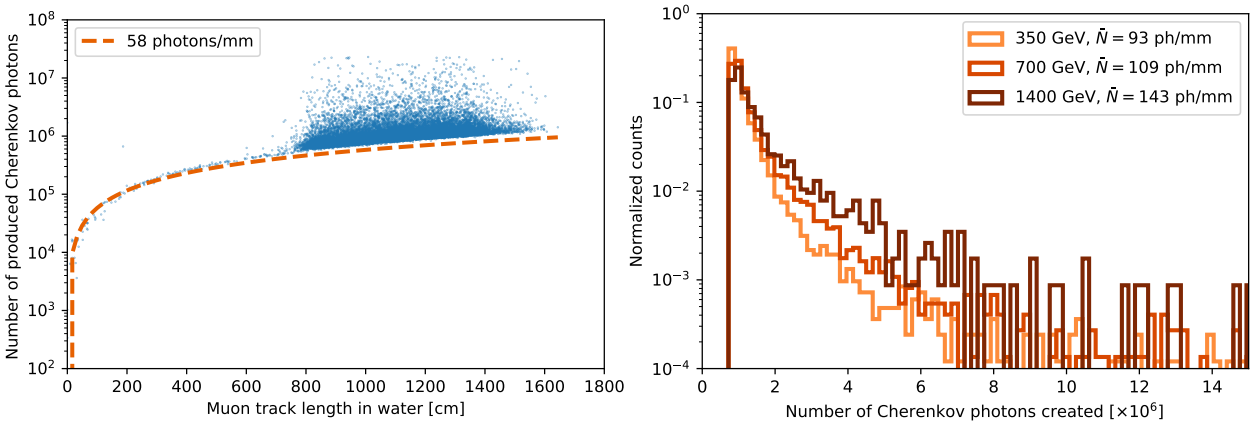

Figure 5.7: Left: distribution of Cherenkov light production from muons in the 1.5 year Geant4 dataset along with a line of 58 photons/mm, the expected light yield from a singly charged particle in the defined wavelength range of Geant4, [230, 800] nm. Right: light yields of muons at various energies in Geant4 passing straight through the 12.5 m vertical water height, shown with their average photon yield across the same [230, 800] nm wavelength range. Note that Chroma produces exactly 33 photons/mm always, as there are is no additional path lengths from secondary charged particles above their respective Cherenkov-thresholds. Moreover, the wavelength range in Chroma was set to [290, 600] nm at the time of these studies.

5.6 Final PMT configuration and reflectivity study

The final PMT distribution including all OD components is shown in Figure 5.8. For each case of the wall and floor reflectivity (40, 80, 98%), a total of 20,000 muons (∼1.2 years at SNOLAB) were simulated in Chroma. The cryostat and its support were set to be fully absorbing and the stainless steel support structures set to a reflectivity of 40%. The trigger condition was set to a 5-PMT single photoelectron coincidence in a 240 ns window. The muon tag efficiency can now be calculated, and an uncertainty assigned according to the Wilson score treatment [222] for a 1σ confidence interval. This treatment is necessary since the muon tag efficiency estimate can be close to 100%, see Appendix B.3 for justification. The results are presented in Figure 5.9.

5.6.1 Geant4 cross check

The Chroma PMT configuration was then reproduced in Geant4 (Figure 5.8b), and the same optical settings were used. The muon tagging efficiency as a function of muon impact parameter was studied, meeting the 95% tagging efficiency goal for muons with impact parameters below 3.35 m, as seen in Figure 5.10.

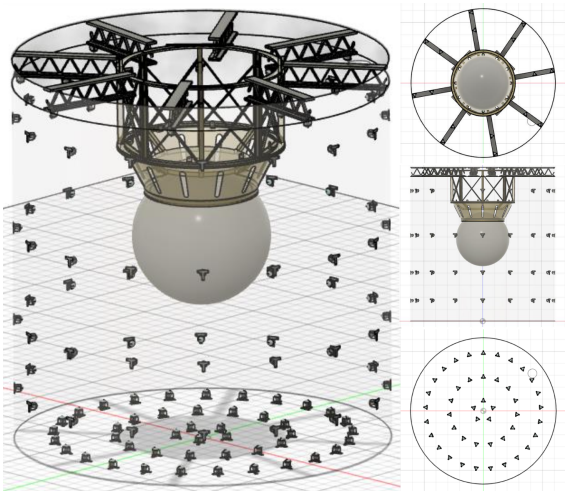

(a) 125 PMT configuration in Chroma.

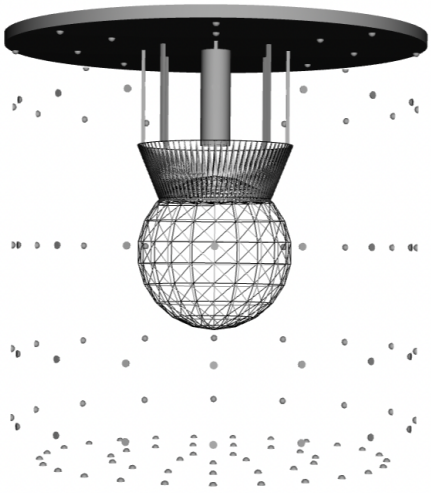

(b) 125 PMT configuration in Geant4.

Figure 5.8: Final PMT configuration studied in Chroma and Geant4, showing a slight asymmetry toward the floor with 125 PMTs. For the cylindrical wall, 32 PMTs are placed in two rings below the cryostat level on the lower third of the tank, and 32 are placed above the TPC level split across two other rings of 16. There are 14 PMTs that are downward facing from the steel trusses at the top of the water level, they are split into two concentric rings of 8 PMTs. The remaining 45 PMTs are placed in 3 concentric rings on the OD floor of 5, 15, and 25 PMTs respectively.

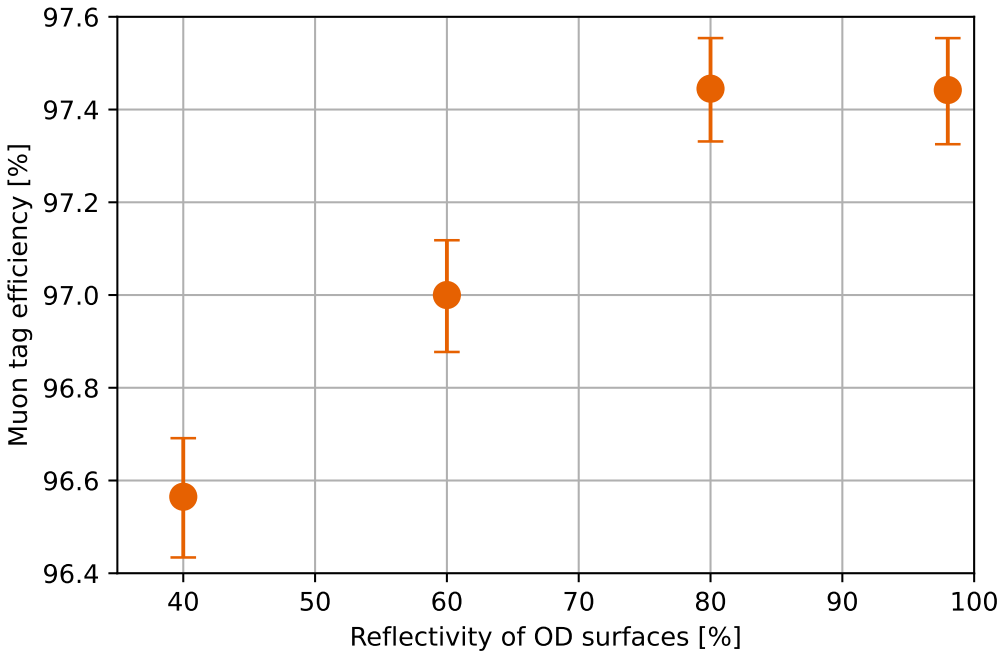

Figure 5.9: Muon tag efficiency results from final Chroma studies with 125 PMTs for all muons passing through the water tank. The reflectivity on the x-axis refers to that of the cylindrical wall and floor only, as the cryostat was set to be fully absorbing and the steel in nitrogen buffer gas space set to 40%. The OD trigger condition was set to 5-fold PMT coincidence at the s.p.e. level in a 240 ns window.

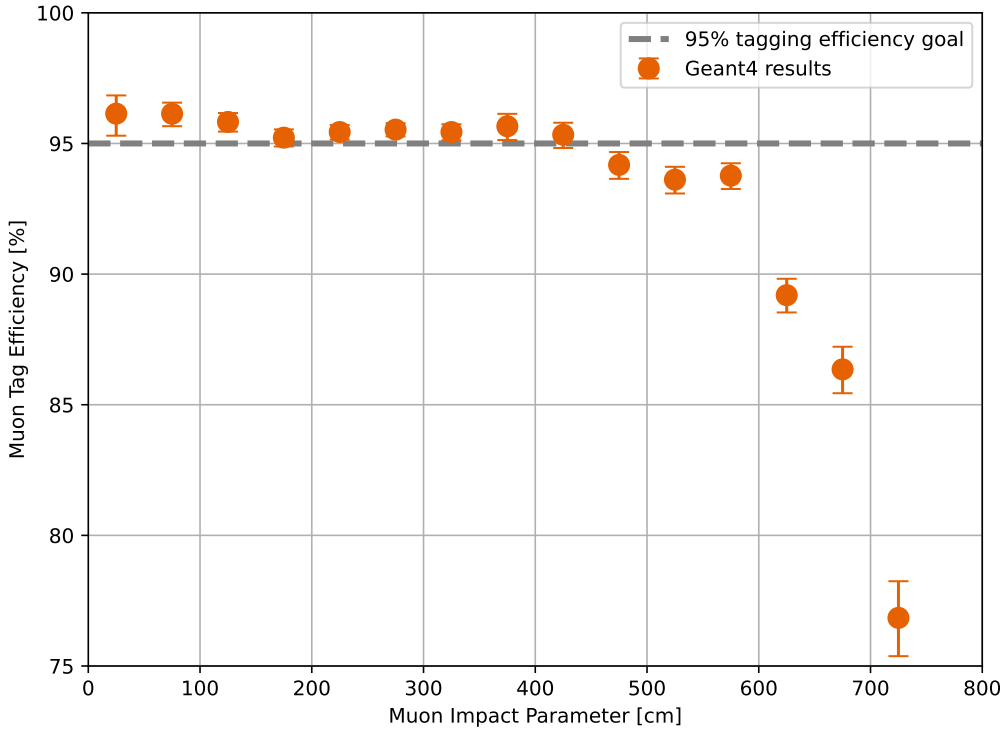

Figure 5.10: Muon tag efficiency versus muon impact parameter for the Geant4 cross check of Chroma results with the 125 PMT configuration, using the same OD trigger condition and reflectivity settings as the Chroma tagging study.

5.7 Summary and discussion

We have developed a baseline muon veto configuration for nEXO at SNOLAB. Considering a nominal 80% coverage for the reflective foil on the OD wall and floor, and 125 PMTs distributed as per Figure 5.8, we obtain a conservative muon tag efficiency estimate of 97.5±0.1%[10] for all muons passing through the water tank. This satisfies our goal of >95% for muons passing within 3.35 meters of the LXe volume, which are the muons that produce the majority of the cosmogenic background via hadronic showers. We did this by simulating muons through the nEXO OD at SNOLAB using the GPU-accelerated ray tracing program Chroma. The Chroma simulations provide a lower bound on the tag efficiency because:

1. The true muon light yield is expected to be higher due to secondary particles that will additionally be produced in muon showers which are not considered in Chroma.

2. There is potential for unaccounted for wavelength-shifting effects from the reflective coating that will be used. As per the experiences from the XENON1T experiment [194], this effect may shift photons from shorter UV wavelengths (where the Cherenkov light peaks) towards longer wavelengths ∼400 nm, where the R5912 quantum efficiency peaks.

3. The reflectivity settings of the uncoated stainless steel components (e.g., the ceiling) are taken as a conservative lower estimate at 40% (the lowest reflectivity in the wavelength range of interest), although the reflectivity varies as a function of wavelength between 40% and 60%.

[10] This error is calculated using the Wilson Score interval (Appendix B.3). However, given the number of MC trials available, the error is consistent with those obtained via the Clopper-Pearson and Bayesian methods found in the standard TEfficiency package from ROOT 6 [223].

4. The reflectivity of the carbon fibre used for the cryostat is taken as 0%, but the true value is likely somewhere below 20%, depending on the finish — albeit only ∼7% of all incident light lands on the cryostat.

The muon tag efficiency of muons passing within 3.35 m of the LXe center was not calculated directly in Chroma as this feature has not been implemented yet, but a cross-check in Geant4 corroborated the Chroma study's findings.

Stopping muons, muon bundles, and other minor effects were neither simulated in Chroma nor investigated in detail in Geant4 since the fraction of muons producing cosmogenic energy deposits in the nEXO TPC is $\lesssim 10^{-3}$ (see Section 4.7.4). Hence, the effect of the aforementioned processes on the sensitivity of nEXO is negligible. Moreover, the ability for this configuration of PMTs to reconstruct muon tracks was not investigated in this thesis, as it is not expected to significantly aid in the rejection of backgrounds or improve the sensitivity of nEXO to $0\nu\beta\beta$ at SNOLAB (see Figure 4.18). However, the reconstruction capability may be worth investigating in future LXe experiments, or if nEXO were to be placed at a shallower underground location with a higher muon flux such as LNGS. There, one could devise a tag based off the 3.35 m impact parameter cut which corresponds to muons with track lengths through the water of 800–1230 cm, and a corresponding minimum light yield measurement (see Figure 5.7).[11] Of these muons, those with track lengths through the TPC will be detected regardless of the muon veto since a 5 cm muon track will produce >10 MeV deposit in the TPC,[12] well above typical radiogenic energy deposits of <3 MeV. An

[11] This is a logical extension of our study if the muon impact parameter distribution at SNOLAB is also valid at LNGS.

[12] The SNOLAB muons are no longer minimum ionizing particles with an average Lorentz factor of $\gamma \sim 3600$, as opposed to 2–3 for a minimum ionizing particle (MIP). This is why >10 MeV is predicted, as only a MIP will deposit ∼10 MeV.

interesting avenue to explore is whether or not the current PMT configuration will be able to detect events which produce hadronic showers based off light yield and timing analyses alone. This may be fruitful in future large LXe experiments where full TPC vetos will be more costly due to deadtime accrual, and the necessity of vetoing muons passing through a larger volume with a correspondingly higher flux.

During the Chroma studies, there was a short trial-and-error period that optimized the computation time for muon tagging studies as a function of the number of muons simulated in a single run. This is a memory issue because Chroma, as of now, does not bunch an optimal number of photons together prior to propagation via GPU and writing the resulting data to disc. For the muon tagging studies presented in this thesis, Chroma output (`.h5`) files of 5000 muons were generated. A similar issue occurs when reading many muon files together for analyses of muon tagging based of PMT trigger conditions. The 64 GB of available RAM was not sufficient, and so in calculating a muon veto efficiency subsets of analysed data (bunches of 5000 muons) had to be combined. Furthermore, many of the Cherenkov physics can be moved to the Chroma source C++ code as opposed to the Python wrapper for further computational speed improvements. This fact will be revisited in the conclusion chapter of this thesis.

In the next chapter, we will evaluate the sensitivity of this OD configuration to supernovae across our galaxy.

Chapter 6

Detecting Supernova Neutrino Bursts with nEXO

Supernovae play a vital role in astrophysics and our understanding of cosmic evolution. These explosive events provide a feedback mechanism pumping energy back into galaxies and seeding subsequent generations of stars. Their extreme environments also provide a unique astrophysical laboratory where we can study the intricacies of neutrino physics in an otherwise unattainable environment of extreme matter temperatures and densities.

One sub-class, core-collapse supernovae (CCSN), categorizes events that mark the demise of the most massive stars ($\gtrsim 8$ solar masses), and the birth of neutron stars and black holes. Searching for a precise understanding of CCSN and their explosion mechanisms is a test bed of physics across many disciplines: subatomic particle interactions, stellar evolution, and general relativity. Thus, a coherent understanding that matches experimental observations will provide a self-consistent check spanning across many fields of physics. This chapter provides a first assessment of nEXO's ability to detect neutrinos from CCSN events in our galaxy, the Milky Way.

6.1 Motivation

Supernovae have had a long and captivating pursuit in astrophysics, primarily motivated by the extraordinary potential of understanding what is hidden deep within the extreme environment of a collapsing stellar core. These environments are laboratories of matter under extreme gravitational and thermal conditions. CCSN are also drivers of nucleosynthesis, high energy cosmic rays, and potentially sources of other exotic particles [224–226].

Our current understanding is that CCSN emit an enormous integrated flux of 10^{58} $\mathcal{O}(10$ MeV) neutrinos across all flavours and anti-flavours, liberating the majority of the gravitational energy during the core collapse process in $\sim$10 seconds. The inability for neutrinos to interact via any force other than the weak force, allows them to freely stream out of the star after crossing the so-called 'neutrinosphere': a radial surface of last scattering for neutrinos. Hence, by understanding the emission mechanisms and measuring the flavour content and energy spectra of the emitted neutrinos one can decipher the internal workings of a CCSN, behind its photosphere. Doing this allows us to build an understanding of supernova dynamics prior to supernova shock breakout, at which point electromagnetic signatures of a supernova begin to be emitted. For a review of CCSN neutrinos see [227].

6.1.1 SNEWS 2.0 and a canonical CCSN neutrino burst

The SuperNova Early Warning System (SNEWS) is an international organization that consists of several neutrino experiments [228]. The primary aim of the SNEWS network is to produce an astronomical alert upon the coincident observation of a burst of neutrinos

across many low-background detectors searching for dark matter, $0\nu\beta\beta$, or ν-oscillations. SNEWS 2.0 is an evolution of the original network [229] which will now also provide sky maps localizing potential CCSN candidates by neutrino triangulation, as well as fast event reconstruction of electron-scattering events, where the emitted electrons point back to the source of neutrinos. SNEWS 2.0 will also lower coincidence level thresholds across the global network of detectors compared to the original network, allowing for a higher false-CCSN alarm rate of once per fortnight.[1] Information on pre-supernova neutrino activity in the galaxy will also be provided. These new measurement goals are only possible now by combining data coming from many upgraded detectors which use different detection media and mechanisms that are distributed across multiple underground sites worldwide. The SNEWS 2.0 consortium will be sensitive to multiple ν-interaction channels, across different neutrino flavours — something that is impossible to do in any single detector.

nEXO is eligible to become a SNEWS 2.0 member experiment. But, even without becoming a SNEWS member, nEXO could use a SNEWS CCSN alarm to, for example, lower trigger thresholds in the TPC in the case of a SN event alerted by SNEWS or go into a trigger-less readout mode for ∼30 seconds. If nEXO were to join the network as a member, a GPS clock synchronised to the data streams of TPC and OD is likely to be a requirement, as per the current SNEWS protocol.

This chapter is dedicated to presenting nEXO's capabilities as a supernova neutrino detector. Using the canonical GVKM model for the CCSN neutrino burst [230], shown in

[1]The once-per-century false alarm rate set by SNEWS 1.0 was deemed too strict, unfit for the current era of MMA where GW alarms of compact binary inspirals occur daily. The astronomical community tolerates this higher false alarm rate, as the observation of a CCSN event would be a once in a lifetime opportunity and LIGO alerts of compact binary inspirals occur daily.

Figure 6.1, we will calculate the neutrino interaction rate and estimate their detectability in both the Outer Detector and TPC. In our analysis, we will disregard the temporal shape of the neutrino flux; interactions in nEXO will predominantly come from the cooling phase of the proto-neutron star, which spans approximately 10 seconds and lacks distinctive temporal features in the dominant detection channel for nEXO: $\bar{\nu}_e$ inverse beta decay (IBD) events on hydrogen nuclei in the water tank. The GVKM model serves as a reference throughout this thesis. It assumes a neutrino burst releasing 3×10^{52} ergs of energy across all neutrino flavors and accounts for some neutrino self-interactions and supernova shock wave effects. Vacuum and MSW oscillations of neutrinos as they propagate towards the detector and through the Earth are not accounted for in this thesis.

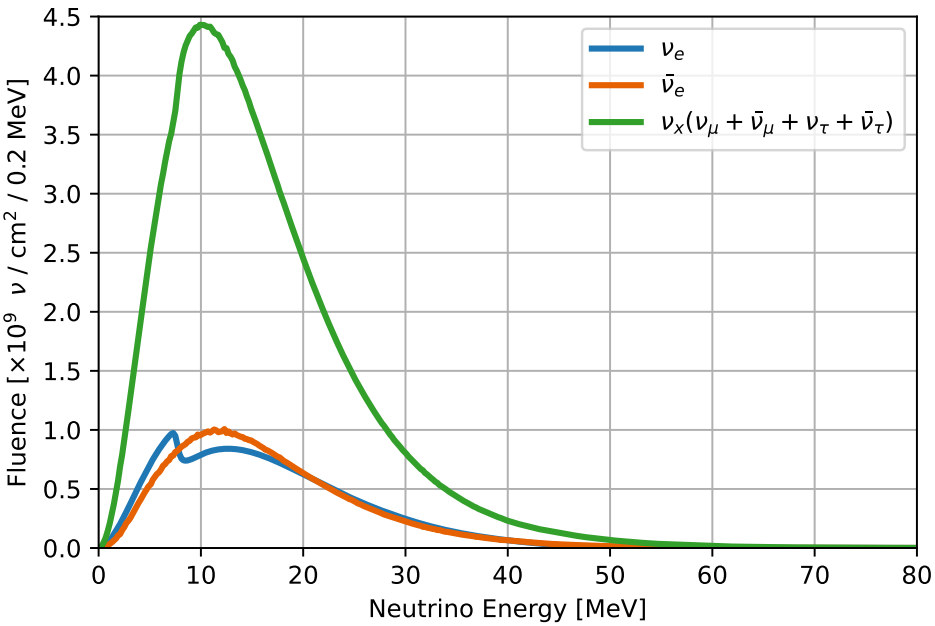

Figure 6.1: GVKM supernova neutrino spectra split by flavour, and integrated in time. Data taken from [230, 231].

6.2 Neutrino Detection with the nEXO TPC

6.2.1 Neutrino interactions in enriched LXe

Liquid argon TPCs have great sensitivity to electron neutrinos from CCSN [231]. Liquid xenon should have similar capabilities through charged and neutral current interaction channels in which de-excitation γ-rays would allow for event tagging.

We can compare the two charged current (CC) channels:

$$\nu_e + {}^{136}\mathrm{Xe} \rightarrow e^- + {}^{136}\mathrm{Cs}^*,$$

$$\bar{\nu_e} + {}^{136}\mathrm{Xe} \rightarrow e^+ + {}^{136}\mathrm{I}^*.$$

In the first case, an electron neutrino is absorbed by a neutron in the ^{136}Xe nucleus converting it into a proton, resulting in an ejected electron and an excited ^{136}Cs nucleus. Similarly, in the second interaction we have an electron anti-neutrino converting a proton into a neutron leaving an excited ^{136}I nucleus and a positron in the final state. Electrons and positrons will both produce scintillation and ionization signals in the TPC. However, the positron will also produce two 511 keV annihilation photons thus making the events distinguishable by this signature. Finally, both of the resulting excited nuclei will de-excite via γ-ray emission to their ground states which will also produce detectable scintillation and ionization signals.

There are also two neutral current, i.e., flavour-blind, interactions that are possible in the LXe. Inelastic interactions will leave an excited Xe nucleus, and coherent-elastic neutrino-

nucleus scattering (CEνNS) events produce nuclear recoils in the $\sim$ keV range. These neutral current events have the form:

$$\nu_x + {}^{136}\mathrm{Xe} \rightarrow \nu_x + {}^{136}\mathrm{Xe}^{*}.$$

Here, ν_x denotes all neutrino and anti-neutrino flavours. Unfortunately, CEνNS interactions produce xenon nuclear recoils with energies in the keV range, which would in turn produce charge signals of a few electrons, far below the noise level of nEXO's baseline charge readout tiles (200 e^- per microsecond) [151], making all these interactions sub-threshold in nEXO's baseline design and impossible to trigger on without external input. In the inelastic scattering cases, the de-excitation of xenon nuclei will occur via γ-ray emission that is detectable.[2]

6.2.2 Estimate of interaction rates in nEXO's liquid xenon volume

We will first focus on the charged current interactions in the LXe. We take cross sections outlined in [233] and perform a linear interpolation in the range 5–80 MeV and set cross sections outside this energy range to zero as shown in Figure 6.2a. Hence, we account for the majority of the GVKM fluence and remain conservative in our estimate. Pirinen *et al.* [233] provide cross sections for axial vector couplings of $g_A = 1$ and $g_A = 0.7$. Since the actual value of this number is currently not known, we will take the optimistic case of $g_A = 1$ for the plots that follow. In the scenario that the value of g_A is found to be closer to 0.7, the

[2] nEXO collaborator Sam Hedges, has since been working on estimates of the detectable electromagnetic energy from the CCSN neutrinos in the LXe TPC and reconstruction of the neutrino energy spectrum using MARLEY [232] event generators in conjunction with the baseline `nexo-offline` Geant4 code. These studies are left outside the scope of this thesis, but the estimated interaction rates presented here are still valid.

total interaction rate in this energy range will decrease by $\sim 40\%$ as per cross sections found in [233].

The full active mass of liquid xenon in nEXO is taken to be 3661 kg, 90% of which is ^{136}Xe. This gives us 2.42×10^4 moles of xenon nuclei. Interactions on ^{134}Xe are ignored. Now, we multiply each bin in the GVKM neutrino fluence by the appropriate (interpolated) cross section for the two interaction channels. This results in the expected event rate at various supernova distances to Earth as shown in Figure 6.2b. From [234], we expect the majority of the ^{136}Cs will be produced in high lying 1^+ nuclear states. The branching ratios to calculate how many of these states will end up in the lower 8^- (metastable), 4^+, or 5^+ (ground) states are currently not known and can only be estimated (see level scheme on p. 416 of [235]). Further, these γ-ray cascades generally happen quickly compared to the timescale of nEXO's readout except for the metastable 8^- state which has a 17.5 s half life with 517.9 keV energy. Assuming that a significant fraction of the 1^+ states decay through the metastable 8^- state, then we should be able to observe the TPC event rate slowly decrease by emission of 517.5 keV γ-rays long past the $\sim$10 s CCSN neutrino emission in the case of a nearby supernova. The available data on the excited states of ^{136}Cs is however lacking, and additional experimental measurements of these states is required to better evaluate the feasibility of such a detection in this neutrino interaction channel.

Next there is the $\bar{\nu}_e$ channel which will produce ^{136}I. Following the same argument as above, the ^{136}I should promptly de-excite to its 1^- ground state, which will then undergo β^- decay to ^{136}Xe with a half life of 83.6 s with $Q_\beta = 6.88$ MeV (see pp. 385–387 of [235]). This signal is less obvious to search for compared to the fixed energy signature of metastable

^{136}Cs decays, but the longer half life and high Q value could make the ^{136}I channel an interesting study considering the well-populated and documented branching ratios and level scheme. However, it is expected that this channel will be greatly suppressed in ^{136}Xe due to excess neutrons [234], and the rates for ^{136}I production are expected to be about 2 orders of magnitude below those for ^{136}Cs production.

Finally, we evaluate the inelastic neutral current (NC) scattering of ^{136}Xe. These, according to [236], will mainly populate the 1^+ $\sim$8 MeV excited states of ^{136}Xe with cascades down to the ground state. All the 1^+ states found in (pp. 369–378) of [235], are expected to cascade on short time scales of $\mathcal{O}$(ns) to the ^{136}Xe ground state, fast compared to nEXO's readout time ($\sim \mu$s). These events will, to some degree, complicate observation of the production of cesium and iodine nuclei but details of disentangling the charged current and neutral current signals are not provided here.

The NC inelastic channel has equal contribution from all neutrino flavours, but the cross section for the interaction is energy dependent. To calculate the total interaction rate, we will sum the GVKM energy spectrum for all neutrino flavours, and follow the same treatment as for the charged current channels but with cross sections found in [236].

The expected total charged-current event rates in LXe are quite low, and any temporal information is unlikely to be evident in the data due to Poisson fluctuation on the number of events per time bin, thus we do not consider pileup in this study. Energy spectrum reconstruction (for supernova model fitting) and studying temporal flux evolution in the LXe is not expected to be feasible at distances close to, or above, 10 kpc (i.e., the scale of the Milky Way). Moreover, other experiments that are sensitive to electron and electron

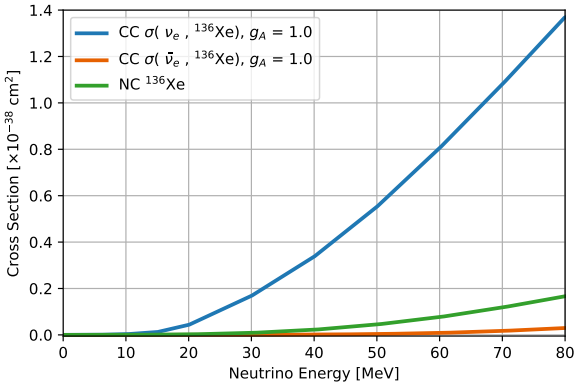

(a) Cross sections of the main supernova neutrino interactions in nEXO's LXe.

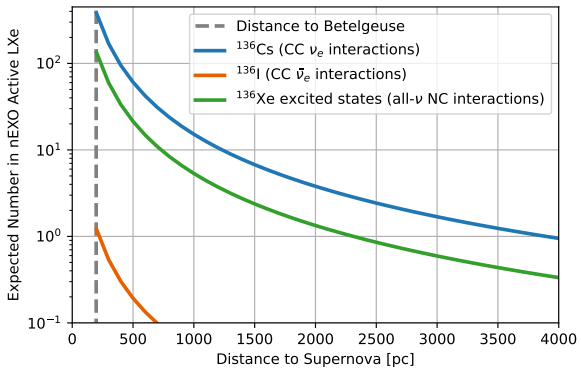

(b) Interactions in nEXO from a GVKM supernova in 3661 kg of enriched LXe.

Figure 6.2: Summary of results for supernova neutrino interactions in nEXO LXe. Cross sections are taken from [234] and linearly interpolated.

anti-neutrino flavours will have much better reconstruction and CCSN model-disentangling capability due to thousands of expected events per neutrino interaction channel: DUNE [237] for ν_e, and Hyper-K [238], Ice-Cube [239], and P-ONE [240] for $\bar{\nu}_e$. The nEXO LXe however, does provide rather unique signals, with identifiable signatures that can allow for some constraint on the overall ν_e flux via ^{136}Cs metastable decays. In the case of a close supernova on the order of a few hundred parsec away, the inelastic neutral current channel is another unique mechanism to constrain the total all-flavour neutrino fluence (ν_x measurements are inaccessible by most experiments) with total interaction numbers shown in Figure 6.2b.

6.3 Neutrino detection with the nEXO Outer Detector

The primary location in nEXO where we expect to have the majority of neutrino interactions is the Outer Detector (OD). Here, the 1.4 kilotonnes of water provides a far greater number of nuclear targets for MeV-scale neutrino interactions compared to the LXe. These neutrinos will produce electrons or positrons in the water which can be detected by their Cherenkov emission incident on the muon veto PMTs.

6.3.1 Neutrino interactions in water

Neutrino interactions in water have been well studied for decades. There are three main categories of event types: elastic scattering of neutrinos on electrons, neutral current interactions of neutrinos on nuclei, and charged current interactions on nuclei. Inverse beta decay (IBD was first described in Section 2.1) is the dominant process by which neutrinos at supernova energies will be detected. These events comprise ∼90% of all supernova neutrino interactions in water. In this process, a $\bar{\nu}_e$ that is above a threshold energy of 1.8 MeV converts a proton (hydrogen nucleus) into a neutron and emits a positron: $\bar{\nu}_e + p \rightarrow e^+ + n$. The emitted positron carries the vast majority of the neutrino energy, providing an energy signature that is detectable, and allowing for the reconstruction of the $\bar{\nu}_e$ energy spectrum. The neutron then captures on another hydrogen nucleus within ∼200 μs, forming deuterium and releasing a 2.2 MeV photon. This γ-ray is too low in energy to provide a signal in the nEXO OD that is above the radiogenic γ-ray background from the surrounding rock. The annihilation γ-rays from the eventual positron annihilation are also

undetectable due to their low energy.[3]

The next leading type of interaction is elastic ν-electron scattering: $\nu_e + e^- \rightarrow \nu_e + e^-$. These events are expected to comprise less than 10% of all supernova neutrino interactions. However, they will produce detectable Cherenkov signals in the water tank at energy scales similar to those of IBD interactions, making these two classes of events effectively indistinguishable in the nEXO OD. It is worth noting that the electrons in ν-electron scattering tend to point back to the neutrino source, whereas the positrons in IBD do not do so at typical CCSN neutrino energies. Finally trace amounts of ^{16}O charged current, and neutral current events on both ^{16}O and H nuclei will have event rates so low relative to the IBD channel that they are ignored.

6.3.2 Estimate of inverse beta decay interaction rates

Using IBD cross sections from [241] (Figure 6.3a), a GVKM supernova at 10 kpc will produce 265 IBD interactions in 1.4 kt of water. This estimate was obtained by multiplying the binned GVKM $\bar{\nu}_e$ energy spectrum (Figure 6.1) by the IBD cross sections, and normalizing it by the number of neutrino interactions expected in the nEXO OD, given the number of nuclei of hydrogen in the 1.4 kt water tank. The interaction rate at 10 kpc was then rescaled as $1/r^2$ for various supernova distances to Earth, this result is shown in Figure 6.3b. For comparison, SN1987A would have produced ∼10, or 270 IBD interactions if placed at 10 kpc [242]. The water mass comes from the 2023 SNOLAB engineering baseline design for the nEXO water

[3]The mechanism one would measure the 2.2 MeV capture signal, and coincident 511 keV annihilation signals is to have the γ-rays transfer energy to electrons, and have them be above Cherenkov-threshold ∼260 keV. This does not produce enough light when compared to the 2.617 MeV ^{208}Tl radiogenic γ-ray background entering the OD at about 500 kHz (Appendix C.1.1).

tank (height 12.8 m, radius 6.17 m) and subtracting off the volume of the spherical outer cryostat with 2.23 m radius, and the height of the 30 cm boil-off nitrogen cover gas layer.

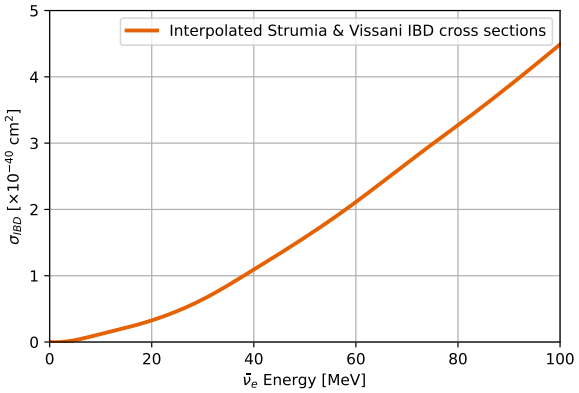

(a) Inverse beta decay cross sections for $\bar{\nu}_e$ interactions on hydrogen nuclei (from [241]).

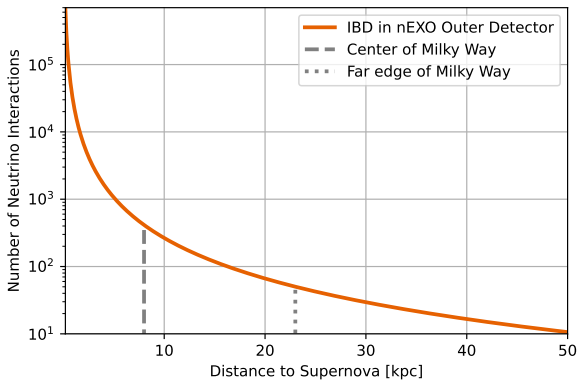

(b) Total number of IBD interactions in the nEXO OD for a GVKM CCSN.

Figure 6.3: Summary of results for nEXO Outer Detector supernova neutrino interaction estimates.

6.4 Neutrino burst detection with the Outer Detector

Using the 125 PMT configuration designed at the end of Chapter 5, we conducted a study to determine the tag efficiency of positrons from IBD events in the OD. This 125 PMT configuration features a fully absorbing cryostat, 40% reflective steel (ceiling, PMT, and structural supports), and 80% reflective foil on the OD floor and cylindrical walls across all optical wavelengths. The trigger condition was set to the same as that for the muons: 5-fold PMT coincidence at the single photoelectron level within a 240 ns window.

The CCSN neutrino events will produce tens-to-hundreds of $\mathcal{O}(10)$ MeV events in the OD over a few seconds, mostly following the shape of the $\bar{\nu}_e$ supernova spectrum. Typically, in water-Cherenkov detectors, a delayed coincidence ($\sim$200 μs) tag of the positron followed

by the neutron is attempted to detect the IBD events above backgrounds. Unfortunately for nEXO, the tagging of the neutron capture signal will not be possible without extremely good position reconstruction at the <1 m level, which will likely be impossible due to the low light yield from single 2.2 MeV γ-rays, buried under a 500 kHz 2.617 MeV ^{208}Tl background [204]. Neutron captures on oxygen and other trace elements are ignored, as these will occur at a level $< 10^{-4}$ compared to hydrogen by ratio of thermal neutron capture cross sections. Nevertheless, the rate of γ-rays with energies greater than 10 MeV originating from the surrounding rock is effectively zero [243]. Furthermore, muon events, which occur at a rate of about 2–3 per hour on average at SNOLAB, deposit hundreds of MeV in energy across the entire tank. Thus, the Cherenkov light emitted by positrons from a galactic supernova should be clearly distinguishable from both radiogenic backgrounds and muon events for a given energy threshold $\gtrsim$10 MeV. The CCSN neutrinos are, therefore, the only expected source of Cherenkov light deposits in the 10–80 MeV energy range that could occur within a few seconds of each other in the nEXO OD at SNOLAB.

6.4.1 IBD positron tag efficiency study

A total of 2.5×10^6 positron events were produced uniformly in the water volume following the GVKM neutrino spectrum for $\bar{\nu}_e$ (Figure 6.1), subtracting 1.8 MeV for the IBD interaction threshold energy on hydrogen. The positrons were distributed homogenously and emitted isotropically across the full water tank.[4] We consider the trigger condition to be a 5-fold PMT coincidence at the single photoelectron level in a 240 ns coincidence window, the same

[4]This code can be found in the `Generate_IBD()` method of `nEXOPrimaryGeneratorAction.cc` in the `nexo-offline` Geant4 codebase.

trigger condition concluded in Chapter 5. The 2.5×10^6 positrons were then divided into bins of 2 MeV in energy and detection efficiency was calculated for each bin, as well as a 1σ confidence interval using the Wilson score method (Appendix B.3). These results are shown in Figure 6.4, which indicates an energy threshold of positrons in the OD of ∼10 MeV is sufficient to meet the OD trigger criteria for the 125 PMT case.

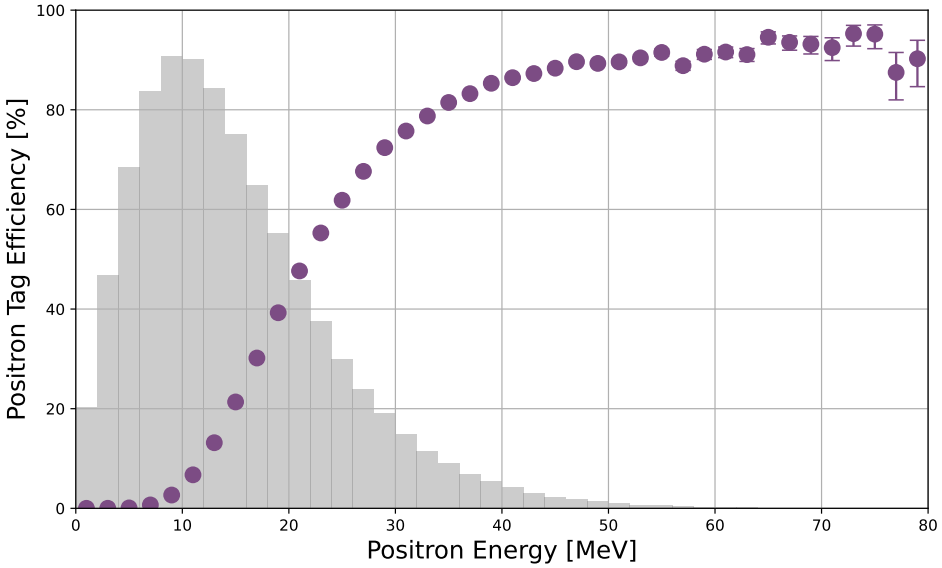

Figure 6.4: Tag efficiency for inverse beta decay (positrons only) in the nEXO Outer Detector, under a 5-fold PMT coincidence within a 240 ns window at the single photoelectron level. The PMT configuration, trigger condition, and optical properties align with the final studies detailed in Chapter 5. The tag efficiency is overlaid on a grey histogram, showing the energies of 2.5×10^6 simulated positrons mirroring the GVKM $\bar{\nu}_e$ spectrum.

6.4.2 Burst detection efficiency estimate

A 2D histogram of tagged events is constructed from the 2.5×10^6 positron dataset and presented in Figure 6.5a. This histogram reveals the correlation between positron energy and total light yield. A rough energy cut of 10 MeV in the water tank corresponds to 15 p.e., as also evidenced by Figure 6.5b. Given the low probability for pile-up of ambient

radiogenic gamma-rays (<3 MeV) within a 240 ns window, as well as the properties of Compton-scattered electrons and Cherenkov light production, we propose a criterion for a core-collapse supernova (CCSN) neutrino burst detection: observing more than 3 events, each with over 10 MeV (15 p.e.) of visible energy deposited, within a 10 second window. This will serve as our 'supernova tag' for the purpose of this thesis.

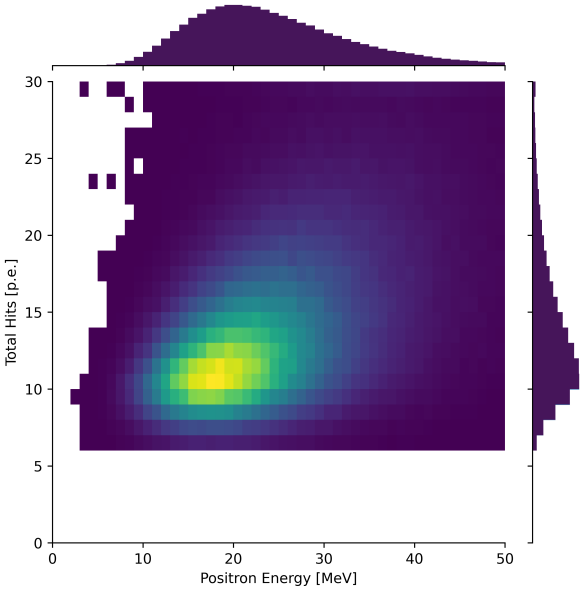

(a) Transfer matrix from e^+ energy to total detected photons.

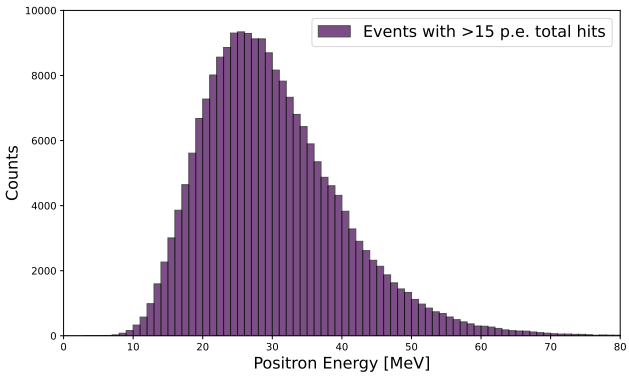

(b) e^+ energies for events with over 15 p.e. total detected photons across all 125 PMTs.

Figure 6.5: left: Transfer matrix from positron energy to total detected hits in the 240 ns coincidence window for a 5-fold PMT coincidence at s.p.e threshold. These plots are for the 125 PMT configuration, and 80% reflectivity on the floor and cylindrical wall, with the cryostat and ceiling set to be fully absorbing and 40% reflective at all wavelengths, respectively. Right: the energy distribution of events that deposited over 15 p.e. in the 240 ns window summed across all 125 PMTs, revealing that a 15 p.e. cut corresponds to an energy threshold of about 10 MeV in the OD.

A toy Monte Carlo simulation was developed to assess the Outer Detector's efficiency in detecting supernova neutrinos. In each MC trial, N_{IBD} events are randomly chosen from the dataset of 2.5×10^6 positrons, including all positrons which did or did not trigger the OD. An event is deemed tagged if it yields more than 15 p.e. across all PMTs, in accordance with the trigger criteria defined in Chapter 5 and the energy threshold argument of the previous paragraph. A supernova is then considered detected if more than three IBD events are successfully tagged with over 15 p.e. each. This simulation is run 1,000 times for various values of N_{IBD}. Both burst detection efficiency and confidence intervals are determined for each value of N_{IBD}. Finally, the quantity N_{IBD} is converted to a GVKM supernova distance in kiloparsecs, using the 270 IBD event estimate at 10 kpc discussed in Section 6.3.2 and considering the inverse-square law for distance scaling. The findings, presented in Figure 6.6, suggest that the nEXO Outer Detector will perform as an effective neutrino burst detector for core-collapse supernovae within the Milky Way.

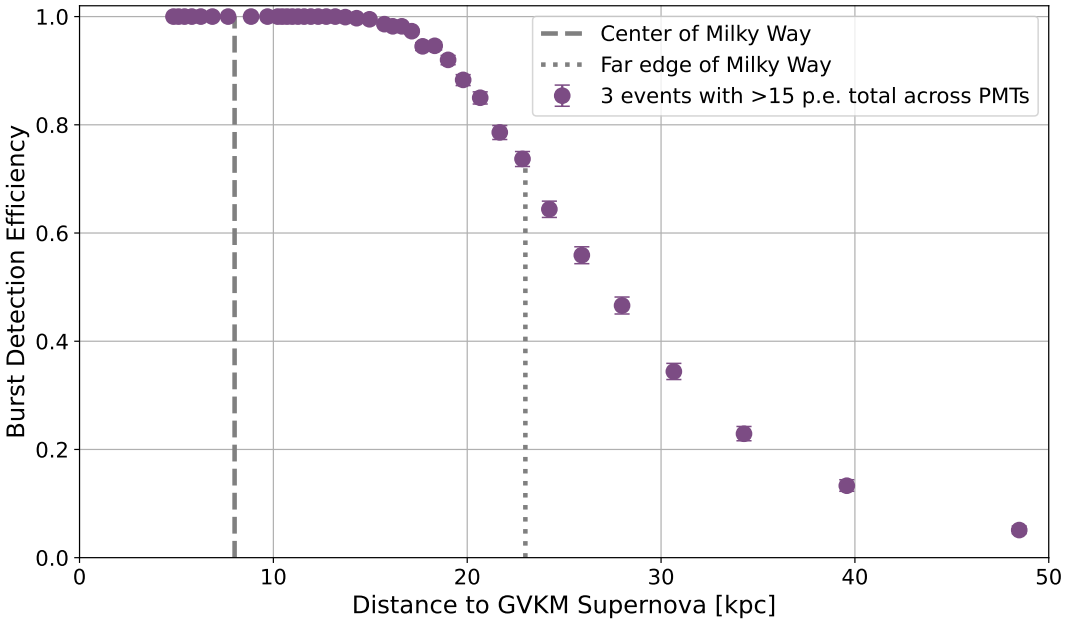

Figure 6.6: Burst detection efficiency as a function of distance to the GVKM host star. For a 5-fold PMT coincidence at s.p.e threshold. This plot is for the 125 PMT configuration, and 80% reflectivity on the floor and cylindrical wall, with the cryostat and ceiling set to be fully absorbing and 40% reflective at all wavelengths, respectively.

6.5 Discussion

nEXO is able to perform as an adequate supernova neutrino burst detector. In the TPC we expect to see a rise in the event rate in the multi-MeV range for core-collapse events a few kpc away. The dominant channel in the LXe will be charged current ν_e interactions on ^{136}Xe producing ^{136}Cs, but with significant contributions from neutral current inelastic scattering of ^{136}Xe nuclei. These events will produce γ-rays of several MeV in the LXe that will be detectable, but the details of these processes, and the exact de-excitation γ-lines are unexplored in this thesis.

In the baseline design with 125 PMTs in the OD, nEXO should be sensitive to CCSN in the Milky Way via the IBD channel for $\bar{\nu}_e$. This supernova trigger can comprisea minimum of three events above 10 MeV (15 p.e.) in 10 seconds. There should be no other interactions producing this amount of light in quick succession, other than a pileup of multiple radiogenic γ-rays in a 240 ns coincidence window, occurring thrice in ten seconds. Given the expected surface flux of γ-rays in the SNOLAB cryopit, this is deemed negligible for the context of this study. In this baseline configuration, nEXO is unlikely to be competitive against other supernova neutrino detectors in terms of temporal flux reconstruction (interaction rates low), or energy spectrum reconstruction (light collection efficiency low, and backgrounds below 10 MeV are significant) capabilities. Moreover, for a CCSN at some minimum distance the number of neutrino interactions will be sufficient to produce pileup, and the γ-rays from delayed neutron captures may contribute additional visible energy to uncorrelated events. This pileup effect has not been explored, but is a potential avenue of further study.

Within the TPC, where few events are expected, with many unmodelled γ-ray cascades

possible, it may be fruitful to have a continuous readout buffer saving the previous 30 seconds of data to disk, in the case of a SNEWS (or OD) CCSN alert. An example of such a readout system can be found in XENONnT [244]. The feasibility of this readout system should be explored, especially since the ability to do neutral current flavour-blind measurements is difficult to do in non-LXe experiments.

Since the conclusion of the studies presented in this thesis, the SNEWPY package has been released [245], providing an easier way to estimate interaction rates for many supernova models given water-Cherenkov and other detector configurations. This software can be coupled to `nexo-offline` to test SN model separation capabilities of nEXO, both in the LXe and the OD.

6.5.1 Dopants in the water?

The ability to tag neutron captures affiliated with IBD events will significantly reduce backgrounds for estimating neutrino interaction rates in the OD. Doping the water with gadolinium is a common method that is used [246], but a detailed study is outside the scope of this document as doing so would likely introduce more complications for purification, material stability, and γ-ray background control: each of the captured ambient underground neutrons will produce a $\sim$ 8 MeV γ-ray cascade about 1 m into the water tank at a rate of about 6 MHz, based on the SNOLAB neutron fluxes of $\sim$4,000 $\mathrm{m^{-2}s^{-1}}$ for both thermal and fast neutrons [247].

Doping the water with liquid scintillator as in [248] is another option, as it would increase the total light yield by a factor of $\sim$1.5 and provide a slightly improved energy resolution.

Unfortunately, this increase in light detection is still not sufficient to give strong motivation for doing so in the nEXO OD, given the existence of contemporary multi-kilotonne water-Cherenkov detectors like Super-K, SuperK-Gd, and its successor Hyper-K, which will be able to measure the energy spectrum of $\bar{\nu}_e$ flux much better due to IBD event statistics alone. Note that is difficult for long string detectors such as IceCube, KM3NeT, and P-ONE to provide much information other than an average energy, and detailed information on temporal flux evolution [249] due to the sparseness of their photosensors and an inability to tag individual events.

6.5.2 Supernova triangulation

Triangulation of supernova neutrinos across multiple experiments has become an increasingly popular topic in recent years [250]. These methods provide a quick and robust way to narrow down the search area for astronomers, and slew telescopes towards potential CCSN candidates sooner. Furthermore, they provide a way to push gravitational wave search sensitivity based on prompt neutrino localization (by focusing computational resources on regions of higher likelihood on a sky map). Triangulation can be done rather quickly if the experiments report the arrival time of the neutrino wave front to their respective locations. Overall this method is expected to produce a localization map much faster than other more precise methods such as reconstruction of electron tracks from elastic scatter ν_e-electron events in LAr (although these reconstruction methods provide a much more constrained search region on the sky). Triangulation methods rely on precise timing of the arrival of the neutrino wavefront from experiments located across the globe (neutrino crossing time

through the Earth at typical SN energies is ∼40 ms). At the moment of core collapse there is a sharp neutronization ν_e-burst emanating from the core of the star: $p+e^- \rightarrow n+\nu_e$. However, these events will not contribute to events in nEXO through the dominant interaction channel (IBD) as they cannot oscillate into anti-neutrino flavours. Moreover, they are likely to produce insufficient statistics to significantly contribute to a precise determination of the arrival of the neutrino wavefront given Poisson fluctuations on the number of events in the first milliseconds of the CCSN, as the full ten-second burst across all flavours is expected to produce $\mathcal{O}(100)$ events in the nEXO OD at 10 kpc. Still, one can imagine a scenario in which all SNOLAB experiments produce a single timestamp for the whole laboratory, and this may prove to be a more fruitful avenue to explore, especially in the case of DUNE (the next closest experiment) being offline during the CCSN event. Such an analysis is not explored in this thesis, albeit the relevant methods are developed in [250].

6.5.3 Pre-supernova neutrinos

The ability to detect pre-supernova neutrinos is possible in hydrogen-rich detectors (water-Cherenkov and liquid scintillator) for host stars at distances up to the 1 kpc scale [251]. This is because in the final days of a massive star's life, its $\bar{\nu}_e$ luminosity is expected to increase dramatically. Thus, by taking an average of IBD event rates (i.e., tagging each individual positron and neutron) every few hours, a statement on the probability of a nearby supernova happening in the proceeding hours can be made. With an increasing number of low-background experiments participating in this search, the ultimate reach of the global sensitivity to pre-SN neutrinos is expected to extend past the kiloparsec level.

nEXO's ability to participate in this effort was evaluated, and SNOLAB is good enough in terms of its geo-neutrino, and reactor neutrino background levels. However, the rate of γ-rays coming in from the rock is still too high to be able to individually tag an IBD neutron capture to any reasonable level without greatly increased localization capability in the OD ($<$ 1 m level), which would require a much higher PMT density and shielding of rock γ-rays in the SNOLAB cryopit. The $\bar{\nu}_e$ interaction rate in the TPC is too small to be fruitful for pre-SN searches.

6.5.4 Unique detection channels in liquid xenon

Observing the 'cooling' of metastable ^{136}Cs states in the LXe during the minutes post-supernova may be a method to constrain the total ν_e exposure in a rather unique way compared to other current and future experiments. However, these constraints will likely be inferior to those coming from LAr and multi-kilotonne water (ice) Cherenkov experiments should they be operational at the time.

The neutral current mechanisms available in nEXO's LXe are able to measure all neutrino and antineutrino fluxes of any flavour. However, the dominant CEνNS channel produces $\sim$keV nuclear recoil events, well below nEXO's trigger levels. Inelastic neutral current events produce ^{136}Xe γ-ray cascades to ground state that are expected to happen rather quickly, and charged current interactions will be of the same order of magnitude in number and of similar energy. However, a detection of prompt inelastic γ-ray cascades can be used to send out a SNEWS supernova alarm considering the typical event rate in the nEXO TPC is expected to be low ($\sim$ 1 Hz). In the case of a very close supernova ($\lesssim$1 kpc), these cascades

may be analysed to provide a crude measurement of the ν_x flux evolution, and total neutrino fluence, as this information is difficult to extract from other experiments.

Finally, unique signatures of nuclear de-excitation in the TPC from neutral current neutrino interactions can potentially trigger the Ba-tagging system of nEXO (this potential upgrade to nEXO is outlined in Section 3.5), whereby nuclei can be counted and backgrounds greatly reduced. I.e., tagging individual cesium and iodine nuclei can separate the charged current and neutral current events in the TPC if we are unable to do so by γ-cascade tagging alone. This can provide for a unique measurement system to constrain the flux of non-electron type neutrinos in non-CEνNS experiments.

Chapter 7

Conclusions and Outlook

In this thesis, I have performed novel calculations to estimate cosmogenic backgrounds in the nEXO experiment, a next-generation project designed to search for neutrinoless double-beta decay and investigate the Majorana nature of the neutrino. This work has led to a deeper understanding of cosmogenic ^{137}Xe production. Specifically, I have refined the sensitivity estimates of nEXO by accounting for activation multiplicity in the liquid xenon and introducing a novel light-only γ-cascade tag inside the TPC for the $^{136}\mathrm{Xe}(n,\gamma)^{137}\mathrm{Xe}$ process. This enhanced understanding has implications for nEXO's sensitivity to $0\nu\beta\beta$, which we found to asymptotically approach a halflife exclusion limit of 1.4×10^{28} years at 90% C.L., within the current background model and analysis framework.

Further investigations into cosmogenic activation were conducted using Geant4 simulations, which showed that muons contributing to backgrounds in the TPC are infrequent. Moreover, background-producing muons were observed to pass within a characteristic distance of less than 3 m from the center of the LXe volume, which is attributed to the characteristic transverse size scale of hadronic showers in the water tank. Therefore, we define the distance of closest approach of a muon to the center of the LXe as

the muon impact parameter and use this information to guide the development of the nEXO Outer Detector muon veto system.

To achieve our goal of a 95% tagging efficiency for muons that pass within a 3 m impact parameter, we developed a toy MC simulation that sampled waveforms from a uniform PMT layout in Geant4. This led us to select 125 PMTs as the baseline number of PMTs for the Outer Detector. We then employed Chroma, a GPU-accelerated photon propagation code, to understand how Cherenkov light from cosmogenic muons is incident on a detailed model of Outer Detector surfaces. This allowed us to explore the impact of varying levels of surface reflectivity on the muon tagging efficiency for our chosen 125 PMT configuration. Our findings suggest that an asymmetric arrangement of PMTs, biased slightly toward the lower half of the water tank, would be most effective, based on the expected light patterns of muons at SNOLAB. According to our Chroma simulations, achieving an average of 80% optical reflectivity on the tank's surfaces and deploying 125 PMTs should allow us to tag more than 97% of muons that pass through the Outer Detector. A cross-check in Geant4 corroborated the findings from Chroma and provided a tagging efficiency curve for muons as a function of muon impact parameter.

In the final chapter of this thesis, we determined that although nEXO will be sensitive to neutrino bursts from core collapse supernovae across the Milky Way, it will not be competitive in measuring supernova properties precisely compared to other experiments. The nEXO TPC will allow for observation of neutral current neutrino interactions, although the total interaction rates are significantly smaller than those of IBD on the hydrogen nuclei in the water tank. In future LXe experiments, these neutral current

interactions should be explored in more detail alongside CEνNS in order to get a handle on the flux and energies of non-electron type neutrinos and antineutrinos. These are expected to decouple deeper in the collapsing star, and so they experience different dynamics (MSW oscillations) as they propagate towards Earth. Non-CEνNS interactions in nEXO will produce MeV-scale γ- and β-like deposits in the TPC, which will reliably trigger the TPC readout. Identification of neutral current de-excitation cascades of xenon nuclei and the ability to constrain the number of neutral current interactions will be the most useful information to come from nEXO in the case of a galactic CCSN burst, as these interaction channels are highly suppressed in non-LXe experiments.

7.1 Future work

Several direct avenues exist for further developing the Geant4 simulations on cosmogenic activation and optimizing the ^{137}Xe veto veto algorithm. While these refinements may not substantially impact nEXO's sensitivity to $0\nu\beta\beta$ at SNOLAB, they become relevant for future LXe-based experiments and especially so for future experiments situated at shallower depths than SNOLAB.

The NEST software (the additional software connected to Geant4 that calculates the quanta released in LXe for specific particle types and electric field strengths) is not used in conjunction with the Shielding physics list for cosmogenic activation studies. Moreover, the ability to run light-enabled simulations in the TPC without optics enabled in the nEXO OD water volume or vice-versa is not possible. This means that it is currently not possible to run simulations of muons passing through the water tank and study their light patterns, yields,

light profiles etc... at the same time as studying cosmogenic activation inside the TPC. This problem should be addressed and the two physics lists used in the separate Geant4 studies reconciled. This upgrade will allow for a more direct MC-to-data comparison of hadronic shower production and characterization of the OD/TPC response for nEXO.

Ongoing FLUKA studies (not presented in this thesis), indicate that the average activation rate of ^{137}Xe matches that of the Shielding physics list in Geant4, i.e., between 10-20 ^{137}Xe atoms/yr in the full LXe volume are predicted. However, the spread in possible yearly activation rates from FLUKA is larger than those obtained from Geant4 studies. This could be a result of a smaller size of bootstrap samples in FLUKA, or an actual difference in the activation multiplicity between the two software frameworks. Moreover, KamLAND results indicate an overproduction of cosmogenic backgrounds in FLUKA compared to their experimental observations, which may translate to a reduced ^{137}Xe estimate for nEXO. Both these effects should be investigated and understood if a ^{137}Xe activation rate estimate with a higher accuracy is required.

The charge ratio of muons in nEXO simulations is held fixed for all simulated muon energies, but this is not necessarily the case. A further investigation into this, provided there is a consensus on the charge-ratio of underground muons as a function of energy, and the charge-dependence of activation (e.g., whether or not μ^--capture on atoms is a significant neutron production mechanism relevant to nEXO) should be investigated in the case of LXe experiments at shallower locations than SNOLAB. There, the muon energy spectrum is softer which enables additional μ^- capture from stopped muons.

The ^{136}Xe$(n, \gamma)^{137}$Xe TPC tag is presumed to trigger an associated veto window of 25

minutes in length. Increasing the length of this veto will not produce a significant change in the ultimate sensitivity of nEXO at SNOLAB, however this has not been explored for alternative sites, where the ^{137}Xe rate is expected to be much higher. This evaluation can follow the methods in Section 4.7.

To improve the ^{136}Xe$(n,\gamma)^{137}$Xe tag beyond what is presented in this thesis, there is a prominent ∼600 keV γ-line resulting from the ^{136}Xe$(n,\gamma)^{137}$Xe de-excitation cascade. This low-energy line can be used as a unique ^{137}Xe tag in the charge-readout of nEXO. By searching for 600 keV charge clusters on the anode of characteristic radius (depending on the attenuation length of this gamma line in LXe), one may be able to improve the ^{136}Xe$(n,\gamma)^{137}$Xe tag further, and approach the asymptotic limit of $0\nu\beta\beta$ sensitivity for a ^{137}Xe-free nEXO. Moreover, if larger LXe TPCs of the future are to be placed at shallower sites than SNOLAB, the 600 keV γ-line may help in reducing accidental deadtime from false coincidences due to activation correlation of ^{137}Xe with other isotopes, provided the γ-line is indeed unique to the ^{136}Xe$(n,\gamma)^{137}$Xe de-excitation process. Similarly, the delayed β-decay of ^{137}Xe, i.e., the background producing β-particle, has a 455 keV γ-line that is emitted simultaneously with a branching ratio of ∼30%. This reduces the DNN score for ^{137}Xe events, mitigating their impact on $0\nu\beta\beta$ sensitivity. This 455 keV line can be searched for in a charge-cluster analysis on the segmented anode of nEXO veto-tagged data, as it will provide an additional handle in cross-checking the efficiency of the ^{136}Xe$(n,\gamma)^{137}$Xe tag.

Optical properties of surfaces in the OD should be measured including potential wavelength-shifting effects from a reflective surface placed on top of bare stainless steel

surfaces. Moreover, measurements of the wavelength-dependent reflectivity of stainless steel, and the carbon fibre should be performed and encoded in both the Geant4 and Chroma codes.

In Chroma, the Cherenkov physics is currently written in the Pythonic-side of `chroma-simulation`, nEXO's Chroma-handling software. Calculations of photon generation points, momenta, and wavelengths, and polarizations are all done outside of the Chroma Singularity container that contains the compiled C++ code and communicates with CUDA-enabled GPUs. This can be refactored for a speed increase, such that all Cherenkov calculations (assuming straight-line trajectories of high energy particles) can be moved to the base C++ code. A new singularity container can then be released and open-sourced as part of the Chroma project on GitHub.

LXe TPCs could offer valuable insights into the dynamics of cosmogenic activation due to their strong particle identification capabilities. If a correlation exists between activation and nearby hadronic showers, the light profiles of muons accompanied by such showers in water-Cherenkov shields might serve as additional discriminators for assessing activation likelihood in a TPC. If this correlation proves strong, it would be worthwhile to incorporate the light profiles of these hadronic and electromagnetic showers into Chroma, provided the software's memory usage is refactored. Currently, Chroma could benefit from optimizations, especially in handling high-energy muon simulations. One avenue for improvement lies in balancing memory usage and data throughput between the GPU and RAM. A study could be conducted using a simple water-only geometry to assess simulation speed as a function of the number of muons and photons per muon. This would help identify an optimal balance and

inform strategies for efficient data processing and storage. Specifically, subsets of photons for each muon track, or even more generally, each event, could be processed and saved in a manner that minimizes data transfer latency between RAM, GPU, and disk storage, tailored to the specific capabilities of the available hardware.

As we look to the future, it is evident that nEXO is poised to become a cornerstone in the ongoing search for $0\nu\beta\beta$. The technological innovations and computational advancements born from the nEXO project serve as a testament to the leaps being made in experimental particle physics, and will continue to influence the research landscape in physics beyond the Standard Model. If nEXO successfully detects $0\nu\beta\beta$, it would prove a significant discovery, revealing the Majorana nature of neutrinos and thereby reshaping our understanding of particle physics and the Universe as a whole.

Bibliography

[1] Workman, R. L. *et al.*, "Review of Particle Physics," *PTEP*, vol. 2022, p. 083C01, **2022**. DOI: 10.1093/ptep/ptac097.

[2] Wikimedia Foundation, *Standard Model of Elementary Particles*, Online, Available at: https://en.wikipedia.org/wiki/File:Standard_Model_of_Elementary_Particles.svg, accessed: July 2023, **2019**.

[3] Noether, E., "Invariante Variationsprobleme," *Nachrichten von der Gesellschaft der Wissenschaften zu Göttingen, Mathematisch-Physikalische Klasse*, vol. 1918, pp. 235–257, **1918**.

[4] Noether, E., "Invariant variation problems," *Transport Theory and Statistical Physics*, vol. 1, no. 3, pp. 186–207, **1971**, ISSN: 0041-1450. DOI: 10.1080/00411457108231446.

[5] Wu, C. S., Ambler, E., Hayward, R. W., *et al.*, "Experimental Test of Parity Conservation in Beta Decay," *Physical Review*, vol. 105, no. 4, pp. 1413–1415, **1957**. DOI: 10.1103/PhysRev.105.1413.

[6] Lee, T. D. and Yang, C. N., "Question of Parity Conservation in Weak Interactions," *Physical Review*, vol. 104, no. 1, pp. 254–258, **1956**, ISSN: 0031-899X. DOI: 10.1103/PhysRev.104.254.

[7] Das, A., *Lectures on Quantum Field Theory*. WORLD SCIENTIFIC, **2008**, ch. 3, ISBN: 978-981-283-285-6 978-981-283-287-0. DOI: 10.1142/6938.

[8] Englert, F. and Brout, R., "Broken Symmetry and the Mass of Gauge Vector Mesons," *Physical Review Letters*, vol. 13, no. 9, pp. 321–323, **1964**, ISSN: 0031-9007. DOI: 10.1103/PhysRevLett.13.321.

[9] Higgs, P. W., "Broken symmetries, massless particles and gauge fields," *Physics Letters*, vol. 12, no. 2, pp. 132–133, **1964**, ISSN: 0031-9163. DOI: 10.1016/0031-9163(64)91136-9.

[10] Guralnik, G. S., Hagen, C. R., and Kibble, T. W. B., "Global Conservation Laws and Massless Particles," *Physical Review Letters*, vol. 13, no. 20, pp. 585–587, **1964**, ISSN: 0031-9007. DOI: 10.1103/PhysRevLett.13.585.

[11] Higgs, P. W., "Spontaneous Symmetry Breakdown without Massless Bosons," *Physical Review*, vol. 145, no. 4, pp. 1156–1163, **1966**. DOI: 10.1103/PhysRev.145.1156.

[12] Weinberg, S., "A Model of Leptons," *Physical Review Letters*, vol. 19, no. 21, pp. 1264–1266, **1967**, ISSN: 0031-9007. DOI: 10.1103/PhysRevLett.19.1264.

[13] Salam, A. and Ward, J. C., "Weak and electromagnetic interactions," *Il Nuovo Cimento (1955-1965)*, vol. 11, no. 4, pp. 568–577, **1959**, ISSN: 1827-6121. DOI: 10.1007/BF02726525.

[14] Glashow, S. L., "Partial-symmetries of weak interactions," *Nuclear Physics*, vol. 22, no. 4, pp. 579–588, **1961**, ISSN: 00295582. DOI: 10.1016/0029-5582(61)90469-2.

[15] Nambu, Y. and Jona-Lasinio, G., "Dynamical Model of Elementary Particles Based on an Analogy with Superconductivity. I," *Physical Review*, vol. 122, no. 1, pp. 345–358, **1961**. DOI: 10.1103/PhysRev.122.345.

[16] Quigg, C., *Gauge Theories Of Strong, Weak, And Electromagnetic Interactions*. Boca Raton: CRC Press, **2021**, ISBN: 978-0-429-03497-8. DOI: 10.1201/9780429034978.

[17] Quigg, C., "Electroweak Symmetry Breaking in Historical Perspective," *Annual Review of Nuclear and Particle Science*, vol. 65, no. 1, pp. 25–42, **2015**. DOI: 10.1146/annurev-nucl-102313-025537.

[18] Anderson, P. W., "Plasmons, Gauge Invariance, and Mass," *Physical Review*, vol. 130, pp. 439–442, **1963**, ISSN: 1536-6065. DOI: 10.1103/PhysRev.130.439.

[19] Goldstone, J., Salam, A., and Weinberg, S., "Broken Symmetries," *Physical Review*, vol. 127, no. 3, pp. 965–970, **1962**. DOI: 10.1103/PhysRev.127.965.

[20] The CMS Collaboration, "A portrait of the Higgs boson by the CMS experiment ten years after the discovery," *Nature*, vol. 607, no. 7917, pp. 60–68, **2022**, Number: 7917 Publisher: Nature Publishing Group, ISSN: 1476-4687. DOI: 10.1038/s41586-022-04892-x.

[21] The ATLAS Collaboration, "A detailed map of Higgs boson interactions by the ATLAS experiment ten years after the discovery," *Nature*, vol. 607, no. 7917, pp. 52–59, **2022**, Number: 7917 Publisher: Nature Publishing Group, ISSN: 1476-4687. DOI: 10.1038/s41586-022-04893-w.

[22] Planck Collaboration, Aghanim, N., Akrami, Y., *et al.*, "*Planck* 2018 results: VI. Cosmological parameters," *Astronomy & Astrophysics*, vol. 641, A6, **2020**, ISSN: 0004-6361, 1432-0746. DOI: 10.1051/0004-6361/201833910.

[23] Abazajian, K., Addison, G., Adshead, P., *et al.*, *CMB-S4 Science Case, Reference Design, and Project Plan*, arXiv:1907.04473, **2019**.

[24] KamLAND-Zen Collaboration, Abe, S., Asami, S., *et al.*, "Search for the Majorana Nature of Neutrinos in the Inverted Mass Ordering Region with KamLAND-Zen," *Physical Review Letters*, vol. 130, no. 5, p. 051 801, **2023**. DOI: 10.1103/PhysRevLett.130.051801.

[25] nEXO Collaboration, Adhikari, G., Al Kharusi, S., *et al.*, "nEXO: Neutrinoless double beta decay search beyond 10^{28} year half-life sensitivity," *Journal of Physics G: Nuclear and Particle Physics*, vol. 49, no. 1, p. 015 104, **2021**, ISSN: 0954-3899. DOI: 10.1088/1361-6471/ac3631.

[26] The KATRIN Collaboration, Aker, M., Beglarian, A., *et al.*, "Direct neutrino-mass measurement with sub-electronvolt sensitivity," *Nature Physics*, vol. 18, no. 2, pp. 160–166, **2022**, ISSN: 1745-2481. DOI: 10.1038/s41567-021-01463-1.

[27] Pauli, W., "Dear radioactive ladies and gentlemen," *Phys. Today*, vol. 31N9, p. 27, **1978**.

[28] Reines, F. and Cowan, C. L., "The Neutrino," *Nature*, vol. 178, no. 4531, pp. 446–449, **1956**.

[29] Davis, R., "A review of the homestake solar neutrino experiment," *Progress in Particle and Nuclear Physics*, vol. 32, pp. 13–32, **1994**, ISSN: 0146-6410. DOI: 10.1016/0146-6410(94)90004-3.

[30] Bahcall, J. N., "Solar Neutrinos. I. Theoretical," *Physical Review Letters*, vol. 12, no. 11, pp. 300–302, **1964**. DOI: 10.1103/PhysRevLett.12.300.

[31] Bahcall, J. N. and Pinsonneault, M. H., "Standard solar models, with and without helium diffusion, and the solar neutrino problem," *Reviews of Modern Physics*, vol. 64, no. 4, pp. 885–926, **1992**. DOI: 10.1103/RevModPhys.64.885.

[32] Pontecorvo, B., "Mesonium and antimesonium," *Zhur. Eksptl'. i Teoret. Fiz.*, vol. Vol: 33, **1957**, Institution: Joint Inst. of Nuclear Research.

[33] Maki, Z., Nakagawa, M., and Sakata, S., "Remarks on the Unified Model of Elementary Particles," *Progress of Theoretical Physics*, vol. 28, no. 5, pp. 870–880, **1962**, ISSN: 0033-068X. DOI: 10.1143/PTP.28.870.

[34] Kawakami, H., Kato, S., Ohshima, T., *et al.*, "New upper bound on the electron anti-neutrino mass," *Physics Letters B*, vol. 256, no. 1, pp. 105–111, **1991**, ISSN: 0370-2693. DOI: 10.1016/0370-2693(91)90226-G.

[35] Holzschuh, E., Fritschi, M., and Kündig, W., "Measurement of the electron neutrino mass from tritium -decay," *Physics Letters B*, vol. 287, no. 4, pp. 381–388, **1992**, ISSN: 0370-2693. DOI: 10.1016/0370-2693(92)91000-Y.

[36] Weinheimer, C., Przyrembel, M., Backe, H., *et al.*, "Improved limit on the electron-antineutrino rest mass from tritium -decay," *Physics Letters B*, vol. 300, no. 3, pp. 210–216, **1993**, ISSN: 0370-2693. DOI: 10.1016/0370-2693(93)90355-L.

[37] Belesev, A. I., Bleule, A. I., Geraskin, E. V., *et al.*, "Results of the troitsk experiment on the search for the electron antineutrino rest mass in tritium beta-decay," *Physics Letters B*, vol. 350, no. 2, pp. 263–272, **1995**, ISSN: 0370-2693. DOI: 10.1016/0370-2693(95)00335-I.

[38] Weinheimer, C., Degenddag, B., Bleile, A., *et al.*, "High precision measurement of the tritium spectrum near its endpoint and upper limit on the neutrino mass," *Physics Letters B*, vol. 460, no. 1, pp. 219–226, **1999**, ISSN: 0370-2693. DOI: 10.1016/S0370-2693(99)00780-7.

[39] Goldhaber, M., Grodzins, L., and Sunyar, A. W., "Helicity of Neutrinos," *Physical Review*, vol. 109, no. 3, pp. 1015–1017, **1958**. DOI: 10.1103/PhysRev.109.1015.

[40] Hirata, K. S., Kajita, T., Kifune, T., *et al.*, "Observation of ^{8}B solar neutrinos in the Kamiokande-II detector," *Physical Review Letters*, vol. 63, no. 1, pp. 16–19, **1989**. DOI: 10.1103/PhysRevLett.63.16.

[41] Suzuki, Y., "Kamiokande solar neutrino results," *Nuclear Physics B - Proceedings Supplements*, Neutrino 94, vol. 38, no. 1, pp. 54–59, **1995**, ISSN: 0920-5632. DOI: 10.1016/0920-5632(94)00733-C.

[42] Super-Kamiokande Collaboration, Fukuda, Y., Hayakawa, T., *et al.*, "Evidence for Oscillation of Atmospheric Neutrinos," *Physical Review Letters*, vol. 81, no. 8, pp. 1562–1567, **1998**. DOI: 10.1103/PhysRevLett.81.1562.

[43] SNO Collaboration, Ahmad, Q. R., Allen, R. C., *et al.*, "Direct Evidence for Neutrino Flavor Transformation from Neutral-Current Interactions in the Sudbury Neutrino Observatory," *Physical Review Letters*, vol. 89, no. 1, p. 011 301, **2002**. DOI: 10.1103/PhysRevLett.89.011301.

[44] Davis, R. and Jr, *Solar Neutrinos: The First Thirty Years*. Boca Raton: CRC Press, **2019**, ISBN: 978-0-429-50281-1. DOI: 10.1201/9780429502811.

[45] Wolfenstein, L., "Neutrino oscillations in matter," *Physical Review D*, vol. 17, no. 9, pp. 2369–2374, **1978**. DOI: 10.1103/PhysRevD.17.2369.

[46] Mikheyev, S. P. and Smirnov, A. Y., "Resonance Amplification of Oscillations in Matter and Spectroscopy of Solar Neutrinos," *Sov. J. Nucl. Phys.*, vol. 42, pp. 913–917, **1985**.

[47] Pontecorvo, B., "Neutrino experiments and the question of leptonic-charge conservation," *Old and New Problems in Elementary Particles*, p. 251, **2012**.

[48] Giganti, C., Lavignac, S., and Zito, M., "Neutrino oscillations: The rise of the PMNS paradigm," *Progress in Particle and Nuclear Physics*, vol. 98, pp. 1–54, **2018**, ISSN: 0146-6410. DOI: 10.1016/j.ppnp.2017.10.001.

[49] Holstein, B. R., "The mysterious disappearance of Ettore Majorana," *Journal of Physics: Conference Series*, vol. 173, p. 012 019, **2009**, ISSN: 1742-6596. DOI: 10.1088/1742-6596/173/1/012019.

[50] Majorana, E., "Teoria simmetrica dell'elettrone e del positrone," *Il Nuovo Cimento (1924-1942)*, vol. 14, no. 4, pp. 171–184, **1937**, ISSN: 1827-6121. DOI: 10.1007/BF02961314.

[51] Minkowski, P., "$\mu \to e\gamma$ at a rate of one out of 10^9 muon decays?" *Physics Letters B*, vol. 67, no. 4, pp. 421–428, **1977**, ISSN: 0370-2693. DOI: 10.1016/0370-2693(77)90435-X.

[52] Gell-Mann, M., Ramond, P., and Slansky, R., "Complex Spinors and Unified Theories," *Conf. Proc. C*, vol. 790927, pp. 315–321, **1979**.

[53] Yanagida, T., "Horizontal gauge symmetry and masses of neutrinos," *Conf. Proc. C*, vol. 7902131, Sawada, O. and Sugamoto, A., Eds., pp. 95–99, **1979**.

[54] Weinberg, S., "Baryon- and Lepton-Nonconserving Processes," *Physical Review Letters*, vol. 43, no. 21, pp. 1566–1570, **1979**. DOI: 10.1103/PhysRevLett.43.1566.

[55] Ma, E., "Pathways to Naturally Small Neutrino Masses," *Physical Review Letters*, vol. 81, no. 6, pp. 1171–1174, **1998**. DOI: 10.1103/PhysRevLett.81.1171.

[56] Bonnet, F., Hirsch, M., Ota, T., *et al.*, "Systematic study of the d = 5 Weinberg operator at one-loop order," *Journal of High Energy Physics*, vol. 2012, no. 7, p. 153, **2012**, ISSN: 1029-8479. DOI: 10.1007/JHEP07(2012)153.

[57] Weldon, H. A. and Zee, A., "Operator analysis of new physics," *Nuclear Physics B*, vol. 173, no. 2, pp. 269–290, **1980**, ISSN: 0550-3213. DOI: 10.1016/0550-3213(80)90218-7.

[58] Aguila, F. del, Aparici, A., Bhattacharya, S., *et al.*, "Effective Lagrangian approach to neutrinoless double beta decay and neutrino masses," *Journal of High Energy Physics*, vol. 2012, no. 6, p. 146, **2012**, ISSN: 1029-8479. DOI: 10.1007/JHEP06(2012)146.

[59] IceCube Collaboration, Aartsen, M. G., Abbasi, R., *et al.*, "First Observation of PeV-Energy Neutrinos with IceCube," *Physical Review Letters*, vol. 111, no. 2, p. 021 103, **2013**. DOI: 10.1103/PhysRevLett.111.021103.

[60] IceCube Collaboration*†, Abbasi, R., Ackermann, M., *et al.*, "Observation of high-energy neutrinos from the Galactic plane," *Science*, vol. 380, no. 6652, pp. 1338–1343, **2023**, ISSN: 0036-8075, 1095-9203. DOI: 10.1126/science.adc9818.

[61] IceCube Collaboration, MAGIC, AGILE, *et al.*, "Multimessenger observations of a flaring blazar coincident with high-energy neutrino IceCube-170922A," *Science*, vol. 361, no. 6398, eaat1378, **2018**. DOI: 10.1126/science.aat1378.

[62] Coloma, P. and Pascoli, S., "Theory and Phenomenology of Mass Ordering and CP Violation," *The State of the Art of Neutrino Physics*, ser. Advanced Series on Directions in High Energy Physics **Volume 28**, vol. Volume 28, WORLD SCIENTIFIC, **2017**, pp. 497–542, ISBN: 978-981-322-608-1. DOI: 10.1142/9789813226098_0013.

[63] Pitrou, C., Coc, A., Uzan, J.-P., *et al.*, "Precision big bang nucleosynthesis with improved Helium-4 predictions," *Physics Reports*, Precision big bang nucleosynthesis with improved Helium-4 predictions, vol. 754, pp. 1–66, **2018**, ISSN: 0370-1573. DOI: 10.1016/j.physrep.2018.04.005.

[64] Sakharov, A. D., "Violation of CP-invariance, C-asymmetry, and baryon asymmetry of the Universe," *In The Intermissions... Collected Works on Research into the Essentials of Theoretical Physics in Russian Federal Nuclear Center, Arzamas-16*, World Scientific, **1998**, pp. 84–87.

[65] 't Hooft, G., "Symmetry Breaking through Bell-Jackiw Anomalies," *Physical Review Letters*, vol. 37, pp. 8–11, **1976**, ISSN: 0031-9007. DOI: 10.1103/PhysRevLett.37.8.

[66] Klinkhamer, F. R. and Manton, N. S., "A saddle-point solution in the Weinberg-Salam theory," *Physical Review D*, vol. 30, no. 10, pp. 2212–2220, **1984**. DOI: 10.1103/PhysRevD.30.2212.

[67] Arnold, P. and McLerran, L., "Sphalerons, small fluctuations, and baryon-number violation in electroweak theory," *Physical Review D*, vol. 36, no. 2, pp. 581–595, **1987**. DOI: 10.1103/PhysRevD.36.581.

[68] Manton, N. S., "The inevitability of sphalerons in field theory," *Philosophical Transactions of the Royal Society A: Mathematical, Physical and Engineering Sciences*, vol. 377, no. 2161, p. 20 180 327, **2019**. DOI: 10.1098/rsta.2018.0327.

[69] Dimopoulos, S. and Susskind, L., "Baryon number of the universe," *Physical Review D*, vol. 18, no. 12, pp. 4500–4509, **1978**. DOI: 10.1103/PhysRevD.18.4500.

[70] Fukugita, M. and Yanagida, T., "Barygenesis without grand unification," *Physics Letters B*, vol. 174, no. 1, pp. 45–47, **1986**, ISSN: 0370-2693. DOI: 10.1016/0370-2693(86)91126-3.

[71] Barbieri, R., Creminelli, P., Strumia, A., *et al.*, "Baryogenesis through leptogenesis," *Nuclear Physics B*, vol. 575, no. 1-2, pp. 61–77, **2000**, ISSN: 05503213. DOI: 10.1016/S0550-3213(00)00011-0.

[72] Davidson, S., Nardi, E., and Nir, Y., "Leptogenesis," *Physics Reports*, vol. 466, no. 4-5, pp. 105–177, **2008**, ISSN: 03701573. DOI: 10.1016/j.physrep.2008.06.002.

[73] Rubakov, V. A. and Shaposhnikov, M. E., "Electroweak baryon number non-conservation in the early Universe and in high-energy collisions," *Physics-Uspekhi*, vol. 39, no. 5, p. 461, **1996**, ISSN: 1063-7869. DOI: 10.1070/PU1996v039n05ABEH000145.

[74] Janka, H.-T., "Explosion Mechanisms of Core-Collapse Supernovae," *Annual Review of Nuclear and Particle Science*, vol. 62, no. 1, pp. 407–451, **2012**. DOI: 10.1146/annurev-nucl-102711-094901.

[75] McCray, R. and Fransson, C., "The Remnant of Supernova 1987A," *Annual Review of Astronomy and Astrophysics*, vol. 54, no. 1, pp. 19–52, **2016**. DOI: 10.1146/annurev-astro-082615-105405.

[76] Arnett, W. D. and Rosner, J. L., "Neutrino mass limits from SN1987A," *Physical Review Letters*, vol. 58, no. 18, pp. 1906–1909, **1987**. DOI: 10.1103/PhysRevLett.58.1906.

[77] Costantini, M. L., Ianni, A., and Vissani, F., "SN1987A and the properties of the neutrino burst," *Physical Review D*, vol. 70, no. 4, p. 043 006, **2004**. DOI: 10.1103/PhysRevD.70.043006.

[78] Ansoldi, S., Antonelli, L. A., Arcaro, C., *et al.*, "The Blazar TXS 0506+056 Associated with a High-energy Neutrino: Insights into Extragalactic Jets and Cosmic-Ray Acceleration," *The Astrophysical Journal Letters*, vol. 863, no. 1, p. L10, **2018**, ISSN: 2041-8205. DOI: 10.3847/2041-8213/aad083.

[79] LIGO Scientific Collaboration and Virgo Collaboration, Abbott, B. P., *et al.*, "GW170817: Observation of Gravitational Waves from a Binary Neutron Star Inspiral," *Physical Review Letters*, vol. 119, no. 16, p. 161 101, **2017**. DOI: 10.1103/PhysRevLett.119.161101.

[80] Cowan, J. J., Sneden, C., Lawler, J. E., *et al.*, "Origin of the heaviest elements: The rapid neutron-capture process," *Reviews of Modern Physics*, vol. 93, no. 1, p. 015 002, **2021**. DOI: 10.1103/RevModPhys.93.015002.

[81] LIGO Scientific Collaboration and Virgo Collaboration, Abbott, B. P., Abbott, R., *et al.*, "Tests of General Relativity with GW170817," *Physical Review Letters*, vol. 123, no. 1, p. 011 102, **2019**. DOI: 10.1103/PhysRevLett.123.011102.

[82] Abbott, B. P., Abbott, R., Abbott, T. D., *et al.*, "A gravitational-wave standard siren measurement of the Hubble constant," *Nature*, vol. 551, no. 7678, pp. 85–88, **2017**, ISSN: 1476-4687. DOI: 10.1038/nature24471.

[83] Chakravarti, K., Chakraborty, S., Phukon, K. S., *et al.*, "Constraining extra-spatial dimensions with observations of GW170817," *Classical and Quantum Gravity*, vol. 37, no. 10, p. 105 004, **2020**, ISSN: 0264-9381. DOI: 10.1088/1361-6382/ab8355.

[84] Abdikamalov, E., Pagliaroli, G., and Radice, D., "Gravitational Waves from Core-Collapse Supernovae," *Handbook of Gravitational Wave Astronomy*, Bambi, C., Katsanevas, S., and Kokkotas, K. D., Eds., Singapore: Springer Singapore, **2021**, pp. 1–37, ISBN: 9789811547027. DOI: 10.1007/978-981-15-4702-7_21-1.

[85] Drago, M., Klimenko, S., Lazzaro, C., *et al.*, "Coherent WaveBurst, a pipeline for unmodeled gravitational-wave data analysis," *SoftwareX*, vol. 14, p. 100 678, **2021**, ISSN: 23527110. DOI: 10.1016/j.softx.2021.100678.

[86] Nakamura, K., Horiuchi, S., Tanaka, M., *et al.*, "Multimessenger signals of long-term core-collapse supernova simulations: Synergetic observation strategies," *Monthly Notices of the Royal Astronomical Society*, vol. 461, no. 3, pp. 3296–3313, **2016**, ISSN: 0035-8711, 1365-2966. DOI: 10.1093/mnras/stw1453.

[87] Maltoni, M. and Yu. Smirnov, A., "Solar neutrinos and neutrino physics," *The European Physical Journal A*, vol. 52, no. 4, p. 87, **2016**, ISSN: 1434-601X. DOI: 10.1140/epja/i2016-16087-0.

[88] Double Chooz Collaboration, Abe, Y., Aberle, C., *et al.*, "Indication of reactor νe disappearance in the double chooz experiment," *Physical Review Letters*, vol. 108, no. 13, p. 131 801, **2012**. DOI: 10.1103/PhysRevLett.108.131801.

[89] An, F. P., Bai, J. Z., Balantekin, A. B., *et al.*, "Observation of Electron-Antineutrino Disappearance at Daya Bay," *Physical Review Letters*, vol. 108, no. 17, p. 171 803, **2012**. DOI: 10.1103/PhysRevLett.108.171803.

[90] RENO Collaboration, Ahn, J. K., Chebotaryov, S., *et al.*, "Observation of Reactor Electron Antineutrinos Disappearance in the RENO Experiment," *Physical Review Letters*, vol. 108, no. 19, p. 191 802, **2012**. DOI: 10.1103/PhysRevLett.108.191802.

[91] Ahn, S. H., An, S., Aoki, S., *et al.*, "Detection of accelerator-produced neutrinos at a distance of 250 km," *Physics Letters B*, vol. 511, no. 2, pp. 178–184, **2001**, ISSN: 0370-2693. DOI: 10.1016/S0370-2693(01)00647-5.

[92] T2K Collaboration, Abe, K., Adam, J., *et al.*, "Observation of Electron Neutrino Appearance in a Muon Neutrino Beam," *Physical Review Letters*, vol. 112, no. 6, p. 061 802, **2014**. DOI: 10.1103/PhysRevLett.112.061802.

[93] Kopp, S., "The NuMI Neutrino Beam at Fermilab," *Proceedings of the 2005 Particle Accelerator Conference*, **2005**, pp. 1–3. DOI: 10.1109/PAC.2005.1590344.

[94] MINOS Collaboration, Michael, D. G., Adamson, P., *et al.*, "Observation of Muon Neutrino Disappearance with the MINOS Detectors in the NuMI Neutrino Beam," *Physical Review Letters*, vol. 97, no. 19, p. 191 801, **2006**. DOI: 10.1103/PhysRevLett.97.191801.

[95] Worcester, E., "Neutrino Mystery Endures," *Physics*, vol. 15, p. 85, **2022**. DOI: 10.1103/PhysRevLett.128.241801.

[96] Xing, Z.-z., "Flavor structures of charged fermions and massive neutrinos," *Physics Reports*, vol. 854, pp. 1–147, **2020**, ISSN: 03701573. DOI: 10.1016/j.physrep.2020.02.001.

[97] Abi, B., Acciarri, R., Acero, M. A., *et al.*, *Deep Underground Neutrino Experiment (DUNE), Far Detector Technical Design Report, Volume II: DUNE Physics*, arXiv:2002.03005, **2020**.

[98] Hyper-Kamiokande Proto-Collaboration, Abe, K., *et al.*, *Hyper-Kamiokande Design Report*, arXiv:1805.04163, **2018**.

[99] An, F., An, G., An, Q., *et al.*, "Neutrino physics with JUNO," *Journal of Physics G: Nuclear and Particle Physics*, vol. 43, no. 3, p. 030 401, **2016**, ISSN: 0954-3899. DOI: 10.1088/0954-3899/43/3/030401.

[100] Faverzani, M., Alpert, B., Backer, D., *et al.*, "The HOLMES Experiment," *Journal of Low Temperature Physics*, vol. 184, no. 3, pp. 922–929, **2016**, ISSN: 1573-7357. DOI: 10.1007/s10909-016-1540-x.

[101] Gastaldo, L., Blaum, K., Chrysalidis, K., *et al.*, "The electron capture in ^{163}Ho experiment – ECHo," *The European Physical Journal Special Topics*, vol. 226, no. 8, pp. 1623–1694, **2017**, ISSN: 1951-6401. DOI: 10.1140/epjst/e2017-70071-y.

[102] Esfahani, A. A., Asner, D. M., Böser, S., *et al.*, "Determining the neutrino mass with cyclotron radiation emission spectroscopy—Project 8," *Journal of Physics G: Nuclear and Particle Physics*, vol. 44, no. 5, p. 054 004, **2017**, ISSN: 0954-3899. DOI: 10.1088/1361-6471/aa5b4f.

[103] Sachs, R. K. and Wolfe, A. M., "Perturbations of a Cosmological Model and Angular Variations of the Microwave Background," *The Astrophysical Journal*, vol. 147, p. 73, **1967**, ISSN: 0004-637X. DOI: 10.1086/148982.

[104] Dodelson, S., Gates, E., and Stebbins, A., "Cold + Hot Dark Matter and the Cosmic Microwave Background," *The Astrophysical Journal*, vol. 467, p. 10, **1996**, ISSN: 0004-637X. DOI: 10.1086/177581.

[105] Hu, W. and Dodelson, S., "Cosmic Microwave Background Anisotropies," *Annual Review of Astronomy and Astrophysics*, vol. 40, no. 1, pp. 171–216, **2002**. DOI: 10.1146/annurev.astro.40.060401.093926.

[106] Koyama, K., "Cosmological tests of modified gravity," *Reports on Progress in Physics*, vol. 79, no. 4, p. 046 902, **2016**, ISSN: 0034-4885. DOI: 10.1088/0034-4885/79/4/046902.

[107] Mangano, G., Miele, G., Pastor, S., *et al.*, "Relic neutrino decoupling including flavour oscillations," *Nuclear Physics B*, vol. 729, no. 1, pp. 221–234, **2005**, ISSN: 0550-3213. DOI: 10.1016/j.nuclphysb.2005.09.041.

[108] Tegmark, M., Blanton, M. R., Strauss, M. A., *et al.*, "The Three-Dimensional Power Spectrum of Galaxies from the Sloan Digital Sky Survey," *The Astrophysical Journal*, vol. 606, no. 2, p. 702, **2004**, ISSN: 0004-637X. DOI: 10.1086/382125.

[109] BOSS Collaboration, Aubourg, É., Bailey, S., *et al.*, "Cosmological implications of baryon acoustic oscillation measurements," *Physical Review D*, vol. 92, no. 12, p. 123 516, **2015**. DOI: 10.1103/PhysRevD.92.123516.

[110] Dark Energy Survey Collaboration: Abbott, T., Abdalla, F. B., *et al.*, "The Dark Energy Survey: More than dark energy – an overview," *Monthly Notices of the Royal Astronomical Society*, vol. 460, no. 2, pp. 1270–1299, **2016**, ISSN: 0035-8711. DOI: 10.1093/mnras/stw641.

[111] Palanque-Delabrouille, N., Yèche, C., Baur, J., *et al.*, "Neutrino masses and cosmology with Lyman-alpha forest power spectrum," *Journal of Cosmology and Astroparticle Physics*, vol. 2015, no. 11, p. 011, **2015**, ISSN: 1475-7516. DOI: 10.1088/1475-7516/2015/11/011.

[112] Ahumada, R., Prieto, C. A., Almeida, A., *et al.*, "The 16th Data Release of the Sloan Digital Sky Surveys: First Release from the APOGEE-2 Southern Survey and Full Release of eBOSS Spectra," *The Astrophysical Journal Supplement Series*, vol. 249, no. 1, p. 3, **2020**, ISSN: 0067-0049. DOI: 10.3847/1538-4365/ab929e.

[113] DESI Collaboration, Aghamousa, A., Aguilar, J., *et al.*, *The DESI Experiment Part I: Science,Targeting, and Survey Design*, arXiv:1611.00036, **2016**. DOI: 10.48550/arXiv.1611.00036.

[114] Ivezić, Ž., Kahn, S. M., Tyson, J. A., *et al.*, "LSST: From Science Drivers to Reference Design and Anticipated Data Products," *The Astrophysical Journal*, vol. 873, no. 2, p. 111, **2019**, ISSN: 0004-637X. DOI: 10.3847/1538-4357/ab042c.

[115] Goeppert-Mayer, M., "Double Beta-Disintegration," *Physical Review*, vol. 48, no. 6, pp. 512–516, **1935**. DOI: 10.1103/PhysRev.48.512.

[116] Wang, M., Huang, W. J., Kondev, F. G., *et al.*, "The AME 2020 atomic mass evaluation (II). Tables, graphs and references*," *Chinese Physics C*, vol. 45, no. 3, p. 030 003, **2021**, ISSN: 1674-1137. DOI: 10.1088/1674-1137/abddaf.

[117] Elliott, S. R., Hahn, A. A., and Moe, M. K., "Direct evidence for two-neutrino double-beta decay in ^{82}Se," *Physical Review Letters*, vol. 59, no. 18, pp. 2020–2023, **1987**. DOI: 10.1103/PhysRevLett.59.2020.

[118] Miley, H. S., Avignone, F. T., Brodzinski, R. L., *et al.*, "Suggestive evidence for the two-neutrino double-beta decay of ^{76}Ge," *Physical Review Letters*, vol. 65, no. 25, pp. 3092–3095, **1990**. DOI: 10.1103/PhysRevLett.65.3092.

[119] Arnold, R., Caurier, E., Guyonnet, J. L., *et al.*, "Observation of two neutrino double beta decay of ^{116}Cd with the tracking detector NEMO-2," *JETP Letters*, vol. 61, p. 170, **1995**.

[120] Barabash, A. S., Avignone, F. T., Collar, J. I., *et al.*, "Two neutrino double-beta decay of ^{100}Mo to the first excited 0^+ state in ^{100}Ru," *Physics Letters B*, vol. 345, no. 4, pp. 408–413, **1995**, ISSN: 0370-2693. DOI: 10.1016/0370-2693(94)01657-X.

[121] EXO Collaboration, Ackerman, N., Aharmim, B., *et al.*, "Observation of Two-Neutrino Double-Beta Decay in ^{136}Xe with the EXO-200 Detector," *Physical Review Letters*, vol. 107, no. 21, p. 212 501, **2011**. DOI: 10.1103/PhysRevLett.107.212501.

[122] Alduino, C., Alfonso, K., Artusa, D. R., *et al.*, "Measurement of the two-neutrino double-beta decay half-life of ^{130}Te with the CUORE-0 experiment," *The European*

Physical Journal C, vol. 77, no. 1, p. 13, **2017**, ISSN: 1434-6052. DOI: 10.1140/epjc/s10052-016-4498-6.

[123] Saakyan, R., "Two-Neutrino Double-Beta Decay," *Annual Review of Nuclear and Particle Science*, vol. 63, no. 1, pp. 503–529, **2013**. DOI: 10.1146/annurev-nucl-102711-094904.

[124] Schechter, J. and Valle, J. W. F., "Neutrinoless double-beta decay in SU(2) × U(1) theories," *Physical Review D*, vol. 25, no. 11, pp. 2951–2954, **1982**. DOI: 10.1103/PhysRevD.25.2951.

[125] Furry, W. H., "On Transition Probabilities in Double Beta-Disintegration," *Physical Review*, vol. 56, no. 12, pp. 1184–1193, **1939**. DOI: 10.1103/PhysRev.56.1184.

[126] Dell'Oro, S., Marcocci, S., Viel, M., *et al.*, "Neutrinoless Double Beta Decay: 2015 Review," *Advances in High Energy Physics*, vol. 2016, pp. 1–37, **2016**, ISSN: 1687-7357, 1687-7365. DOI: 10.1155/2016/2162659.

[127] Dolinski, M. J., Poon, A. W., and Rodejohann, W., "Neutrinoless Double-Beta Decay: Status and Prospects," *Annual Review of Nuclear and Particle Science*, vol. 69, no. 1, pp. 219–251, **2019**. DOI: 10.1146/annurev-nucl-101918-023407.

[128] Agostini, M., Bakalyarov, A. M., Balata, M., *et al.*, "Probing Majorana neutrinos with double-β decay," *Science*, vol. 365, no. 6460, pp. 1445–1448, **2019**. DOI: 10.1126/science.aav8613.

[129] Zsigmond, A.J. for the LEGEND Collaboration, "LEGEND: The future of neutrinoless double-beta decay search with germanium detectors," *Journal of*

Physics: Conference Series, vol. 1468, no. 1, p. 012 111, **2020**, ISSN: 1742-6596. DOI: 10.1088/1742-6596/1468/1/012111.

[130] CUPID-Mo Collaboration, Armengaud, E., Augier, C., *et al.*, "New Limit for Neutrinoless Double-Beta Decay of ^{100}Mo from the CUPID-Mo Experiment," *Physical Review Letters*, vol. 126, no. 18, p. 181 802, **2021**. DOI: 10.1103/PhysRevLett.126.181802.

[131] Hartnell, J. and, t. S. collaboration the, "Neutrinoless Double Beta Decay with SNO+," *Journal of Physics: Conference Series*, vol. 375, no. 4, p. 042 015, **2012**, ISSN: 1742-6596. DOI: 10.1088/1742-6596/375/1/042015.

[132] CUORE Collaboration, Alduino, C., Alessandria, F., *et al.*, "First results from CUORE: A search for lepton number violation via $0\nu\beta\beta$ decay of ^{130}Te," *Physical Review Letters*, vol. 120, no. 13, p. 132 501, **2018**. DOI: 10.1103/PhysRevLett.120.132501.

[133] Arnold, R., Augier, C., Baker, J., *et al.*, "First Results of the Search for Neutrinoless Double-Beta Decay with the NEMO 3 Detector," *Physical Review Letters*, vol. 95, no. 18, p. 182 302, **2005**. DOI: 10.1103/PhysRevLett.95.182302.

[134] NEMO Collaboration, Argyriades, J., Arnold, R., *et al.*, "Measurement of the double-β decay half-life of ^{150}Nd and search for neutrinoless decay modes with the NEMO-3 detector," *Physical Review C*, vol. 80, no. 3, p. 032 501, **2009**. DOI: 10.1103/PhysRevC.80.032501.

[135] Argyriades, J., Arnold, R., Augier, C., *et al.*, "Measurement of the two neutrino double beta decay half-life of Zr-96 with the NEMO-3 detector," *Nuclear Physics A*, vol. 847, no. 3, pp. 168–179, **2010**, ISSN: 0375-9474. DOI: 10.1016/j.nuclphysa.2010.07.009.

[136] NEMO-3 Collaboration, Arnold, R., Augier, C., *et al.*, "Measurement of the $\beta\beta$ decay half-life of ^{130}Te with the NEMO-3 detector," *Physical Review Letters*, vol. 107, no. 6, p. 062 504, **2011**. DOI: 10.1103/PhysRevLett.107.062504.

[137] Engel, J. and Menéndez, J., "Status and future of nuclear matrix elements for neutrinoless double-beta decay: A review," *Reports on Progress in Physics*, vol. 80, no. 4, p. 046 301, **2017**, ISSN: 0034-4885. DOI: 10.1088/1361-6633/aa5bc5.

[138] Belley, A., Miyagi, T., Stroberg, S. R., *et al.*, *Ab initio calculations of neutrinoless $\beta\beta$ decay refine neutrino mass limits*, arXiv:2307.15156, **2023**. DOI: 10.48550/arXiv.2307.15156.

[139] Machleidt, R. and Entem, D. R., "Chiral effective field theory and nuclear forces," *Physics Reports*, vol. 503, no. 1, pp. 1–75, **2011**, ISSN: 0370-1573. DOI: 10.1016/j.physrep.2011.02.001.

[140] Anton, G., Badhrees, I., Barbeau, P. S., *et al.*, "Search for Neutrinoless Double-β Decay with the Complete EXO-200 Dataset," *Physical Review Letters*, vol. 123, no. 16, p. 161 802, **2019**, ISSN: 0031-9007, 1079-7114. DOI: 10.1103/PhysRevLett.123.161802.

[141] Aprile, E. and Doke, T., "Liquid xenon detectors for particle physics and astrophysics," *Reviews of Modern Physics*, vol. 82, no. 3, pp. 2053–2097, **2010**. DOI: 10.1103/RevModPhys.82.2053.

[142] Doke, T., Hitachi, A., Kikuchi, J., *et al.*, "Absolute Scintillation Yields in Liquid Argon and Xenon for Various Particles," *Japanese Journal of Applied Physics*, vol. 41, no. 3R, p. 1538, **2002**, ISSN: 1347-4065. DOI: 10.1143/JJAP.41.1538.

[143] EXO-200 Collaboration, Anton, G., Badhrees, I., *et al.*, "Measurement of the scintillation and ionization response of liquid xenon at MeV energies in the EXO-200 experiment," *Physical Review C*, vol. 101, no. 6, p. 065 501, **2020**. DOI: 10.1103/PhysRevC.101.065501.

[144] Baudis, L., Sanchez-Lucas, P., and Thieme, K., "A measurement of the mean electronic excitation energy of liquid xenon," *The European Physical Journal C*, vol. 81, no. 12, p. 1060, **2021**, ISSN: 1434-6052. DOI: 10.1140/epjc/s10052-021-09834-x.

[145] Akerib, D., Alsum, S., Araújo, H., *et al.*, "Low-energy (0.7–74 keV) nuclear recoil calibration of the LUX dark matter experiment using DD neutron scattering kinematics," **2016**, arXiv:1608.05381.

[146] Baldini, A. M., Baracchini, E., Bemporad, C., *et al.*, "The design of the MEG II experiment," *The European Physical Journal C*, vol. 78, no. 5, p. 380, **2018**, ISSN: 1434-6052. DOI: 10.1140/epjc/s10052-018-5845-6.

[147] Conti, E., DeVoe, R., Gratta, G., *et al.*, "Correlated fluctuations between luminescence and ionization in liquid xenon," *Physical Review B*, vol. 68, no. 5, p. 054 201, **2003**. DOI: 10.1103/PhysRevB.68.054201.

[148] Hill, K. D. and Steele, A. G., "The triple point of xenon," *Metrologia*, vol. 42, no. 4, p. 278, **2005**, ISSN: 0026-1394. DOI: 10.1088/0026-1394/42/4/013.

[149] Jamil, A., Ziegler, T., Hufschmidt, P., *et al.*, "VUV-Sensitive Silicon Photomultipliers for Xenon Scintillation Light Detection in nEXO," *IEEE Transactions on Nuclear Science*, vol. 65, no. 11, pp. 2823–2833, **2018**, Conference Name: IEEE Transactions on Nuclear Science, ISSN: 1558-1578. DOI: 10.1109/TNS.2018.2875668.

[150] Gallina, G., Giampa, P., Retière, F., *et al.*, "Characterization of the Hamamatsu VUV4 MPPCs for nEXO," *Nuclear Instruments and Methods in Physics Research Section A: Accelerators, Spectrometers, Detectors and Associated Equipment*, vol. 940, pp. 371–379, **2019**, ISSN: 0168-9002. DOI: 10.1016/j.nima.2019.05.096.

[151] nEXO Collaboration, Al Kharusi, S., Alamre, A., *et al.*, *nEXO Pre-Conceptual Design Report*, arXiv:1805.11142, **2018**.

[152] Li, Z., Cen, W. R., Robinson, A., *et al.*, "Simulation of charge readout with segmented tiles in nEXO," *Journal of Instrumentation*, vol. 14, no. 09, P09020, **2019**, ISSN: 1748-0221. DOI: 10.1088/1748-0221/14/09/P09020.

[153] nEXO Collaboration, Albert, J. B., Anton, G., *et al.*, "Sensitivity and discovery potential of the proposed nEXO experiment to neutrinoless double-β decay,"

Physical Review C, vol. 97, no. 6, p. 065 503, **2018**. DOI: 10.1103/PhysRevC.97.065503.

[154] Tsang, R., Piepke, A., Al Kharusi, S., *et al.*, "An integrated online radioassay data storage and analytics tool for nEXO," *Nuclear Instruments and Methods in Physics Research Section A: Accelerators, Spectrometers, Detectors and Associated Equipment*, vol. 1055, p. 168 477, **2023**, ISSN: 01689002. DOI: 10.1016/j.nima.2023.168477.

[155] Agostinelli, S., Allison, J., Amako, K., *et al.*, "Geant4—a simulation toolkit," *Nuclear Instruments and Methods in Physics Research Section A: Accelerators, Spectrometers, Detectors and Associated Equipment*, vol. 506, no. 3, pp. 250–303, **2003**, ISSN: 0168-9002. DOI: 10.1016/S0168-9002(03)01368-8.

[156] Szydagis, M., Barry, N., Kazkaz, K., *et al.*, "NEST: A comprehensive model for scintillation yield in liquid xenon," *Journal of Instrumentation*, vol. 6, no. 10, P10002, **2011**, ISSN: 1748-0221. DOI: 10.1088/1748-0221/6/10/P10002.

[157] Gómez Cadenas, J. J., Álvarez, V., Borges, F. I. G., *et al.*, "Present Status and Future Perspectives of the NEXT Experiment," *Advances in High Energy Physics*, vol. 2014, e907067, **2014**, ISSN: 1687-7357. DOI: 10.1155/2014/907067.

[158] Moe, M. K., "Detection of neutrinoless double-beta decay," *Physical Review C*, vol. 44, no. 3, R931–R934, **1991**. DOI: 10.1103/PhysRevC.44.R931.

[159] Brunner, T., Fudenberg, D., Varentsov, V., *et al.*, "An RF-only ion-funnel for extraction from high-pressure gases," *International Journal of Mass Spectrometry*, vol. 379, pp. 110–120, **2015**, ISSN: 1387-3806. DOI: 10.1016/j.ijms.2015.01.003.

[160] nEXO Collaboration, Mong, B., Cook, S., *et al.*, "Spectroscopy of ba and Ba^+ deposits in solid xenon for barium tagging in nEXO," *Physical Review A*, vol. 91, no. 2, p. 022 505, **2015**. DOI: 10.1103/PhysRevA.91.022505.

[161] Chambers, C., Walton, T., Fairbank, D., *et al.*, "Imaging individual barium atoms in solid xenon for barium tagging in nEXO," *Nature*, vol. 569, no. 7755, pp. 203–207, **2019**, Number: 7755 Publisher: Nature Publishing Group, ISSN: 1476-4687. DOI: 10.1038/s41586-019-1169-4.

[162] Rasiwala, H., Murray, K., Lan, Y., *et al.*, "'Searching for a needle in a haystack': A Ba-tagging approach for an upgraded nEXO experiment," *Nuclear Instruments and Methods in Physics Research Section B: Beam Interactions with Materials and Atoms*, vol. 541, pp. 298–300, **2023**, ISSN: 0168-583X. DOI: 10.1016/j.nimb.2023.05.047.

[163] Gomez-Cadenas, J. J., Benlloch-Rodríguez, J. M., Ferrario, P., *et al.*, "Investigation of the coincidence resolving time performance of a PET scanner based on liquid xenon: A Monte Carlo study," *Journal of Instrumentation*, vol. 11, no. 09, P09011, **2016**, ISSN: 1748-0221. DOI: 10.1088/1748-0221/11/09/P09011.

[164] Romo-Luque, C., "PETALO: Time-of-Flight PET with liquid xenon," *Nuclear Instruments and Methods in Physics Research Section A: Accelerators, Spectrometers, Detectors and Associated Equipment*, Proceedings of the Vienna

Conference on Instrumentation 2019, vol. 958, p. 162 397, **2020**, ISSN: 0168-9002. DOI: 10.1016/j.nima.2019.162397.

[165] Stiegler, T., Sangiorgio, S., Brodsky, J. P., *et al.*, "Event reconstruction in a liquid xenon Time Projection Chamber with an optically-open field cage," *Nuclear Instruments and Methods in Physics Research Section A: Accelerators, Spectrometers, Detectors and Associated Equipment*, vol. 1000, p. 165 239, **2021**, ISSN: 0168-9002. DOI: 10.1016/j.nima.2021.165239.

[166] Albert, J. B., Auty, D. J., Barbeau, P. S., *et al.*, "Cosmogenic backgrounds to $0\nu\beta\beta$ in EXO-200," *Journal of Cosmology and Astroparticle Physics*, vol. 2016, no. 04, p. 029, **2016**, ISSN: 1475-7516. DOI: 10.1088/1475-7516/2016/04/029.

[167] Al Kharusi, S., "nEXO cosmogenics list," Tech. Rep., **2020**, NEXO-SIM-023.

[168] Mughabghab, S. F., "Thermal neutron capture cross sections resonance integrals and g-factors," **2003**.

[169] Al Kharusi, S., Anton, G., Badhrees, I., *et al.*, "Measurement of the spectral shape of the β-decay of Xe-137 to the ground state of Cs-137 in EXO-200 and comparison with theory," *Physical review letters*, vol. 124, no. 23, p. 232 502, **2020**.

[170] Ortega, G. S. U., "Thermal Fluid Simulations and Onset of Boiling Analysis in Liquid Xenon for the nEXO Detector," Ph.D. dissertation, Washington State University, **2020**.

[171] Zou, J. H., Huang, X. T., Li, W. D., *et al.*, "SNiPER: An offline software framework for non-collider physics experiments," *Journal of Physics: Conference Series*, vol. 664, no. 7, p. 072 053, **2015**, ISSN: 1742-6596. DOI: 10.1088/1742-6596/664/7/072053.

[172] Smith, N. J. T., "The SNOLAB deep underground facility," *The European Physical Journal Plus*, vol. 127, no. 9, p. 108, **2012**, ISSN: 2190-5444. DOI: 10.1140/epjp/i2012-12108-9.

[173] Ahdida, C., Bozzato, D., Calzolari, D., *et al.*, "New capabilities of the FLUKA multi-purpose code," *Frontiers in Physics*, vol. 9, p. 788 253, **2022**.

[174] Battistoni, G., Boehlen, T., Cerutti, F., *et al.*, "Overview of the FLUKA code," *Annals of Nuclear Energy*, vol. 82, pp. 10–18, **2015**.

[175] Mei, D.-M. and Hime, A., "Muon-induced background study for underground laboratories," *Physical Review D*, vol. 73, no. 5, p. 053 004, **2006**. DOI: 10.1103/PhysRevD.73.053004.

[176] SNO Collaboration, Aharmim, B., Ahmed, S. N., *et al.*, "Measurement of the cosmic ray and neutrino-induced muon flux at the Sudbury neutrino observatory," *Physical Review D*, vol. 80, no. 1, p. 012 001, **2009**. DOI: 10.1103/PhysRevD.80.012001.

[177] Miyake, S., "Rapporteur paper on muons and neutrinos," Tokyo Univ.; Denver Univ., Colo. (USA), Tech. Rep. **CONF-730804-P5**, **1973**.

[178] Woodley, W., Fedynitch, A., and Piro, M.-C., "Challenges and Opportunities for Predicting Muons in Underground and Underwater Labs Using MUTE," *Proceedings*

of 38th International Cosmic Ray Conference — PoS(ICRC2023), vol. 444, **2023**, p. 476. DOI: 10.22323/1.444.0476.

[179] Cassiday, G. L., Keuffel, J. W., and Thompson, J. A., "Calculation of the Stopping-Muon Rate Underground," *Physical Review D*, vol. 7, no. 7, pp. 2022–2031, **1973**, ISSN: 0556-2821. DOI: 10.1103/PhysRevD.7.2022.

[180] Gaisser, T. K., Engel, R., and Resconi, E., *Cosmic rays and particle physics*. Cambridge University Press, **2016**.

[181] Eidelman, S., Hayes, K., Olive, K., *et al.*, "Review of particle properties," *Physics Letters B*, vol. 592, no. 1-4, pp. 1–5, **2004**.

[182] Aharmim, B., Ahmed, S. N., Anthony, A. E., *et al.*, "Cosmogenic neutron production at the Sudbury Neutrino Observatory," *Physical Review D*, vol. 100, no. 11, p. 112 005, **2019**, ISSN: 2470-0010, 2470-0029. DOI: 10.1103/PhysRevD.100.112005.

[183] Schreiner, P., Reichenbacher, J., and Goodman, M., "Interpretation of the underground muon charge ratio," *Astroparticle Physics*, vol. 32, no. 1, pp. 61–71, **2009**, ISSN: 09276505. DOI: 10.1016/j.astropartphys.2009.06.002.

[184] Aharmim, B., Ahmed, S. N., Andersen, T. C., *et al.*, "Measurement of the cosmic ray and neutrino-induced muon flux at the Sudbury neutrino observatory," *Physical Review D*, vol. 80, no. 1, p. 012 001, **2009**, ISSN: 1550-7998, 1550-2368. DOI: 10.1103/PhysRevD.80.012001.

[185] Abgrall, N., Aguayo, E., Avignone, F. T., *et al.*, "Muon flux measurements at the davis campus of the sanford underground research facility with the majorana demonstrator

veto system," *Astroparticle Physics*, vol. 93, pp. 70–75, **2017**, ISSN: 0927-6505. DOI: 10.1016/j.astropartphys.2017.01.013.

[186] "Cosmic-muon flux and annual modulation in Borexino at 3800 m water-equivalent depth," *Journal of Cosmology and Astroparticle Physics*, vol. 2012, no. 05, p. 015, **2012**, ISSN: 1475-7516. DOI: 10.1088/1475-7516/2012/05/015.

[187] Li, S. W. and Beacom, J. F., "First calculation of cosmic-ray muon spallation backgrounds for MeV astrophysical neutrino signals in Super-Kamiokande," *Physical Review C*, vol. 89, no. 4, p. 045 801, **2014**, ISSN: 0556-2813, 1089-490X. DOI: 10.1103/PhysRevC.89.045801.

[188] Li, S. W. and Beacom, J. F., "Spallation backgrounds in Super-Kamiokande are made in muon-induced showers," *Physical Review D*, vol. 91, no. 10, p. 105 005, **2015**, ISSN: 1550-7998, 1550-2368. DOI: 10.1103/PhysRevD.91.105005.

[189] Li, S. W. and Beacom, J. F., "Tagging spallation backgrounds with showers in water Cherenkov detectors," *Physical Review D*, vol. 92, no. 10, p. 105 033, **2015**, ISSN: 1550-7998, 1550-2368. DOI: 10.1103/PhysRevD.92.105033.

[190] Zhu, G., Li, S. W., and Beacom, J. F., "Developing the MeV potential of DUNE: Detailed considerations of muon-induced spallation and other backgrounds," *Physical Review C*, vol. 99, no. 5, p. 055 810, **2019**, ISSN: 2469-9985, 2469-9993. DOI: 10.1103/PhysRevC.99.055810.

[191] Cheng, J.-P., Kang, K.-J., Li, J.-M., *et al.*, "The China Jinping Underground Laboratory and Its Early Science," *Annual Review of Nuclear and Particle Science*, vol. 67, no. 1, pp. 231–251, **2017**. DOI: 10.1146/annurev-nucl-102115-044842.

[192] Yu-Cheng, W., Xi-Qing, H., Qian, Y., *et al.*, "Measurement of cosmic ray flux in the China Jinping underground laboratory," *Chinese Physics C*, vol. 37, no. 8, p. 086 001, **2013**, ISSN: 1674-1137. DOI: 10.1088/1674-1137/37/8/086001.

[193] Guo, Z.-y., Bathe-Peters, L., Chen, S.-m., *et al.*, "Muon flux measurement at China Jinping underground laboratory," *Chinese Physics C*, vol. 45, no. 2, p. 025 001, **2021**.

[194] Aprile, E., Agostini, F., Alfonsi, M., *et al.*, "Conceptual design and simulation of a water Cherenkov muon veto for the XENON1T experiment," *Journal of Instrumentation*, vol. 9, no. 11, P11006, **2014**, ISSN: 1748-0221. DOI: 10.1088/1748-0221/9/11/P11006.

[195] Rogers, L., Jones, B. J. P., Laing, A., *et al.*, "Mitigation of backgrounds from cosmogenic ^{137}Xe in xenon gas experiments using ^{3}He neutron capture," *Journal of Physics G: Nuclear and Particle Physics*, vol. 47, no. 7, p. 075 001, **2020**, ISSN: 0954-3899. DOI: 10.1088/1361-6471/ab8915.

[196] Wilks, S. S., "The Large-Sample Distribution of the Likelihood Ratio for Testing Composite Hypotheses," *The Annals of Mathematical Statistics*, vol. 9, no. 1, pp. 60–62, **1938**, ISSN: 0003-4851.

[197] Feldman, G. J. and Cousins, R. D., "Unified approach to the classical statistical analysis of small signals," *Physical Review D*, vol. 57, no. 7, pp. 3873–3889, **1998**, ISSN: 0556-2821, 1089-4918. DOI: 10.1103/PhysRevD.57.3873.

[198] Freund, K., Falkenstein, R., Grabmayr, P., *et al.*, "The performance of the Muon Veto of the GERDA experiment," *The European Physical Journal C*, vol. 76, no. 5, p. 298, **2016**, ISSN: 1434-6052. DOI: 10.1140/epjc/s10052-016-4140-7.

[199] Murray, K., "The design and optimization of a multi-reflection time-of-flight mass-spectrometer for Barium tagging with nEXO and optimization of the Xenon-137 veto with EXO-200," Publisher: McGill University, M.S. thesis, McGill University, **2018**.

[200] Albert, J. B., Daugherty, S. J., Johnson, T. N., *et al.*, "Measurement of neutron capture on ^{136}Xe," *Physical Review C*, vol. 94, no. 3, p. 034 617, **2016**. DOI: 10.1103/PhysRevC.94.034617.

[201] Schwartz, S., "Cosmogenic ^{137}Xe Analysis of Alternatives for nEXO," Lawrence Livermore National Laboratory, Tech. Rep., **2023**, LLNL-TR-849598.

[202] Al Kharusi, S., Saldanha, R., Sangiorgio, S., *et al.*, "nEXO performance at different underground locations," Tech. Rep., **2023**, NEXO-SIM-029.

[203] Abe, S., Asami, S., Eizuka, M., *et al.*, "Measurement of cosmic-ray muon spallation products in a xenon-loaded liquid scintillator with KamLAND," *Physical Review C*, vol. 107, no. 5, p. 054 612, **2023**, ISSN: 2469-9985, 2469-9993. DOI: 10.1103/PhysRevC.107.054612.

[204] Tsang, R., Piepke, A., and Sangiorgio, S., "Water shield study," Tech. Rep., **2016**, NEXO-SIM-009.

[205] Tsang, R., "Revisiting the impact of concrete γ on water tank size," Tech. Rep., **2019**, NEXO-SIM-010.

[206] Natzke, C., "Water shield study," Tech. Rep., **2019**, NEXO-SIM-011.

[207] Al Kharusi, S., "nEXO outer detector size: Updates (higher energy rock gammas, neutrons)," Tech. Rep., **2020**, NEXO-SIM-012.

[208] Jetter, S., Dwyer, D., Jiang, W.-Q., *et al.*, "PMT waveform modeling at the Daya Bay experiment," *Chinese Physics C*, vol. 36, no. 8, pp. 733–741, **2012**, ISSN: 1674-1137. DOI: 10.1088/1674-1137/36/8/009.

[209] Saldanha, R., Grandi, L., Guardincerri, Y., *et al.*, "Model independent approach to the single photoelectron calibration of photomultiplier tubes," *Nuclear Instruments and Methods in Physics Research Section A: Accelerators, Spectrometers, Detectors and Associated Equipment*, vol. 863, pp. 35–46, **2017**, ISSN: 01689002. DOI: 10.1016/j.nima.2017.02.086.

[210] CAEN, *VX2740*, https://www.caen.it/products/vx2740/, accessed August 2023.

[211] Hale, G. M. and Querry, M. R., "Optical Constants of Water in the 200 nm to 200 μm Wavelength Region," *Applied Optics*, vol. 12, no. 3, p. 555, **1973**, ISSN: 0003-6935, 1539-4522. DOI: 10.1364/AO.12.000555.

[212] Twardowski, M. S., Claustre, H., Freeman, S. A., *et al.*, "Optical backscattering properties of the "clearest" natural waters," *Biogeosciences*, vol. 4, no. 6, pp. 1041–1058, **2007**, ISSN: 1726-4189. DOI: 10.5194/bg-4-1041-2007.

[213] Fewell, M. P. and Von Trojan, A., "Absorption of light by water in the region of high transparency: Recommended values for photon-transport calculations," *Applied Optics*, vol. 58, no. 9, p. 2408, **2019**, ISSN: 1559-128X, 2155-3165. DOI: 10.1364/AO.58.002408.

[214] Abe, K., Hayato, Y., Iida, T., *et al.*, "Calibration of the Super-Kamiokande detector," *Nuclear Instruments and Methods in Physics Research Section A: Accelerators, Spectrometers, Detectors and Associated Equipment*, vol. 737, pp. 253–272, **2014**, ISSN: 01689002. DOI: 10.1016/j.nima.2013.11.081.

[215] Hamamatsu Photonics, "R5912 PMT datasheet," Tech. Rep., https://hep.hamamatsu.com/eu/en/products/R5912.html, accessed July 2023.

[216] Chow, K., Cummings, J., Edwards, E., *et al.*, "Waterproofed photomultiplier tube assemblies for the Daya Bay reactor neutrino experiment," *Nuclear Instruments and Methods in Physics Research Section A: Accelerators, Spectrometers, Detectors and Associated Equipment*, vol. 794, pp. 25–32, **2015**, ISSN: 0168-9002. DOI: 10.1016/j.nima.2015.05.002.

[217] Land, B., *Chroma: Ultra-fast photon Monte Carlo*, https://github.com/BenLand100/chroma, accessed August 2023, **2016**.

[218] Seibert, S. and LaTorre, A., *Fast optical monte carlo simulation with surface-based geometries*, https://github.com/BenLand100/chroma/blob/master/doc/source/chroma.pdf, accessed August 2023, **2011**.

[219] Jackson, J. D., "Classical electrodynamics," 3rd. Wiley, **1999**, pp. 646–654.

[220] L'Annunziata, M. F., "Chapter 15 - Cherenkov Counting," *Handbook of Radioactivity Analysis (Third Edition)*, L'Annunziata, M. F., Ed., Amsterdam: Academic Press, **2012**, pp. 935–1019, ISBN: 978-0-12-384873-4. DOI: 10.1016/B978-0-12-384873-4.00015-3.

[221] An, F., Balantekin, A., Band, H., *et al.*, "The muon system of the Daya Bay reactor antineutrino experiment," *Nuclear Instruments and Methods in Physics Research Section A: Accelerators, Spectrometers, Detectors and Associated Equipment*, vol. 773, pp. 8–20, **2015**.

[222] Wilson, E. B., "Probable Inference, the Law of Succession, and Statistical Inference," *Journal of the American Statistical Association*, vol. 22, no. 158, pp. 209–212, **1927**, ISSN: 0162-1459. DOI: 10.1080/01621459.1927.10502953.

[223] Brun, R. and Rademakers, F., "ROOT—an object oriented data analysis framework," *Nuclear instruments and methods in physics research section A: accelerators, spectrometers, detectors and associated equipment*, vol. 389, no. 1-2, pp. 81–86, **1997**, Web: https://root.cern/, accessed: Dec 2023. DOI: 10.5281/zenodo.848818.

[224] Bar, N., Blum, K., and D'Amico, G., "Is there a supernova bound on axions?" *Physical Review D*, vol. 101, no. 12, p. 123 025, **2020**. DOI: 10.1103/PhysRevD.101.123025.

[225] Lucente, G., Carenza, P., Fischer, T., *et al.*, "Heavy axion-like particles and core-collapse supernovae: Constraints and impact on the explosion mechanism," *Journal of Cosmology and Astroparticle Physics*, vol. 2020, no. 12, p. 008, **2020**, ISSN: 1475-7516. DOI: 10.1088/1475-7516/2020/12/008.

[226] Sakstein, J., Croon, D., and McDermott, S. D., "Axion instability supernovae," *Physical Review D*, vol. 105, no. 9, p. 095 038, **2022**. DOI: 10.1103/PhysRevD.105.095038.

[227] Mirizzi, A., Tamborra, I., Janka, H.-T., *et al.*, "Supernova neutrinos: Production, oscillations and detection," *La Rivista del Nuovo Cimento*, vol. 39, no. 1, pp. 1–112, **2016**, ISSN: 1826-9850. DOI: 10.1393/ncr/i2016-10120-8.

[228] Antonioli, P., Fienberg, R. T., Fleurot, F., *et al.*, "SNEWS: The supernova early warning system," *New Journal of Physics*, vol. 6, no. 1, p. 114, **2004**.

[229] Kharusi, S. A., BenZvi, S. Y., Bobowski, J. S., *et al.*, "SNEWS 2.0: A next-generation supernova early warning system for multi-messenger astronomy," *New Journal of Physics*, vol. 23, no. 3, p. 031 201, **2021**, ISSN: 1367-2630. DOI: 10.1088/1367-2630/abde33.

[230] Gava, J., Kneller, J., Volpe, C., *et al.*, "Dynamical collective calculation of supernova neutrino signals," *Physical review letters*, vol. 103, no. 7, p. 071 101, **2009**.

[231] Scholberg, K., "Supernova neutrino detection," *Annual Review of Nuclear and Particle Science*, vol. 62, pp. 81–103, **2012**.

[232] Gardiner, S., "Simulating low-energy neutrino interactions with MARLEY," *Comput. Phys. Commun.*, vol. 269, p. 108 123, **2021**, ISSN: 0010-4655. DOI: 10.1016/j.cpc.2021.108123. arXiv: 2101.11867 [nucl-th].

[233] Pirinen, P., Suhonen, J., and Ydrefors, E., "Charged-current neutrino-nucleus scattering off xe isotopes," *Physical Review C*, vol. 99, no. 1, p. 014 320, **2019**.

[234] Ydrefors, E., Suhonen, J., and Zhao, Y., "Neutrino-nucleus scattering off Xe 136," *Physical Review C*, vol. 91, no. 1, p. 014 307, **2015**.

[235] Mccutchan, E., "Nuclear data sheets for A = 136," *Nuclear Data Sheets*, vol. 152, pp. 331–667, **2018**.

[236] Pirinen, P., Suhonen, J., and Ydrefors, E., "Neutral-current neutrino-nucleus scattering off Xe isotopes," *Advances in High Energy Physics*, vol. 2018, **2018**.

[237] Abi, B., Acciarri, R., Acero, M. A., *et al.*, "Supernova neutrino burst detection with the deep underground neutrino experiment: DUNE collaboration," *The European Physical Journal C*, vol. 81, no. 5, p. 423, **2021**.

[238] Abe, K., Adrich, P., Aihara, H., *et al.*, "Supernova model discrimination with hyper-kamiokande," *The Astrophysical Journal*, vol. 916, no. 1, p. 15, **2021**.

[239] Abbasi, R., Abdou, Y., Abu-Zayyad, T., *et al.*, "IceCube sensitivity for low-energy neutrinos from nearby supernovae," *Astronomy & astrophysics*, vol. 535, A109, **2011**.

[240] Agostini, M., Böhmer, M., Bosma, J., *et al.*, "The pacific ocean neutrino experiment," *Nature Astronomy*, vol. 4, no. 10, pp. 913–915, **2020**.

[241] Strumia, A. and Vissani, F., "Precise quasielastic neutrino/nucleon cross-section," *Physics Letters B*, vol. 564, no. 1-2, pp. 42–54, **2003**.

[242] Aloisio, R., Coccia, E., and Vissani, F., *Multiple messengers and challenges in astroparticle physics*. Springer, **2018**, pp. 267–270.

[243] Dayon, M., "Study of the cavity wall background in the SNO detector," M.S. thesis, Queen's University, **1999**.

[244] Aprile, E., Aalbers, J., Abe, K., *et al.*, "The triggerless data acquisition system of the XENONnT experiment," *Journal of Instrumentation*, vol. 18, no. 07, P07054, **2023**, ISSN: 1748-0221. DOI: 10.1088/1748-0221/18/07/P07054.

[245] Baxter, A. L., BenZvi, S., Jaimes, J. C., *et al.*, "SNEWPY: A Data Pipeline from Supernova Simulations to Neutrino Signals," *The Astrophysical Journal*, vol. 925, no. 2, p. 107, **2022**, ISSN: 0004-637X, 1538-4357. DOI: 10.3847/1538-4357/ac350f.

[246] Fernández, P. and Super-Kamiokande collaboration, "Benefits of Gd for High Energy Neutrinos in SuperK-Gd," *Journal of Physics: Conference Series*, vol. 888, p. 012 054, **2017**, ISSN: 1742-6588, 1742-6596. DOI: 10.1088/1742-6596/888/1/012054.

[247] SNOLAB, "SNOLAB User's Handbook Rev. 2," Tech. Rep., **2006**.

[248] Yeh, M., Hans, S., Beriguete, W., *et al.*, "A new water-based liquid scintillator and potential applications," *Nuclear Instruments and Methods in Physics Research Section*

A: Accelerators, Spectrometers, Detectors and Associated Equipment, vol. 660, no. 1, pp. 51–56, **2011**.

[249] Köpke, L., "Improved detection of supernovae with the IceCube Observatory," **2017**, arXiv:1704.03823.

[250] Linzer, N. and Scholberg, K., "Triangulation pointing to core-collapse supernovae with next-generation neutrino detectors," *Physical Review D*, vol. 100, no. 10, p. 103 005, **2019**.

[251] Asakura, K., Gando, A., Gando, Y., *et al.*, "KamLAND sensitivity to neutrinos from pre-supernova stars," *The Astrophysical Journal*, vol. 818, no. 1, p. 91, **2016**.

[252] Brading, K. A., "Which symmetry? Noether, Weyl, and conservation of electric charge," *Studies in History and Philosophy of Science Part B: Studies in History and Philosophy of Modern Physics*, vol. 33, no. 1, pp. 3–22, **2002**, ISSN: 1355-2198. DOI: 10.1016/S1355-2198(01)00033-8.

[253] Kirillov, A. A., *An Introduction to Lie Groups and Lie Algebras*. Cambridge University Press, **2008**, ISBN: 978-0-521-88969-8.

[254] Fantini, G., Gallo Rosso, A., Zema, V., *et al.*, "Introduction to the formalism of neutrino oscillations," *The State of the Art of Neutrino Physics: A Tutorial for Graduate Students and Young Researchers*, World Scientific, **2018**, pp. 37–119.

[255] Gómez-Cadenas, J. J., Martín-Albo, J., Sorel, M., *et al.*, "Sense and sensitivity of double beta decay experiments," *Journal of Cosmology and Astroparticle Physics*,

vol. 2011, no. 06, p. 007, **2011**, ISSN: 1475-7516. DOI: 10.1088/1475-7516/2011/06/007.

[256] Gomez-Cadenas, J. J., Martin-Albo, J., Mezzetto, M., *et al.*, "The search for neutrinoless double beta decay," *La Rivista del Nuovo Cimento*, vol. 35, no. 2, pp. 29–98, **2012**, ISSN: 0393697X, 0393697X. DOI: 10.1393/ncr/i2012-10074-9.

[257] Newcombe, R. G., "Two-sided confidence intervals for the single proportion: Comparison of seven methods," *Statistics in Medicine*, vol. 17, no. 8, pp. 857–872, **1998**, ISSN: 1097-0258. DOI: 10.1002/(SICI)1097-0258(19980430)17:8<857::AID-SIM777>3.0.CO;2-E.

[258] SNOLAB, "COAX Run 211207," SNOLAB, Tech. Rep., **2021**, https://www.snolab.ca/~tjsonley/HPGE_Test/COAX/211207/, accessed May 2023.

[259] Remington, H., Caio, L., and Ubi, W., "nEXO OD PMT Backgrounds v2.0," Tech. Rep., **2019**, NEXO-SIM-013.

[260] Kudryavtsev, V. A., Pandola, L., and Tomasello, V., "Neutron- and muon-induced background in underground physics experiments," *The European Physical Journal A*, vol. 36, no. 2, pp. 171–180, **2008**, ISSN: 1434-6001, 1434-601X. DOI: 10.1140/epja/i2007-10539-6.

[261] Lenardo, B. and Mong, B., "Neutron activation of ^{136}Xe outside the water tank as a background for nEXO: rate estimation and mitigation," Tech. Rep., **2019**, NEXO-SIM-004.

Appendix A

Noether's theorems

Commonly taught in the context of classical mechanics, with examples including the association of translational invariance (a spatial symmetry) with the conservation of linear momentum (the conserved quantity), Noether's theorems also apply to the realm of quantum field theory (QFT) and particle physics alike. In these realms, it is gauge invariances that give rise to conservation laws associated with various charges of particles. These conservation laws limit the diversity of allowed particle interactions in our world.

The most common example of a gauge invariant theory (a gauge theory) is that of classical electromagnetism. Here, the electromagnetic potential $A_\mu = (V, \mathbf{A})$, is the gauge field of interest. It contains two terms, the electric (scalar) potential, V, and the vector potential, $\mathbf{A}$; where $\mu = \{0, 1, 2, 3\}$ denotes components of the four spacetime dimensions. The values associated with each point of A_μ in spacetime are unobservable. However, calculating the field strength tensor ($F_{\mu\nu} = \partial_\mu A_\nu - \partial_\nu A_\mu$) gives you electric and magnetic field strengths which are measurable. Transformations of the form:

$$A_\mu \rightarrow A'_\mu = A_\mu + \partial_\mu \lambda, \tag{A.1}$$

where $\partial_\mu \lambda$ is the gradient of some unitary complex scalar field (e.g., $\lambda = e^{i\theta}$), leaves $F_{\mu\nu}$ unchanged. In other words, the field strengths of the electric and magnetic fields are invariant under particular transformations of the electromagnetic potential, A_μ. The associated conserved quantity in this context, is the conservation of electric charges and currents. For a historical review and additional context see [252].

The mathematical framework of the Standard Model (SM) is written in terms of Lagragians, the integral of the action with respect to time.[1] Analogously to classical mechanics, solutions to the Euler-Lagrange (E-L) equations for a given Lagrangian describe the dynamics of a system, i.e., they provide the physical equations of motion, following from the principle of stationary action. Particular transformations applied to the Lagrangian can leave the solutions to (E-L) equations unchanged, e.g., transforming our physical coordinates $x \to x'$, where $x' = x - c$ and c is some constant. This is an example of a global transformation, where every x in our Lagrangian has been offset by the same constant c. These global transformations fall under the domain of Noether's first theorem, stating that there is a globally conserved quantity; examples include energy, as well as linear and angular momentum conservation.

In the context of QFT, the transformations applied need not be global, but can be made local while still keeping the theory mathematically sound, i.e., $x \to x'$ where $x' = x - c(x)$; the transformations applied are now a function of spacetime coordinates. These local transformations, if they still leave the E-L solutions unchanged, are also associated with physical conservation laws by Noether's second theorem. Recall that this example implies x is a physical coordinate in space, but in the context of a QFT these local transformations can

[1] Symmetries of the action are also symmetries of the Lagrangian and so Noether's theorems also apply.

be applied to the gauge fields themselves, e.g., phase shifts of the electromagnetic potential.

The set of transformations that leave the E-L solutions unchanged, while locally altering the value of a gauge field form a particular kind of symmetry group, called a Lie group. Lie groups are mathematical objects that possess both the properties of an algebraic group (a set of operations that are associative, invertible, and contain an identity element) and those of a differentiable, smooth manifold (a geometric structure such as a circle or sphere) [253]. Thus, Lie groups allow us connect the algebra of our gauge transformations with symmetries that can be associated with some geometrical object. The reason gauge transformations form a symmetry group is because any valid gauge transformation must be:

1. Smooth: can be continuously parameterized by a set of real numbers.

2. Differentiable: can be differentiated with respect to the continuous parameters that describe them.

3. Invertible: for every transformation, there exists an inverse to reverse the effect.

Hence, the properties of a gauge transformation on a Lagrangian, because they form a Lie group, necessarily fall under the domain of Noether's theorems — there is a continuous, differentiable symmetry in the action that must necessarily lead to a conserved current.[2] Experimental observations of particle interactions have allowed us to decipher the Lie group (symmetry) structure of the SM, and make predictions on the allowed and disallowed processes in nature.

[2]Although the logic in this paragraph flows from symmetry groups → conservation laws, Noether's 1918 paper proves the theorem in both directions, making it a much more general and powerful tool in investigations of fundamental physics.

Appendix B

Derivations

B.1 Neutrino mass and oscillations

Neutrino oscillations arise from the quantum mechanical interference between different neutrino mass eigenstates (ν_1, ν_2, ν_3) when their wavepackets overlap as they propagate through space. The flavor state of a neutrino is as a superposition of its mass eigenstates:

$$|\nu_\alpha\rangle = \sum_{i=1}^{3} U_{\alpha i}|\nu_i\rangle, \tag{B.1}$$

where U is the PMNS mixing matrix (Equation 2.4), and $|\nu_i\rangle$ is the i-th mass eigenstate. In natural units ($\hbar = c = 1$), we can apply the time evolution operator e^{-iHt} to both sides of the equation, where H is the neutrino Hamiltonian. Here, a free neutrino takes the Hamiltonian $H = E_i = \sqrt{p^2 + m_i^2}$.

$$|\nu_\alpha(t)\rangle = \sum_{i=1}^{3} U_{\alpha i} e^{-iE_i t}|\nu_\alpha(0)\rangle. \tag{B.2}$$

Now, we will consider the case where the neutrino is born initially in a flavor eigenstate ν_α at $t = 0$:

$$|\nu_\alpha(0)\rangle = |\nu_\alpha\rangle.$$

The probability of finding the neutrino at a later time in the state ν_β is:

$$P(\nu_\alpha \to \nu_\beta) = |\langle \nu_\beta | \nu_\alpha(t)\rangle|^2 \tag{B.3}$$

Substituting Equation B.2 into the above yields:

$$P(\nu_\alpha \to \nu_\beta) = \left| \sum_{i,j=1}^{3} U_{\alpha i} U^*_{\beta j} e^{-iE_i t} e^{-iE_j t} \right|^2, \tag{B.4}$$

In the ultra-relativistic limit ($E \gg m$ for neutrinos), we have the approximations $E_i \approx p + \frac{m_i^2}{2p}$:

$$P(\nu_\alpha \to \nu_\beta) = \left| \sum_{i,j=1}^{3} U_{\alpha i} U^*_{\beta j} e^{-i(p+\frac{m_i^2}{2p})t} e^{-i(p+\frac{m_j^2}{2p})t} \right|^2, \tag{B.5}$$

Now can can define a mass squared difference $\Delta m^2_{ij} = m_i^2 - m_j^2$. Because we are in the ultra-relativistic regime, we can substitute $E = p$ and also substitute $t = L$:

$$P(\nu_\alpha \to \nu_\beta) = \left| \sum_{i,j=1}^{3} U_{\alpha i} U^*_{\beta j} e^{-i\frac{\Delta m^2_{ij}}{2E} L} \right|^2, \tag{B.6}$$

and we see that for $\Delta m^2_{ij} \to 0$ the exponential term will be equal to 1, and no neutrino oscillations will occur.[1]

[1] This exemplifies the effect of non-zero masses on the transition amplitude between the initial and final neutrino states, really the neutrino momenta are not the same and there is a finite coherence length where these oscillations will occur before the wavepackets of the different mass states no longer overlap; see [254].

The probability to detect the neutrino in one lepton state versus another (e.g., electron versus muon states) varies as both a function of energy and distance travelled. For neutrino oscillation to occur between all three neutrino flavours e, μ, and τ (as is now observed) there must be at least two non-zero mass-squared splittings, and at most one neutrino mass state that is massless. This is because production (and detection) of neutrinos can only occur through weak interactions, which produce neutrinos in pure, definite, flavour eigenstatesthat are coherent superpositions of mass states.

B.2 Counting experiments in background-free and background-limited regimes

Following the treatment and notation found in [255, 256], the number of signal counts in a $0\nu\beta\beta$ decay experiment grows as:

$$N_{sig} = \frac{\ln(2) M_{\beta\beta} N_A}{W_{\beta\beta}} \, \varepsilon_1 \, \frac{t}{T^{0\nu}_{1/2}}, \tag{B.7}$$

where $M_{\beta\beta}$ is the mass of the $\beta\beta$-isotope in grams, and $W_{\beta\beta}$ is the molar mass of the $\beta\beta$-isotope, N_A is Avogadro's number, ε_1 is the signal detection efficiency, and t is the livetime of the experiment. The sensitivity of this experiment, in terms of a half life exclusion limit, can be written as:

$$T^{0\nu}_{1/2} = k \varepsilon_1 M_{\beta\beta} t, \tag{B.8}$$

where k is now a constant that depends on the confidence level desired (e.g., the standard 90% C.L. exclusion limit).

In the case of an experiment with a mean background rate b, that is also proportional to the exposure $b \propto M_{\beta\beta}t$, we have the number of background events in the signal region equal to $N = \varepsilon_2 M_{\beta\beta}t$ where ε_2 is the efficiency for a background event to end up in the signal region (capturing energy resolution effects around $Q_{\beta\beta}$).

The sensitivity now depends on the number of events in the signal region, divided by the uncertainty on the number of signal counts. In the case of $T^{0\nu}_{1/2}$, where the hypothesis being tested is the absence of signal (no uncertainty), and the fact that the expected background rate b has an associated Poissonian uncertainty $\sqrt{b} = \sqrt{\varepsilon_2 M_{\beta\beta}t}$, the limit now given by:

$$T^{0\nu}_{1/2} = k' \frac{\varepsilon_1 M_{\beta\beta}t}{\sqrt{M_{\beta\beta}t\varepsilon_2}} = k'\sqrt{\varepsilon_1/\varepsilon_2 M_{\beta\beta}t}, \tag{B.9}$$

with k' being a new constant that is set based on the desired confidence level, and the equation shows the scaling of the sensitivity growing as the square root of exposure.

Notice that in the case of nEXO, there is no good single-value choice for b since the experiment has a mean background rate that varies in a non-trivial way across each 3-dimensional bin in energy, standoff, and topology score (DNN). Hence, nEXO's sensitivity scaling with livetime (Section 4.7.1) is somewhere between linear (background-free) and quadratic (case of large background) over the full LXe volume.

B.3 Justification of Wilson score treatment for efficiency estimates

The standard error on the mean of a binomial distribution is commonly taken as:

$$\sigma_n = \sqrt{\frac{p(1-p)}{n}}, \tag{B.10}$$

where p is the probability of success, and n is the number of trials. In the case of the muon tagging data sets, p is near 100% ($p \approx 0.97$), and $n \approx 20,000$. Notice the formula yields nonsensical results for $p = 1$, where the error goes to zero. Additionally, the error is always symmetric about the mean estimate. This method is called the Wald method without continuity correction.

The Wilson score confidence intervals [222] are derived by taking the score statistic assuming a normal distribution, i.e., the σ_n from the Wald estimate, but also considering the difference between the observed success rate, $\hat{p}$, and the true success rate, p. We first define the score statistic as $z = \frac{p-\hat{p}}{\sigma_n}$, which is related to the maximum likelihood estimate of (the score statistic will be zero when $\hat{p} = p$). Squaring both sides of the equation and subbing in the full form of σ_n we have

$$(p-\hat{p})^2 = z^2 \frac{(p(1-p))}{n} \tag{B.11}$$

Subtracting the right side from the left yields a quadratic equation in p, the solutions of

which correspond to the cases where the value of p is minimized, given a value for z:

$$p_{\pm} = (\hat{p} + \frac{z^2}{2n})(\frac{1}{1 + z^2/n}) \pm \frac{z}{1 + z^2/n}\sqrt{\hat{p}(1 - \hat{p}/n + z^2/4n^2)} \tag{B.12}$$

.

Hence, we can set $z = 1 - \alpha$, where α is the confidence level desired, e.g. $\alpha = 0.682$ corresponds to 1σ and solve for the values of $p_{\pm}$ yielding the 1σ confidence band. This can be interpreted as the Wilson score interval, for a given $z = 1 - \alpha$ will contain the true value of p a fraction α of the time. The center of the interval is shifted relative to $\hat{p}$, making the interval asymmetric for values of $\hat{p} \approx 1$ or 0, unlike the standard Wald interval. For additional discussion, see [257].

Appendix C

Outer detector size

C.1 Radiogenic shielding

C.1.1 Gamma radiation

The dominant external sources of gamma radiation backgrounds to nEXO emanate from the surrounding underground environment. In particular, these sources include the natural underground rock and the concrete/shotcrete used to line the SNOLAB cryopit.

Geant4 v10.5 MC studies presented in [204–206] indicated that of all the natural gamma lines of the ^{238}U and ^{232}Th decays series, only two were of serious concern: ^{214}Bi (2.447 MeV) and ^{208}Tl (2.617 MeV). These two isotopes produced line intensities high enough (as read measured by high purity germanium detectors of rock, and shotcrete samples at SNOLAB), and emit γ-rays with energies at or above the $Q_{\beta\beta}$ (see Figure C.1).

The Geant4 MC studies utilized importance sampling techniques to obtain an upper bound on the contribution of these γ-lines to the ROI, by propagating the γ-rays from up to 1 m in the cryopit concrete all the way to the TPC. Direct radiogenic γ-ray contributions from the steel, cabling and up to 500 PMTs are deemed insignificant to the $0\nu\beta\beta$ search,

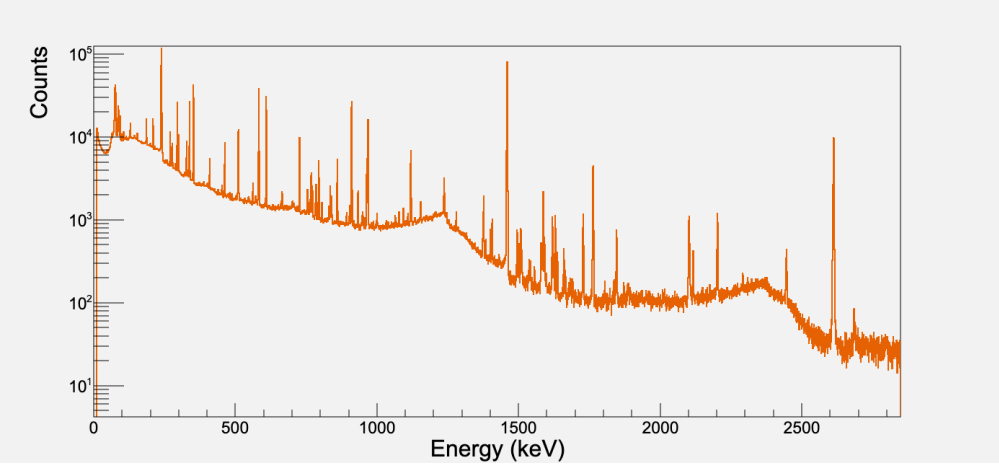

Figure C.1: HPGe spectrum taken of SNOLAB shotcrete. Data retrieved from [258].

relative to the contributions from rock/shotcrete and concrete which have a much larger mass and surface area [259]. A buffer volume of boil-off nitrogen is designed to keep the water clear of ^{222}Rn (a forebearer of ^{214}Bi) dissolving into the water and circulating close to the cryostat vessels. The Geant4 studies determined that the dominant contributor is ^{208}Tl, accounting for over 97% of ROI contributions from background sources external to the cryostat vessels [206]. Shielding against ^{208}Tl conservatively sets the minimum water thickness required for the water tank at 11 m in diameter and 12 m in height [205]. Throughout this thesis, the default OD size is taken to be 12.3 m in diameter, and 12.8 m in height as determined by these minimum shielding requirements. The surface gamma rate in the SNOLAB cryopit for the ^{214}Bi and ^{208}Tl γ-lines are 39 and 508 $\mathrm{m^{-2}s^{-1}}$, respectively [204]. This translates into a 500 kHz 2.617 MeV γ-ray flux entering the Outer Detector.

C.1.2 Neutrons and neutron-induced backgrounds

There are two sources of neutron flux in an underground laboratory: neutrons created by radioactivity in the rock or concrete surrounding the laboratory environment, and neutrons

produced by cosmic ray muons interacting in or near the experiment. This section describes the potential backgrounds arising from the former, and mitigation strategies against backgrounds arising from these radiogenic neutrons; the latter is addressed in Chapter 4.

Radiogenic neutrons in underground caverns are produced by the trace concentrations of ^{238}U and ^{232}Th in the surrounding rock, which create neutrons via (α, n) reactions or spontaneous fission (in the case of ^{238}U). Both processes create a spectrum of fast neutrons with an average energy 1.5–2 MeV and a higher-energy tail extending out to ∼8 MeV [260]. The energy spectrum of these neutrons can then degrade via scattering in the rock, meaning the natural radiogenic neutron flux in an underground laboratory is a mixture of the primary fast neutron flux and a degraded spectrum extending down to thermal energies. Though an exact evaluation of the spectrum is currently unavailable, we estimate the induced backgrounds using the approximate flux in the SNOLAB underground laboratory; the SNO experiment estimated a flux of ∼4000 neutrons $\mathrm{m}^{-2}\mathrm{day}^{-1}$ of fast neutrons and measured a thermal flux of $4144.9 \pm 49.8 \pm 105.3$ $\mathrm{m}^{-2}\mathrm{day}^{-1}$ [247].

Thermalized neutrons will capture on hydrogen within 25 cm of water, well below the minimum water thickness to the cryostat vessel 392 cm. Hence, direct capture of external radiogenic neutrons on ^{136}Xe (producing ^{137}Xe) is negligible, provided the xenon recirculation systems are shielded and placed inside the water, or surrounded by a few centimeters borated polyethylene outside the water as described in [261].

Neutron-induced γ-rays

Neutron-induced reactions can produce gammas of various energies due to the de-excitation of nuclei relaxing back to the ground state after neutron capture or inelastic scattering. By analytically calculating the rate of these interactions in the water, we can place limits on the rate at which they will reach the LXe volume from outside the water tank, and their contribution to the ROI; the full calculations can be found in [207].

The main interactions of concern are the 3.2 MeV gamma line from $^{16}\mathrm{O}(n,\ \gamma)^{17}\mathrm{O}$ interactions, occurring with an intensity of 6.6%. Fortunately, due to the much higher thermal capture cross section on hydrogen relative to ^{16}O, and the 2:1 molar ratio between hydrogen and oxygen in water, this interaction is deemed a negligible contribution to the background model as it occurs in the first ∼meter of water shielding, far from the TPC.

The second interaction investigated is the fast transmutation $^{16}\mathrm{O}(n,\ p)^{16}\mathrm{N}$, which produces a β-delayed γ-ray of 6.17 MeV. Here, the neutron energy threshold for this interaction is >10 MeV. Given the expected radiogenic neutron energy spectra and the fact that most fast neutrons quickly drop below threshold after a single collision with a hydryogen nucleus, this γ-line is also deemed to have a negligible impact on the $0\nu\beta\beta$ search.

C.2 Cosmogenic activation

	External Gamma Constraints (small)	Engineering Baseline 2019 (large)
Radius [m]	5.0	6.17
Height [m]	11.0	13.3

Table C.1: Water tank dimensions used in shielding studies in determining the outer detector size.

	Small Water Tank	Large Water Tank
Number of ^{137}Xe events (raw simulation result)	1758	1821
Number of ^{137}Xe atoms (raw simulation result)	4790	5402
^{137}Xe events [/yr]	4.6 ± 0.3	4.7 ± 0.3
^{137}Xe atoms [atoms/full LXe/yr]	12.5 ± 0.7	14.1 ± 0.7

Table C.2: Summary of results for ^{137}Xe cosmogenics simulations. The first two rows give the raw number of ^{137}Xe events, and atoms (as defined in the preceding paragraph) that come from the simulation. The bottom two rows use the effective underground muon exposure to convert the raw numbers into expected per-year averages for nEXO at SNOLAB. Note that these simulations used an older detector design than the one in Chapter 4, where the total mass of the LXe inside the TPC vessel was 5109 kg.

Appendix D

Additional cosmogenics studies

D.1 Doping the HFE with neutron poisons

Boron is a common neutron absorber used in nuclear reactors. The isotope ^{10}B ($\sim$20% natural abundance) has a thermal neutron capture cross section of about 3800 barns, $\sim$12600 times higher than that of hydrogen. Boron salts, such as borax ($Na_2B_4O_7$), can potentially be dissolved into the HFE to preemptively capture neutrons before they reach the TPC, and therefore reduce activation of ^{136}Xe. Furthermore, captures on ^{10}B produces α-emitting isotopes which do not travel far in the HFE and will not penetrate the copper TPC vessel.

The study was performed by adding varying amounts of borax salt (made with natural boron) in the HFE, and simulating 6×10^5 muons through target 1. Results (shown in Figure D.1) clearly indicate that even for mass concentrations of borax as low as 0.1%, a significant reduction in the cosmogenic ^{137}Xe rate can be attained.

The chemistry of the dissolved borax and the impact it would have on corrosion and cryogenics has not been explored. Hence, this method is not being used in the baseline design for nEXO, though similar neutron-absorbing dopants can be considered for future

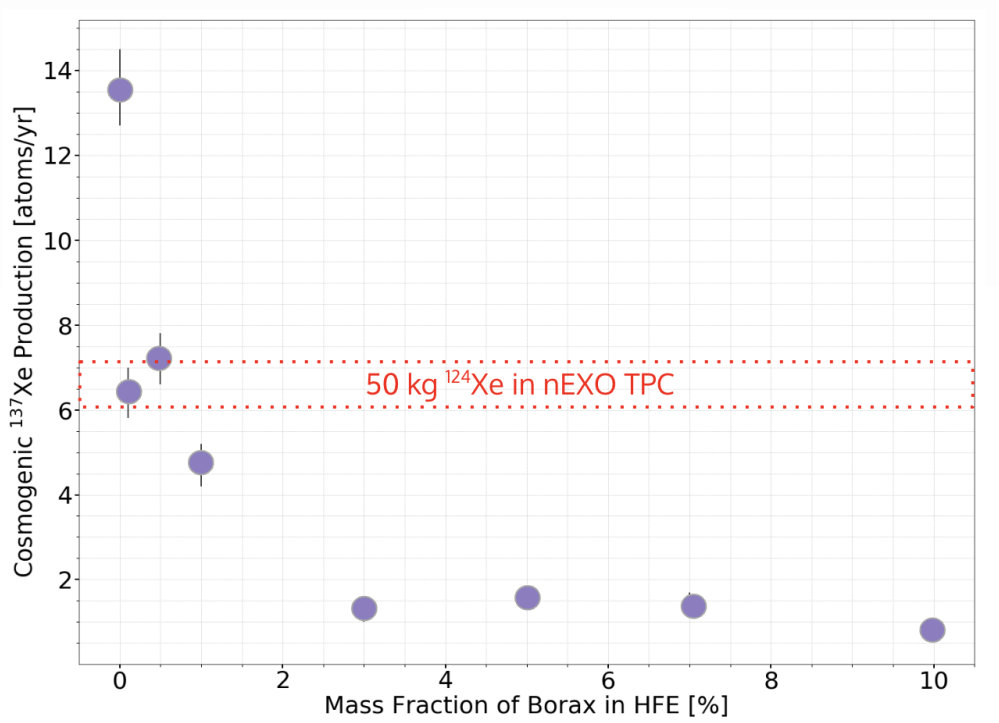

Figure D.1: Isotopic modification and cosmogenic ^{137}Xe activation rates

kiloton LXe detectors using organics as a heat transfer fluid and radiogenic shield.

D.2 Optimizing isotopic ratios in LXe

The xenon enrichment process to obtain ∼5 tonnes of ^{136}Xe will produce xenon isotopes that are particularly neutron absorbing as byproducts including ^{124}Xe. This isotope has a thermal neutron capture cross section of 165 ± 11 barns, 600 times larger than both ^{136}Xe and ^{134}Xe [168]. Preliminary Geant4 simulations showed that for an LXe mixture with 1% ^{124}Xe there will be a corresponding factor of 2 reduction in ^{137}Xe activation rates as shown in Table D.1.

Baseline LXe (90% ^{136}Xe/ 10% ^{134}Xe)	**Modified LXe** (90% ^{136}Xe/ 9% ^{134}Xe / 1% ^{124}Xe)
13.6 $\pm$ 0.9	6.6 $\pm$ 0.6

Table D.1: ^{137}Xe activation rates with ^{124}Xe added into the nEXO LXe. Results shown for simulations on target 1 (see text) with 5109 kg of xenon. Results are given in ^{137}Xe atoms/year.

Appendix E

Documentation on the Geant4 studies

In the scope of the Geant4 simulations: the entire documentation, along with example codes and configuration files, can be found on the nEXO GitHub organization, accessible via the following link (if you are a nEXO collaborator): nexo-offline. The repository is continuously updated to reflect the most current nEXO configurations.

For the data analysis part, the codebase is located in a specific directory within the repository, named `nexo-offline/Analysis/CosmogenicsAlg/` and `nexo-offline/Analysis /ODPMTAlg/` for the cosmogenics analysis and the muon veto PMT processing, respectively. In addition to the Geant4 studies, a separate repository is available for the PMT toy Monte Carlo code used to determine the number of PMTs and is linked here, where there is also more documentation and plotting scripts available (e.g., the violin plots, box plots).

This PMT toy MC code was run on ComputeCanada clusters and can be accessed here. For those who are utilizing the SLAC cluster running Centos7, job submission scripts are also provided in the repository to facilitate the computational processes here.

E.1 Code Compilation Guide

E.1.1 General Information

General information on compiling the code with Singularity can be found at the following link, assuming you are working on the SLAC cluster with Centos7 computers.

- https://github.com/nEXO-collaboration/nexo-offline/blob/main/Doc/singularity.md

Note, these are now superseded by the Shard Data Facility (SDF) framework and instructions will need to be adapted accordingly.

E.1.2 Compilation Instructions

The specific compilation and singularity shell I used is outlined below:

```
cd $NEXOTOP

singularity shell --home  $PWD \

/nfs/slac/g/nexo/software/prod/singularity/nexo-base_v4r1p0.sif

cd /opt/nexo/software

source bashrc.sh

source sniper-install/setup.sh

cd $HOME/nexo-build

cmake -DSNIPER_ROOT_DIR=/opt/nexo/software/sniper-install  \

-DCMAKE_CXX_FLAGS="-std=c++11" ../nexo-offline

make
```

E.2 Cosmogenic activation macros

The macros used for all the Geant4 studies can be found in nexo-offline/od-group/Cards/examples/.

Note that the lines: 37–42 of `nEXOSimFactorySvc.cc`, need to be changed to set the physics lists appropriately. The whole codebase will need to be recompiled after changing the physics lists.

E.3 Geant4 macros

Cosmogenics simulation macros The macros used for the cosmogenic activation studies can be found under Cosmogenics.mac.

Muon veto study The macros used for the Geant4 muon veto studies can be found under MuonVeto.mac.

Inverse beta decay macros The macros used for the cosmogenic activation studies can be found under IBD.mac.

E.4 Geant4 tests

After compiling, and while still in the singularity shell, you can test your code by running the following, or an equivalent whereby the macro file is replaced with your own.

```
source /opt/nexo/software/bashrc.sh

source /opt/nexo/software/sniper-install/setup.sh

source $HOME/nexo-build/setup.sh

cd $HOME/nexo-build/Cards

python3 ./RunDetSim.py --evtmax 1 --seed 1 \

--run $HOME/nexo-offline/Cards/examples/MuonVeto.mac \

--output $HOME/MuonVeto.root > $HOME/MuonVeto.out 2> $HOME/MuonVeto.err
```

Appendix F

Chroma studies documentation

F.1 Repository and Code Information

Comprehensive documentation is available for the Chroma studies in various `README.md` files that are in the appropriate directories hosted on our GitHub repository, available for access via the following link (again, assuming you are a nEXO collaborator):

- https://github.com/nEXO-collaboration/chroma-simulation

The analysis codes, and various plotting scripts associated with the muon veto studies can be found in the `Analysis/OD/` directory within the `chroma-simulation` repository.

F.2 Example Chroma submission

All of the Chroma studies in this thesis were conducted on the `EXO-SIM1` computer located at McGill. The below is a copy of an example simulation execution.

```
cd ~/Soud/Chroma-OD/chroma-simulation;

conda activate chroma-od;

singularity exec --nv \

../chroma_image/Chroma.sif \

python3 RunSim.py -y Yaml/OD/FullPMTs/nonUniform/SimTagging.yaml
```

The below is a copy of an example analysis execution.

```
cd ~/Soud/Chroma-OD/chroma-simulation;

conda activate chroma-od;

python3 Analysis/OD/MuonTagging/MuonTagging.py \

-y Analysis/OD/MuonTagging/MuonTagging.yaml
```

In either case, configuration will need to be set in the respective `.yaml` files, including pointing to the correct geometry directory.